Ductile damage study for low stress triaxiality and during load path changes via 3D imaging and FE simulations

Xiang Kong

To cite this version:

Xiang Kong. Ductile damage study for low stress triaxiality and during load path changes via 3D imaging and FE simulations. Material chemistry. Université Paris sciences et lettres, 2022. English. NNT : 2022UPSLM054 . tel-04011202

HAL Id: tel-04011202
https://pastel.hal.science/tel-04011202

Submitted on 2 Mar 2023

PSL
UNIVERSITÉ PARIS

THÈSE DE DOCTORAT
DE L'UNIVERSITÉ PSL

Préparée à Ecole des Mines de Paris

Ductile damage study for low stress triaxiality and during load path changes via 3D imaging and FE simulations

Étude de l'endommagement ductile lors de chargements complexes et à basse triaxialité par imagerie 3D synchrotron et calculs élément finis

Soutenue par
Xiang KONG
Le 13 juin 2022

École doctorale n°621
Ingénierie des Systèmes, Matériaux, Mécanique, Energétique

Spécialité
Mécanique

Composition du jury :

Ahmed BENALLAL ENS Paris Saclay	*Président*
Krishnaswamy RAVI-CHANDAR University of Texas at Austin	*Rapporteur*
Dirk MOHR ETH Zürich	*Rapporteur*
Jérémy HURE CEA Saclay	*Examinateur*
Fanny MAS Constellium	*Examinateur*
Thilo MORGENEYER Mines Paris	*Directeur de thèse*
Djamel MISSOUM-BENZIANE Mines Paris	*Examinateur*

MINES PARIS | PSL

Acknowledgement

> *"Sorrow an ephemeral life span we have, yet envy how infinite Yangtze River is."*
>
> Former Ode on the Red Cliffs
> Su Shi (1037-1101)

Before starting this thesis, I had heard that Ph.D student is one of the best job because you are sent to an *event horizon* and enjoy an adventure freely even with a wage. During last three years and half, I have been excitedly exploring and noting the unknown area with the guides of my supervisors and now it is time to complete the mission. However, as the selected quote indicated a millennium ago, all good things must come to an end. I would like to thank all the people who contributed to this thesis along this wonderful journey.

First of all, I would like to express the sincerest gratitude to my supervisors, Mr. Thilo F. Morgeneyer, Mr. Djamel Missoum-Benziane and Mr. Gilles Rousselier for their continuous guidance and support. Thilo, thanks for your kind advice and encouraging me as a *freeman* to think and act. I really admire your serious attitude toward work and your responsibility as supervisor fully dedicated to solving my scientific questions and administrative problems. Djamel, I always enjoy working with you for your inspiring ideas and thank for solving every problem that I met within Zebulon. I also like each discussion in culture, history and politics during coffee break or lunch. Gilles, although you are not my official supervisor, I truly appreciate your generous guidance in the modelling part. It was a real pleasure to work with you.

Then I want to express my deep gratefulness to the members of my thesis committee, Mr. Krishnaswamy Ravi-Chandar, Mr. Dirk Mohr, Mr. Jeremy Hure, Mrs. Fanny Mas and the president Mr. Ahmed Benallal. Special thanks are due to Mr. Ravi-Chandar and Mr. Mohr for your precious time to review my thesis as rapporteurs and I truly appreciate the encouraging and rewarding words in the report.

Next, the financial support of the ANR and DFG is gratefully acknowledged. I would like to thank the project members (Lambdaers), Mathias, Daniel, Andrea, Rebecca and Mr. Tilo Baumbach from KIT in Karlsruhe, Germany and Lukas, Yin from ESRF in Grenoble. The memory to the enthusiastic work shift from 3:00 am, as well as the hang out after the experiment, never fade.

I would like to thank all the people met at Centre des Matériaux. After getting off the Paris-Evry shuttle bus every morning, I am always welcomed by Catherine's big smile, thank you! I want to thank every discussion and exchange to build this thesis. I want to thank Fabrice and Maria for each SEM observation; Henry for sharing package Pymicro and his help in Tango system; Yazid for the material identification as well as the encouragement at synchrotron Soleil after my wrong operation. Thank Stéphanie for the guidance to DIC and help for optical setups; Yann, Abdennour for mechanical testing and especially Regis for the cooperation during TP course; Kevin for polishing guide and micro-hardness test; Cédric for Python training course. Thanks all the colleagues from workshop, René, Frederic, Vasco for the specimen manufacture so that I could finish my experiments in time. Particular thank to IT support members: Gregory, Patrice and Yann, I could not launch my calculations or even the software without your help. Final thank goes to the administrative colleagues: Vérnonique, Claudine and Zak. I could not concentrate on my research without your dedicated help.

Thanks all members in B106 (Clément B., Clément R., Houssem, Maxime, Tuan and Baptiste) although hardly see a day that everyone is present at the same time, we share the good memory during-and-after work. Thanks our numerous 'Dont starve' lunch team: Aron, Harris, Julie, Daniel, Alexandre, Johan, Simon, David, Vikram, Raffaele, Mohamed Abator, Rami, Richi, Ana. I really miss the cafe time on the terrace every lunch! Moreover, I want to thank Chinese group at CdM: Wan Lili, Ren Sicong, Lv Fang, Chen Youbin, Huang Qi for the DIY dumpling party.

Finally, I would like to express my deepest thanks to my family for their unconditional love from nearly 10 000 km. I would like to thank Nora for her company and in particular walking and biking in the Vincennes forest to release my stress during thesis preparation. I could not image finishing this thesis without her support.

Contents

List of Figures

List of Tables

Chapter 1

General Introduction

1 Research objectives

1.1 Industrial background and motivation

Climate change is affecting every earth inhabitant in daily life, e.g., global warming and accelerating frequency of extreme weather around the world (IPCC, 2021). According to the Paris Agreement, the long term goal is to keep the rise in mean global temperature below 2°C compared to pre-industrial level since 1850, to keep the climate change impact to a controllable level. To achieve the goal, the concept of net-zero emission is globally considered as a goal (UNEP, 2021), which requires rapid and deep reduction in global greenhouse gas emissions. Fossil Fuel combustion in transportation is responsible for a large part of the CO_2 emissions. The lightweighting trends are assessed as a part of the circular economy solutions in modern mobility and transportation to reduce CO_2 emissions (Czerwinski, 2021).

Among the light materials, aluminum alloys have been widely used for a long time in the industry, mostly aerospace, because of the high strength to weight ratio and formability and are increasingly considered in automotive industry (FLAMINGo, 2021). Light weight thin-walled components play an important role in engineering, particularly for transportation purpose. At the meanwhile, the reliability and lifetime of these products are essential. The consequence of fracture can be minor or costly, even deadly. The better the knowledge about the mechanism ductile damage, the lower the safety factor can be set, which means, to some extent, the lighter materials and structures can be used. During manufacturing and (or) in service, damage is not regarded as failure but considered as a cumulative property of forming products (Tekkaya et al., 2020). The mechanical properties can be improved by damage-based process design and potential challenges have to be emphasized to realize damage-controlled metal forming processes.

In order to better analyze and understand the damage mechanism evolution of metal sheets, an adequate three-dimensional (3D) imaging of the microstructure inside flat sheet specimens, i.e. synchrotron laminography, is suited to study damage under engineering relevant boundary conditions as well as a wide range of stress states and loading paths (Helfen et al., 2012). The interaction between deformation and damage can be established in the material bulk with the knowledge about the underlying microstructure and its evolution. Advanced 4D (3D volume plus time) image analysis now opens the possibility to observe the micro-mechanical behaviour (e.g., damage nucleation and growth kinetics) under non-proportional load paths from micrometer down to nanometer scale. Such hierarchical 3D data would serve as valuable evidence for the formulation and validation of sophisticated damage models to predict engineering-relevant mechanical behaviours.

If the damage processes are well understood and modeled under complex stress state and load paths during forming processes, a reliable fracture prediction would be very significant to decrease enormous expense and to guarantee the security (Park et al., 2020). During the service time of parts and structures, they will be more reliable, durable and lighter, which is one of most important factor meaning less energy consumption in transportation industry. Note that the latest generation light AA2198 is used to exemplify the approach in this thesis but the methodology would be applied to different formable alloys, e.g., AA6061 (Granum et al., 2021).

1.2 Position in LAMBDA project

This thesis is a part of the LAMBDA project ("In-Situ X-ray *LAM*inography with *B*i-axial Loads for the Multiscale Investigation of *DA*mage Formation in Materials for Transportation", Agence Nationale de la Recherche: ANR 17-CE08-0051 grant) aiming to study and understand the ductile damage mechanism under non-proportional load paths in direct link to the mechanical deformation by applying advanced 4D imaging during mechanical tests. The microstructure inside specimens can be observed from micrometer to nanometer scale under complex load paths. The extension of physics-based models would benefit from the 3D hierarchical data to predict damage and failure for a large range of stress state and under complex non-proportional load path changes.

The LAMBDA project consists of four tasks T1-T4, which are distributed among the project partners Centre des Matériaux (CdM) Mines ParisTech, laboratory for Applications of Synchrotron radiation at Karlsruhe Institute of Technology (KIT) Campus South (CS-LAS) and the Institute for Photon Science and synchrotron radiation at KIT Campus North (CN-IPS) illustrated in Fig.1.1.

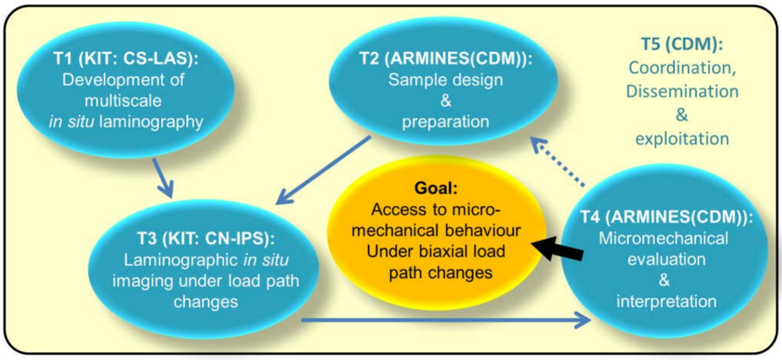

Figure 1.1: Tasks in the LAMBDA project.

- Task 1 coordinated by CS-LAS is devoted to the methodical development of multiscale *in situ* X-ray laminography. It provides the necessary toolbox for the 3D imaging performed within Task 3 (noted as T3). Adapting and extending the instrumentation and measurement routines for X-ray laminographhy and microscopy, the methodical principles of the multiscale *in situ* approach will be worked out and realized.

- Task 2, led by CdM, is devoted to the selection and design of suitable sample geometries for the *in situ* 3D imaging experiments. Suitable materials with particles as well as with and without porosity are selected, in addition to the scientific relevance also considering the required X-ray imaging contrast. The geometrical sample design is based on suitable numerical continuum mechanical simulations. After fabrication, the specimen is pre-characterized by conventional mechanical testing and surface digital image correlation.

- Task 3, CN-IPS organize the application of the novel approach (developed in T1) for the investigation of the samples (delivered by T2) under biaxial load path changes. Besides the experimental data acquisition at KIT and based on proposals at the European Synchrotron Radiation Faculty (ESRF), this will cover the laminographic reconstructions, the correlation and combination of the multiscale data, as well as the image analysis including segmentation, digital volume correlation, the optical flow for strain field determination and the quantification of temporal changes in general.

- Task 4 coordinated by CdM, deal with the evaluation of the data provided from T3 in terms of the qualitative and quantitative evaluation and interpretation from the micromechanical point of view. Mesoscale simulations and micromechanical unit cell calculations provide new insight into the microstructural behaviour and also provide valuable input for the focus of the subsequent measurements, in particular guiding the design of the next sample series and applied load-path changes.

This thesis is mainly involved in Task 2 and Task 4 about mechanical testing and simulation, but also in task 3 for performing *in situ* experiments in cooperation with KIT. Tasks have been accomplished in terms of sample design, mechanical testing and numerical simulation. An *in situ* experiment (2018-ma4333) under a ‘shear to tension’ load path has been performed at beamline ID19 at the ESRF in Dec 2018 with the researchers from KIT. However, due to the shutdown of ESRF in 2019 for the EBS upgrade and due to the sanitary situation since 2020, the experimental *in situ* laminography program for other load path changes was modified into analyzing and post-processing the acquired and existing data.

The present project follows two other ANR projects: ALICANTDE (ANR-06-MAPR-0001, "Alumininium Lithium pour Constructions Aéronautiques Tolérantes aux Dommages") and COMINSIDE (ANR-14-CE07-0034-02, "Understanding, observation, modelling and simulation of ductile damage mechanism"). The mechanical results of macro specimens (uniaxial tensile and notched tensile) from ALICANTDE project are used in this thesis for the calibration of AA2198 elasto-plastic material behaviour. The *in situ* shear experiment of µ resolution (2016-ma3237) was performed at beamline ID19 at the ESRF within COMINSIDE project and analyzed further in the present thesis. The hierarchical data (2016-mi1269) of *ex situ* shear experiment was scanned at beamline ID16b at the ESRF from 250 nm to 50 nm as pixel size as preparation of the present project and the data was reconstructed recently by researchers of KIT (in 2020). The relevant volumes were segmented, visualized and analyzed in this thesis. In addition, the recent work in (Tancogne-Dejean et al., 2021) is related to this project as well.

2 Thesis organization

The thesis is paper draft based and there may unfortunately be repetitions in the introduction part of each chapter. The reader is asked for kind understanding of this way to disseminate research. The content is structured as following in this thesis:

- **Chapter** 1 presents the industrial background, research objectives in the project as well as an outline of the thesis.

- **Chapter** 2 gives a non-exhaustive literature review in terms of aluminum alloys, ductile damage under shear and load path changes as well as mechanism. Relevant damage models, the technique of X-ray synchrotron 3D imaging and its recent applications are also detailed.

- **Chapter** 3 characterizes the material behaviour including the plastic anisotropy of AA2198 in two different heat treatment conditions by experiments using different specimen geometries under complex load paths. The macroscopic model is first identified using the database under proportional load paths and the model manages to predict the mechanical responses for the non-proportional load paths. The effect of load path changes on plasticity and ductility is studied and discussed.

- **Chapter** 4 investigates the shear damage mechanism using *smiley* sample via synchrotron laminography on the multiscale from micrometer to nanometer scale. The shear damage features are analyzed via scan electron microscopy (SEM) and electron back-scatter diffraction (EBSD) as well.

- **Chapter** 5 is devoted to the ductile damage evolution via a 4D *in situ* X-ray laminographic experiment under a ‘shear to tension’ load path change. The interaction between strain and damage evolution is assessed via digital image correlation (DIC) and numerical finite element (FE) simulation.

- **Chapter** 6, a polycrystalline damage model is applied to understand mechanical behaviour under complex load paths. The physics-based model aims to reproduce failure numerically for shear and tension loading as well as to predict the damaging effect of the pre-loading during non-proportional load paths.

- **Chapter** 7 gives general conclusions and perspectives in the future.

The multiscale analyses on different sample geometries from uniaxial tensile (UT), notched tensile (NT), shear-only (SO), tension-only (TO), shear-tension (ST) and *smiley* shear are illustrated in the overview figure below. The results in **μm** and **nm** scale are studied non-destructively in three dimensions via synchrotron laminography and the numbers of relevant experiments at the ESRF are noted in grey boxes.

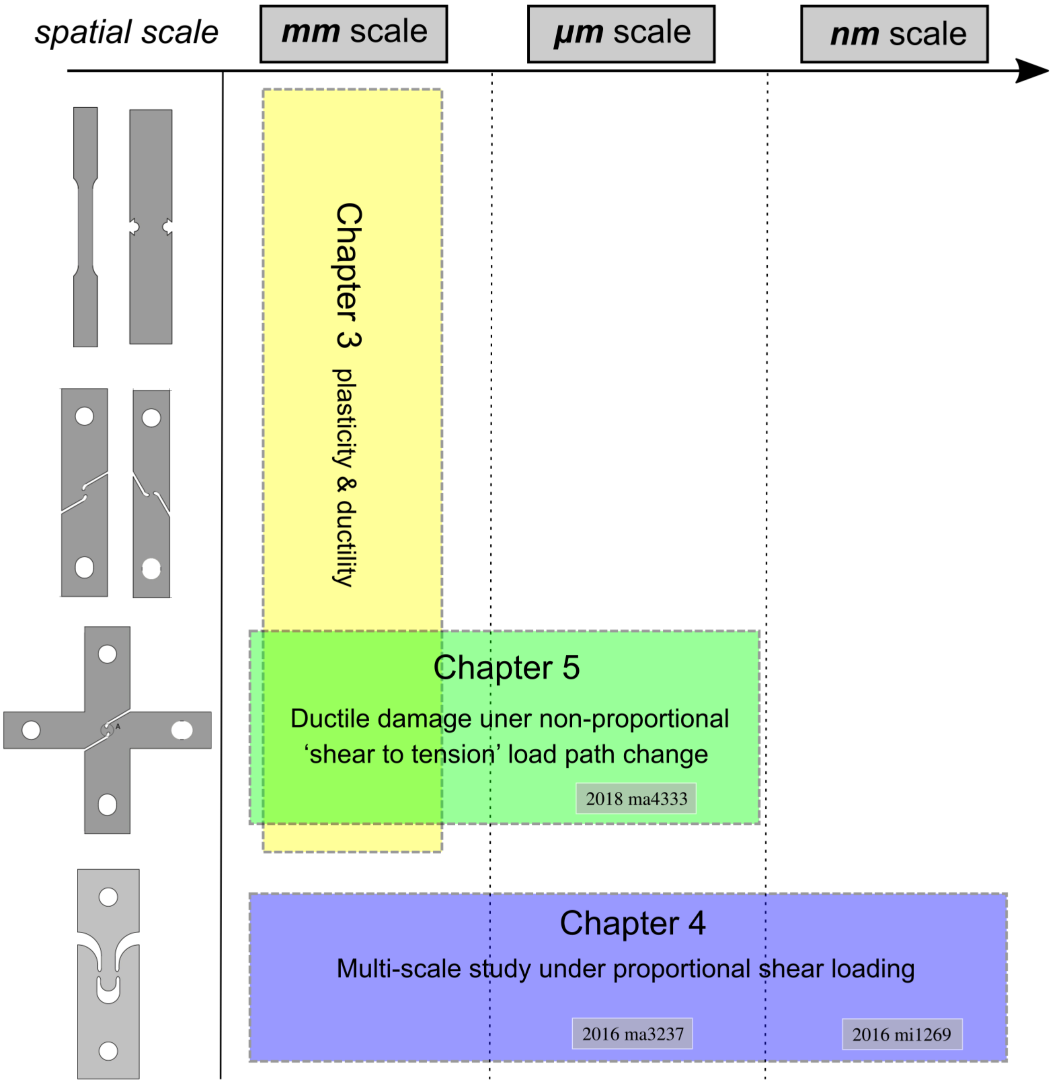

Figure 1.2: Overview over the studied sample geometries and the scales at which they were studied in the different chapters.

Résume en français

Cette thèse est basée sur des artiles publiés et donc il peut y avoir des répétitions dans l'introduction de chaque chapitre. Le lecteur est prié de bien vouloir comprendre cette manière de de diffuser la recherche. Le contenu de cette thèse est structuré comme suivant:

- Le chapitre 1 présente le contexte industriel, les objectifs de la recherche dans le projet ainsi qu'un aperçu de la thèse.
- Dans le chapitre 2, un aperçu non exhaustif de l'état de l'art est présenté à partir des alliages d'aluminium et du matériau étudié, du mécanisme d'endommagement ductile, des modèles d'endommagement. Des études utilisant une technique d'imagerie 3D avancée sont également abordées. Les principales motivations pour ce sujet de thèse et les questions scientifiques pertinentes sont mentionnées en détail à la fin.
- L'objectif de ce chapitre 3 est de caractériser le comportement plastique du AA2198, y compris l'anisotropie plastique du matériau dans deux conditions de traitement thermique différentes (T3R et T8R), et de concevoir une géométrie d'échantillon miniaturisée appropriée pour un changement de trajectoire de chargement 'cisaillement à traction' ou 'traction à cisaillement' dans un environnement d'imagerie in situ qui sera présenté au chapitre 5. Il vise également à étudier l'effet de la miniaturisation de l'échantillon sur la répétabilité de l'essai. En outre, l'objectif est d'identifier l'effet d'un changement de chemin de charge sur la ductilité. Un modèle de plasticité anisotrope macroscopique est calibré à l'aide d'essais de chargement proportionnel et ses capacités de prédiction sont évaluées pour le chargement non-proportionnel et les champs mécaniques associés dans ces conditions. Les surfaces de fracture sont observées par MEB. Les champs de déformation issus du calcul par éléments finis sont comparés aux champs expérimentaux par corrélation d'images numériques (DIC), ainsi qu'aux chemins de fracture.
- L'objectif du chapitre 4 est d'étudier les mécanismes d'endommagement par cisaillement à l'aide d'un échantillon de cisaillement plat, appelé échantillon 'Smiley' (Roth and Mohr, 2016). Des expériences de laminographie 3D synchrotron in situ et de nano-laminographie ex situ ont été menées respectivement pour un essai jusqu'à la rupture et un essai interrompu. L'expérience 3D in situ avait été réalisée et partiellement analysée dans la thèse de Buljac (2017). Afin d'évaluer

la déformation et l'endommagement, la déformation a été mesurée à l'intérieur du matériau en utilisant des données 3D projetées et l'endommagement 3D a été quantifié comme fraction de vide de surface dans ce chapitre. Outre ces observations 3D, à l'aide de techniques 2D corrélatives (MEB et EBSD), la localisation des caractéristiques de l'endommagement par rapport à la microstructure grainulaire a été identifiée pour l'essai interrompu.

- Une réduction substantielle de la ductilité causée par un changement de chemin de charge 'cisaillement à traction' a été trouvée dans le chapitre 3 pour AA2198T8R. Similaire à la méthodologie présentée dans le chapitre 4 précédent pour une charge de cisaillement proportionnelle, un test de laminographie aux rayons X in situ est effectué pour étudier le mécanisme d'endommagement lors de ce changement de trajectoire de charge complexe dans ce chapitre 5. Les champs de déformation sont mesurés et comparés entre la corrélation d'images numériques (DIC) expérimentale et les calculs numériques par éléments finis (FE). L'interaction entre la déformation et l'évolution de l'endommagement est évaluée via la DIC réalisée sur les données de laminographie 3D projetées et les micro-mécanismes correspondantes sont suivies et analysées quantitativement en termes de fraction de surface vide pendant le chargement. Les mécanismes d'endommagement liés à la microstructure du matériau sont détaillés à l'échelle microscopique. Les états de contrainte (par exemple, la triaxialité de la contrainte) sont analysés de manière approfondie par des simulations par éléments finis en utilisant le même modèle macroscopique avec une plasticité anisotrope.

- La ductilité pour un changement de patch de charge 'cisaillement à traction' a été trouvé réduite dans les chapitres précédents par rapport à un essai de traction proportionnelle. Deux types de dommages, les fissures plates liées aux grains et les porosités liés aux particules, ont été observés dans le chapitre 4 sous une charge de cisaillement dans un alliage d'aluminium 2198. Les fissures plates nocifs se sont avérées être à la fois transgranulaires et intergranulaires. Comme l'AA2198 contient une porosité initiale négligeable, l'évolution des vides est limitée en l'absence d'une haute triaxialité de la contrainte. Le but de ce chapitre 6 est d'identifier un modèle approprié et de reproduire numériquement la rupture en cisaillement et en tension ainsi que de prédire l'effet néfaste de la précharge de cisaillement.

- Le chapitre 7 présente des conclusions générales et des perspectives.

Chapter 2

State of the art

In this chapter, a non-exhaustive overview of state of the art is outlined from the aluminum alloys and the material under study, ductile damage mechanism, damage models. The applications using an advanced 3D imaging technique are also addressed. The principal motivations for this thesis subject and relevant scientific questions are mentioned in details in the following.

1 Materials: aluminum alloy

1.1 Classification

Aiming to designate the alloys from different countries, the introduction of an International Alloy Designation System for wrought products has been accepted gradually since 1970. A four-digit numerical designation system is used to identify aluminum alloys, where the first digit indicates the major alloying elements (Polmear, 2005):

- 1xxx series: for pure aluminum with more than 99% (w.t)
- 2xxx series: alloyed with copper (Cu)
- 3xxx series: alloyed with manganese (Mn)
- 4xxx series: alloyed with silicon (Si)
- 5xxx series: alloyed with magnesium (Mg)
- 6xxx series: alloyed with magnesium (Mg) and silicon (Si)
- 7xxx series: alloyed with zinc (Zn)
- 8xxx series: alloyed with other elements

1.2 Al-Cu-Li alloys

Aluminum alloys have been widely used and their performance has been improved to meet the demands in aerospace industry for a long time (Ehrström and Warner, 2000). Compared to the conventional commercial 2xxx and 7xxx series aluminum alloys, Al-Cu-Li-(Mg-Ag-Zn) alloys exhibit excellent performance in terms of low density, improved specific strength, damage tolerance and high stiffness to weight (Dorin et al., 2018; Giummarra et al., 2008), principally developed for military and space applications (Warner, 2006). More damage tolerant variant have been developed in order to meet the requirements of potential commercial airframes. As seen in Fig.2.1, the third generation of Al-Cu-Li alloys (i.e. 2198, 2098 and 2050 in solid box) increased the Cu/Li ratio than the second generation alloys (2090 and 2091 in dashed box), resulting in higher strength potential and thermal stability while partly sacrificing the advantage of Li addition (e.g., the increase in modulus and the decrease in density). Among this third generation, 2198 Al-Cu-Li alloy exhibits a good combination of static tensile properties, damage tolerance, formability and good properties after friction stir welding (Chen, 2011; Le-Jolu et al., 2010). AA2198 in various heat treatment conditions has been studied in (Deschamps et al., 2013; Nayan et al., 2019) and an anisotropic plastic behaviour has been found (Chen, 2011; Nayan et al., 2019). This anisotropy is particularly strong for the fibrous material according to Chen et al. (2011). Two different heat treatment conditions T351 and T851 are applied to the target materials: all sheets are first heat treated (solutionizing and quenching), and then stretched by 2-4% (as T-51); Secondly, the stretched

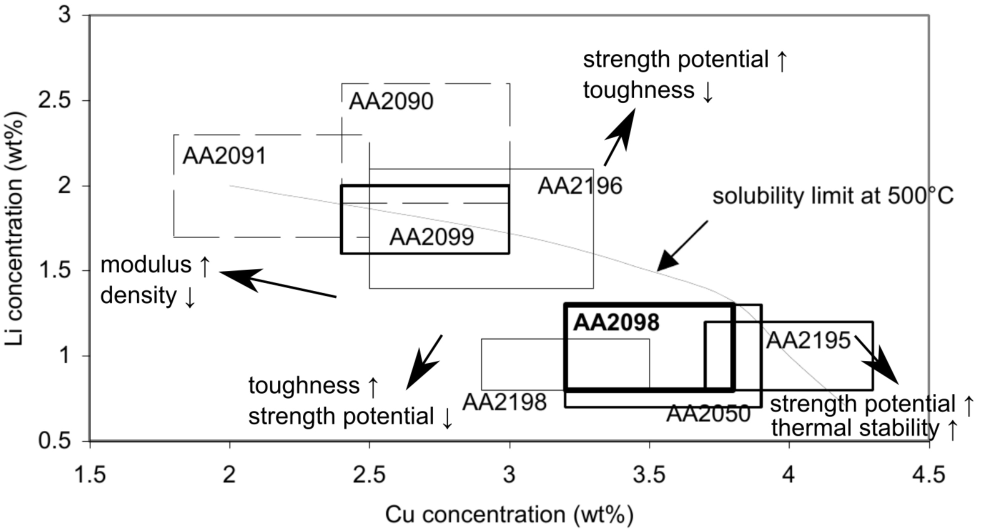

Figure 2.1: Positioning of the second (dashed box) and third (solid box) generations aluminum alloys in the Li and Cu concentrations adapted, after Warner (2006).

sheets naturally aged to obtain T351 condition materials, then an additional artificial ageing step was applied to achieve T381 temper materials. The recrystallized sheets are formed by cold rolling at temperature below the recrystallization temperature (Chen, 2011). The materials in recrystallized state from both conditions are referred to as T3R and T8R respectively in the following. A CT-like specimen geometry has been chosen to investigate deformation and damage micromechanism in AA2198-T3R (Buljac et al., 2018b; Morgeneyer et al., 2014) or AA2198-T8R (Rousselier et al., 2017). In Fig.2.2, 2198-T8 shows a optimized combination with high toughness and strength compared to other alloys. Meanwhile, these third generation Al-Cu-Li alloys have lower density and the good fatigue crack growth rate (Wanhill, 1994).

2 Ductile damage mechanism

The damage mechanism of aluminum alloys, as well as other ductile materials (e.g., steels) have been studied for decades. A void nucleation-growth-coalescence damage mechanism has been established especially for high stress triaxiality (Anderson, 2005). More recent studies have focused on the fracture at low stress triaxiality and the mechanism becomes more complex under engineering-revelant non-proportional load paths (e.g., forming process or in-service). The relationships between strain to fracture and stress invariants (e.g., triaxiality and the Lode parameters) have been explored in Bao and Wierzbicki (2004); Roth and Mohr (2016). However, strain to fracture is an ambiguous definition and difficult to measure especially in regions where strains are highly localized, not to mention the strain definition during complex non-proportional load

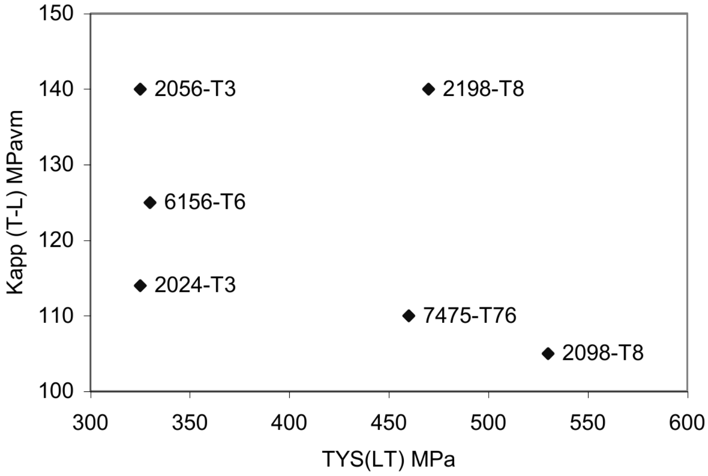

Figure 2.2: Comparison of toughness and strength balance for the aluminum alloys, where toughness K_{app} from w = 760 T-L specimens and data correspond to 5-7 mm sheet or light gauge plate, after (Warner, 2006).

path changes.

2.1 Proportional loading

2.1.1 High stress triaxiality

Ductile fracture at high stress triaxiality (i.e. above 1) has been widely studied over the last decades and the governing damage mechanisms have been identified as void nucleation-growth-coalescence (Anderson, 2005; Pineau et al., 2016). Fig.2.3 presents the damage evolution that can be sorted into three stages:

- (i). Void nucleation at an inclusion or second-phase intermetallic particle by either matrix-particle interface decohesion or particle cracking;
- (ii). Void growth around the particle, driven by means of plastic strain and stress triaxiality (particular mean or hydrostatic stress);
- (iii). Void coalescence due to a local plastic instability that leading to final macro failure.

Within the last stage, void coalescence can also be sorted into three types (Benzerga and Leblond, 2010; Pineau et al., 2016): 1. internal necking; 2. void sheeting and 3. void column (so called *necklace* coalescence). Internal necking is the most common observed mode for fracture, where the ligament between two voids shrinks with a shape typical of a necking process. An example of internal necking is illustrated in Fig.2.4 (a). The second mode is frequently called void sheeting in a shear localization between large primary voids, at which many secondary voids are located. A micrograph provides the

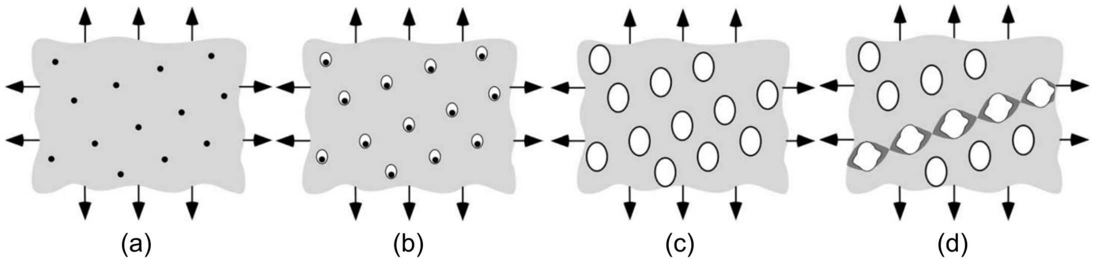

Figure 2.3: (a) Initial state with second-phase particles (black) in the matrix (grey). Damage evolution of void (b) nucleation, (c) growth and (d) coalescence under loading for high stress triaxialities, adapted after Anderson (2005).

shear localization mechanism from a deformed specimen in steel (Cox and Low, 1974) in Fig.2.4 (b). Furthermore, the transition from shear localization to internal necking has been observed in many aluminum alloys (Asserin–Lebert et al., 2005; Bron et al., 2004) and it can be related to the transition between slant fracture to flat fracture mode (Morgeneyer et al., 2014). The third mode of void coalescence is the formation of voided columns (so called *necklace*). A localization of voids gathered in column parallel to the loading axis. It is the most dominant model in steels containing MnS inclusions that favored in moderately notched bars (Benzerga et al., 2004) shown in Fig.2.4 (c). Another example in Fig.2.4 (d) presents a column of voids resulting from a long cluster of copper oxide particles in the copper matrix.

In order to investigate the strain to fracture on dependence of stress triaxiality, some researchers performed experiments using different specimens to achieve a wide stress state (Bao and Wierzbicki, 2004; Roth and Mohr, 2016). On the other hand, the complex geometries were specifically designed for various stress state by applying different loading conditions (Mae et al., 2007; Papasidero et al., 2015). Bao and Wierzbicki (2004) provided a relationship between the equivalent strain to fracture and average stress triaxiality from the experimental fracture points on AA2024-T351 in Fig. 2.5. The 11 experiments were divided into three regimes as upsetting tests with negative triaxiality (-0.3 to 0), shear tests for low stress triaxiality (0 to 0.4), and tensile tests for high stress triaxiality (0.4 to 0.95) respectively. In each of the three regimes, a simple analytical expression was developed to link fracture points. Fracture type was concluded on for each regime as well: shear fracture dominated the upsetting tests for negative stress triaxiality and fracture occurred due to void formation on notched tensile specimens for stress triaxiality greater than 0.4. For the low stress triaxiality, fracture may develop as a transition, combining shear and void growth modes. It was still not well understood for shear dominant loading condition. In addition, the local measurement of equivalent strain to fracture under shear was ambiguous in this work. The difference between strain at crack initiation ε_c and strain at final failure ε_f could be negligibly small for smooth specimens but large enough to take it into consideration for the notched specimens (Benzerga and Leblond, 2010). Instead of using average stress triaxiality (Bao and

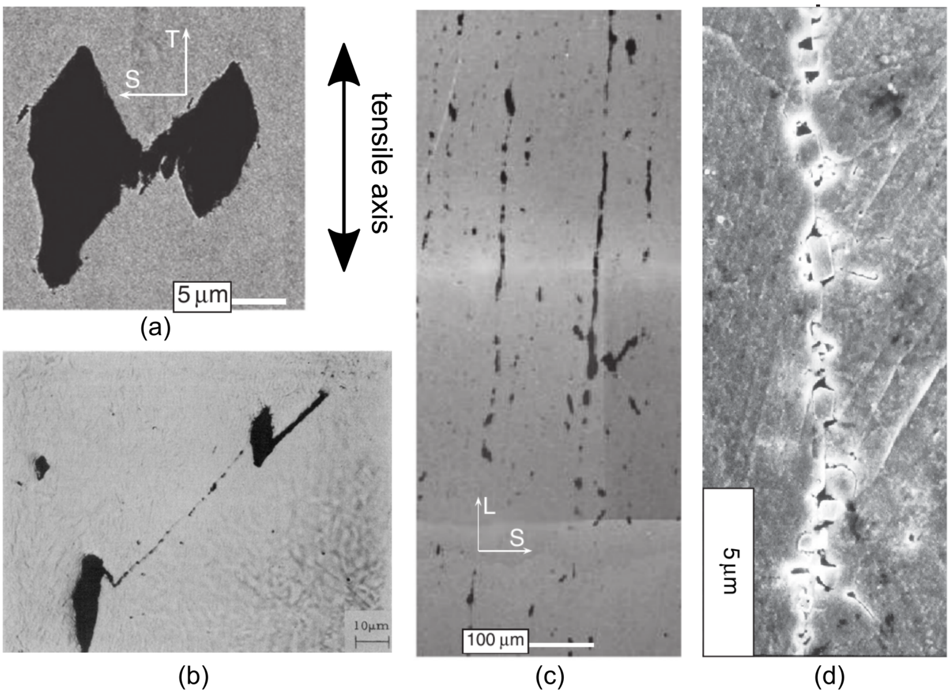

Figure 2.4: Observations demonstrating void coalescence in metals: (a) an internal necking process of intervoid ligament in a layer of steel (Benzerga and Leblond, 2010), (b) void sheeting mechanism on the microshear band with secondary voids in AISI 4340 steel (Cox and Low, 1974), and void column (*necklace*) of (c) a steel containing MnS inclusions (Benzerga and Leblond, 2010), (d) a copper (Pineau et al., 2016).

Wierzbicki, 2004), Roth and Mohr (2016) designed and optimized a series of flat specimen geometries to achieve stable stress state till the point of fracture initiation. Four basic fracture experiments using specific specimens in Fig.2.6 (b)-(e), were performed during proportional loading on dual phase steel DP780. A miniature punch specimen in (b) is aimed to perform equi-biaxial tension (EBT) experiment and the bending strip in (c) for plane strain tension (PST) state, while a flat specimen with a central hole in (d) guaranteed the uniaxial tension (UT) state at the fracture region and a *smiley* shear geometry in (e) is designed for pure shear (SH) state. The strain to fracture was measured by DIC in each experiments, according to the equivalent strain definition:

$$\varepsilon_{eq} = \frac{2}{\sqrt{3}}\sqrt{\varepsilon_I^2 + \varepsilon_I\varepsilon_{II} + \varepsilon_{II}^2} \tag{2.1}$$

Material parameters of Hosford-Coulomb criteria were identified by four fracture points at typical stress state. Fig.2.6 (a) presents the equivalent strain to fracture evolution as a function of stress triaxiality. This criteria was transformed into a mixed stress-strain space (Mohr and Marcadet, 2015) leading to an expression of equivalent strain at fracture dependent on the stress triaxiality T and Lode angle parameter $\bar{\theta}$, the latter, a

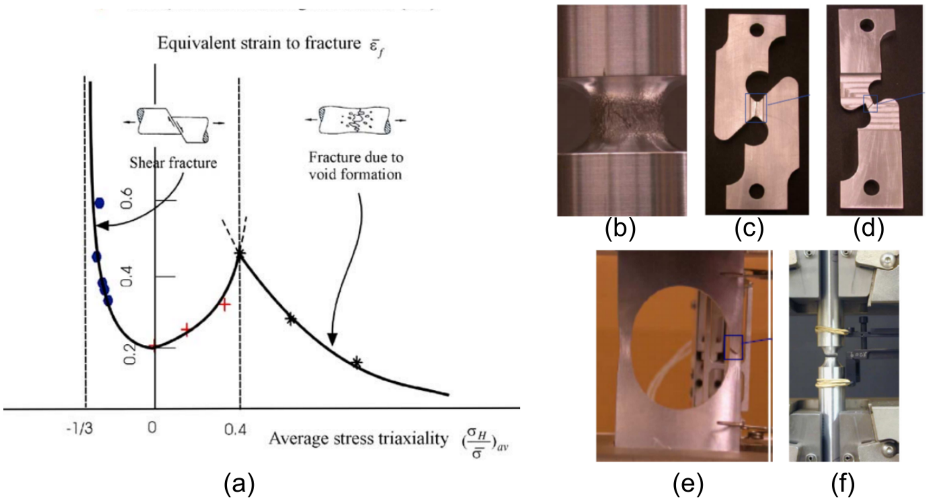

Figure 2.5: (a) The curves strain to fracture – average stress triaxiality, where blue points represent compression tests with (b) round specimens with different ratios of diameter and height, red plus symbols for the shear dominant tests with flat specimens (c: pure shear, d: shear-tension combined, e: tensile with a circular hole) and black star points for the tensile tests with (f) round specimens with different notches, adapted after (Bao and Wierzbicki, 2004).

function of the third invariant of the stress deviator, is defined in Eq.2.2:

$$\bar{\theta} = 1 - \frac{2}{\pi} \arccos(-\frac{27}{2} T (T^2 - \frac{1}{3})) \tag{2.2}$$

The so called fracture surface in terms of strain to fracture as a function of triaxiality and Lode angle parameter is exhibited in Fig.2.6 (f). The 3D plot describes a monotonic dependency of the strain to fracture on the stress triaxiality and a convex shaped function of the Lode angle parameter. Unlike Bao and Wierzbicki (2004) indicated that strain to fracture under shear stress state (T=0) is lowest, the stress state of plane strain tension (PST, T=0.58) is regarded as minimum ductility in the fracture surface. However, the surface was only validated at four distinct stress states with flat specimens under plane stress conditions. The model still need more experimental validations at various stress states. Mae et al. (2007) proposed a so called *butterfly* specimen to achieve multi stress state by changing loading orientation on a special universal biaxial testing device (Mohr and Doyoyo, 2004) in Fig.2.7 (b). The orientation angle α with respect to the loading direction varies from -10° to +20° for a wide range of states such as pure tension (T=1/3), combined tension and shear (T=0 to 1/3), pure shear (T=0), and combined compression-shear (T=-1/3 to 0). In this work, biaxial loading tests were carried out to characterize fracture behaviour of a cast aluminum alloy as well as tensile tests on round bars for higher triaxiality (T=1/3 to 0.8). The equivalent strain was determined from the numerical simulations corresponding to the measured global displacement to fracture.

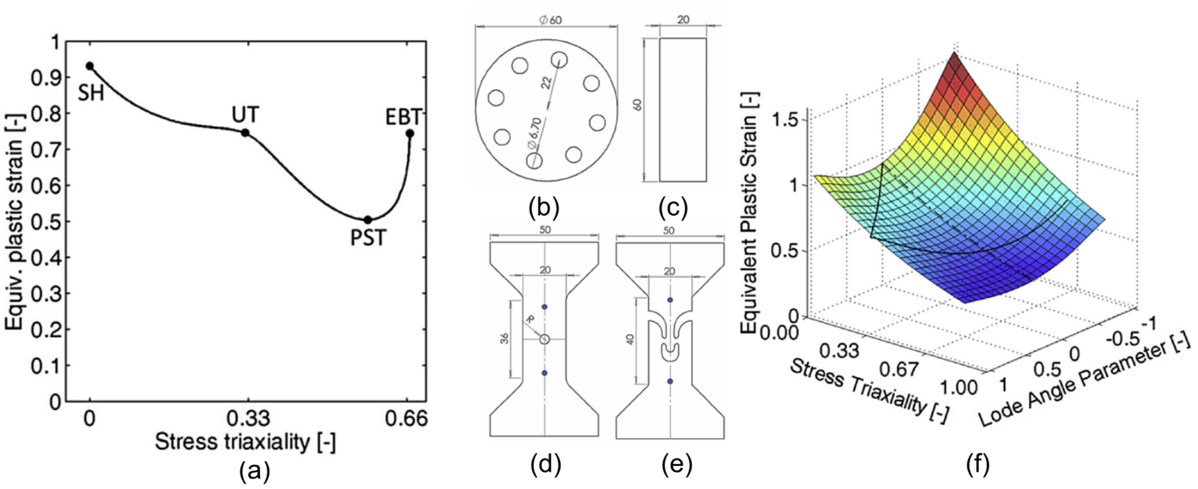

Figure 2.6: (a) Equivalent strain to fracture versus stress triaxiality from four experiments on steel DP780 under plane stress state: (b) a miniature punch specimen for equi-biaxial tension (EBT), (c) a bending strip for plane strain tension (PST) state, (d) a tension specimen with central hole for uniaxial tension (UT) and (e) a *smiley* shear specimen for pure shear (SH) state. (f) A 3d plot of fracture surface in terms of strain to fracture as a function of stress triaxiality and the Lode angle parameter, according to the Hosford-Coulomb model for proportional loadings, after (Roth and Mohr, 2016).

Fig.2.7 (a) presents the fracture strain evolution with different average stress triaxiality, in which experimental fracture points from *butterfly* specimens were marked as point. Similar as three regimes (Bao and Wierzbicki, 2004), three branches were re-calibrated using analytical curves to represent fracture locus in green. Moreover, the exponential function agrees well with the experimental results of round bar samples (Børvik et al., 2001). A Johnson-Cook fracture criterion (Johnson and Cook, 1985) is shown as blue dashed line and defined as:

$$\bar{\varepsilon}_f = D_1 + D_2 \exp(D_3 T) \tag{2.3}$$

where D_1, D_2 and D_3 are three coefficients to be determined. It is worth nothing that two fracture points from *butterfly* specimens (+10° and +20°) were obviously different from those of round bars. This mismatch might come from the error due to numerical-experimental measurement for strain to fracture, or could be related to the different Lode angle parameter as seen in Fig.2.6 (c). Dunand and Mohr (2011) carried out the four experiments with the same specimen for a wider range of stress triaxiality from 0 to 0.8 (α=0°, 25°, 63° and 90°) on TRIP780 steel. The critical surface was measured by DIC to estimate fracture strain. They emphasized the dependency on the Lode angle and effect of loading history in order to predict the onset of ductile fracture. Papasidero

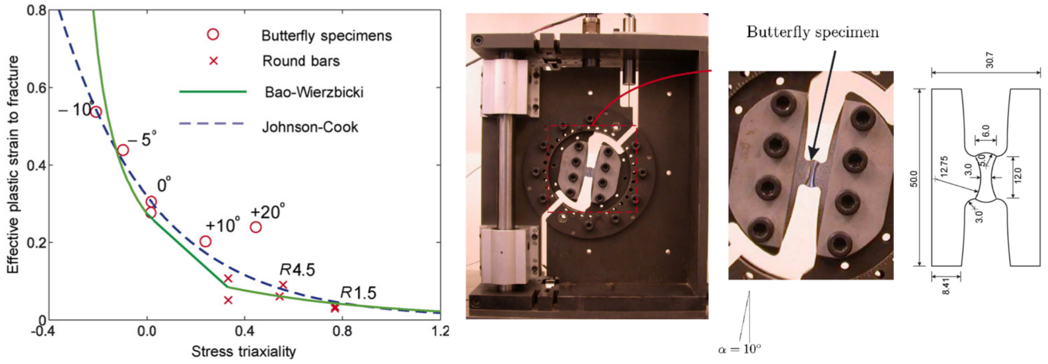

(a) (b) (c) (d)

Figure 2.7: (a) The curve in terms of effective plastic strain to fracture versus average stress triaxiality. (c) A special geometry so called *butterfly* designed for multi can be loaded in (b) a universal biaxial testing device. (d) The major dimensions of *butterfly* specimen geometry, after Mae et al. (2007).

et al. (2015) carried out tension-torsion experiments on a tubular specimen (Papasidero et al., 2014, 2013) under different stress states. The dimension of geometry was optimized from Barsoum and Faleskog (2007a) in Fig.2.8 (b), with adding a height with constant thick within the gauge section, to obtain uniform stress and strain fields. The section was measured by 3D-DIC during loading. The biaxial loading angle β is defined by the ratio of torsion and axial loading, to control stress state in the specimen gauge section as below:

$$\tan\beta = \frac{FD}{2M} \cong \frac{\sigma}{\tau} \tag{2.4}$$

where F is the axial force, D is specimen inner diameter, M is the torque, σ denotes the stress along the height direction and τ is the shear stress in plane. For β=0°, the specimen is loaded only with the torsion under pure shear state (F=0); For $0° < \beta \leq 55°$, the specimen is under shear-dominated stress state; For $55° \leq \beta < 90°$, the specimen is under tension-dominated stress state; For β=90°, the specimen is under transverse plane strain state without any torque (M=0). Fig.2.8 (a) demonstrates a monotonic decrease of strain to fracture with increasing the stress triaxiality from 0 to 0.6 according to (Papasidero et al., 2015), with comparison to Bao and Wierzbicki (2004) for the same aluminum alloy 2024. This mismatch might be due to the differences in the microstructure according to (Papasidero et al., 2014). More importantly, there are significantly opposite tendency at low stress triaxialities between 0 to 0.33. On the one hand, the fracture strain can be measured from either hybrid experimental-simulation method or direct DIC result. The latter relies on the correlation parameters such as subset size and step size. On the other hand, it is also noted that the determination of the stress state (e.g. average triaxiality or final triaxiality) can affect the curves as well.

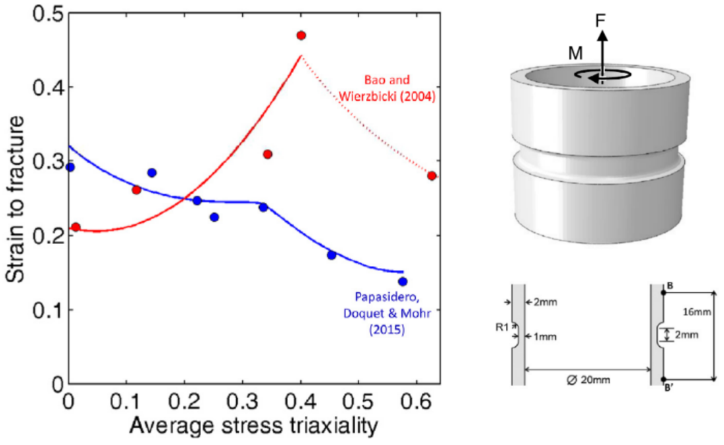

(a) (b)

Figure 2.8: (a) Comparison of experimental results (Papasidero et al., 2015) as blue points with those of (Bao and Wierzbicki, 2004) as red points for the same AA2024 in terms of strain to fracture and average stress triaxiality under proportional loading. (b) The tubular tension-torsion specimen geometry with major dimensions in the area of interest, after Papasidero et al. (2013).

To some extent, this relationship between fracture strain and stress triaxiality (or even the Lode parameters) has been established for a wide range of stress state. Although this curve (or surface) was only identified by fracture points at representative stress states, it is of significance under proportional load paths. However, the mechanism behind leading to these curves is still not clearly known especially under shear dominated stress state. The definition and measurement of strain to fracture must be universal for different experiments. In addition, the meaningfulness of single stress triaxiality becomes less representative under non-proportional load path changes (e.g. from shear to tension).

2.1.2 Low stress triaxiality nearly zero

Shear experiments In order to characterize the shear behaviour and better understand shear mechanism, diverse shear flat specimen geometries (Achouri et al., 2013; Bao and Wierzbicki, 2004; Gross and Ravi-Chandar, 2016; Peirs et al., 2012; Roth and Mohr, 2016) have been designed in Fig.2.9 since new century as well as *butterfly* specimen (Mae et al., 2007) and the tubular torsion geometries (Barsoum and Faleskog, 2007a; Haltom et al., 2013; Papasidero et al., 2013). A perfect shear geometry not only requires a homogeneous pure shear stress state in the fracture region, but also meet the requirements as below (Peirs et al., 2012): Homogeneity of the stress and strain fields; a straight relationship between global force and local stress; avoid stress concentration; no out-of-plane motion of the mid surface; easy and reproducible manufacturing etc. Peirs et al. (2012) optimized the dimension of the specimen in 2.9 (c) to obtain a 3mm×1mm homogeneous region under static and dynamic shear testing for Ti6Al4V alloy. Based on the geometry, Roth and Mohr (2016) proposed a in plane shear geometry so called *smiley* in (e) and optimized the dimensions such as vertical and horizontal offsets of notches, notch shape, thickness for the ductile alloys (DP780 steel, DP590 steel, AA2198-T8R and Ti6Al4V) respectively (Roth and Mohr, 2016).

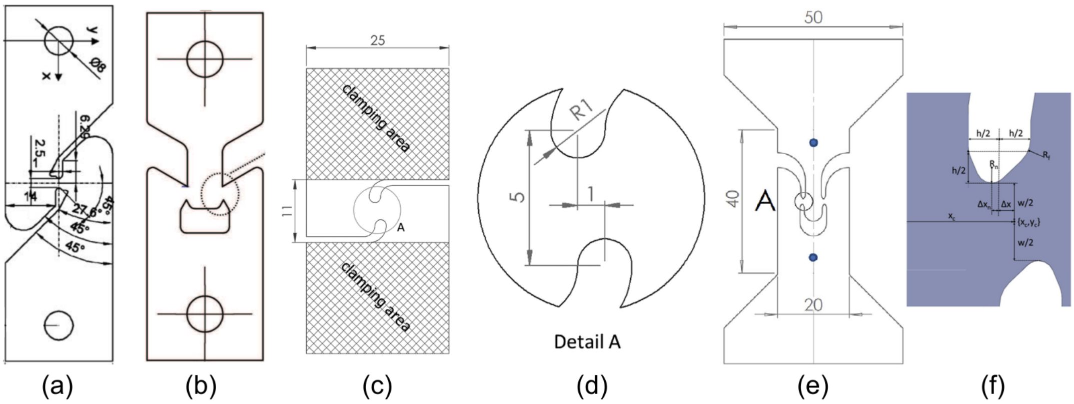

Figure 2.9: Flat specimen geometries designed for shear state: (a) 1.5mm thick shear sample in dual phase steel DP800 (Tarigopula et al., 2008); (b) a 2mm thick shear sample in high-strength low-alloy (HSLA) steel (Achouri et al., 2013); (c)(d) a 0.6mm thick shear sample in Ti6Al4V titanium alloy (Peirs et al., 2012); (e)(f) the *smiley* shear sample optimized for the 1mm thick sample in DP780 steel, 1.4mm thick in DP590 steel, 2mm thick in AA2198-T8R, and 1.5mm thick in Ti6Al4V titanium alloy (Roth and Mohr, 2016, 2018).

Shear micromechanism observation With using specific geometries for shear state, the shear damage features have been detected and followed via 2D SEM (Achouri et al., 2013; Gross and Ravi-Chandar, 2016; Papasidero et al., 2013) and 3D synchrotron imaging (Roth et al., 2018; Tancogne-Dejean et al., 2021). They observed the evolution of damage feature such as (i) pre-existing voids, and (ii) intermetallic particle cracks under intense shearing. Roth et al. (2018) tracked a group of three round particles (CaO) about 5 µm diameter in FB600 steel, that was located inside the shear zone in the 2D projections (of minimum contrast in 17 µm thick slice) from the volume data in Fig.2.10 (a). The initial round black particles at step 0 became approximately elliptical after loading. The voids, nucleated from particle-matrix decohesion in the form of sharp edges, continued to rotate from 51° to 76° and simultaneously extended along the loading direction. Eventually the blunt cracks grew from the voids into the matrix at the last step 6. A shear damage feature, where the particle-initiated-void nucleation-rotation-extension into flat macro cracks, was observed via 3D imaging on dual phase steel. During an *in situ* SEM torsion test on the tubular specimen mentioned in Fig.2.8 (b) for a textured 2024-T351,Papasidero et al. (2014) observed the strain localization near the grain boundaries, where a cluster of rotated particles was found. In the top figure of Fig.2.10 (b), strain differentials between neighboring grains gave rise to surface undulations, which might be triggered by the stress concentration of broken particles. The intense slip bands along the broken particles, either on the grain boundaries as intergranular damage, or out of boundaries as transgranular damage in the highly deformed region. In addition to the particle related feature, one-grain-large shear microcracks were found in the bottom figure of Fig.2.10 (b) seemly without any visible broken particle in the vicinity on the surface. Local distorted grid next to microcrack was seen with up to 110% shear strain. Achouri et al. (2013) observed the evolution of a single inclusion at higher magnification

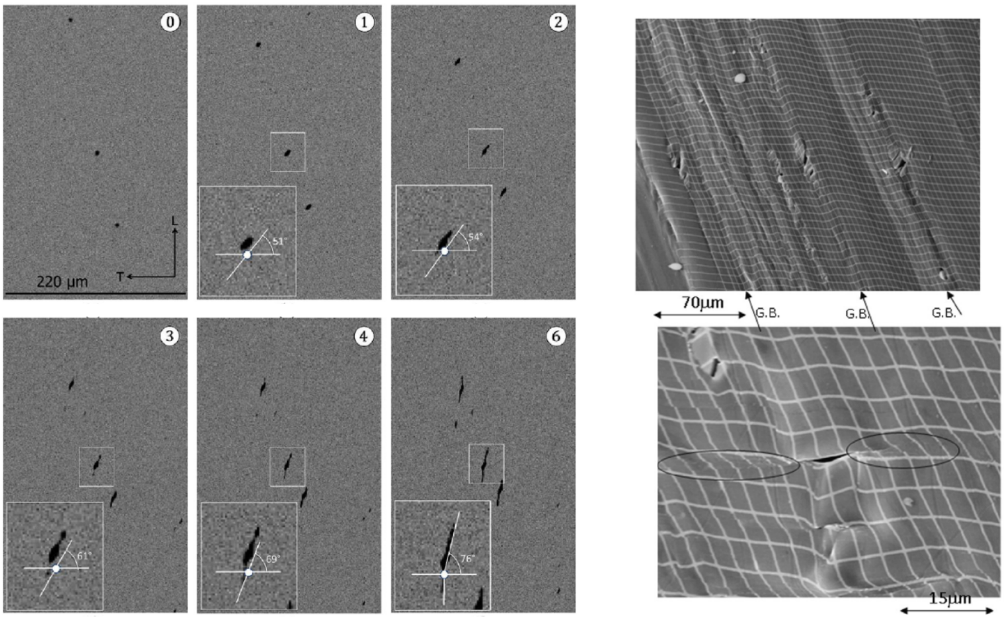

(a) (b)

Figure 2.10: Shear damage features: (a) evolution of particle-related voids in 2D projections under intense shear on FB600 steel via 3D imaging after Roth et al. (2018); (b) slips band triggered by at grain boundaries (top) and microcracks (bottom) on AA2024-T351 under torsion via SEM, after (Papasidero et al., 2014).

in HSLA steel via *in situ* SEM. The debonding of inclusion Al_2O_3 from the matrix due to stress concentration under shearing, and the inclusion-matrix interface was regarded as a nucleation sites for voids. The void rotated and extended under intense shearing shown in Fig.2.11 (a). The same phenomenon was observed in AA6061 (Gross and Ravi-Chandar, 2016) in Fig.2.11 (b). Moreover, an intermetallic particle was rotated and broken into debris in the highly deformed shear zone. Buljac (2017) investigated the shear damage mechanism using *smiley* shear geometry in AA2198-T8R via 3D laminography in his thesis. The flat crack was found in the highly deformed region between two notches and this feature led to the final macro crack path illustrated in blue arrow in Fig.2.12. Tancogne-Dejean et al. (2021) observed the damage evolution on the same *smiley* shear sample of AA2024-T351 via 3D synchrotron imaging in Fig.2.13. The initial void inside

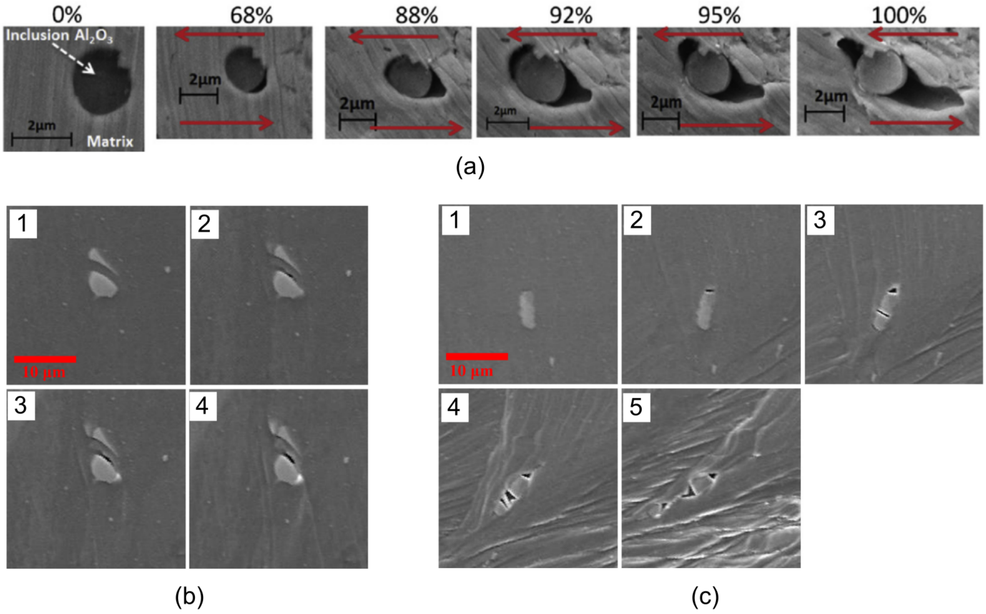

Figure 2.11: The evolution of voids under intense shear condition via *in situ* SEM: (a) An Al_2O_3 rich inclusion decohered from matrix in HSLA steel, after (Achouri et al., 2013); (b) a matrix-particle debonding as void and (c) the particle cracks in AA6061, after (Gross and Ravi-Chandar, 2016).

particle grew under shear in (a). A second void formed at step 6 and coalesced to a large void. On the other hand, a pre-existing void particle was tracked in the deformed field in Fig.2.13 (b). It rotated and elongated upon loading. The flattened void was attached to the fracture path after broken.

Fractography Fig.2.14 (a) presents a large elongated dimple resulting from the first population of voids that nucleated on a CaO particle, is relatively flat compared to those at high stress triaxiality. Sub-micrometer sized dimples were seen on the area, which were probably associated with the void sheeting mechanism. The sub-micro shear dimples were also observed at higher magnification after torsion (Pineau et al., 2016) in (b) and shear (Tancogne-Dejean et al., 2021) in (c). In the latter work, small precipitates (i.e. dispersoids around 150 nm) seemed an initiation site for these sub-micro dimples.

In summary, three main types of damage features were found under shear state.
(i) Damage initiated on the intermetallic particles:

- particle break and matrix-particle decohesion; (Achouri et al., 2013; Gross and Ravi-Chandar, 2016; Roth et al., 2018; Tancogne-Dejean et al., 2021)
- granular slip bands triggered by the void formation on particles (Buljac, 2017; Papasidero et al., 2014);

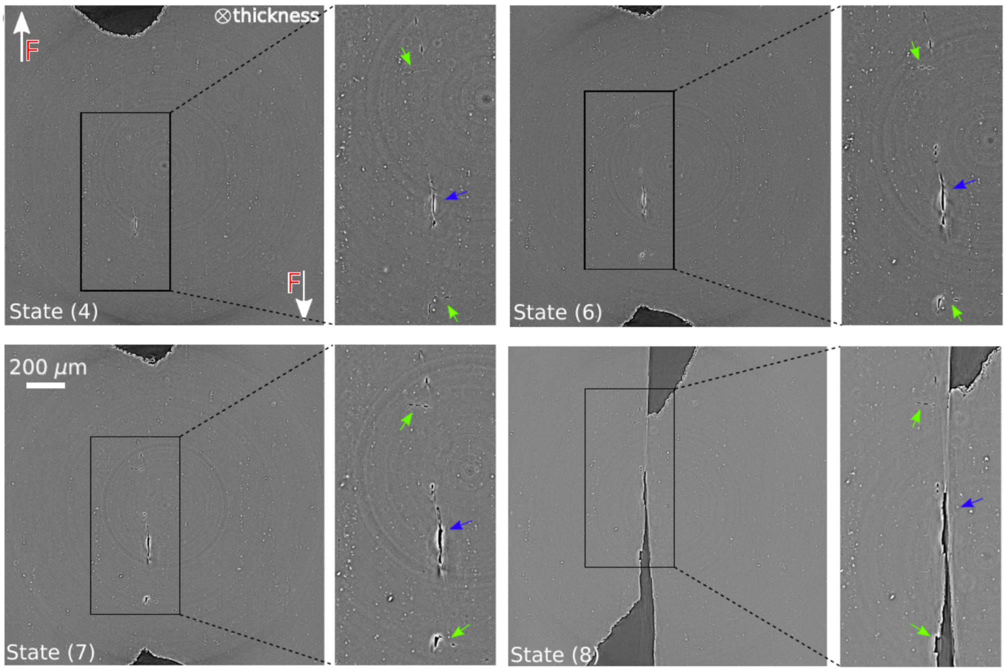

Figure 2.12: The shear damage evolution via 3D observation on AA22198-T8R at different load steps, where a flat damage feature was found in the highly deformed region between two notches, after (Buljac, 2017).

(ii) Void flattening from pre-existing porosity without particles attached (Tancogne-Dejean et al., 2021);
A void nucleation-rotation-elongation is regarded as one main of detrimental shear damage mechanism as experimentally observed for ductile materials.

Schematic model 2D unit cell with pre-existing cylindrical void simulations (Nielsen and Tvergaard, 2011; Tvergaard, 2008, 2009) and 3D unit cell with primarily spherical void simulations (Barsoum and Faleskog, 2007b; Nielsen et al., 2012) have been performed to study ductile failure under simple shear state. Instead of void growth to coalescence at high stress triaxiality, the void closure leading to micro-cracks that subsequently rotate and elongate in the shear field. They have revealed that ductile failure is governed by the interaction of neighboring voids in the collapse-rotation-elongation mode till coalescence in 2D case. The same governing mechanism was demonstrated as well for spherical void in full 3D unit cell. Torki and Benzerga (2018) illustrated the evolution of a sub-cell with initial porosity to investigate process of void-mediated failure under simple shear state. At the absence of increasing void volume fraction, the stress softening strongly depends on the ratio of shear band width (the vertical distance between blue dashed line) to in-plane void spacing. The shear mechanism can be qualified as in Fig.2.15 (a): (i) void-induced strain localization; (ii) void rotation and elongation;

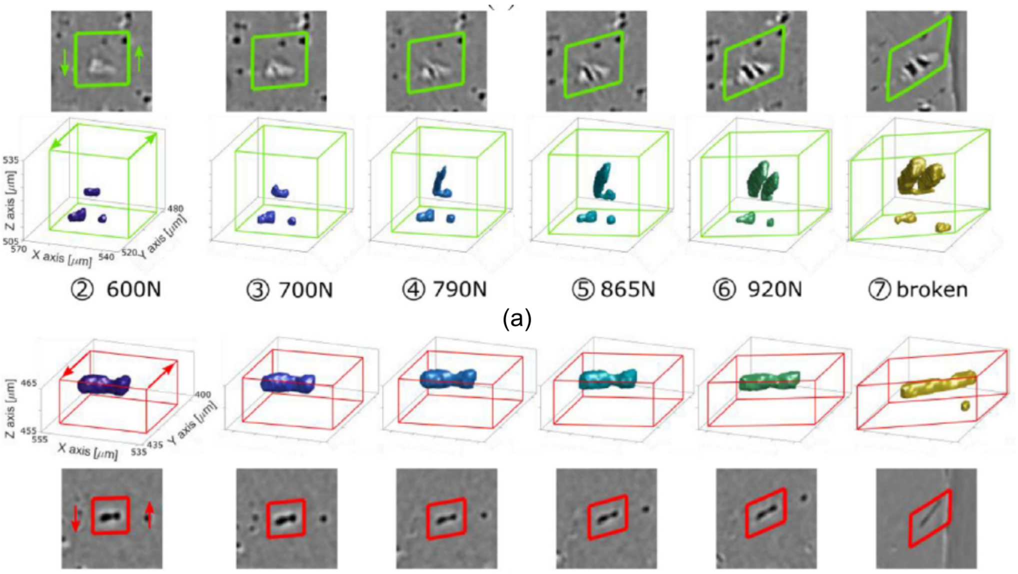

(a)

(b)

Figure 2.13: The shear damage evolution via 3D observation on AA2024-T351: 2D sections and a close-up view on (a) an intermetallic particle with void primarily existed inside and (b) a pre-existing void flattening, after (Tancogne-Dejean et al., 2021).

(iii) coalescence and failure as shear dimples.

For those materials with negligible initial void, Roth et al. (2018) modeled a RVE simulation with spherical rigid particle in Fig.2.15 (b). They found that particle failure is normal to the direction of maximal principal stress under shear loading. The mechanism under shear-dominated loading condition is summarized. Phase 1 as shear damage in Fig.2.15 (b): (i) void nucleated due to particle-matrix decohesion; (ii) void grew slightly and rotated, where its elongation direction is parallel to the direction of the maximum principal strain as seen in the RVE simulation; (iii) highly deformed voids formed into micro crack-like features. Then it enters into the phase 2 as formation of a localization band illustrated in the colored region around the void and particle. Eventually failure occurs by a macroscopic fracture crack in the phase 3.

2.2 Non-proportional load path change

Most engineering structures, especially thin sheet, usually undergo load path changes during manufacturing and/or forming followed by in service loading. Xavier et al. (2015) found that non-proportional strain paths of an interstitial steel sheet showed significantly smaller limit strains than the proportional path based on the values from the forming limit curve. The ductile damage mechanism already becomes complicated for low stress triaxialities and even more under load path changes. In order to achieve load path change experiment, some research groups conducted the pre-straining of the raw sheet

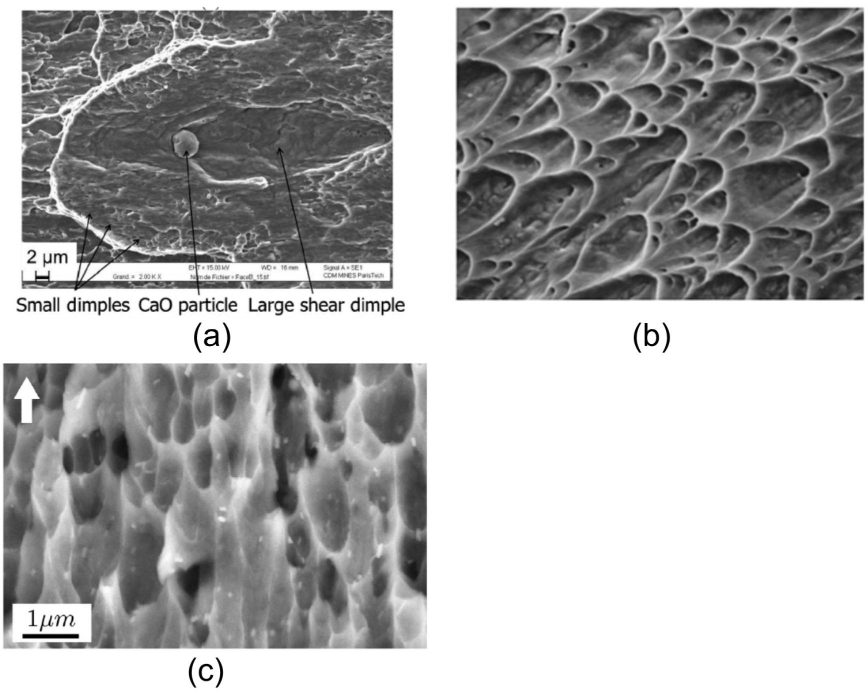

Figure 2.14: The final fractures surface via post-mortem SEM fractography of: (a) a *smiley* sample in dual phase steel after shear, after (Roth et al., 2018) , (b) a cast Ti6Al4V titanium alloy after torsion (1500×), after (Pineau et al., 2016), and (c) a *smiley* sample in AA2024-T531 after shear, where sub-micro dimples with dispersoids were observed at nanometer scale, after (Tancogne-Dejean et al., 2021).

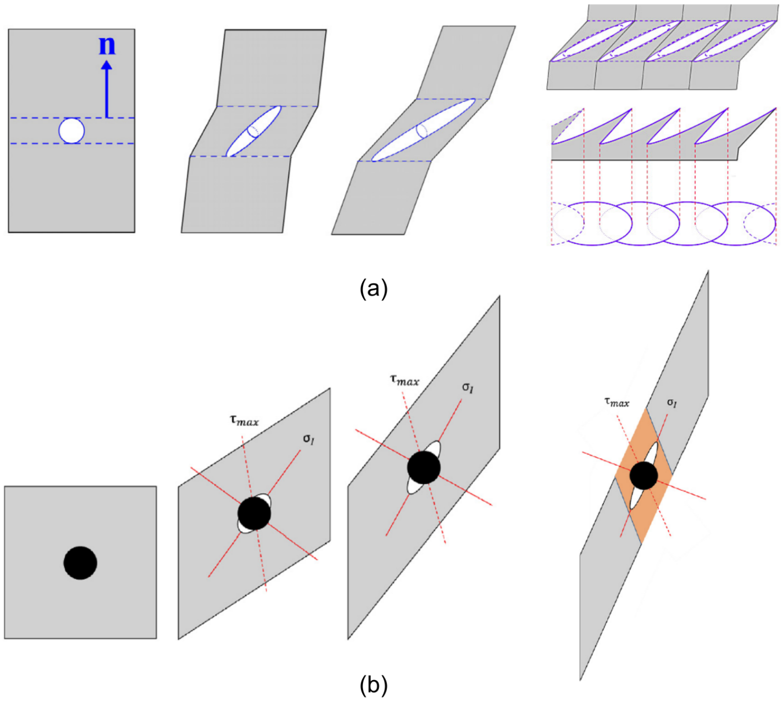

(a)

(b)

Figure 2.15: Schematic of failure mechanism under simple shear for the unit cells (a) with an initial circular void, adapted after (Torki and Benzerga, 2018) and (b) with a rigid intermetallic particle, after (Roth et al., 2018).

and then the specimens were cut from the deformed sheet as virgin one before turning to the second loading (Abedini et al. (2018); Madi et al. (2020); Tarigopula et al. (2009)). Other researchers have designed special geometries particularly for the load path change (Papasidero et al. 2015; Gerke et al. 2019; Brünig et al. 2021).

2.2.1 Specimens manufactured from the pre-loaded sheet

Tarigopula et al. (2009) performed complex loading path experiments under two-stage non-proportional loadings. The raw dual phase steel DP800 sheets of 1.49 mm thickness were pre-strained in uniaxial tension to 1%, 4% and 8% effective strains respectively and then the shear specimens in Fig.2.9 (a) machined from the deformed region were subsequently tested till fracture. Macroscopically, the global displacement at fracture under shear loading decreased obviously for the 8% pre-strained samples: it was significantly reduced by nearly 30% with respect to the tests from as received samples without pre-straining. Madi et al. (2020) investigated the effect of uniaxial tensile pre-strain on ductility and toughness in a high strength steel. The smooth and notched tensile bars were manufactured from the 200 mm×100 mm homogeneous pre-strained (2%, 4% to 6%) zone of large flat tensile specimens. They found a crucial decrease in both ductility and toughness with increasing the tensile prestrain level, where the effect of merely 2% prestrain (0 to 2%) is even more pronounced than at higher levels (2 to 4% and 4 to 6%). In order to characterize fracture properties of an anisotropic magnesium alloy ZEK100 in proportional and non-proportional loading paths, Abedini et al. (2018) performed experiments under multiple stress state in proportional loading paths, and also two-stage non-proportional load to induce significant changes in stress states including four paths uniaxial or equi-biaxial tensile as preloadings followed by shear or plane strain tensile tests. For the first loading stage as pre-straining, the Marciniak specimens were pre-loaded as equi-biaxial tensile at the equivalent plastic strain as 10% while flat tensile specimens were pre-strained as 9%, and then shear and V-bend (for plane strain tensile) specimens were respectively fabricated from the uniformly deformed regions of two raw sheets. In the second stage of deformation, shear and plane-strain tests were carried out till fracture occurred. Globally, the displacement at fracture of two pre-strained tests decreased by around 20% under shear in Fig.2.16 (a) while the effect of two pre-loadings on the plane strain tension was hardly seen in terms of global displacement at fracture in (b). Microscopically, (c)(d) shows the loading paths in the curve of equivalent strain to fracture versus stress triaxiality. It is clearly found that experimentally the cumulative equivalent strain at fracture under non-proportional loading paths (in blue) was interestingly increased compared to those under proportional loading paths (in green). A damage indicator was applied in this work but not for all stress states. However, the physical mechanism behind these pre-loadings was not yet investigated. For the three mentioned research works, the specimens were manufactured from deformed large sheets. The loading history was not easily tracked after cutting into new specimen geometries. To counter this, some geometries have been designed in particular for complex load paths without the second fabrication.

2.2.2 Particular specimen geometry for load path change

Some special geometries have been designed particularly for the load path change (Brünig et al., 2021; Gerke et al., 2019; Papasidero et al., 2015) in Fig.2.17. Papasidero et al. (2015) applied the complex two-stage torsion-tension/compression non-proportional loadings on an axisymmetric tubular specimen in AA2024-T351 as illustrated in Fig.2.17 (a). With applying different loading angle β defined by the ratio of torsion and axial loading as described in Eq.2.4, the specimen achieved multiple stress triaxialities between 0 and 0.6. To illustrate the effect of the loading path on the strain to fracture, three types of pre-loadings, including pre-compression, pre-tension and pre-torsion strainings, haven been conducted up to a strain of 10%. On the stage of second loading, three types of loading conditions such as torsion (β=0°), tension (β=90°) and the combined tension-torsion tests (β=55°), were carried out subsequently. The global results of force-displacement and torque-rotation are shown in Fig.2.18. The global displacement to fracture under tension after pre-torsion was reduced by 10% compared to the proportional tension test in (a), while the global rotation to fraction under torsion after pre-tension was remarkably decreased nearly by 30% compared to the proportional torsion in (b). The ductility reduction due to pre-tension and pre-torsion was found as well in (c) and (d).

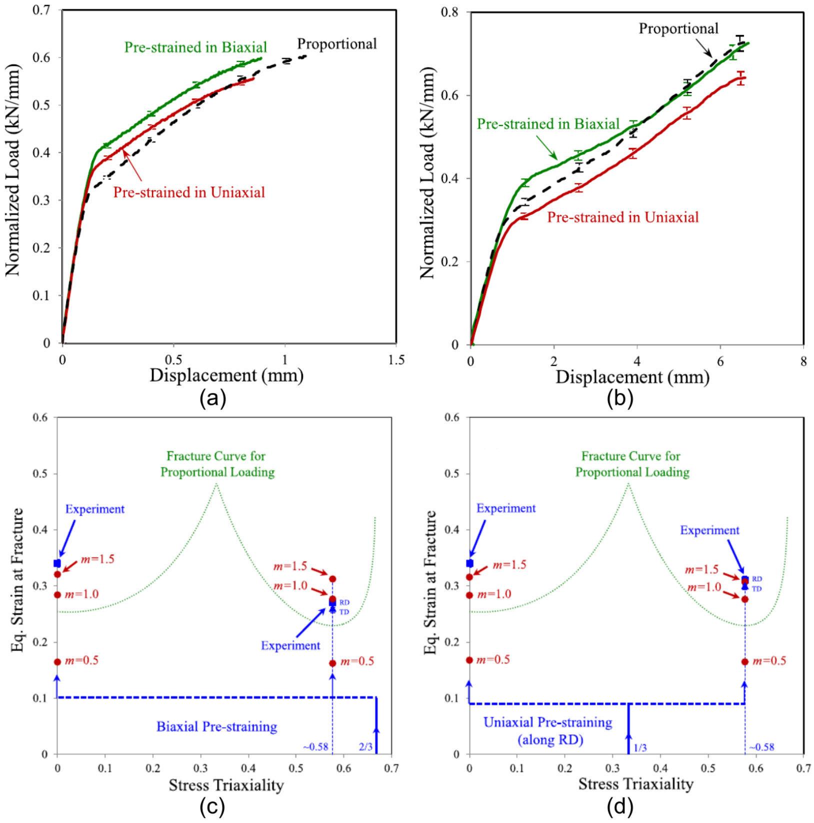

Figure 2.16: The normalized load - displacement responses for the specimens of (a) shear and (b) v-bend (plane strain tensile) after pre-straining. Results of proportional loading are also presented for comparison. The load path in terms of equivalent strain to fracture versus stress triaxiality: shear and plane strain tensile load paths with initially (c) equi-biaxial pre-straining and (d) uniaxial pre-straining, where load path histories are shown as blue dashed lines adapted after Abedini et al. (2018).

Locally, the fracture envelops for two-step loading in terms of strain to fracture and stress triaxiality are shown in Fig.2.19. The comparison with experimental results can be concluded that pre-torsion and pre-compression increase the strain to fracture whereas pre-tension decreases the strain to fracture. However, the conclusion on the effect of pre-tension loading is exactly contrary to that from (Abedini et al., 2018) in Fig.2.16 (c)(d). It could be due to the different definition and measurement of strain to fracture.

Gerke et al. (2019) conducted a series of experiments with the biaxial X0-specimen in the AA6082-T6 in Fig.2.17 (b) under proportional and non-proportional loading conditions. With controlling load ratio $\xi = F_1/F_2$, complex tension-tension and tension-compression loading paths were achieved under different stress state. The non-proportional three sub-steps is: (i) apply the pre-loading with keep F_2=0, where $\xi = F_1/0$ (F_2=0) was kept till the critical displacement $u^{M,as}$; (ii) modify F_2 till (F_1=F_2) by controlling

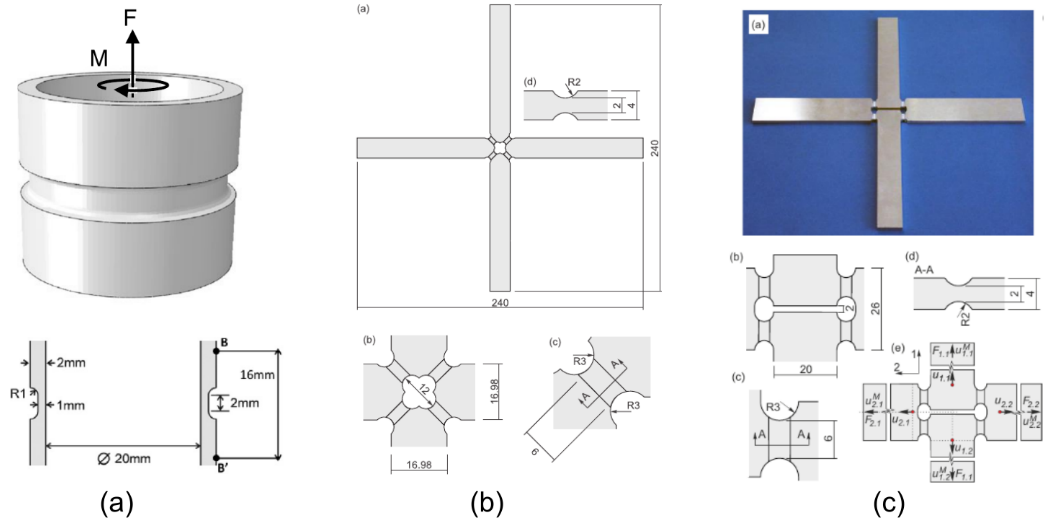

Figure 2.17: (a) A tubular specimen for the combined torsion-tension/compression loading after Papasidero et al. (2015), (b) a X0 shaped cruciform specimen after Gerke et al. (2019), and (c) an H crucial shaped specimen for the combined shear-tension loadings after Brünig et al. (2021)

displacement; (iii) apply the load ratio $\xi = F_1/F_2$. The different proportional load ratio $\xi = F_1/F_2$ can be compared with the corresponding non-proportional loading paths as illustrated in Fig.2.20. The difference between proportional and non-proportional load paths in terms of the first principal strain field at fracture was clearly indicated but the path-dependent damage was hardly quantified under different load ratio. However, for tension-tension loading (high stress triaxiality) major void growth mechanism can be observed while for tension-compression loading (around 0 stress triaxiality) predominant shear mechanisms were observed via fractography.

Brünig et al. (2021) investigated very recently the complex shear and tension load path changes using an H shaped geometry in Fig.2.17 (c) made of an 6082 T6 Aluminum alloy. The vertical load F_1 leads to shear behaviour in the notches, whereas the horizontal load F_2 leads to superimposed tension or compression, achieving a wide range of stress states. The results of a non-proportional loading path from different extents of shear pre-straining followed by tension are shown in Fig.2.21, while the results of another tension pre-strainings followed by shear are presented in Fig.2.22. Fig.2.21 exhibits a remarkable reduction of ductility as displacement at fracture due to pre-shear strainings from (b) 45%, (c) 65% and (d) 90% of final displacement to fracture. The ductility significantly reduced 33%, 46% and 80% respectively. It is concluded that the higher the shear pre-strain was, the higher the reduction in ductility. In Fig.2.22, the ductility reduction from pre-tension loading was less obvious in (b) 50% of final displacement to fracture. The other two highly pre-deformed experiments presented the reduction of ductility as well as Fig.2.21 but with a large experimental scatter of 14-47% decrease in

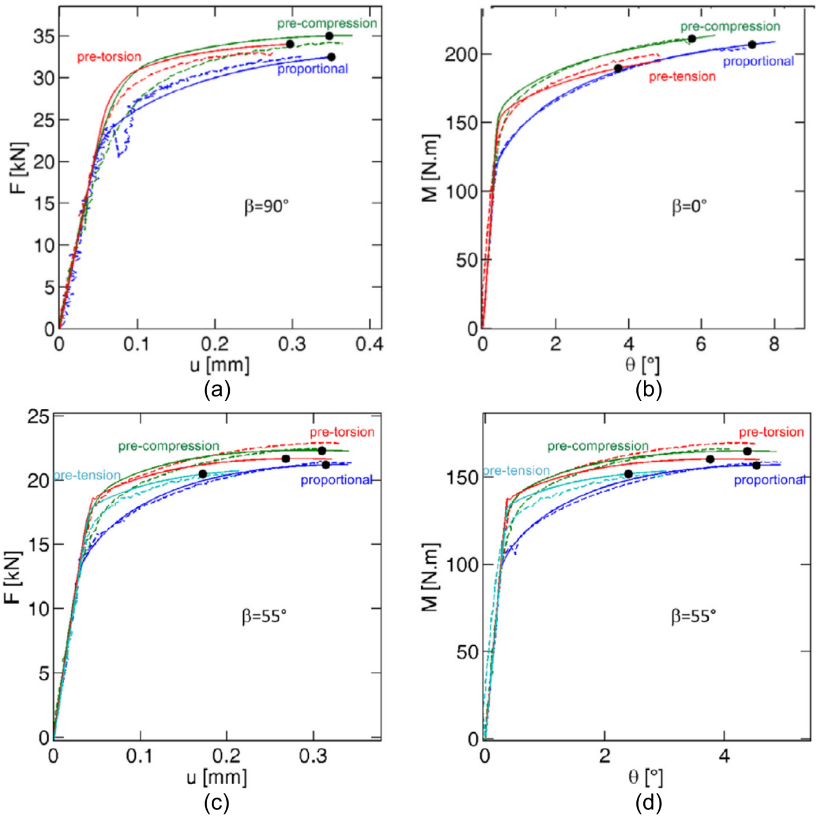

Figure 2.18: Force-displacement and torque-rotation curves under non-proportional loading: (a) tension tests (β=90°), (b) torsion tests (β=0°) and (c)(d) the combined tension-torsion tests (β=55°) as the second stage, after (Papasidero et al., 2015).

(c) and 20-33% reduction in (d). The effect of pre-tension seemed more sensitive according to the pre-loading extent. However, the physical mechanism under non-proportional load path change was not clearly identified by these experiments, and the origin of these ductility reduction was not discovered experimentally, especially the physical damage features, if exist, have not been observed from the first stage of pre-loading.

2.3 Strain measurement during complex load path

The strain to fracture was obtained by either numerical-experiment hybrid method (Bao and Wierzbicki, 2004) or experimental DIC results (Papasidero et al., 2015; Roth and Mohr, 2016). A unified definition in terms of equivalent (effective) strain is essential to estimate fracture strain under complex, both proportional and non-proportional, load paths.

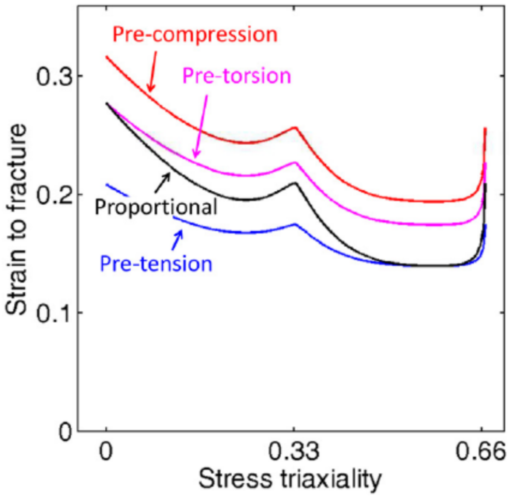

Figure 2.19: Fracture envelop after pre-compression (T=-0.58, red curve), pre-tension (T=0.58, blue) and pre-torsion (T=0, magenta) testings, after (Papasidero et al., 2015).

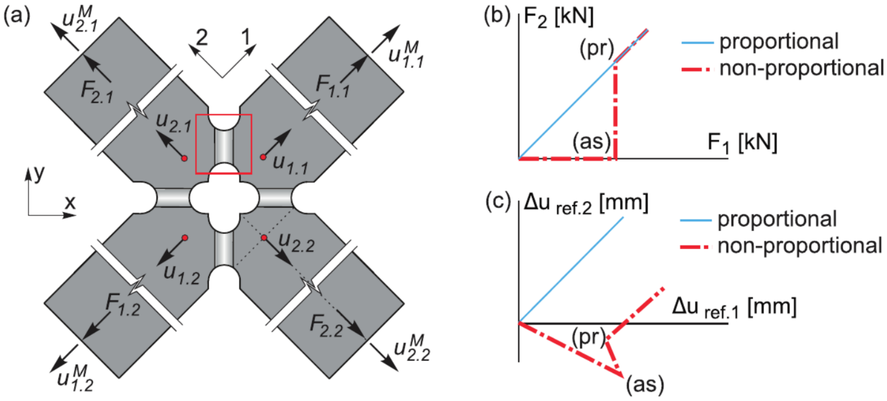

Figure 2.20: (a) The notation in the schematic X0 shaped specimen. The proportional and non-proportional loading paths achieved by controlling (b) F_1-F_2 and (c) Δu_1-Δu_2, after (Gerke et al., 2019).

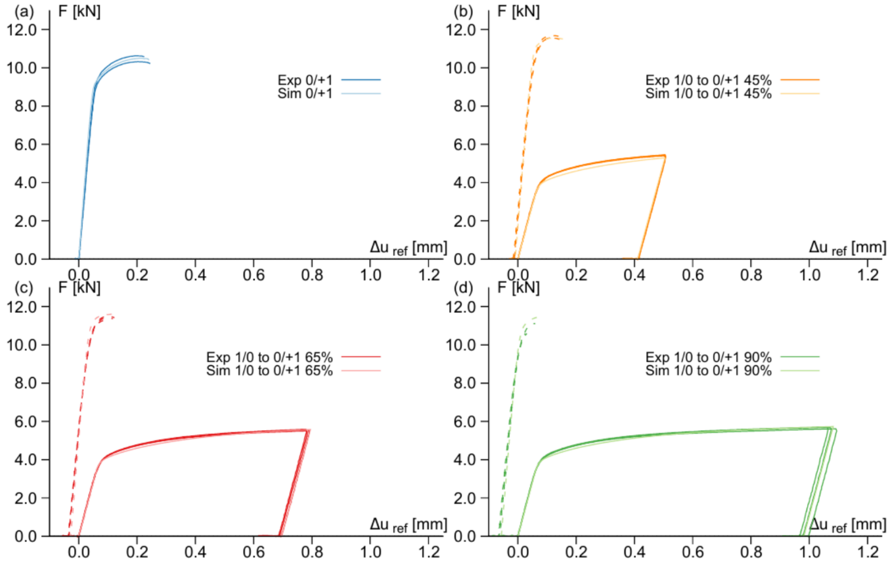

Figure 2.21: Load-displacement curves under (a) proportional tension loading, (b) 45%, (c) 65% and (d) 90% of final displacement pre-shear loadings followed by tension non proportional loadings, after (Brünig et al., 2021).

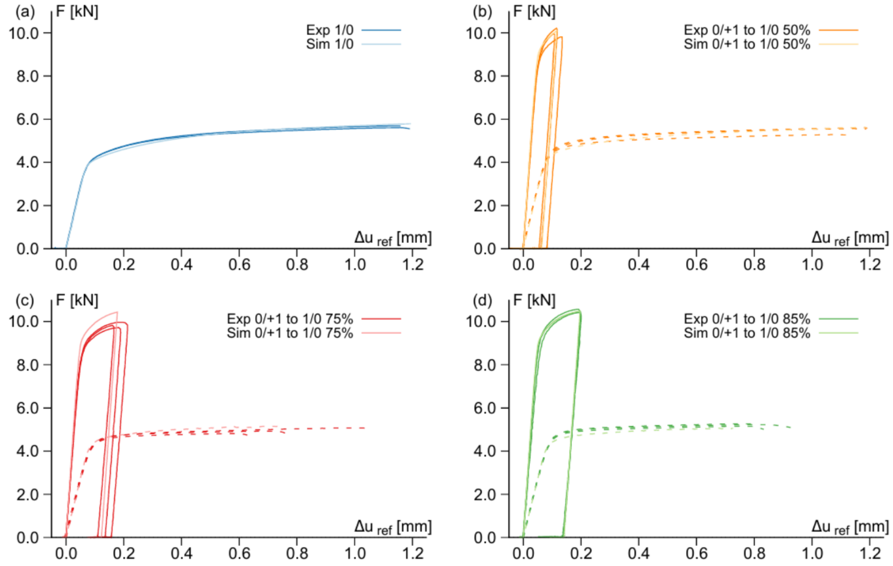

Figure 2.22: Load-displacement curves under (a) proportional shear loading, (b) 50%, (c) 75% and (d) 85% of final displacement pre-tension loadings followed by shear non proportional loadings, after (Brünig et al., 2021).

2.3.1 Finite strain at large strain

The deformation gradient F_{ij} is the derivative of the deformed configuration position vector x_i with respect to the reference configuration position vector X_j (Belytschko et al. (2000)). It can be decomposed via the polar decomposition theorem into:

$$\mathbf{F} = \mathbf{R} \cdot \mathbf{U} = \mathbf{V} \cdot \mathbf{R} \tag{2.5}$$

where the orthogonal rotation tensor $\mathbf{U}$ represents pure rotation part in $\mathbf{F}$, while the right-stretch tensor $\mathbf{U}$ and the left-stretch tensor $\mathbf{V}$ represent the essential deformation part in original and deformed configuration respectively. The logarithmic strain (Hencky strain or true strain) $\boldsymbol{\varepsilon}_H$ provides the correct measurement of the final strain when deformation takes place in a series of coaxial strain increments, taking into account the influence of the strain path (Onaka, 2010, 2012) and is defined as:

$$\boldsymbol{\varepsilon}_H = \frac{1}{2} \log (\mathbf{F}^T \cdot \mathbf{F}) = \log \mathbf{U} \tag{2.6}$$

Onaka (Onaka (2010, 2012)) analyzed and confirmed that the Hencky strain is an appropriate measurement especially for large simple shear strain. However, Butcher and Abedini (2017) pointed out that the equivalent strain in Eq.2.7 directly using the closed-form solution for von Mises equivalent strain is only valid for proportional and coaxial loading.

$$\varepsilon_{eq}^{VM} = \frac{2}{\sqrt{3}} \sqrt{(\varepsilon_I - \varepsilon_{II})^2 + (\varepsilon_{II} - \varepsilon_{III})^2 + (\varepsilon_{III} - \varepsilon_I)^2} \tag{2.7}$$

where ε_I, ε_{II} and ε_{III} denote three principal strains from the logarithmic strain tensor. Experimentally, the strain field of flat specimen surface was measured from 2D surface DIC (Abedini et al., 2018; Roth et al., 2018). The information in thickness direction lacks in the 2D image correlation. The third component ε_{III} is computed assuming plastic incompressibility $\varepsilon_I + \varepsilon_{II} + \varepsilon_{III} = 0$. Hence, the equivalent strain is calculated as:

$$\varepsilon_{eq}^{2D} = \frac{2}{\sqrt{3}} \sqrt{\varepsilon_I^2 + \varepsilon_{II}^2 + \varepsilon_I \varepsilon_{II}} \tag{2.8}$$

Damage is cumulative during the non-proportional loading path. It is thus important to define an accumulated strain, arithmetically always increasing as damage variable, to estimate the strain to fracture from one loading to the other.

2.3.2 Accumulated strain under non-proportional load paths

Roth and Mohr (2016) proposed a scalar damage indicator D (0 to 1) to predict fracture initiation under non-proportional loading based on the equivalent strain to fracture under proportional loading.

$$dD = \frac{d\bar{\varepsilon}_p}{\bar{\varepsilon}_f^{pr}[T, \bar{\theta}]} \tag{2.9}$$

During the load path change, the equivalent strain needs to be cumulative from one loading to the second. Typically, the equivalent strain is computed from plastic work equivalence with the equivalent stress. The work-conjugate equivalent strain was defined in terms of the adopted constitutive model (Abedini et al., 2018). The plastic work increment is in Eq.2.10:

$$\omega_p = \int \sigma : d\varepsilon_p \tag{2.10}$$

According to Butcher and Abedini (2017), the difference between the work-conjugate and the coaxial equivalent strain is negligible when strain is less than 0.8. The equation Eq.2.11 is used to determine the equivalent fracture strain including under non-proportional load path:

$$\varepsilon_{cum} = \int \sqrt{\frac{2}{3} d\boldsymbol{\varepsilon} : d\boldsymbol{\varepsilon}} \tag{2.11}$$

Abedini et al. (2018, 2017) calculated the von Mises equivalent strain by integrating the equivalent strain rate using the measured DIC time increments as:

$$\dot{\varepsilon}_{eq} = \frac{2}{3}\sqrt{\dot{\varepsilon}_I^2 + \dot{\varepsilon}_{II}^2 + \dot{\varepsilon}_I \dot{\varepsilon}_{II}} \tag{2.12}$$

It is worth nothing that the strain calculation in DIC depends on the parameters such as subset size and step size, equivalent to the element length in finite element calculation. When comparing different equivalent strain to fracture, the physical parameter needs be consistent at length scale.

3 Ductile damage models

3.1 Phenomenological constitutive models

In the Continuum Damage Mechanics (CDM) (Krajcinovic, 1985; Lemaitre, 1996) models, damage is represented by a scalar (D) or tensorial ($\underline{D}$,$\underline{\underline{D}}$) variable. Based on the early fundamental developments of Kachanov (1958), Lemaitre (Lemaitre, 1985, 1996) presented the phenomenological constitutive models where no explicit physical interpretation of damage at the microscale. The effective stress tensor that actually resists to the load is defined as:

$$\underline{\tilde{\sigma}} = \underline{\sigma}/(1-D) \tag{2.13}$$

$$\tilde{\sigma}_{eq} = \sqrt{\frac{3}{2}(\frac{\underline{\boldsymbol{s}}}{1-D}):(\frac{\underline{\boldsymbol{s}}}{1-D})} \tag{2.14}$$

where $\underline{\tilde{\sigma}}$ is the effective stress tensor and the parameter D quantifies the damage extent ($0 \leq D \leq 1$, 0 for the undamaged state and 1 for failure), and the scalar $\tilde{\sigma}_{eq}$ for the equivalent effective stress. Furthermore, tensorial damage ($\underline{D}$,$\underline{\underline{D}}$) can either be applied to material characteristic properties (i.e. composite) or under complex loading path (Lemaitre and Desmorat, 2005). The models deal with the damage quantification with a single damage variable in a conciser way on the macroscopic scale, but the complex physical damage mechanism (e.g. void nucleation and shape change) is not taken into consideration at the microscale level.

3.2 Micromechanical models

3.2.1 Void nucleation-growth-coalescence mechanism

The analytical models for ductile damage developed by (McClintock, 1968; Rice and Tracey, 1969) described the cylindrical or spherical voids grow in a rigid perfectly plastic matrix. They both found that the void growth rate depends on the stress triaxiality T (i.e. the ratio of mean stress to equivalent stress) and plastic strain rate. Rice and Tracey (1969) concluded the rate of the spherical void radius variation $\dot{R}$ could be expressed at high stress triaxiality. Huang (1991) modified and extended into the bifurcation equation according to stress triaxiality as:

$$\frac{\dot{R}}{R} = \begin{cases} \alpha \exp(\beta T)\dot{\varepsilon}_{eq} & T > 1 \\ \alpha T^{1/4} \exp(\beta T)\dot{\varepsilon}_{eq} & T \leq 1 \end{cases} \tag{2.15}$$

where R denotes the radius of the void and $\dot{\varepsilon}_{eq}$ stands for the von Mises equivalent strain rate. Two numerical factors α=0.427 and β=1.5 were proposed by Huang (1991) for a better accuracy. The model was only for void growth and Marino et al. (1985) proposed a simple criterion of the normalized void radius when fracture occurs:

$$(R/R_0) = (R/R_0)_c \tag{2.16}$$

where R_0 is the initial void radius. $(R/R_0)_c$ is a material-dependent parameter defining the critical value for void coalescence. However, the coupling between void and its effect of void growth on material behaviour (i.e., softening) was not taken into consideration in these analyses.

Gurson (1977) first proposed a finite sphere containing a spherical void in the rigid perfectly plastic matrix, where void volume fraction (or porosity) f represents the damage. The only damage variable denotes the ratio of void volume over the matrix volume. A plastic yield surface that coupled with the porosity is defined as below:

$$\Phi = \frac{\sigma_{eq}^2}{\sigma_0^2} + 2f\cosh(\frac{\sigma_{kk}}{2\sigma_0}) - 1 - f^2 \tag{2.17}$$

where σ_0 is yield limit of matrix, σ_{kk} for the trace of the stress tensor and σ_{eq} for the von Mises equivalent stress. In the case of f=1, it indicates only voids exist in the matrix and failure occurs. The derivation of the yield criterion implies that the normality rule applies to determine the plastic strain rate tensor, $\underline{\dot{\boldsymbol{\varepsilon}}}_p$:

$$\underline{\dot{\boldsymbol{\varepsilon}}}_p = \dot{\lambda}\frac{\partial\Phi}{\partial\underline{\sigma}} = \dot{\lambda}[\frac{3}{\sigma_0^2}\underline{\mathbf{s}} + \frac{f}{\sigma_0}\sinh(\frac{\sigma_{kk}}{\sigma_0})\underline{\mathbf{1}}] \tag{2.18}$$

The damage evolution in terms of the porosity is defined from applying mass conservation as below:

$$\dot{f} = (1-f)\text{trace}(\underline{\dot{\boldsymbol{\varepsilon}}}_p) \tag{2.19}$$

It is worth nothing that the evolution law for damage variable is entirely determined by the definition of the yield surface (Besson, 2010). The Gurson model created interesting micromechanical basis to describe void growth interacting with plasticity, but voids are assumed as pre-existing. The void nucleation and furthermore, void coalescence leading to final rupture were not included in the model. In addition, unit cell simulations using the finite element method proved that void growth rate were not accurately predicted in the Gurson model. Tvergaard and Needleman (1984) proposed a modified yield surface (so called Gurson-Tvergaard-Needleman, GTN) from the Gurson one to represent actual experiments as below:

$$\Phi = \frac{\sigma_{eq}^2}{\sigma_f^2} + 2q_1 f_\star \cosh(\frac{q_2}{2}\frac{\sigma_{kk}}{\sigma_f}) - 1 - q_1^2 f_\star^2 \tag{2.20}$$

where σ_f denotes matrix flow stress and q_1, q_2 are material parameters to describe more accurately void growth kinetics. q_1=1.5 or 1.25 and $q2 = 1$ are used frequently according to Koplik and Needleman (1988). These parameters depend on the plastic hardening exponent and the ratio of the yield stress and the Young's modulus (Faleskog et al., 1998; Gao et al., 1998). A new term $\dot{f}_n$ representing void nucleation is added and the porosity rate is then written:

$$\dot{f} = (1-f)\text{trace}(\underline{\dot{\varepsilon}}_p) + \dot{f}_n \tag{2.21}$$

where the nucleation rate is expressed as:

$$\dot{f}_n = A_n \dot{p} \tag{2.22}$$

$$\dot{\underline{\varepsilon}}_p : \underline{\sigma} = (1-f)\dot{p}\sigma_\star \tag{2.23}$$

It indicates the macroscopic plastic work in the left side while the microscopic plastic work in the right. p is scalar variable for the plastic strain of the matrix material from Shima and Oyane (1976). Here A_n is the strain rate controlled nucleation rate and the specific form was proposed by Chu and Needleman (1980) and often used under strain controlled nucleation within the GTN model as below:

$$A_n = \frac{f_N}{s_N\sqrt{2\pi}} \exp(-\frac{1}{2}(\frac{p-\varepsilon_N}{s_N})^2) \tag{2.24}$$

where f_N for the porosity at nucleation, ε_N for the strain where 50% of the clusions are broken, and s_N for the standard deviation on the nucleation strain. $f_\star$ in Eq.2.20, regarded as an effective porosity, is a function of the porosity f to model coalescence in two stages. The void growth rate is faster when reaching a critical porosity f_c. The effective porosity is written as:

$$f_\star = \begin{cases} f & f \le f_c \\ f_c + (\frac{1}{q_1} - f_c)\frac{f-f_c}{f_R - f_c} & f > f_c \end{cases} \tag{2.25}$$

where f_R stands for the fracture porosity, and fracture occurs when $f_\star = 1/q_1$. f_c is a function of stress triaxiality (Zhang and Niemi, 1994) and can be determined from unit cell simulations (Zhang et al., 2000). Furthermore, Benzerga and Besson (2001) extended the Gurson model in the case of a matrix obeying the Hill (Hill, 1950) yield criterion to account for the plastic anisotropy. An expression coupling void shape and plastic anisotropy has been proposed by Monchiet et al. (2008, 2006). The GTN model is the Gurson model with extensions with the simple treatments of void nucleation and coalescence. Although the model is phenomenological, it describes the microstructure of the material in a micromechanical way. However for the predicted fracture at low stress triaxialities, no void growth is seen especially under zero stress triaxiality (i.e. pure shear state for σ_{kk}=0). Experimentally, failure still can occur under pure shear state as described in 2.1.2.

3.2.2 Shear mechanism for low stress triaxialities

One of major limitations of the Gurson-like model is that it can only deal with the growth of spherical voids that remains spherical during loading (it keeps true at intermediate stress triaxialities around 1.5). The spherical voids rotated, elongated and became no longer spherical under shear deformation according to experimental observations (Achouri et al., 2013; Gross and Ravi-Chandar, 2016; Roth et al., 2018; Tancogne-Dejean et al., 2021) and unit cell simulations (Nielsen et al., 2012; Nielsen and Tvergaard, 2011; Tvergaard, 2008, 2009), and meanwhile void fraction, as the only damage variable, did not grow obviously as for high stress triaxialities. Gologanu and other co-authors have investigated the effects of void shape for the ellipsoidal voids (Gologanu et al., 1993, 1994, 1997) and the Gologanu-Leblond-Devaux (GLD) model extended the Gurson model to account for void shape effects. This model was valided by the cell unit simulations (Gologanu et al., 1997; Pardoen and Hutchinson, 2000). Siruguet and Leblond (2004) extended GLD model to take the void locking by hard inclusions into consideration under low stress triaxiality. More recently, Madou and Leblond proposed an alternative extension (Madou and Leblond, 2012a,b, 2013; Madou et al., 2013) of Gurson model of porous plastic solids, modelling void shape varied from spherical to ellipsoidal modifiable in three axes. A second porosity variable g contributes to the material softening with the usual one f. The former can characterize the detrimental effect of voids during shear in case f is zero. Morin et al. (2016) applied ML model to the micromechanical simulations (Nielsen et al., 2012; Nielsen and Tvergaard, 2011; Tvergaard, 2008, 2009) under shear with initial voids of different shape. Morin et al. (2017) even applied this model to macro specimen so called *butterfly* under shear loading with comparison to experiments in Dunand and Mohr (2011). Similar as the stress triaxiality and von Mises stress, the third stress invariant, the Lode parameter $\mathcal{L}$, affects the ductile fracture as well (Bai et al., 2009; Bai and Wierzbicki, 2008, 2009). Within the GTN framework, Nahshon and Hutchinson (2008) first proposed to add a Lode parameter dependent void evolution term as:

$$\dot{f} = (1-f)\mathrm{trace}(\underline{\dot{\varepsilon}}_p) + k_\omega f \omega(\underline{\sigma}) \frac{\underline{\mathbf{s}} : \underline{\dot{\varepsilon}}_p}{\sigma_{eq}} \tag{2.26}$$

where

$$\omega(\underline{\sigma}) = 1 - \mathcal{L}(\underline{\sigma})^2 \tag{2.27}$$

$$\mathcal{L}(\underline{\sigma}) = \frac{27}{2}\frac{\det \underline{\mathbf{s}}}{\sigma_{eq}^3} = \frac{\sigma_{II} - (\sigma_I + \sigma_{III})/2}{(\sigma_I - \sigma_{III})/2} \tag{2.28}$$

where σ_I,σ_{II} and σ_{III} denote the three principal stresses. It is noted that the nucleation term depends on the porosity f. As numerical constant, one new parameter k_ω represents the rate of damage development in shear. The modified model is able to model localization and fracture in shear-dominated stress state with low stress triaxiality (Nahshon and Hutchinson, 2008). Similarly, a shear-controlled nucleation term, which depends on the Lode parameter of the plastic strain rate $\mathcal{L}(\underline{\dot{\varepsilon}}_p)$ but not on the porosity f, was proposed in (Morgeneyer and Besson, 2011) and is written as:

$$\dot{f} = (1-f)\mathrm{trace}(\underline{\dot{\varepsilon}}_p) + A_n \dot{p} \tag{2.29}$$

with

$$A_n(\dot{\underline{\varepsilon}}_p) = A_0 \exp(-(\frac{\mathcal{L}(\dot{\underline{\varepsilon}}_p)}{\mathcal{L}_0})^2) \quad \text{if} \quad p > p_c \quad \text{otherwise} \quad A_n = 0 \tag{2.30}$$

where A_0, $\mathcal{L}_0$ and p_c are material parameters to be adjusted. The aim is to add the nucleation of a second population of small voids as a function of the stress sate (e.g., pure shear).

3.3 Polycrystalline model

In metals, plasticity is directly related to slips. Slips occur by either the dislocation movement or dislocation climbing and twinning. In the present thesis a polycrystalline model will be used.

3.3.1 Single crystal plasticity

This subsection presents the constitutive equations at the scale of a single crystal. The single crystal model relates the slip rate $\dot{\gamma}_s = 2\dot{\epsilon}_s$ and the resolved shear stress τ_s of each slip system ($s = 1$ to M). The resolved shear stress τ_s at the given slip system number s is defined:

$$\tau_s = \underline{\sigma}_g : \underline{m}_s \quad \text{with} \quad \underline{m}_s = (\vec{n}_s \otimes \vec{n}_s + \vec{n}_s \otimes \vec{n}_s)/2 \tag{2.31}$$

where the orientation tensor $\underline{m}_s$ is defined with slip plane normal vector $\vec{n}_s$ and slip direction vector $\vec{l}_s$ in this plane. For each slip system, an internal variable r_s is introduced for hardening, which depends on the slip $\dot{\gamma}_s$ of all M the slip systems. Crystal plasticity finite element method (CPFEM) applied crystal plasticity directly at the Gauss point scale of polycrystalline aggregates, which has been employed on a periodic unit cell in simulating and assessing grain interactions (Gérard et al., 2009; Kanjarla et al., 2010; Roters et al., 2010). Frodal et al. (2021) applied CPFEM to different micro tensile specimens. However, a high computational cost is needed in this method where 300-800 hours with 24 cores are needed even with a simple damage model σ_{eff}=σ/(1-D) for micro specimens, not to mention macro samples of complex geometry.

3.3.2 Rousselier polycrystalline models

The Rousselier polycrystalline model (Rousselier et al., 2009, 2010, 2012) described the damage in the backbone of a self-consistent polycrystalline model (Méric et al., 1991). Each of N grains is considered as an inclusion in the homogeneous equivalent material, which represents a set of physical grains with close crystallographic orientations (or phase). Cailletaud (1987, 1992) used the physical related hardening variable from the microscale (e.g. slip rate) to represent complex macroscopic behaviours. The Reduced Texture Methodology (RTM) is used to provide the computation efficiency,limiting the number of representative crystallographic orientations, for numerical applications (Rousselier et al., 2009, 2010, 2012). The porous plasticity model can be embedded with plasticity and damage models at the slip system scale, for instance, the Coulomb ductile fracture model (Rousselier and Luo, 2014) as well as the nucleation and growth models of small secondary void population at the slip and scale (Rousselier, 2021).

3.3.3 Classic damage model for void growth

Porous plasticity is coupled with polycrystalline plasticity (Luo and Rousselier, 2014; Rousselier and Leclercq, 2006; Rousselier and Luo, 2014) where Rousselier and Leclercq (2006) proposed an additional *grain* g=0 (G0) with a variable void volume fraction f. G0 represents the physical voids but it is not a void in the sense of homogenization theories since the resulting stress is not zero in G0. The volume fraction of the classical *grains* (g=1 to N) is (1-f)f_g in stead of f_g. Once f is added, the homogenized strain rate at the macroscopic scale is written as:

$$\underline{\dot{E}}^p = (1-f)\sum_{g=1}^{N} f_g \underline{\varepsilon}_g^p + f\dot{\varepsilon}_m^p \underline{1} = \underline{\dot{E}}_{dev} + \dot{E}_m^p \underline{1} \quad \text{with} \quad \sum_{g=1}^{N} f_g + f = 1 \tag{2.32}$$

where the plastic mean strain ε_m^p=$trace(\underline{\varepsilon}^p)/3$. The Gurson model (Gurson, 1977) as well as its extensions, the GTN model (Tvergaard and Needleman, 1984) and other derivative models (Nahshon and Hutchinson, 2008), are widely used for numerical applications. However, they are not easy to reformulate within the polycrystalline plasticity model because of its quadratic formulation in the deviatoric stress space. The Rousselier model (Rousselier, 1981, 1987, 2001; Rousselier and Luo, 2014) is selected for the development in this study. The yield condition for polycrystalline material is expressed as:

$$\Phi = \frac{\Sigma_{eq}}{1-f} - (\sum_{g=1}^{N} f_g \underline{\sigma}_g)_{eq} + D_1 f \sigma_1 \exp(\frac{\Sigma_m^*}{(1-f)\sigma_1}) \tag{2.33}$$

where Σ_{eq} is the von Mises equivalent stress and Σ_m is the mean (or hydrostatic) stress. D_1 and σ_1 are material parameters. As proposed in Morgeneyer et al. (2009), Σ_m is substituted with Σ_m^* to represent 3D anisotropic. The void volume fraction rate $\dot{f}$ indicates the sum of a first terms due to the mass conservation law and a second term for void nucleation is similar as Eq.2.29. It has to be remarked that the polycrystalline model does not consider neither the grain location in the aggregate, the grain size effect nor the strain and stress within grains. It is a compromise between physical related model (e.g., CPFEM) and computational time of macro samples.

4 X-ray synchrotron 3D imaging

X-ray computed tomography (CT) was developed during the 1960s for cross-sectional imaging in medicine (Cormack, 1963). Nowadays, with recent advances in synchrotron three dimensional (3D) imaging as nondestructive testing (NDT), damage features inside the material bulk can be studied both qualitatively and quantitatively *in situ* with the spatial resolution from micrometer down to nanometer scale.

4.1 Computed tomography (CT)

Using different contrast mechanisms (e.g. absorption, phase, diffraction, scattering), a three-dimensional volumetric image is reconstructed from 2D radiographs recorded at each angle. Phase imaging (Wilkins et al., 1996) has been widely used (Stock, 2008) for increasing the contrast between objects that attenuate the beam similarly. The enhanced edge contrast means, one type of phase contrast imaging, can be processed and segmented easily. It enables to quantify the microstructure in low contrast that would be impossible to achieve with attenuation contrast (Maire and Withers, 2014). Since images are collected non-destructively, the technique can be applied repeatedly to follow material structure changes during mechanical loading in real-time. The series of 3D images often called 4D imaging (3D plus time). However, the structure change under load (e.g. relaxation) during one scan cannot be ignored if it requires long time. So far, the compromise between spatial resolution (i.e. pixel size) and scan time has to be made and these developments are summarized in Fig.2.23.

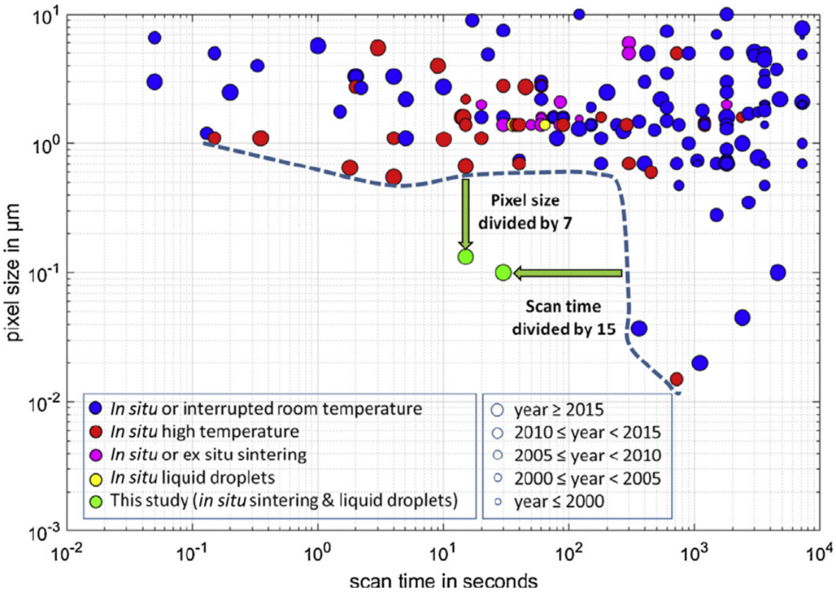

Figure 2.23: State of the art of *in situ* X-ray tomography in terms of pixel size versus scan time, after (Villanova et al., 2017).

4.2 Computed laminography (CL)

In cases of scanning flat samples at high resolution, computed tomography (CT) causes specifically the artefacts stepping from projection angles close to the sample surface (Xu et al., 2012a). X-ray transmission is strongly reduced in this case. To overcome this problem, synchrotron radiation computed laminography (SRCL) is aimed at scanning regions of interest in flat laterally extended objects (Helfen et al., 2005, 2012). Xu et al. (2012a) compared the image quality between CT and CL for flat samples and concluded that CL reconstructed flat structures in every direction equally well whereas structures in some directions could not be reconstructed well in CT. Fig.2.24 presents the typical (a) CT and (b) CL set-ups at synchrotron facilities. Unlike the rotation axis perpendicular (θ=90°) to the beam direction in CT, the rotation axis is inclined at an angle of θ<90° with respect to the beam direction in the computed laminography. The projected images of the sample are acquired over an angular range between 180 to 360° around the rotation axis. Since the whole scan process takes few minutes, the sample usually has to stay stationary before being scanned (Morgeneyer et al., 2013). The stack of radiography is then processed to reconstruct 3D volumetric image by using a filtered-back projection algorithm (Myagotin et al., 2013). The 3D imaging technique of computed laminography with sub-micrometer pixel size has been applied to several types of thin-walled flat samples such as Kahn (Morgeneyer et al., 2009, 2008), CT-like (Buljac et al., 2018b; Morgeneyer et al., 2013, 2014), central hole (Buljac et al., 2017) and more recently *smiley* shear (Roth et al., 2018; Tancogne-Dejean et al., 2021) geometries from cast iron to FB-steel to aluminum alloys. Fig.2.25 presents the 3D damage rendering in the notched region for a CT-like sample of AA2198-T8R. The slant crack was captured at the distance (less than 0.5 mm) from the notch. Fig.2.26 exhibits the 3D damage evolution in the region of interest (440 µm×770 µm) via 3D *in situ* shear experiment in ferrite-bainite steel (FB600), where features (i.e. voids and particles) were segmented and visualized in blue and matrix was made transparent. This technique allows to follow and trace the damage formation and growth under load inside the flat sample. Tancogne-Dejean et al. (2021) quantified the volume void fraction in terms of pre-existing and newly nucleated void at each loading step. By the global statistics, an analysis of shear

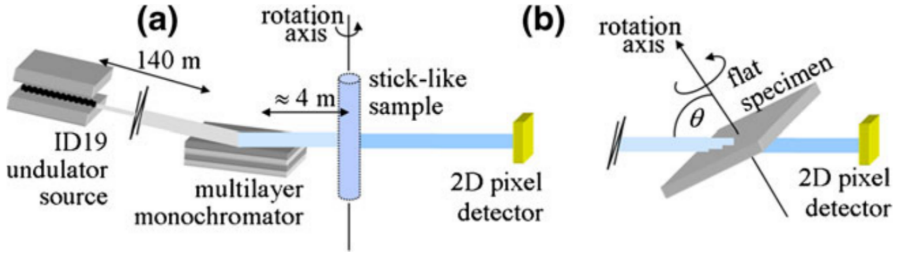

Figure 2.24: Schematic representation of synchrotron radiation (a) computed tomography and (b) computed laminography set-ups after Helfen et al. (2005); Morgeneyer et al. (2013).

damage mechanism leading to macroscopic crack was performed. The damage features (i.e. pre-existing void and broken intermetallic particles) were found and followed at micrometer scale.

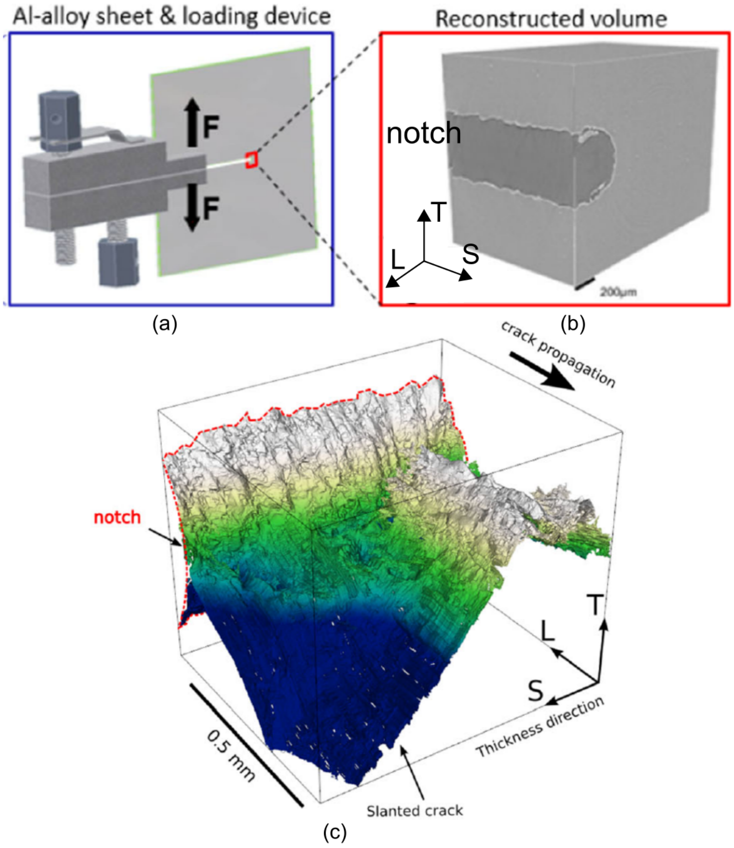

Figure 2.25: (a) Schematic view of laminographic experimental set-up for a CT-like sample in AA2198-T8R. (b) The reconstructed volume from the scanned region in front of the notch root and (c) 3D rendering of the final crack where height represents in color via 3D X-ray synchrotron computed laminography (CL) adapted after (Rousselier et al., 2017).

4.3 Holo-laminography on the nanoscale

In order to observe physical features such as damage nucleation and growth kinetics at higher magnification, the scanning fluorescence laminography, using the propagation based imaging (also called in-line holography), offers the 3D imaging with voxel size down to nanoscale (Helfen et al., 2009; Xu et al., 2012b). Fig.2.27 exhibits the schematic of the nanolaminography set-up on ID22NI at the ESRF (Xu et al., 2012b). A single-line undulator source and subsequent mirror-based focusing optics produce a monochromatic

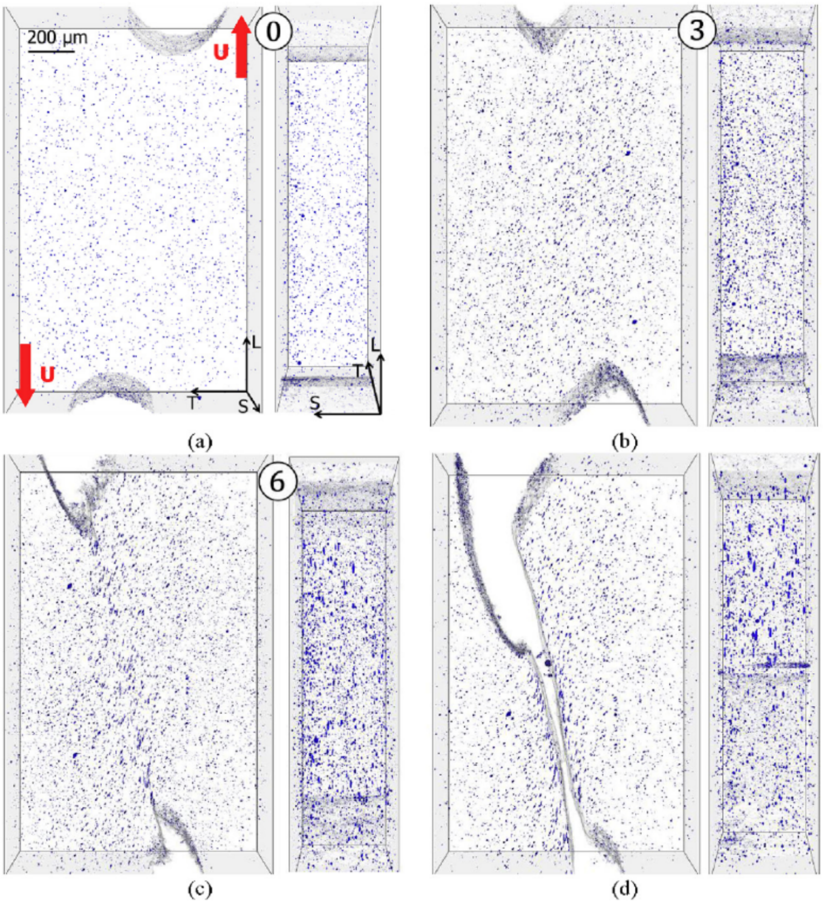

(a) (b) (c) (d)

Figure 2.26: 3D views of the damage evolution under shear loading till fracture, where the steel matrix was made transparent and particles and voids were colored in blue after (Roth et al., 2018).

X-ray focus of about 47×88 nm^2 with a flux of 10^{12} photons/s. The set-up enables full-field intensity measurements with scanning fluorescence laminography at four distances, resulting in effective pixel size from 500 nm to 50 nm.

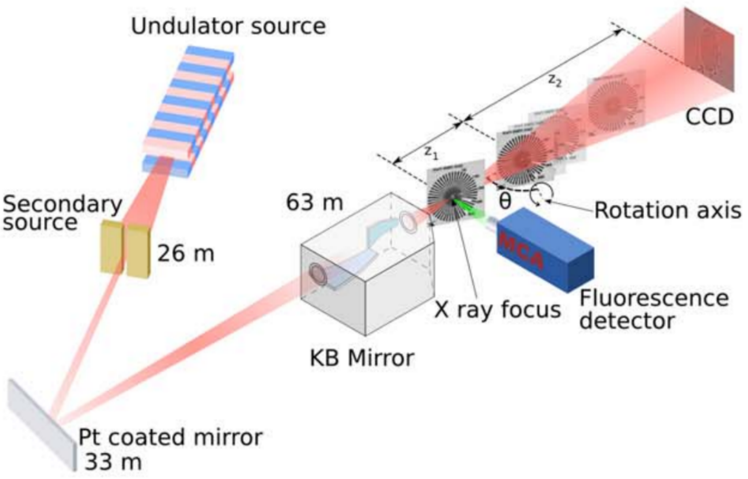

Figure 2.27: Schematic of the nano-laminography setup on the beamline ID22NI at the ESRF after (Xu et al., 2012b).

5 Conclusion

5.1 Ductile mechanism under shear in aluminum alloy

Few studies focused on the shear mechanism with 2D methods, e.g. *in situ* SEM from Achouri et al. (2013); Gross and Ravi-Chandar (2016). They provide access to very high resolution observations of the shear damage, but these observations are limited to either the surface or the fracture surface via post-mortem SEM. Only 2D information is often insufficient to explain the mechanism. From the unit cell micromechanical simulations under shear, a void rotation-elongation-coalescence was established for the cell with pre-existing void (Torki and Benzerga, 2018) while Roth et al. (2018) found a similar mechanism in the RVE model with spherical rigid particle. Only very recently, works by this research group have investigated shear mechanisms for ductile materials via 3D *in situ* experiments (Buljac, 2017; Roth et al., 2018; Tancogne-Dejean et al., 2021). Although Tancogne-Dejean et al. (2021) investigated the damage mechanism of AA2024-T3 with pre-existing porosity under shear using a 3D *in situ* experiment at the micro scale recently, the damage features deserve observations at higher magnification for the nucleation and the shear mechanism could be material dependent. A qualitative analysis on shear mechanism would be of interest at higher magnification, down to nanometer scale by 3D advanced multiscale observations (e.g., 3D nano-laminography). In summary, damage nucleation site deserves an investigation especially for the aluminum alloy 2198 with negligible pre-existing porosity. Damage is believed to hardly grow at the absence of hydrostatic stress according to classic Gurson type models (Gurson, 1977). Moreover, the porosity (i.e. void volume fraction) remains low during shear experiments till fracture, a representative damage variable is required to quantify the damage under shear. Last but not least, the interaction between damage and plasticity strain has been always interesting, and a universal definition and measurement of strain to fracture is of significance for different experiments under not only proportional loading, but also non-proportional load paths. Meanwhile, the high resolution observations allow to detect the location of damage and failure.

5.2 Mechanism under load path changes for low stress triaxiality

The ductile mechanism becomes more complex under non-proportional load paths, e.g. very recently from shear to tension (Brünig et al., 2021), from torsion to tension (Papasidero et al., 2015). Few studies have focused on the damage mechanism under load path changes and, if any, only with the evidences of SEM fractography (Brünig et al., 2021). Since damage associated with forming can be cumulative (Tekkaya et al., 2020) between different forming steps, damage features deserve being directly observed and followed by 3D imaging during load path changes. Furthermore, damage evolution should be quantified and compared with the accumulated strain fields measured from experiments (i.e. image correlation) and FE simulation. The effect of pre-strain loading on the ductility and strain to fracture is still befogged with the loading types (Papasidero et al., 2015). In order to investigate damage mechanism under load path changes for low stress triaxialities, flat samples can be the candidate since the stress component in thickness direction is small enough. A specific sheet geometry for shear to tension is highly needed. The 3D X-ray laminography is aimed to scan these flat thin-walled samples (Helfen et al., 2009, 2005).

5.3 Strain measurement and definition of equivalent strain to failure

Strain measurement and failure prediction are difficult under complex loading. A hybrid experimental-numerical approach was applied to measure strain to fracture in Bao and Wierzbicki (2004), or it can be measured using digital image correlation (DIC) in (Papasidero et al., 2015). With 3D imaging techniques at high resolution, the damage inside can be located to predict the potential failure location under complex load paths from proportional to non-proportional loading. The strain inside material can be accessed using robust projection DIC technique (Buljac et al., 2018b; Morgeneyer et al., 2021; Tancogne-Dejean et al., 2021) from 3D data. The definition of strain to fracture needs to be cumulative and thus suited for non-proportional load paths. Besides, whether pre-straining is counted for the total strain to fracture is also an interesting point to be discussed.

5.4 Suitable damage model for complex load paths

At the absence of hydrostatic stress, the classic Gurson-type models failed to predict void growth under pure shear state. According to physical observation under shear, a physics-based damage model is needed. The suitable model not only is able to predict mechanical properties during complex load path changes, but also represent the shear damage in quantity for low stress triaxiality.

The model needs to take low stress triaxiality into consideration, as well as the computational efficiency. The model should be able to predict damage in more non-proportional load paths to explore the effect of pre-loading on the ductility and cumulative strain to fracture.

Chapter 3

Plasticity and ductility of an anisotropic recrystallized AA2198 Al-Cu-Li alloy in T3 and T8 conditions during proportional and non-proportional loading paths: simulations and experiments

The aim of this chapter is to characterize the plastic behaviour of AA2198 including the plastic anisotropy of the material in two different heat treatment conditions, T3R and T8R, and to design a suitable miniaturized sample geometry for a 'shear to tension' or 'tension to shear' load path change in an *in situ* imaging environment that will be shown in chapter 5. It also aims at studying the effect of sample miniaturization on test repeatability. Additionally, the objective is to identify the effect of a load path change on ductility. A macroscopic anisotropic plasticity model is calibrated using proportional loading tests and its predictive capabilities are assessed for non-proportional loading and associated mechanical fields under these conditions. The fracture surfaces are observed by SEM. The strain fields from finite element (FE) calculation are compared with experimental fields by digital image correlation (DIC), as well as the fracture paths.

This chapter has been submitted to journal of Theoretical, Computational and Applied Mechanics. It is referred to as Kong et al. (2021).

Abstract

The anisotropic material behaviour of a recrystallized AA2198 Al-Cu-Li alloy in T3 and T8 conditions was assessed by proportional loading of uniaxial-tension specimens in rolling (L), transverse (T) and diagonal (D) orientations. The width and longitudinal strains were measured to quantify plastic anisotropy. Notched-tension samples were tested in L and T directions. The material showed weak anisotropy in terms of stress strain curves and a moderate plastic anisotropy, consistent with its texture obtained by EBSD. An anisotropic Bron-Besson type material model was identified using this data base and a micro shear-only (SO) test. The model succeeded in predicting the behaviour of micro specimens for proportional tension-only (TO) loading and non-proportional load path changes including 'shear to tension' (ST) as well as 'tension to shear' (TS) tests. The non-proportional loading was achieved using a newly designed cross shaped sample. It was loaded in one direction, unloaded and subsequently loaded in the orthogonal direction till fracture. The average stretch to fracture of both alloys measured by a four point frame optical extensometer decreased by 29% and 16% for T3 and T8 respectively for the 'shear to tension' experiment compared to the proportional TO experiment. This reduction was suspected to be linked to either damage development under shear and/or high stress levels during tension due to the hardening of the material during shear. The average stretch to fracture of 'tension to shear' tests was reduced by 10% for 2198T3 and hardly reduced for 2198T8 compared to the stretch to fracture of the SO tests. However, the results exhibited a strong scatter for both heat treatments. The ductility scatter was attributed to necking and damage development in tension that can affect strain localization, associated fracture path and ductility, as observed by DIC and fractography.

1 Introduction

aluminum alloys have been widely used and their performance has been improved to meet the demands in aerospace industry for a long time (Ehrström and Warner, 2000; Warner, 2006). The latest Al-Cu-Li alloys are increasingly used for their high specific strength and excellent damage tolerance. The third generation of Al-Cu-Li alloys (i.e. 2198, 2098 and 2050) have successfully balanced the toughness and strength after optimizing the Cu/Li ratio. While partly sacrificing the advantage of Li addition, which is the increase in modulus and the decrease in density, it led to an increase in strength potential and thermal stability (Warner, 2006). Among this third generation, 2198 Al-Cu-Li alloy exhibits a good combination of static tensile properties, damage tolerance, formability and good properties after friction stir welding (Chen, 2011; Le-Jolu et al., 2010). AA2198 in various heat treatment conditions has been studied in Deschamps et al. (2013); Nayan et al. (2019) and an anisotropic plastic behaviour has been found (Chen, 2011; Nayan et al., 2019). This anisotropy is particularly strong for the fibrous material (Chen et al., 2011).

Ductile fracture at high stress triaxiality (i.e. above 1) has been widely studied over the last decades and the governing damage mechanisms have been identified as void nucleation-growth-coalescence (Pineau et al., 2016). More recent studies have focused on the fracture at low stress triaxiality and complex relationships between strain to fracture and stress triaxiality have been found by Bao and Wierzbicki (2004). Phenomenological models have been applied and attempted to fit the experimental behaviour in terms of strain, stress triaxiality and the Lode parameter (Bao and Wierzbicki, 2004). However, strain to fracture is an ambiguous definition and difficult to measure especially in regions where strains are highly localized, not to mention the strain definition during complex non-proportional load path changes.

Mechanisms under proportional loading at low stress triaxiality are not as clear as at high stress triaxiality yet. Gross and Ravi-Chandar (2016) performed a shear experiment via *in situ* scanning electron microscope on a sheet specimen of Aluminum alloy 6061-T6. Second phase particles on the free surface were seen to break, debond or rotate and pre-existig voids were suspected to have a minimal influence on the deformation of this material under shear. No severe damage and/or failure were found on the surface region of nearly zero triaxiality even the local strain reached up to 1.

With the aim of studying the damage evolution inside the bulk of the material during complex load path changes, advanced techniques as three-dimensional (3D) synchrotron imaging are necessary to perform *in situ* experiments. 3D synchrotron laminography is suited to image the regions of interest in flat samples (Helfen et al., 2012). In order to achieve high resolution observation, samples need to be miniaturized with dimensions of the regions of interest in the order of 1 mm^3. Roth et al. (2018) investigated the interior damage mechanism of a ‘smiley’ shear specimen via *in situ* laminography of a dual phase steel. Tancogne-Dejean et al. (2021) analysed the same specimen geometry for a 2024 alloy with the same technique. They both observed the void nucleation on intermetallic particles, rotation and growth. The debonding or failure of the brittle particles was normal to maximum principal stress direction.

Concerning small samples, there is a doubt if the limited grain number in miniaturized sample is still able to guarantee the homogeneous mechanical fields and good repeatability of the macroscopic sample behaviour. Gorji et al. (2021) performed different uni-axial tension, notched tension, central hole and in plane shear tests on a steel alloy for both 2 mm thick macro-samples and the miniaturized 0.1 mm thickness micro-samples. They found that the plasticity obtained from micro-samples matched the one from conventional macro-samples but failure strain slightly reduced in the miniaturized samples due to the deleterious effect of surface roughness that is substantial for the micro-samples.

Most engineering structures, especially thin sheet, usually undergo load path changes during manufacturing and/or forming followed by in service loading. Xavier et al. (2015) found that non-proportional strain paths of an interstitial steel sheet showed significantly smaller limit strains than the proportional path based on the values from the forming limit curve. The macroscopic effect of pre-load has been investigated for some complex load path change experiments. In order to achieve load path change experiments, some research groups conducted the pre-straining of the raw sheet and then the specimens were cut from the deformed sheet as virgin ones before turning to the second loading (Abedini et al., 2018; Madi et al., 2020; Tarigopula et al., 2009). Tarigopula et al. (2009) conducted the uniaxial tension pre-strainings to 1%, 4% and 8% on raw sheet of dual phase steel and shear specimens were machined from the deformed region then they were tested till fracture. At the macroscale, the deformation at fracture under shear-only decreased for the 8% pre-strained samples: the macroscopic strain to fracture was reduced by about 30% compared to the tests without pre-loading. The effects of the 2%, 4% to 6% pre-strainings were studied using tensile bars for a high-strength steel (Madi et al., 2020). They found a decrease in both ductility and toughness with increasing prestrains. The ductility can decrease pronouncedly even with only 2% pre-straining. Abedini et al. (2018) performed shear tests after uniaxial and bi-axial preloadings using a Mg alloy ZEK100 and they found that the global displacement at fracture for both prestrain conditions decreased by around 20% compared to proportional shear tests. Other groups designed special geometries for the load path change (Brünig et al., 2021; Gerke et al., 2019; Papasidero et al., 2015). Papasidero et al. (2015) applied torsion-tension test on an axisymmteric tube specimen of AA2024 T351. Macroscopically, the global displacement to fracture of tension tests conducted after pre-torsion was reduced by 10% compared to the proportional tension test. Remarkably, the global rotation to fracture in torsion tests conducted after pre-tension loading decreased nearly by 30% compared to the proportional torsion test. Gerke et al. (2019) designed a suitable cruciform X0-specimen on Aluminum alloy 6082 T6. The different stress states and load paths were achieved by controlling the ratio of bi-axial displacements. Brünig et al. (2021) investigated the complex shear and tension load path changes using an H shaped geometry made of the same 6082 T6 Aluminum alloy. Non-proportional loadings including different extents of shear pre-straining followed by tension and different tension pre-strainings followed by shear were conducted. A remarkable displacement reduction was found due to pre-straining. The higher the pre-strain was, the higher the reduction in ductility. However, the knowledge on damage mechanism under non-proportional load path change was not clearly identified by only observing fracture surfaces.

The present chapter has several objectives:

- To characterize the plastic behaviour including the plastic anisotropy of the material in two different heat treatment conditions.
- To design a suitable miniaturized sample geometry for a ‘shear to tension’ or ‘tension to shear’ load path change in an *in situ* imaging environment for another study (Kong et al., 2022a).
- To study the effect of sample miniaturization on test repeatability.
- To identify the effect of a load path change on ductility.
- To fit a macroscopic anisotropic plasticity model using proportional loading tests and assess its predictive capabilities for non-proportional loading and associated mechanical fields under these conditions.

In this chapter, the material microstructure is characterized first in terms of grain size and texture, as well as particle and void content. The strain measurement using an optical extensometer is detailed. The anisotropic material model is shortly recalled and the parameter identification procedure explained. In terms of mechanical test results, the microhardness profile through the sample thickness are given and stress strain curves for different loading directions of smooth and notched samples are then gathered for the two heat treatment conditions. The results of repeated testing of small samples for proportional shear loading or tension loading are shown. They are then compared to 'shear to tension' or 'tension to shear' load path change results. The non-proportional tests use a specially designed cross shaped sample. Strain fields before fracture obtained by DIC and FE simulations as well as fractography are given. In the modelling part of the paper, the anisotropic plasticity model is first identified using the database of the smooth and notched tensile samples and the small shear sample. The identified model is used to predict the stress-stretch responses for the non-proportional loading paths. The results are subsequently discussed.

2 Materials and methods

2.1 Materials and microstructures

AA2198 was developed by Constellium. The alloy has a slightly lower copper content compared to AA2098 and also has some other minor chemistry adaptations (Ag, Zr ...) to optimize toughness. Table.3.1 gives the chemical composition limits for AA2198 alloy. In this work, two different tempers of recrystallized AA2198 aluminum-copper-lithium alloy sheets with a nominal thickness of 2 mm were supplied by Constellium. The two different heat treatment conditions (T351 for naturally aged and T851 for artificially aged) are studied. They are referred to as 'R' (recrystallized materials). The alloys are obtained by cold rolling followed by industrial finishing treatment: solution heat treatment, water quench, stretch and either naturally aging (T351 condition), or artificial aging to obtain T851 temper. The materials will be referred to as 2198T3R and 2198T8R. In the following, the rolling direction is noted as L, the long transverse direction as T and short transverse direction (thickness direction) as S. D stands for the diagonal direction (45° between L and T in the sheet plane).

	Cu	Li	Zn	Mn	Mg	Zr	Si	Ag	Fe
wt.%	2.9-3.5	0.8-1.1	$\leq$0.35	$\leq$ 0.5	0.25-0.8	0.04-0.18	$\leq$ 0.08	0.1-0.5	$\leq$ 0.01

Table 3.1: Nominal chemical composition limits of 2198 alloy (wt %).

Micrographs of grain structure were obtained from electron back-scatter diffraction (EBSD) analysis in a FEI Nova nanosem 450FEG with the EDAX-TSL Hikari camera using a step size of 0.5 micrometer and an acceleration voltage of 15 kV. A representative grain structure for 2198T8R is shown in Fig.3.1 (a). Large pancake shaped grains can be found in the L-T plane. The grain size was measured by using a mean linear intercept method on EBSD data as 82 µm in L, 80 µm in T and 20 µm in S directions. A moderate texture is found in the inverse pole figure Fig.3.1 (b). This moderate texture is consistent with the moderate anisotropic plasticity for this material as will be seen in the following. 2D sections from Synchrotron Radiation Computed Laminography (SRCL, Helfen et al. (2005)), which was performed at European Synchrotron Radiation Facility (ESRF) ID19, for the undeformed material 2198T8R is shown in Fig.3.1 (c) where the matrix appears in grey and intermetallic particles in white. The voxel size was 0.72 µm. The mean intermetallics content is 0.34% and the initial porosity is very limited (less than 0.04%) compared to other aerospace aluminum alloys (2024 in Tancogne-Dejean et al. (2021) and 2139 in Morgeneyer et al. (2009)).

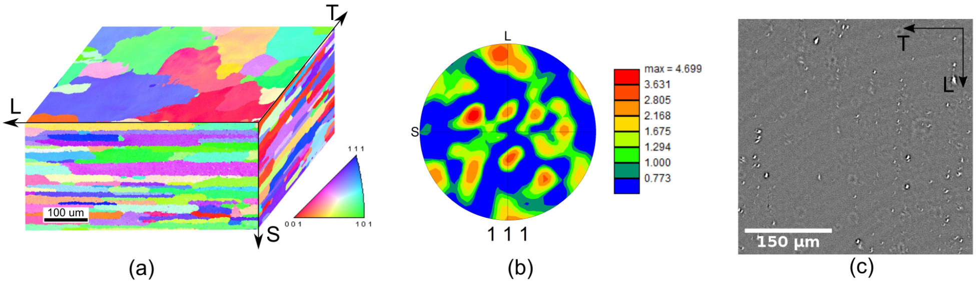

Figure 3.1: (a) Inverse pole figure indicating the 3D grain structure of 2198T8R sheet material via EBSD (the crystal orientations are given with respect to the normal of each plane), (b) Pole figure of 2198T8R and (c) 2D section of 2198T8R from high resolution 3D X-ray laminography in the L-T plane.

2.2 Mechanical testing

A series of experiments was performed to characterize the mechanical behaviour of both alloys (2198T3R and 2198T8R). Specimens were designed for different stress states varying from low triaxiality to more elevated levels of triaxiality and from proportional to non-proportional loadings.

2.2.1 Specimen geometries: macro and micro specimens

All specimens were manufactured from 2 mm thick raw sheet by the means of electrical discharge machining (EDM). Macro specimens of 2 mm thickness including (a) uniaxial-tension (UT), (b) notched-tension samples (NT2) with a notch of 2 mm radius were designed for proportional loadings at elevated triaxiality in Fig.3.2. The UT samples were loaded in L, T and D directions and the NT sample in L and T direction. A series of 1 mm thick micro specimens were tested to generate a shear state shear inspired by Roth and Mohr (2018) including (c) shear-only (SO) loaded in L direction, (d) tension-only (TO) loaded in T direction and (e) cruciform sample geometry were especially designed for non-proportional loadings: ‘shear to tension’ (ST) or ‘tension to shear’ (TS), see table 3.2. The original geometry was miniaturized to be able to image the region of interest at micrometric spatial resolution by 3D synchrotron laminography imaging (Morgeneyer et al., 2021). The vertical and horizontal offset of the region between both notches in Fig.3.2 (f) have been calculated and optimized by finite element simulations. The offset is necessary to keep the triaxiality levels around the notches small and to let the sample fail from the shear zone. The idea of the present work is to load the sample also in the direction normal to the shear ligament to achieve a load path change. It should be noted that due to the shift of the notches the tensile loading state may be slightly different to the one obtained by classical notched tensile samples with aligned notches: Some local shear loading may be induced during tension due the offset of the notches. This will be measured in any case by the four point extensometer as explained in the following.

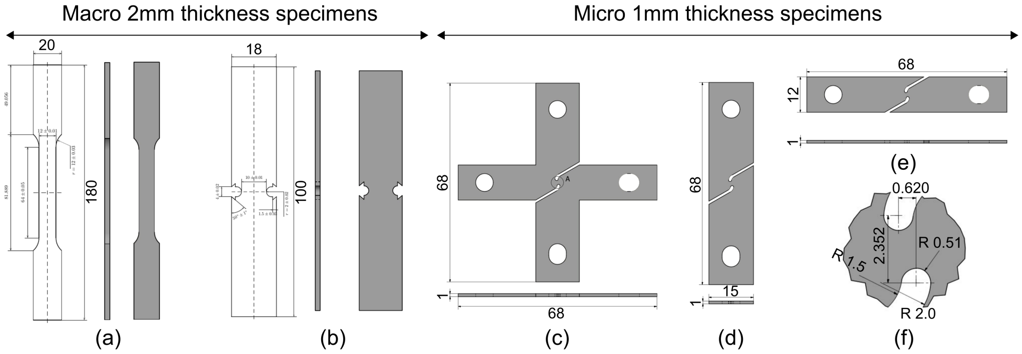

Figure 3.2: Macro specimen geometries with 2 mm thickness: (a) Uniaxial-tension (UT), (b) Notched-tension (NT2) and micro specimen geometries with $t_0 = 1$ mm thickness: (c) Shear-tension cruciform for non-proportional loadings, (d) Shear-only (SO), (e) Tension-only (TO) samples and (f) the detailed geometry of the region of interest (ROI), where the area of minimum ligament $S_0 = w_0 t_0$ ($w_0 = 1.4$ mm for micro specimens in this study).

2.2.2 Loading machine setup

All mechanical tests were carried out at room temperature. Macro tension tests (UT and NT2) were conducted on a servo-hydraulic testing machine. Classical extensometers were used to measure gauge length change both in longitudinal and width directions for UT at strain rate of $10^{-4}\ s^{-1}$. Notch opening displacements on both the left and the right side were measured for NT2 specimens and the cross head velocity was set as 200 µm/min. Micro specimen tests including proportional loadings (SO, TO) and non-proportional loadings (ST, TS) were performed on a dedicated electromechanical loading device for *in situ* laminography testing with 5 kN load cell (ME-Meßsysteme KD40s, Morgeneyer et al. (2021)) where cross heads pulled or unloaded at a speed of 5 µm/s during both loading and unloading, see table 3.2.

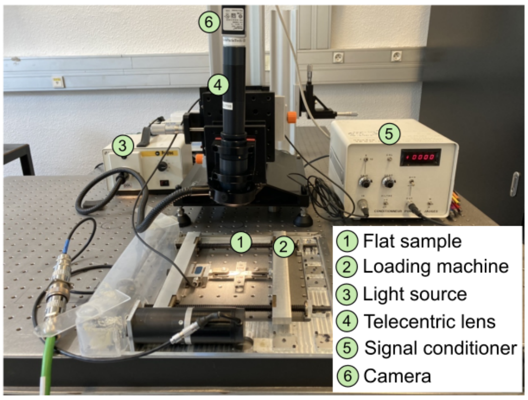

Figure 3.3: Experimental set up: ① Flat sample on ② Loading machine. Optics: ⑥ camera ④ telecentric lens and ③ light source. The signal of load cell is connected to ⑤ signal conditioner.

Specimen	cross head velocity (μm/min)	loading directions
Uniaxial-tension (UT)	384	L, T and D
Notched-tension (NT2)	200	L and T
Shear-only (SO)	300	L
Tensino-only (TO)	300	T
Cross sample	300	shear in L, tension in T

Table 3.2: Macro and micro specimen loading conditions.

2.2.3 Optics setup for strain measurement for micro specimens

In order to measure deformation in the region of interest (ROI) of the complex micro specimens and to avoid being influenced by machine elastic deformation, an optical setup was used to measure the deformation in the region of interest by an optical flow technique (digital image correlation, DIC). In addition, the measurement was used to compare the experiments with finite element simulations. A fine random speckle pattern was deposited by airbrush on the micro specimen surface to measure the displacement fields. The average speckle size was about 15 μm and can be seen in Fig.3.4 (a). Surface images were continuously captured at a frequency of 2 Hz. The detector size is 2048×2048 pixels (Basler acA2040 25g) with optic lens (SILL TZM 0420/3.0-C telecentric lens) resulting in a physical pixel size around 1.87×1.87 μm^2. Based on the commercial software $vic2D-6$ (Correlated Solutions), the displacement field was measured with subset size set as 55 pixels (102 μm) and step size as 5 pixels (9 μm). The Hencky strain field was obtained with filter size of 15.

Macro measurement Instead of utilising the local displacement of two points as traditional extensometer for uniaxial tensile experiments, a 4-point-frame optical extensometer, shown in Fig.3.4 was introduced to measure tension stretch in both vertical and horizontal directions as well as the shear angle in the ROI and to obtain an average macro measurement in the reference frame. The same 4-point-frame measurement was applied in numerical simulations to compare to experiments.

The relative displacement was obtained from the correlation results of optical images at each step. The displacement field was generated using bi-linear interpolation functions corresponding to the 4 selected material points. The region of interest is mainly under simple shear state, according to the specific geometry, when vertical shear load is applied. The deformation gradient F_{ij} is the derivative of the deformed configuration position vector x_i with respect to the reference configuration position vector X_j (Belytschko et al. (2000)). In order to remove the rigid body rotation term, **R** can be written by polar decomposition as the product of two tensors: a rotation tensor **R** and a symmetric right stretch tensor **U**.

$$F_{ij} = \frac{\partial x_i}{\partial X_j} = R_{ik} \cdot U_{kj} \tag{3.1}$$

Tension stretch U_{11} and the absolute value of shear stretch U_{12} were chosen as the tension and shear local measurements respectively.

$$\mathbf{U} = \begin{bmatrix} U_{11} & U_{12} \\ U_{12} & U_{22} \end{bmatrix} \tag{3.2}$$

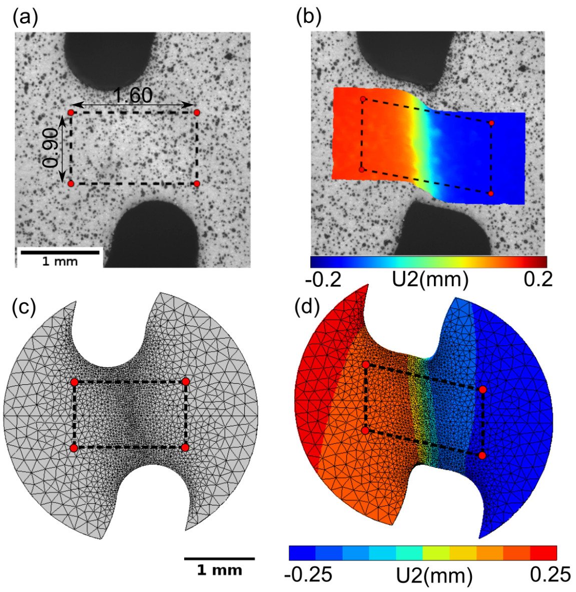

Figure 3.4: 4-point-frame optical extensometer on (a) reference and (b) deformed images for image correlation and the same 4-point-frame is chosen in (c) initial and (d) deformed steps from finite element model to compare experiment with the simulation. The shown displacement field was calculated by VIC2D locally.

Accumulated equivalent strain measurement Damage is accumulated during the complex non-proportional loading path. It is thus important to define an accumulated strain to estimate the strain to fracture under complex loading paths. The logarithmic strain (Hencky strain or true strain) provides the correct measurement of the final strain when deformation takes place in a series of increments, taking into account the influence of the strain path and is defined as:

$$\boldsymbol{\varepsilon} = \frac{1}{2}\log\left(\mathbf{F}^T \cdot \mathbf{F}\right) \tag{3.3}$$

Onaka (2010, 2012) confirmed that the measure is appropriate especially for large simple shear strain.
During the load path change, the equivalent strain needs to be cumulative to estimate an effective strain. The work-conjugate equivalent strain was defined in terms of the adopted constitutive model (Abedini et al., 2018). Butcher and Abedini (2017) pointed out that the difference between the work-conjugate strain and the accumulated equivalent strain is negligible when strain is less than 0.8. The present work aims to compare the experimental results from DIC with the FEA ones and offer an appropriate measure during complex load path change. The equivalent strain is defined as:

$$\varepsilon_{cum} = \int \sqrt{\frac{2}{3} d\boldsymbol{\varepsilon} : d\boldsymbol{\varepsilon}} \tag{3.4}$$

However, the information in thickness direction lacks in the 2D image correlation. The third component ε_{III} is computed assuming plastic incompressibility $\varepsilon_I + \varepsilon_{II} + \varepsilon_{III} = 0$, where ε_I, ε_{II}, ε_{III} are the eigenstrains. Hence, the accumulated equivalent strain increment is calculated as:

$$\Delta\varepsilon_{cum}^{2d} = \sqrt{\frac{2}{3}(\Delta\varepsilon_I^2 + \Delta\varepsilon_{II}^2 + \Delta\varepsilon_{III}^2)} = \frac{2}{\sqrt{3}}\sqrt{\Delta\varepsilon_I^2 + \Delta\varepsilon_{II}^2 + \Delta\varepsilon_I\Delta\varepsilon_{II}} \tag{3.5}$$

2.3 Numerical simulation

The finite element method was applied to fit an anisotropic plasticity model and predict the stress response under different non-proportional load paths. The macro UT samples were meshed as single element of the quadratic hexahedral element (c3d8). Due to geometry symmetry, an eighth of macro NT2 sample was meshed, while half thickness of the micro sample series was meshed. Micro specimens were meshed using tetrahedra elements (10 nodes, 4 Gauss points), whereas macro specimens were meshed with hexahedral elements (20 nodes and 8 Gauss points). For computation efficiency in model calibration, the coarse mesh size is 200 µm. After the model was optimized, the fine mesh size varied from 30 µm to 100 µm illustrated in Fig. 3.4 (c)(d). For brevity, the mesh convergence study on stretch-stress from 200 µm down to 10 µm is shown in Appendices 3. A mixed displacement-pressure updated Lagrangian formulation was applied for the tetraedral element (c3d10) to account for large plastic strain and incompressibility especially for the micro specimen series (Al Akhrass et al., 2014; Taylor, 2000). All simulations are performed in the finite element software Z-set (Besson and Foerch, 1997).

2.3.1 Anisotropic model

The material under study presents an anisotropic plastic behaviour that cannot be represented by a simple quadratic yield surface such as the one proposed in Hill (1950) as this model is unable to satisfactorily describe yield anisotropy and Lankford coefficients simultaneously in all directions. To overcome this difficulty, the yield function proposed by Bron and Besson (2004) was used in this work. This phenomenological yield function was developed to represent the plastic anisotropy of the aluminum alloy. It is an extension of the functions given in (Barlat et al., 1991; Karafillis and Boyce, 1993). Plastic anisotropy is represented by 12 parameters in the form of two fourth order symmetric tensors. Four other parameters influence the shape of the yield surface uniformly. The model is based on the definition of an equivalent stress $\bar{\sigma}$ function of the stress tensor $\boldsymbol{\sigma}$:

$$\bar{\sigma} = (\alpha_1 \bar{\sigma}_1^a + \alpha_2 \bar{\sigma}_2^a)^{1/a} \tag{3.6}$$

with $\alpha_2 = 1 - \alpha_1$. $\bar{\sigma}_1$ and $\bar{\sigma}_2$ are respectively given by:

$$\bar{\sigma}_1 = (\frac{1}{2}(|S_1^2 - S_1^3|^a + |S_1^3 - S_1^1|^a + |S_1^1 - S_1^2|^a))^{1/a} \tag{3.7}$$

$$\bar{\sigma}_2 = (\frac{3^a}{2^a + 2}(|S_2^1|^a + |S_2^2|^a + |S_2^3|^a))^{1/a} \tag{3.8}$$

where S_1^1,S_1^2,S_1^3 (resp. S_2^1,S_2^2,S_2^3) are the eigenvalues of a modified stress deviator $\mathbf{s_1}$ (resp. $\mathbf{s_2}$) defined as: $\mathbf{s_1} = \mathbf{L_1} : \boldsymbol{\sigma}$ (resp. $\mathbf{s_2} = \mathbf{L_2} : \boldsymbol{\sigma}$) where the fourth order $\mathbf{L_{1,2}}$ have the following form using Voigt notation:

$$\mathbf{L_k} = \begin{pmatrix} (c_k^{LL} + c_k^{SS})/3 & -c_k^{SS}/3 & -c_k^{LL}/3 & 0 & 0 & 0 \\ -c_k^{SS}/3 & (c_k^{SS} + c_k^{TT})/3 & -c_k^{TT}/3 & 0 & 0 & 0 \\ -c_k^{LL}/3 & -c_k^{TT}/3 & (c_k^{TT} + c_k^{LL})/3 & 0 & 0 & 0 \\ 0 & 0 & 0 & c_k^{TL} & 0 & 0 \\ 0 & 0 & 0 & 0 & c_k^{LS} & 0 \\ 0 & 0 & 0 & 0 & 0 & c_k^{ST} \end{pmatrix} \tag{3.9}$$

The yield surface is expressed as:

$$\Phi = \bar{\sigma} - R(p) \tag{3.10}$$

where $R(p)$ corresponds to the flow stress expressed as a function of the accumulated plastic strain p. $R(p)$ is expressed:

$$R(p) = R_0 + Q_1(1 - e^{-b_1 p}) + Q_2(1 - e^{-b_2 p}) \tag{3.11}$$

Parameter R_0 is set to the normalised yielding stress in rolling direction (L) for each material. Q_1, b_1, Q_2 and b_2 are 4 parameters that mainly control hardening. Plastic anisotropy is only controlled by 12 components in $\mathbf{L_k}$ (4 parameters $c^{LS}_{1,2}$,$c^{ST}_{1,2}$ are set as 1). a and α_1 influence the shape of yield surface.

2.3.2 Strategy for parameter identification and prediction

The identification of the various material parameters including 5 hardening parameters and 10 anisotropic parameters was performed using different experimental data. Macro uniaxial-tension (UT) tests in L, T and D loadings, notched-tension (NT2) tests in L, T loadings and micro shear-only (SO) test in L loading were chosen to calibrate hardening and the anisotropy model. The identified model is used to predict the micro tension-only (TO) and two non-proportional loadings ‘shear to tension’ (ST) as well as ‘tension to shear’ (TS) in comparison with experimental results.

Step I – optimization of macro UT tests: For the optimization of the computation time, single element calculations were carried out to calibrate with uniaxial-tension (UT) tests. Young’s modulus E was set as 74 GPa and the Poisson’s ratio was set to 0.3. First, the plastic hardening parameters (R_0,Q_1,b_1,Q_2 and b_2), the anisotropic parameters (12 components c^k_i in $\mathbf{L_k}$) and yield surface parameter, a (α_1 was set to 0.5), under uniaxial-tension state along L, T and D directions were adjusted. Ranges of permitted parameter values were chosen. Besides, 4 parameters $c^{LS}_{1,2}$,$c^{ST}_{1,2}$ are set to 1 as the yield function is optimized for thin sheets. The nominal stress F/S_0 and width reduction $\Delta W/W_0$ versus engineering strain $\Delta L/L_0$ in loading direction are chosen to calibrate the parameters on experimental results.

Step II – optimization of macro NT2 and micro SO tests: This step aimed at optimizing parameters to fit plasticity for different stress states and higher levels of strain: higher stress triaxiality of notched-tension (NT2) and nearly zero stress triaxiality of shear-only (SO) tests. To achieve this aim, two 3D calculations simulations were added to the optimization to calibrate the parameters on experimental results. Starting from the parameters obtained from step I, all parameters are calibrated again with comparison between nominal stress F/S_0 and notch opening displacement (NOD) for NT2, shear stretch U_{12} for SO. In addition, these tests allow to identify the material hardening at more elevated strain levels.

Step III – prediction on micro TO and non-proportional tests: The parameters obtained from step II are applied to predict the other loading conditions on micro specimens including tension-only (TO) and particularly non-proportional loadings: ‘shear to tension’ (ST) and ‘tension to shear’ (TS). These predictions using optimized parameters are compared with experimental results in terms of nominal stress F/S_0 versus shear stretch U_{12} or tension stretch U_{11}.

3 Results

3.1 Mechanical testing results

3.1.1 Vickers hardness test results

The hardness of the 2 mm thick sheets (2198T3R and 2198T8R) was identified by an automatic hardness tester HZ30-4 (Presi). The force (0.1 kgf) with Vickers indenter was applied along two different lines through the sheet thickness (S). The testing points were distributed along two columns with 50 µm distance to avoid the effect of previous indent as illustrated in Fig.3.5 (b). The vickers hardness (Hv) profile along the thickness direction is shown in Fig.3.5 (a). Artificially aged alloy 2198T8R exhibited a higher hardness (average 164 Hv) than naturally ageing alloy 2198T3R (average 119 Hv). For each alloy, an obvious hardness reduction of 10% near the middle thickness of raw sheets was found.

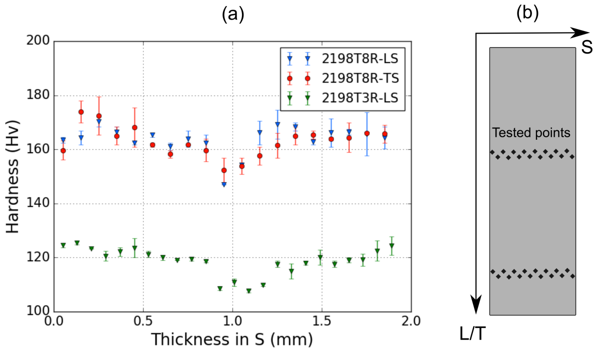

Figure 3.5: Micro hardness test: (a) Vicker's hardness profiles of average value through the thickness direction and (b) Position of the testing points along two lines.

3.1.2 Proportional loading experiments

Proportional loading results including those of macro specimens of (a) uniaxial-tension (UT) in L,T,D directions, (b) notched-tension (NT2) in L,T directions as well as micro specimens of (c) shear-only (SO) in L direction and (d) tension-only (TO) in T direction are presented in Fig.3.6 for 2198T3R and Fig.3.7 for 2198T8R respectively.

2198T3R: Fig.3.6 (a) shows the experimental curves in terms of the nominal stress F/S_0 and width reduction ΔW as a function of engineering strain $\Delta L/L_0$ for macro UT tests in L, T and D directions. The curve of nominal stress versus notch opening displacement (NOD) is exhibited in (b) for macro NT2 specimens in L and T directions.

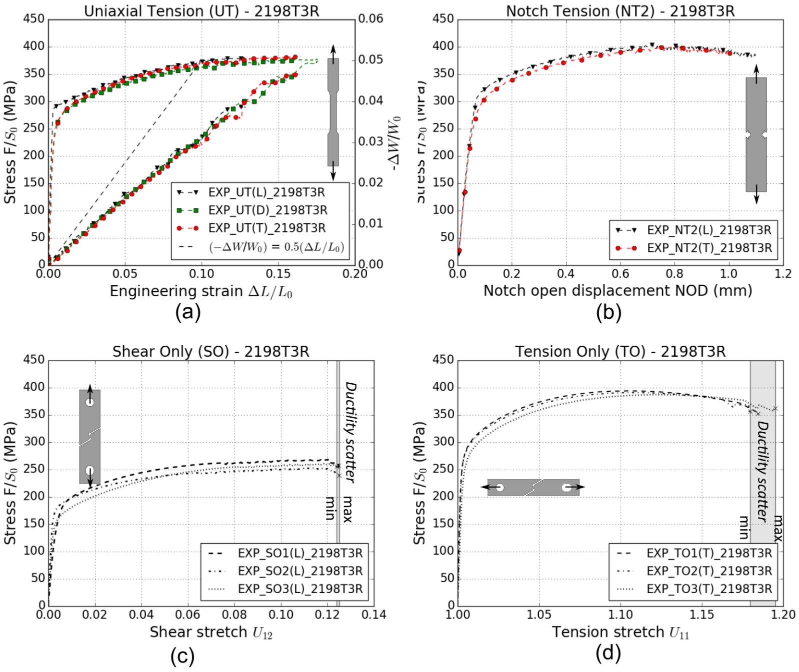

Figure 3.6: 2198T3R proportional loading experimental results: (a) uniaxial-tension (UT), (b) notched-tension (NT2), (c) shear-only (SO) and (d) tension-only (TO). Here three symbols represent three loading orientations respectively. Repeated testing results are shown for SO and TO samples.

The maximum nominal stress of macro UT and NT2 reached 382 MPa and 402 MPa, respectively. A moderate plastic anisotropy is found for this alloy. The width reduction was indeed about -0.3 times the longitudinal strain and thereby different from the value for the isotropic case which would be -0.5, as indicated in form of a dotted line in Fig.3.6 (a). The yield stress in L-loading is slightly higher, which can be explained by the pre-straining in rolling direction (L) during manufacturing. The nominal stress versus shear stretch of micro specimens SO and tension stretch of TO are presented in Fig.3.6 (c)(d) respectively. The maximum stress levels of SO and TO are 260 MPa and 394 MPa. Repeated testing results are shown for the small samples to investigate repeatability in terms of plasticity and stretch to fracture. The scatter in shear stretch to fracture U_{12}^{SO} was low and ranged from 0.124 to 0.125 and the tension stretch to fracture U_{11}^{TO} varied from 1.180 to 1.195. The grey zone indicates the scatter range from minimum to maximum found values.

2198T8R: The tests for artificially aged alloy 2198T8R in the same layout as Fig.3.6 are shown in Fig.3.7. The maximum nominal stress level of macro specimens UT is 497 MPa and NT2 is 540 MPa. 2198T8R exhibits a higher stress level but less ductility

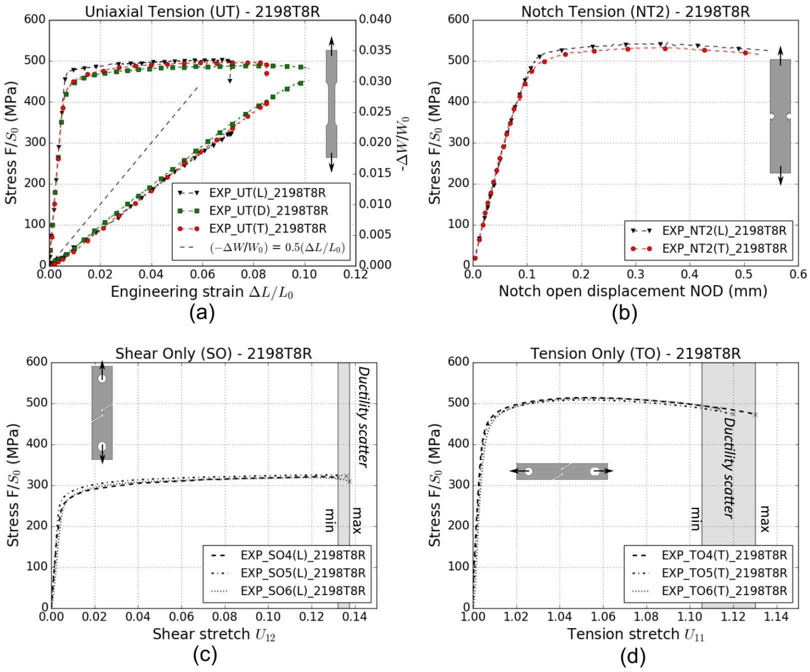

Figure 3.7: 2198T8R proportional loading experimental results: (a) uniaxial-tension (UT), (b) notched-tension (NT2), (c) shear-only (SO) and (d) tension-only (TO). Here three different symbols represent three loading orientations respectively. Repeated testing results are shown for SO and TO samples.

than naturally aged alloy 2198T3R. The same moderate plastic anisotropy is seen as well. The width reduction was also about -0.3 times the longitudinal strain. For micro specimens of 2198T8R in Fig.3.7 (c)(d), the maximum nominal stress of SO and TO are 322 MPa and 512 MPa respectively. The shear stretch to fracture scatter of SO (U_{12}^{SO}) was low and ranged from 0.132 to 0.137 and the tension stretch to fracture of TO (U_{11}^{TO}) ranged from 1.105 to 1.130 shown by the scatter bar (grey) for repeated testing. For the TO test an increased scatter in ductility was found compared to the T3 condition. This might be linked to the higher stress levels that might lead to a stronger sensitivity to microstructure governed damage nucleation. As the samples are small, they may or not contain numerous particle clusters or weak grain boundaries (Rousselier et al., 2017), which may make them prone to the influence of statistics and may have an effect on the macroscopic ductility scatter.

Between two heat treatments of the alloy T3R and T8R, obvious ductility reductions were seen in macro UT ($(\Delta L/L_0)_{T3R}^{f}$=0.16 versus $(\Delta L/L_0)_{T8R}^{f}$=0.08), NT2 (NOD_{T3R}^{f} =1.0 versus NOD_{T8R}^{f} =0.5) experiment as well as the micro TO (U_{11}^{f-T3R}=1.19 versus U_{11}^{f-T8R}=1.12) experiment. The artificially aged alloy T8R presents a higher stress level than natural ageing one T3R, which probably is one of the causes of the ductility reduction. Interestingly, the ductility of micro SO test remains close and even stretch to fracture of T3R (U_{12}^{f-T3R}=1.124) is less than that of T8R (U_{12}^{f-T8R}=1.135). The fact that the ductility in shear was so similar between the two heat treatment conditions could be explained by the shear sample geometry that is designed to localize strain in a shear band from the beginning of the test onward. This is different compared to the larger, more homogeneous plastic zone of other sample geometries that may benefit form hardening in the T3 condition and lead to bigger plastic zones and associated macroscopic ductility in T3 condition. Another reason for the similar ductility in T3 and T8 condition in shear could be the relatively low stress levels achieved in shear compared to tensile stress states that may lead to less damage nucleation (Petit et al., 2019).

The macroscopic material behaviour is summarized for both heat treatment conditions in table 3.3 in terms of yield stress, UTS, engineering strain at the end of uniform elongation and Lankford coefficient. The Lankford coefficient is defined as ratio of the true thickness strain over the true sample width strain: L_k=$\varepsilon_{width}/\varepsilon_{thickness}$. The thickness strain was obtained by the assumption of incompressibility.

	2198T3R					2198T8R				
	YS	UTS	YS/UTS	UE	L_k	YS	UTS	YS/UTS	UE	L_k
L	290	389	0.745	18.0	0.49	476	504	0.944	7.3	0.48
T	258	386	0.668	18.3	0.50	441	497	0.887	8.7	0.50
D	257	380	0.676	22.1	0.52	435	490	0.888	9.0	0.52

Table 3.3: Room temperature tensile properties of tested materials (2198T3R and 2198T8R) along L, T and D directions. (YS: yield strength for 0.2% plastic strain (MPa), UTS: ultimate tensile strength (MPa), UE: uniform elongation (%), L_k: Lankford coefficient for a plastic deformation of 5%.

3.1.3 Non proportional tests

Two different types of non-proportional load path change tests on micro cross specimens were performed by loading, unloading and turning the sample by 90°: shear loading in L direction followed by tension loading in T called ‘shear to tension’ (ST) test and tension loading in T followed by shear loading in L called ‘tension to shear’ (TS) tests are presented in Fig.3.8 for 2198T3R and Fig.3.9 for 2198T8R respectively.

2198T3R: The curves in terms of nominal stress versus (a) shear stretch U_{12} and (b) tension stretch U_{11} from two loading periods of ‘shear to tension’ (ST) are presented in Fig.3.8. The cross specimen was loaded to around U_{12} = 0.06, which was half of monotonic SO shear stretch to fracture (U_{12} = 0.124). Subsequently, it was unloaded before applying tension loading till fracture. The 4 initial points were tracked to measure stretch via an optical extensometer during different loading paths, see section 2.2.3. The shear part of the ST-test showed a similar curve as the monotonic SO test that is also plotted for comparison. The nominal stress of tension after shear reached 450 MPa, and the stress at yielding is higher than for the proportional test due to the hardening during the shear loading. In addition, the tension stretch U_{11} started with an initial shift of 0.025 on the tension curve as there was a slight tension stretch during shear loading. The tension stretch to fracture of the 'shear to tension' tests ranged from 1.122 to 1.143 with an average value $U_{11}^{ST} = 1.130$, which was reduced by 30% compared to the average stretch to fracture value of TO tests $U_{11}^{TO} = 1.185$. This reduction would be even higher if the initial tension stretch shift during shear loading was not taken into account. The curves of the 'tension to shear' (TS) load path change are shown in Fig.3.8 (c) and (d). The specimen was loaded in tension first till $U_{11} = 1.11$ then unloaded, and it was loaded in shear till fracture. The nominal stress versus tension stretch U_{11} and shear stretch U_{12} are shown in (c)(d) respectively. During the tension period in (c), the stress level of non proportional load TS was very repeatable compared to the proportional TO dashed curve in black. The specimens were unloaded at near maximum stress level around 400 MPa. When the samples were turned and loaded in shear, see (d), the stress level decreased to 220 MPa mainly due to thickness reduction effect during tension loading. The initial offset of shear stretch is due to the shear stretch induced during tension loading. This is mainly due to the fact that the two notches are not aligned. A large scatter zone (blue) of shear stretch to fracture U_{12}^{TS} was found and ranged from 0.100 to 0.126, whose maximum value was close to the monotonic SO shear stretch to fracture U_{12}^{SO} scatter. The average value of stretch to fracture in shear was reduced by about 10% compared to the average stretch to fracture value for the monotonic test. The pre-tension test thereby seems less detrimental than the pre-shear test.

2198T8R: The same two types of non proportional loadings are presented in Fig.3.9 for for 2198T8R. (a) Shear period and (b) tension period of stress – stretch curves for 'shear to tension' (ST) are shown. The specimens were loaded in shear loading in L to $U_{12} = 0.06 - 0.08$ for repeated tests and then unloaded. Tension loading in T was applied again till failure. Maximum stress levels reached 600 MPa on tension loading after shear loading, which is higher than that of monotonic TO test (512 MPa). The strain to fracture of ST varied from 1.084 to 1.105 while the scatter of TO ranged from 1.105 to 1.130. The average value of stretch to fracture for the ST test was 1.098, which represents a reduction of around 16% compared to the average value of stretch to fracture for TO (1.117). Here if the tension stretch shift in pre-shear loading was neglected, the reduction would be even higher.

The results of the 'tension to shear' load path change (TS) are shown in Fig.3.9 (c)(d). The specimens were loaded in tension in T direction to $U_{12} = 1.05 - 1.06$, which is about one half of the fracture stretch under monotonic tensile loading (TO). They were unloaded and then loaded in shear in L direction. The maximum stress levels of shear loading after tension were 300 MPa, which slightly decreased compared to the monotonic SO group. This stress reduction mainly resulted from the thickness reduction effect (cross section reduction) due to pre-tension loading. The strain to fracture scatter (blue) of TS U_{12}^{TS} was large and ranged from 0.117 to 0.157, see Fig.3.9 (d). The average

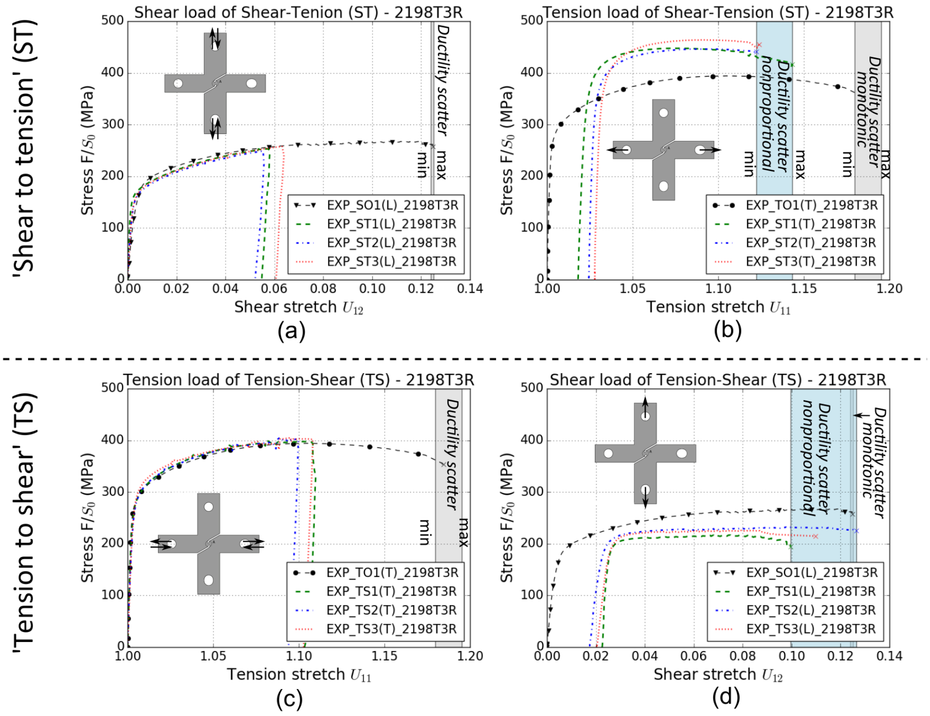

Figure 3.8: 2198T3R non-proportional loading experimental results: (a) shear period and (b) tension period of ‘shear to tension’ (ST) loadings, (c) tension period and (d) shear period of ‘tension to shear’ (TS) loadings.

shear stretch to fracture value of the TS load path change was similar to the average value of shear stretch to fracture of the monotonic test, but the scatter of the shear stretch to fracture of the load path change was a lot stronger than for the monotonic test. The origins of scatter in ductility will be discussed in more detail in the discussion section 4.2 using fields obtained by DIC and fractography.

The shear and tension stretch to fracture under different loading paths are gathered in table 3.4 for two materials.

	Proportional U_{11}^{TO}	Non-proportional U_{11}^{ST}	Proportional U_{12}^{SO}	Non-proportional U_{12}^{TS}
2198T3R	1.180-1.195	1.122-1.143	0.124-0.125	0.100-0.126
2198T8R	1.105-1.130	1.084-1.105	0.132-0.135	0.117-0.157

Table 3.4: Stretch to fracture under different proportional and non proportional loading conditions for the micro specimens of both materials.

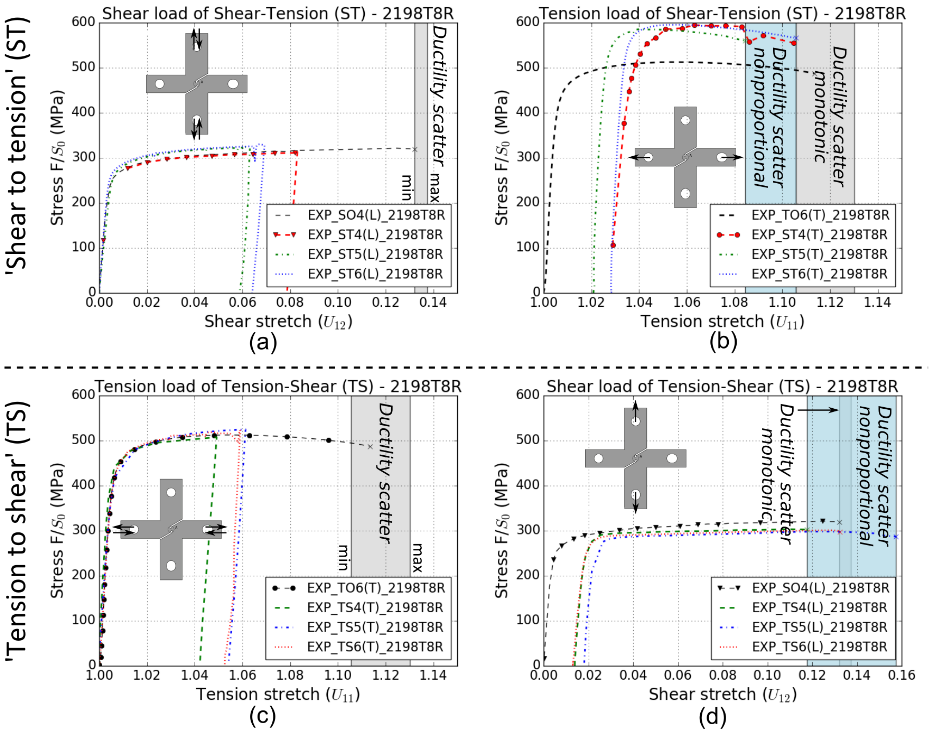

Figure 3.9: 2198T8R non-proportional loading experimental results: (a) shear period and (b) tension period of ‘shear to tension’ (ST) loadings, (c) tension period and (d) shear period of ‘tension to shear’ (TS) loadings.

3.1.4 Fracture paths and surfaces under different loading conditions

Macroscopic fracture features include the fracture path and fracture surface. The macroscopic fracture path can be identified as flat path or slant path through the sample thickness while the fracture surface can be regarded as rough surface or smooth surface. The fracture paths under different loading conditions will be shown in the following for both 2198T3R and 2198T8R. The corresponding results for last strain field before fracture measured by DIC are also given. Microscopically, different types of features are observed on the fracture surfaces. They can be divided into four main types: i) large dimples with sizes larger than 10 μm that are initiated at the coarse precipitates, ii) sub-micrometer dimples that are initiated at dispersoid particles down to nanometer scale, iii) typical shear feature void sheeting that consists of a cluster of sub-micrometer dimples and iv) flat regions without voids. The fractography of four loading conditions TO, ST, SO and TS at various magnifications are exhibited in Fig.3.11, Fig.3.12, Fig.3.13 and Fig.3.14 respectively obtained by scanning electron microscopy (SEM). Two detectors are utilized: secondary electron (SE2) and back-scattered (HDBSD). The first focus on the fracture shape and more precise relative positions while the latter distinguishes the different phases (i.e. matrix and particle). The applied detector is noted as its abbreviation in the signal A of each image.

2198T3R: Fig.3.10 shows the accumulated equivalent strain field at the last step both obtained by the 3D FE simulations and also by surface DIC. The final fracture path of broken micro specimens for four different loadings of the alloy is also given. There is a good agreement between simulations and DIC measurement in terms of the shape of the localized region and also its magnitude. The shapes of the notches are also well reproduced. It can be seen in Figs (a) and (e) that some shear strain is induced during proportional tension loading. Two tension fracture paths of 2198T3R are seen in Fig.3.10 (b) tension-only (TO) and (d) 'shear to tension' (ST). The proportional loading failed with a flat crack through the thickness. However in the sheet plane (L-T plane) the crack had an angle of 110° and superposed well with the strain field before failure. In contrast, the crack was slant through the thickness for the ST sample as can be seen in Fig.3.12 (a). In other words, there is a clear change in fracture plane due to pre-shear. The accumulated equivalent strain level reached only less than 0.45 for both tension fracture groups, but it should be noted that the maximum strain typically occurs at middle thickness of specimen, as known from FE simulations.

The shear fracture planes of 2198T3R are exhibited in Fig.3.10 for (f) shear-only (SO) and (h) 'tension to shear' (TS). The fracture paths were oriented parallel to shear loads and located at the maximum strain regions for both shear loading conditions in (e) SO and (g) TS. The strain field of the SO test was highly localized up to a magnitude of 0.8 while the field of TS has a wider shear band with maximum value as 0.6 due to the deformed notch from tension preloading. As FE results showed, the strain field of proportional loading SO slightly varied along the thickness direction but the maximum strain region of the non-proportional loading TS is situated in the middle plane due to the pre-tension straining. Fig.3.13 (a) and Fig.3.14 (a) show the smoother shear fracture

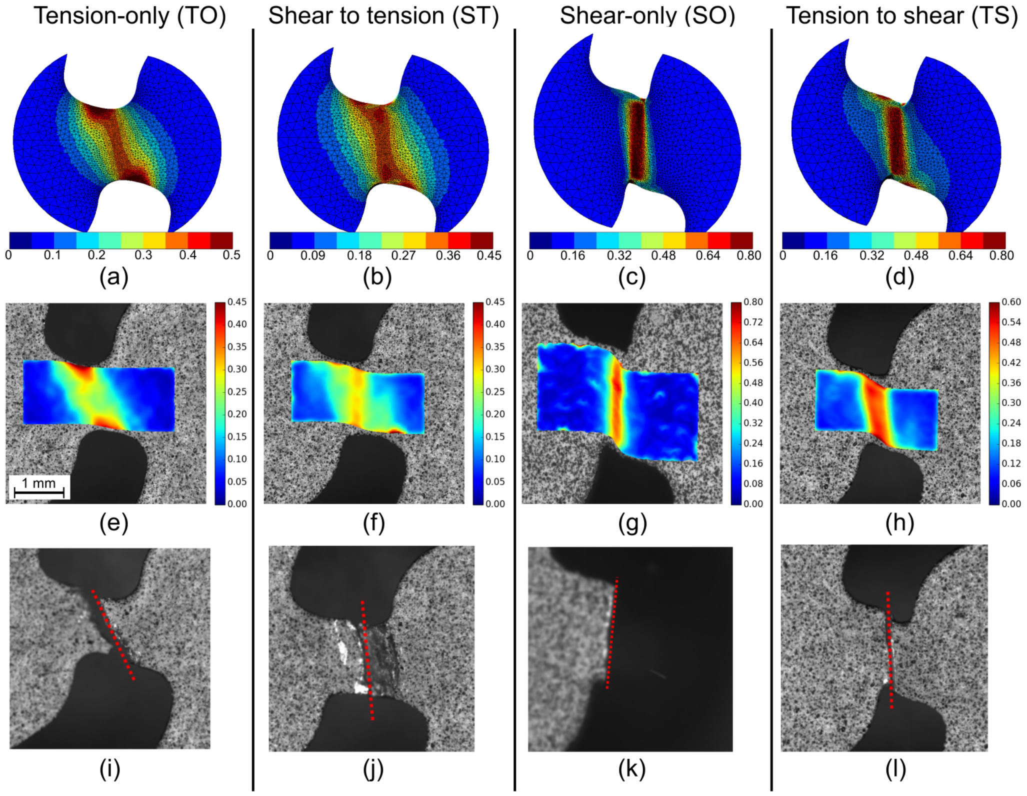

Figure 3.10: 2198T3R: (a-d) accumulated equivalent strain on the surface before fracture obtained by 3D FE simulations (e-h) accumulated equivalent strain fields from DIC at last step before fracture and (i-l) Fracture path of proportional tension-only (TO), non-proportional ‘shear to tension’ (ST), proportional shear-only (SO) and non-proportional ‘tension to shear’ (TS) loadings.

surfaces than tension fractures.

Fig.3.11 (b) exhibits the macroscopic rough fracture surface for the proportional loading TO. Large dimples of size up to 20 μm are shown in (c), which are linked to the intermetallic particles. Broken particles and particle decohesions from the matrix are also found. Locally sub-micrometer dimple features are observed as well in (d). Fig.3.12 presents the SEM images of non-proportional loading ST. A relatively smooth surface and grain-shaped steps are shown in Fig.3.12 (a). On the microscopic scale, the steps of grain-shaped features are shown at higher magnification in (c)(d), and these could correspond to the cracks during the pre-shear loading. Some dimples with medium size 1 μm are found and part of them is considered to be initiated on the grain boundaries.

SEM fracture surface images of two loadings that end with shear are shown in Fig.3.13 of shear-only (SO) and Fig.3.14 of ‘tension to shear’ (TS). Both fracture surfaces under proportional SO and non-proportional TS are macroscopically smooth. On the microscopic scale, the elongated dimple cluster is oriented normal to the loading direction in

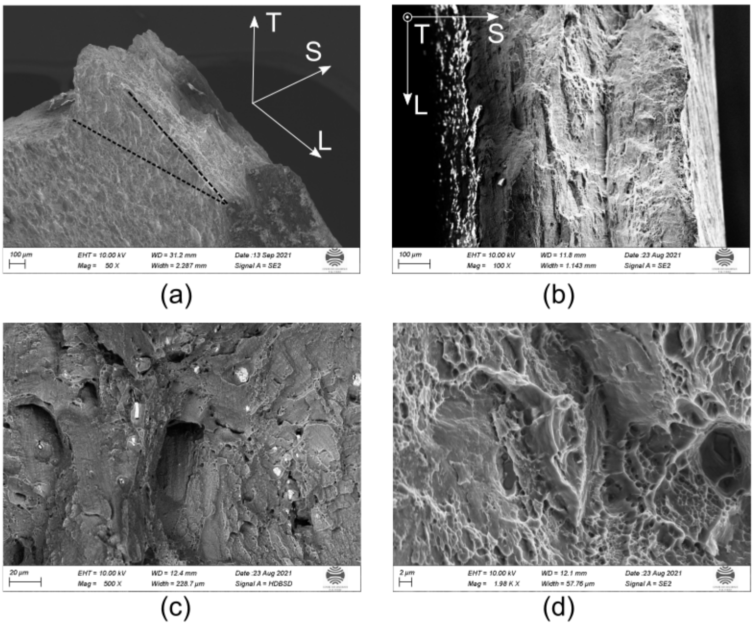

(a) (b) (c) (d)

Figure 3.11: Fractography via scanning electron microscopy (SEM) of 2198T3R under tension-only (TO): (a)(b) Macroscopic rough fracture surface with (c) large dimple that initiated to the intermetallic particles and (d) medium dimples with size down to 2 μm, some of which probably initiated to the grain boundaries.

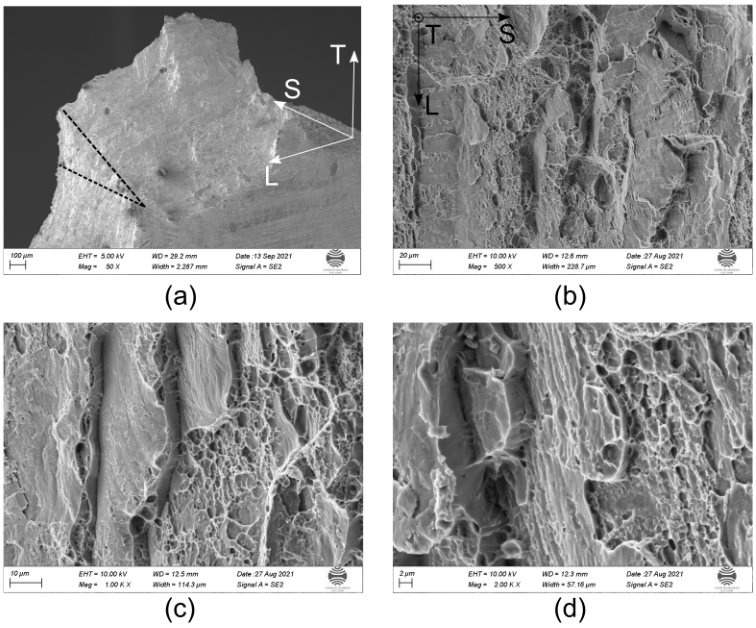

Figure 3.12: Fractography via scanning electron microscopy (SEM) of 2198T3R under 'shear to tension' (ST): (a) Macrosopic slant fracture path in T-S plane and relative smooth fracture surface, microscopic fracture features like (b) large dimples and (c)(d) grain-shaped steps with medium dimples.

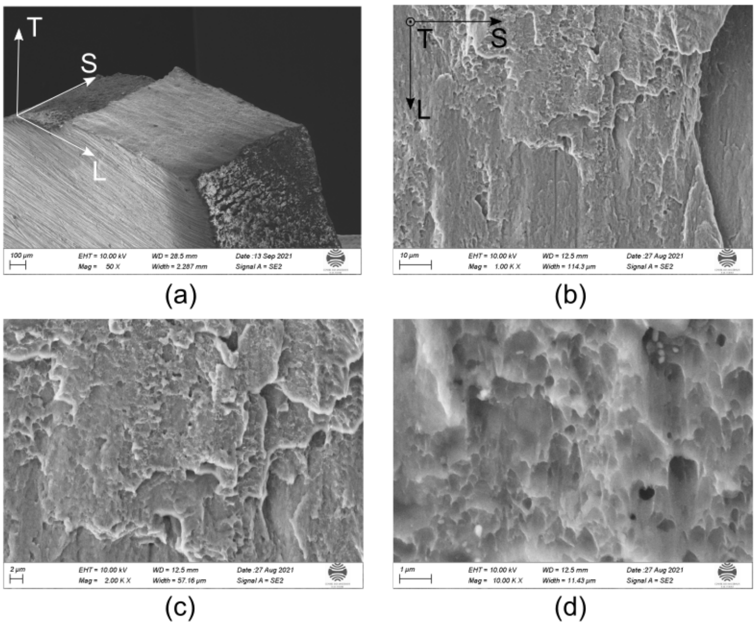

Figure 3.13: Fractography via scanning electron microscopy (SEM) of 2198T3R under shear-only (SO): (a) Macroscopic smooth fracture surface, (b)(c) Flat fracture surface and (d) Elongated ductile dimple cluster that initiated on the dispersoids.

Fig.3.13 (d). The presence of dispersoids, supposedly Al_3Zr (Nayan et al., 2019), less than 100 nm in diameter are probably the initiation sites of these ductile dimples. For the non-proportional group TS, a flat crack-like feature of 100 µm in length is observed at mid-thickness and it is suspected as the damage from tension pre-loading in Fig.3.14 (b). The rest area of the fracture surface is more close to the shear damage mechanism as proportional SO loading with void sheeting. Some intermetallic particles are elongated and decohered as shown in (c)(d).

2198T8R: The same layout of accumulated equivalent strain field of last step before fracture and fracture path of 2198T8R are presented in Fig.3.15. Fracture paths match well with their maximum strain locations as 2198T3R. Similar to the global tension stretch reduction, the local strain level on surface of 2198T8R shows lower strain values as well than the material in T3R condition. It showed a lower strain value around 0.40 compared to 0.45 of 2198T3R in TO. For shear dominated cracks shear-only (SO) and 'tension to shear' (TS), the cracks are oriented parallel to the loading direction as shown in T3R. For the sake of brevity, the fractography of 2198T8R result is given in Appendix A.4. Conclusions are similar to those of T3R condition.

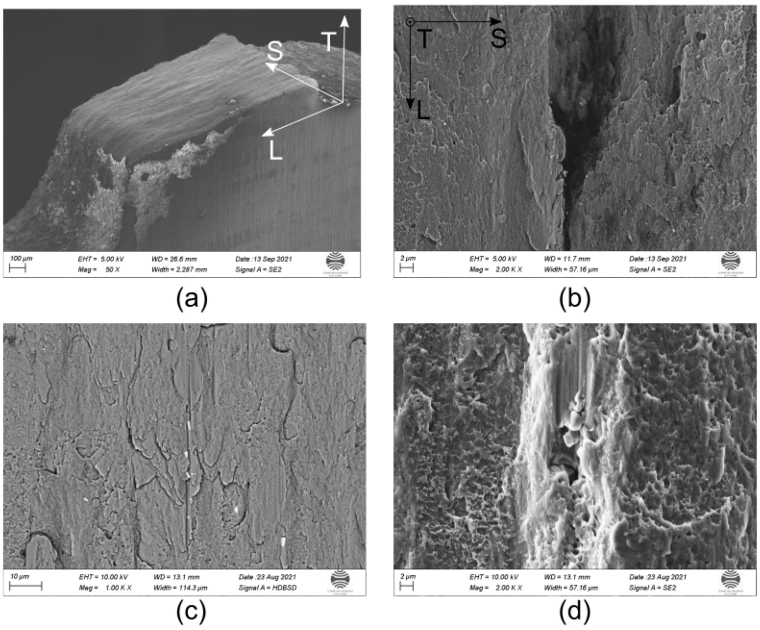

Figure 3.14: Fractography via scanning electron microscopy (SEM) of 2198T3R under ‘tension to shear’ (TS): (a) Macroscopic smooth fracture surface, (b) A flat crack-like feature is observed near middle thickness plane, (c) Intermetallic particles are elongated, broken and decohered, (d) Deformed intermetallic particles, medium dimples features including the void sheeting shear feature.

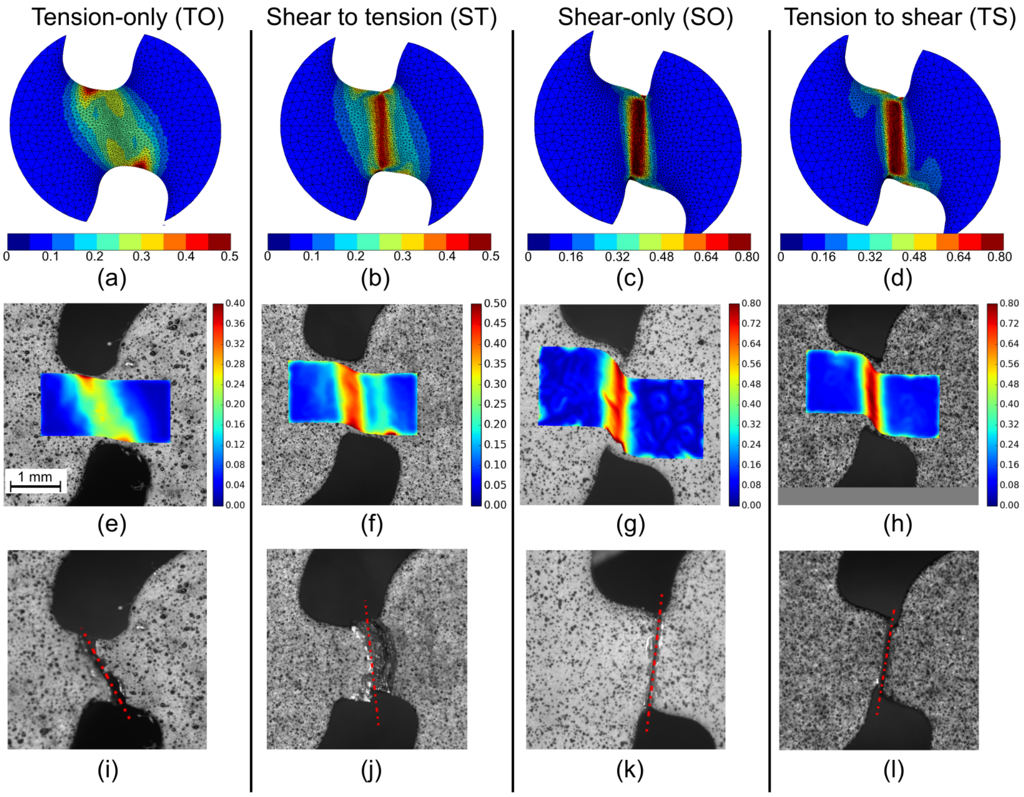

Figure 3.15: 2198T8R: (a-d) Accumulated equivalent strain on the surface before fracture obtained by 3D FE simulations, (e-h) Accumulated equivalent strain fields from DIC at last step before fracture, (i-l) Fracture path of proportional tension-only (TO), non-proportional ‘shear to tension’ (ST), proportional shear-only (SO) and non-proportional ‘tension to shear’ (TS) loadings.

3.2 Identification of material parameters and optimization

Based on the strategy detailed in section 2.3.2, the model accounting for plastic anisotropy was identified by using calibrations with proportional loadings macro uniaxial-tension (UT) in L, T and D directions, notched-tension (NT2) in L,T tests and micro test shear-only (SO) in L. The 5 optimized hardening parameters are given in table 3.5 and thee 10 anisotropic parameters are shown in table 3.6 for each material. The fits of numerical simulations using the optimized parameters with experimental results are given in Fig.3.16 for 2198T3R and Fig.3.17 for 2198T8R.

The macro UT stress-strain curves of experiment (point) and simulations (full line) in three directions were fitted and exhibited in Fig.3.16 (a). The macro NT2 stress versus displacement curves in L, T are presented in (b). Plasticity model simulations fit well with experimental results. The micro SO stress – shear stretch curve from simulation agreed well with one representative experimental test in (c) despite a small mismatch near yield point. The width reduction is also well fitted.

The same tests and numerical results as above are shown in Fig.3.17 for 2198T8R. There are good agreements in (a) macro UT and (c) micro SO tests between numerical and experimental results. Less than 2% stress difference is found in NT2 in both L, T directions is found in (c), which is due to the less weight set in macro NT2 tests than in UT tests during the optimization of plasticity parameters.

Material	R_0	Q_1	b_1	Q_2	b_2
2198T3R	217.2	18.370	578.855	166.561	10.909
2198T8R	450	41.645	749.659	98.278	25.551

Table 3.5: Optimized parameters for hardening.

Material	a	α_1	c_1^{TT}	c_1^{LL}	c_1^{SS}	c_1^{TL}	c_1^{LS}	c_1^{ST}
			c_2^{TT}	c_2^{LL}	c_2^{SS}	c_2^{TL}	c_2^{LS}	c_2^{ST}
2198T3R	6.160	0.500	1.084	1.058	0.702	0.901	1	1
			0.767	0.790	0.853	0.712	1	1
2198T8R	15.9	0.500	1.192	1.219	0.867	1.070	1	1
			0.720	0.772	1.343	1.155	1	1

Table 3.6: Optimized parameters for plastic anisotropy.

3.3 Prediction results of tension-only and non-proportional loadings

The model with optimized parameters was used to simulate the small specimens under tension-only (TO) and non-proportional loadings including ‘shear to tension’ (ST) and ‘tension to shear’ (TS) to predict and compare with the experimental results in Fig.3.18 for 2198T3R and Fig.3.19 for 2198T8R.

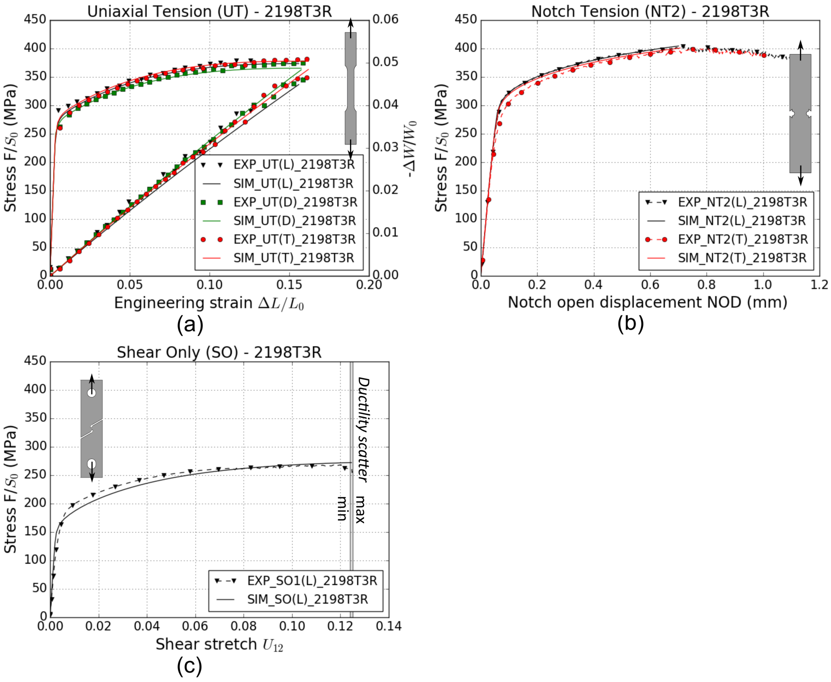

(a) (b) (c)

Figure 3.16: 2198T3R calibrated FE simulation results (full line) with experimental groups: (a) uniaxial-tension (UT), (b) notched-tension (NT2), and (c) shear-only (SO).

2198T3R predictions (full line) not only fit well the TO experimental result (dashed line), but also in both loading periods of non proportional loadings ST and TS in Fig.3.18. In Fig. 3.19 (d) the nominal stress drop at the very end of the shear load is not predicted correctly. This can be explained by the fact that some damage development may occur in the experiment at high strains which is not accounted for in the simulation.

On the other hand, a good agreement between predictions and experiments is obtained as well for 2198T8R in Fig.3.19 except 2.4% maximum stress over-prediction in micro TO compared to the average experimental data. Consider that the model is identified using macro tension tests (UT and NT2), experimental result of micro TO can be effected by specimen size. It is believed that the mechanical fields predicted by the 3D FE simulation can be used to interpret future *in situ* testing results in terms of strain, stresses and, in particular, stress triaxiality.

4 Discussion

4.1 Suitability of the plasticity model for load path change

The constitutive model with Bron-Besson anisotropic yield condition succeeded in predicting the mechanical behaviours of two alloys for non-proportional load path change tests. In this model, flow stress only contains the isotropic hardening part not kinematic

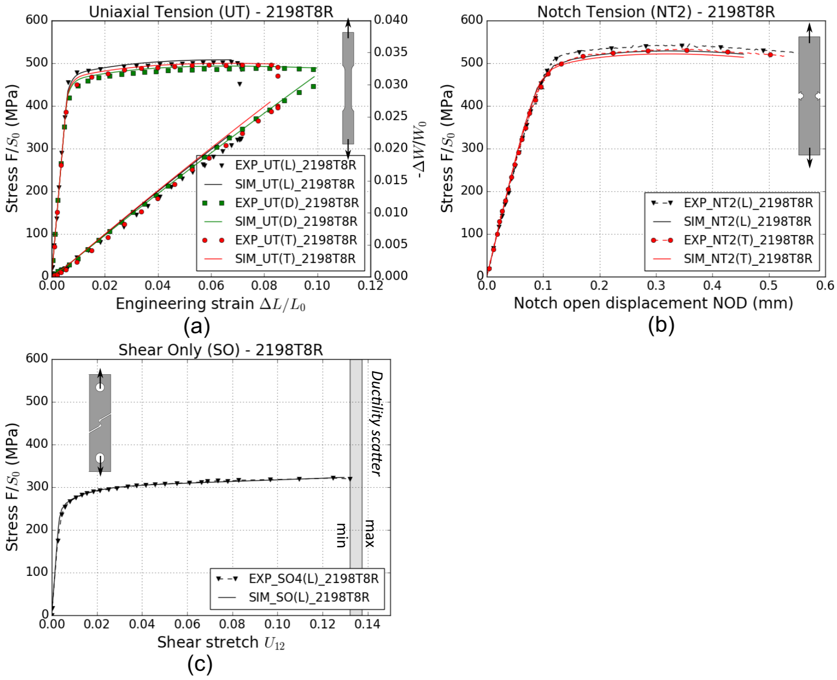

Figure 3.17: 2198T8R calibrated FE simulation results (full line) with experimental groups: (a) uniaxial-tension (UT), (b) notched-tension (NT2) and (c) shear-only (SO).

part although Deschamps et al. (2013) found a Bauschinger tests (tension – compression) for a similar alloy provided as a 6 mm thick sheet. In the present work, shear and tension loadings do not reach the compression yielding point. In addition, the data base lacks compression data to optimize since buckling often occurs for thin sheet specimen under compression. Due to the lack of compression data and the fact that at the chosen strain levels no Bauschinger effect was seen, the present model identification is considered as suitable to predict mechanical fields during the load path changes that can then be used to interpret the strain and damage seen in *in situ* laminography tests (Kong et al., 2022a).

4.2 Load path change effect on ductility

Compared to proportional loading tension-only (TO) loading, an obvious reduction on ductility is found for non-proportional ‘shear to tension’ (ST) for both materials. The average stretch to fracture of non-proportional ST reduced 29% and 16% for the alloy in T3R and T8R condition respectively compared to the proportional TO test result. Brünig et al. (2021) also found 33% displacement reduction from experimental results between tension-only and shear (45% failure displacement of shear only)-followed-by-tension based on an H-shaped cross sample in aluminum alloy 6082T6. These reductions suggest that pre-shear loading might nucleate damage before tension, which can be

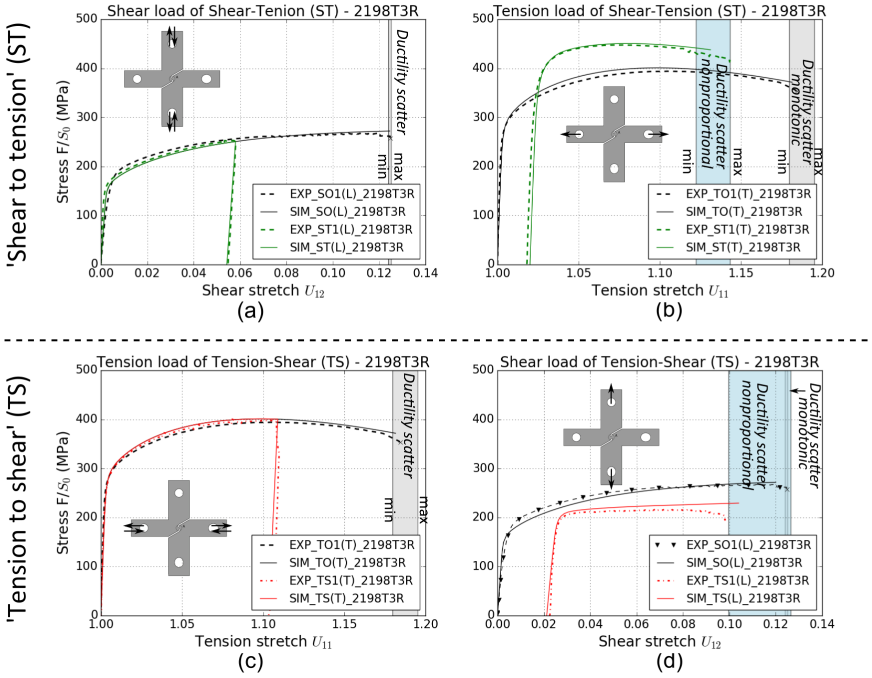

Figure 3.18: 2198T3R optimised FE prediction results (full line) with experimental groups: (a) shear period and (b) tension period of 'shear to tension' (ST) loadings, (c) tension period and (d) shear period of 'tension to shear' (TS) loadings.

identified in *in situ* experiments (Kong et al., 2022a). In addition, pre-shear loadings harden the material and lead to a higher yield stress, which also could be the cause of ductility reduction if brittle damage nucleation processes are at play (Petit et al., 2019).

On the other hand, for two loadings that end with shear: shear-only (SO) and 'tension to shear' (TS), the reduction varies from 0% to 20% strongly as a function of the extent of pre-tension loading. Two TS tests (TS2, TS3) were chosen to discuss here: TS2 and TS3 were loaded in tension till different levels of tension stretch: $U_{11}^{TS2} = 1.05$ and $U_{11}^{TS3} = 1.06$, see Fig.3.8 (c), and then they were loaded in shear till failure at $U_{12}^{TS2} = 0.126$ and $U_{12}^{TS3} = 0.109$ in Fig.3.8 (d). The stress level of TS is lower than that of proportional SO because of the thickness reduction during the pre-tension period. The local accumulated equivalent strain fields on pre-tension end of both tests are shown in Fig.3.20 (a)(d). The highly strained region of test TS3, that was more loaded in pre-tension than TS2, is larger than that of TS2. It means that the higher pre-loading in tension resulted in more detrimental effect on stretch to fracture. The strain fields show two shear bands with different width at (b) shear end before fracture in Fig.3.20. The maximum strain level reached 0.80 on surface of TS2, whose values (both shear stretch and local strain level) are close to proportional shear-only (SO) test. On the other hand, the test with higher pre-load (TS3) generated a wider shear band with lower maximum strain around 0.60 on specimen surface. It is suspected that strain is less localized but

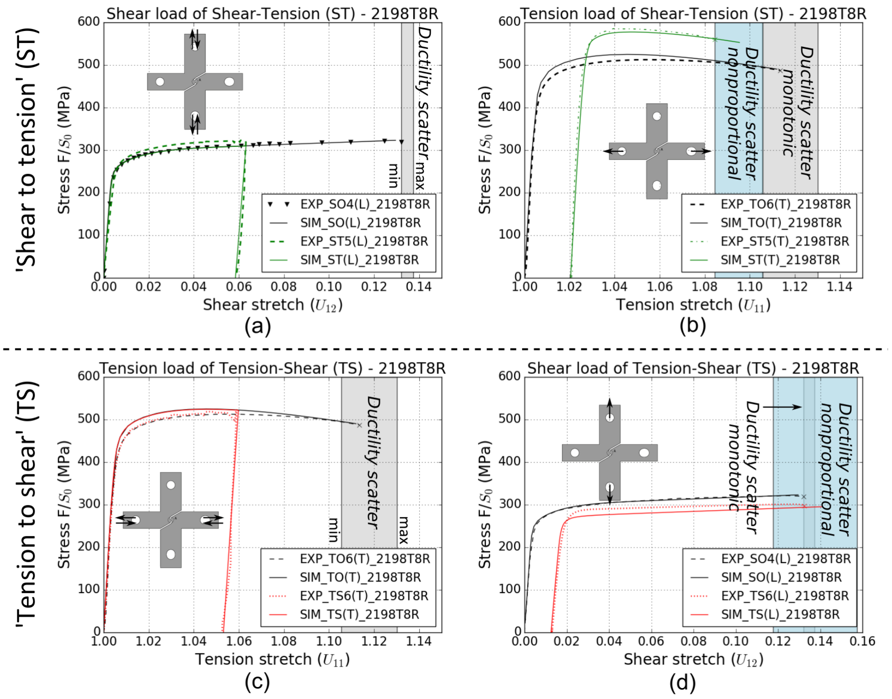

Figure 3.19: 2198T8R optimized FE prediction results (full line) with experimental groups: (a) shear period and (b) tension period of 'shear to tension' (ST) loadings, (c) tension period and (d) shear period of 'tension to shear' (TS) loadings.

more widely distributed in shear band due to the deformed geometry of two notches. In pre-tension load in Fig.3.8 (c), the TS2 was loaded to the maximum stress while the TS3 was loaded after maximum stress point. The force drop in the latter TS3 is likely to be linked to the necking effect. Brünig et al. (2021) found a strong scatter as well (from 0% to 47%) for 'tension to shear' load path change experiments using a H-shaped cross sample. This ductility reduction sensitively relies on the applied pre-tension extent and the subsequent local thickness reduction effect.

4.3 Specimen size effect

In this study, the model with optimized parameters using the macro-test dataset succeeded in predicting the experimental results of micro 1 mm thickness samples except micro TO of 2198T8R with 2.4% maximal stress over-prediction. In order to discuss this conclusion, a 2× magnified tension-only (TO) specimen with 2 mm thickness was manufactured and tested. The stress level of macro TO specimen coincided with the numerical prediction shown in Fig.3.21. The numerical simulations give a same stress – stretch curves for both dimensions. The slight stress drop could be explained by the limited number of grains in the ligament or by lower hardness in the middle plane for micro TO sample. On the other hand, the strain to fracture of macro TO was well

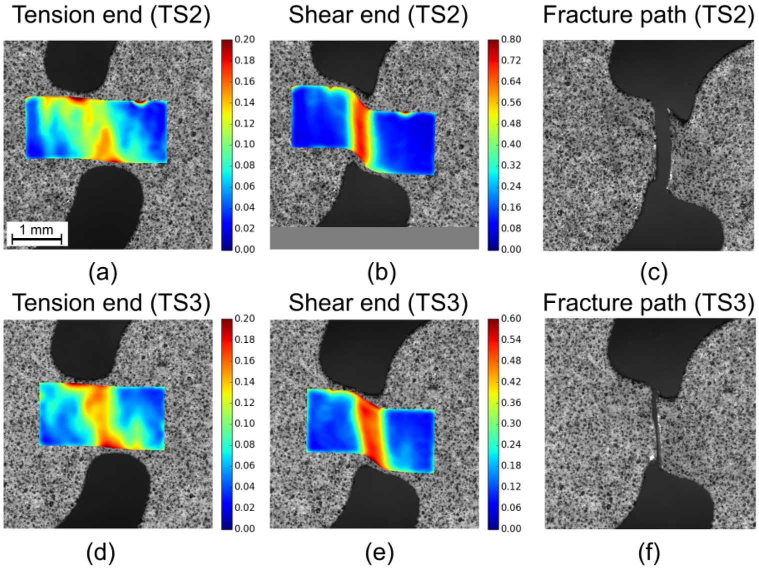

Figure 3.20: 2198T3R accumulated equivalent strain fields of (a)(d) tension end and (b)(e) shear end periods from two tension-followed-by-tension (TS) tests TS2, TS3 and their (c)(f) fracture paths.

within the range of micro TO ductility scatter. The identification is proved to be specimen size independent. Gorji et al. (2021) compared specimens with a size ratio of 20:1 with thickness 2 mm and 100 µm, and they found that the plasticity obtained from micro experiments matched those obtained from conventional macro experiments whereas the ductility was slightly reduced in micro experiments. They declared the differences are small within the range of uncertainty and concluded that the model identified on micro-experiments validates the results of conventional macro-experiments.

5 Conclusion

The microstructure of the material was characterized in terms of grain size, texture and particle as well as void volume fraction.

Concerning the **mechanical testing** of the material in T3 and T8 heat treatment conditions, the following conclusions can be drawn:

- Uniaxial tensile tests were performed on the full thickness (2 mm) samples in L, T and diagonal directions and in L and T directions for notched tensile samples.
- The material in both heat treatment conditions showed a moderate anisotropy, particularly in the width reduction during tensile testing.
- A small 1 mm thick cross shaped sample was designed to be able to perform ‘shear to tension’ or ‘tension to shear’ load path changes in a 3D *in situ* imaging environ-

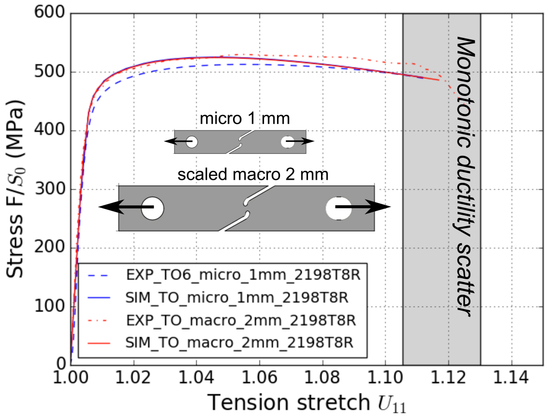

Figure 3.21: The nominal stress - tension stretch curves of tension-only (TO) specimens with scaled macro 2 mm thickness and micro 1 mm thickness.

ment for another study (Kong et al., 2022a). The loading was first performed in one direction followed by unloading and rotation of the sample by 90° and reloading up to fracture.

- A four point optical extensometer based on DIC was defined to measure stretch in tension and shear. The aim was to be unaffected of any rigid body rotations and to synchronize the experiment with 3D finite element simulations.
- Shear, tension as well as 'shear to tension' and 'tension to shear' experiments were carried out using the small samples.
- As expected, the yield strength of the T8 condition was about twice the one of the T3 condition. The ductility during tensile testing and notched tensile testing was about half for the T8 condition compared to the T3 condition. Interestingly, the shear-stretch to fracture measured during shear experiments was very similar for both materials.
- The 'shear to tension' load path change led to a reduction of tension stretch at fracture of 29% and 16% for T3 and T8 respectively.
- The 'tension to shear' load path change did not lead to a significant reduction in shear stretch to fracture but increased substantially the scatter in shear stretch to fracture for both heat treatment conditions.
- The fracture plane of the 'shear to tension' load path change sample was slant though the sample thickness and the crack was straight in the sample plane, indicating the pre-shear affected the failure mode as it was different from the one of the TO sample.

- Fractography revealed micrometre sized dimples for the tension loading, grain related flat zones and very small shear dimples linked to dispersoid particles under shear loading.

Concerning the **simulations** using the anisotropic finite element model and isotropic hardening, the conclusions are:

- The model was fitted using data obtained on the uniaxial tensile and notched tensile samples loaded in different directions as well as the small shear sample. A good fit is obtained in terms of stress train curves as well as in terms of width strains for the uniaxial tension samples.
- The load path changes are predicted using the model with identified parameters. A good prediction of the stress-stretch curves was achieved and it is assumed that the predicted mechanical fields give a good estimate of the reality.

The damage development during load path changes should be investigated in more detail by 3D imaging to identify the role of damage on ductility reduction during the load path changes (Kong et al., 2022a).

Acknowlegements

ANR (Lambda project:ANR17-CE08-0051 and Alicandte project) is gratefully acknowledged for its financial support. The European Synchrotron Radiation Facility (ESRF) beamline ID19 is thanked for providing beamtime (experiment ma4333). We thank Constellium for materials supply.

Part I

Proportional Shear Loading Path: Multiscale Observations

Chapter 4

Ductile damage study under shear via *in situ* micro-laminography and *ex situ* nano-laminography observations

The aim of this chapter is to investigate the shear damage mechanisms using a thin sheet shear sample, a so called *smiley* sample (Roth and Mohr, 2016). 3D synchrotron laminographic *in situ* and nano-laminography *ex situ* experiments were conducted respectively for a test till fracture and an interrupted test. The 3D *in situ* experiment had been performed and partly analyzed in the thesis of Buljac (2017). In order to assess further strain and damage, the strain was measured inside material using projected 3D data and 3D damage was quantified as surface void fraction in this chapter. Besides these 3D observations, with help of correlative 2D techniques (SEM and EBSD), the location of the damage features with respect to the grain microstructure were identified for the interrupted test.

This chapter is under preparation for a potential paper (Kong et al., 2022b).

Abstract

An *in situ* synchrotron laminographic experiment was performed on a thin sheet *smiley* sample that causes simple shear stress states in the two ligaments. One of the ligaments was imaged at nine load increments till fracture. The results had been partly analyzed in the thesis of Buljac (2017). The scanned volumes were post-processed further in the present thesis. The shear damage evolution was visualized in 3D. Two main damage features, flat cracks and particle cracks, were found and followed under shear loading at the microscale. In order to observe these features at higher resolution and to understand damage nucleation, a second *smiley* sample β was loaded till 85% of the failure displacement and then unloaded. One ligament of the deformed sample β was scanned using *ex situ* nano-laminography at resolution down to voxel sizes of 50 nm. The other ligament of the specimen β was observed via SEM and EBSD, which revealed that the flat cracks were both intergranular and transgranular.

1 Introduction

Over last half century, hydrostatic stress and equivalent strain have been regarded as the key driving forces for the fracture of ductile metals (McClintock, 1968; Rice and Tracey, 1969). The complex relationship between fracture strain and stress triaxiality has been found experimentally by different researchers since 21st century (Bao and Wierzbicki, 2004; Barsoum and Faleskog, 2007a; Papasidero et al., 2015; Roth and Mohr, 2016). In order to achieve more stress states in a wider range of stress triaxiality, two approaches are suggested: whether choose dedicated specimen geometries or apply combined loadings (e.g. tension and torsion) on the boundaries of single specimen. For the former approach, Bao and Wierzbicki (2004) conducted experiments for a wide of stress triaxiality by using different specimen geometries on 2024-T351 aluminum alloy. Roth and Mohr (2016, 2018) carried out experiments with various specimen geometries from pure shear, uniaxial tension, plane strain tension to equi-biaxial tension on ductile metals. Secondly, Barsoum and Faleskog (2007a) and Papasidero et al. (2015) performed a series of tension-torsion experiments with applying a combined tension-shear load ratio on a double notched tube specimen. A *butterfly* specimen was under combined shear-tension with different loading angles to investigate the onset of fracture from low to intermediate stress triaxiality (Dunand and Mohr, 2011; Mae et al., 2008; Mohr and Henn, 2007). They all gave a complex and empirical relationship between fracture strain and stress triaxiality. Various trends were exhibited at low stress triaxiality (i.e. below 0.4). Moreover, the fracture strain is an ambiguous definition for different experiments and difficult to measure especially in the highly deformed regions. The physical mechanism of deformation and damage leading to these curves are still unknown.

At the absence of high stress triaxiality, the classic Gurson model (Gurson, 1977) failed to predict shear failure. Nahshon and Hutchinson (2008) proposed a modification of the Gurson model to account for softening under shear assuming the initial porosity. The simulations using micromechanical unit cell with pre-existing cylindrical void have been performed to study shear ductile failure (Nielsen et al., 2012; Nielsen and Tvergaard, 2011; Tvergaard, 2008, 2009), and they found the void closure leading to micro-cracks that rotate in the shear field, instead of void growth to coalescence. Torki and Benzerga (2018) captured the features of sub-cell with initial porosity during shear deformation: a. void-induced strain localization; b. void rotation and shape change; c. coalescence. (Tancogne-Dejean et al., 2021) modeled RVE simulation with rigid particles and found that particle failure is always normal to the direction of maximal principal stress under shear loading.

Ductile fracture at high stress triaxiality (i.e. above 1) has been widely studied and the governing damage mechanisms have been identified as a void nucleation-growth-coalesence (Pineau et al., 2016). However, the mechanism at lower stress triaxiality are less clear. Recently, more researches have focused on the lower stress triaxiality range (i.e. below 0.4) since hydrostatic stress is missing under shear-dominated experiments for void growth. Achouri et al. (2013) performed a shear experiment via *in situ* scanning electron microscope (SEM) on the High-Strength Low-Alloy steel (HSLA). They observed the voids nucleated from the fragmentation and/or the inclusion-matrix debonding, subsequently elongated and rotated in the shearing direction till the onset of coalescence Papasidero et al. (2014) investigated the ductile fracture mechanisms through direct monitoring of surface damage during *in situ* SEM torsion tests on notched tubular specimens for 2024T3 aluminum alloy. The damage initiated at particles on surface was observed at the strain localization region from meso-scale, micro-scale to sub-grain scale under pure shear state. Gross and Ravi-Chandar (2016) investigated deformation and failure under shear loading via *in situ* SEM on a sheet specimen of 6061T6 aluminum alloy. They found that second phase particles broke, debonded or rotated. No severe damage and/or failure were found on the highly deformed surface region of nearly zero triaxiality even the local strain was elevated to 1. A specimen geometry so called *smiley* designed for shear loading has been optimized in geometric dimensions of two notches especially for several ductile sheet metals including the target material aluminum alloy 2198 T8 in this chapter and other steels DP780, DP590 and titanium alloy Ti6Al4V under shear loading (Roth and Mohr, 2016).

Recently, with advanced 3D technique X-ray synchrotron imaging, 3D *in situ* non-destructive observation becomes feasible (Helfen et al., 2005; Villanova et al., 2017). Similar as synchrotron radiation computed tomography (SRCT) but using a rotation axis tilted by less than 90 degrees with respect to X-ray, synchrotron radiation computed laminograpy (SRCL) aims at scanning regions of interest in flat specimens in particular (Helfen et al., 2005, 2012; Xu et al., 2012a). Many experiments on thin specimens have been performed under beamline (Buljac, 2017; Morgeneyer et al., 2014; Roth et al., 2018; Tancogne-Dejean et al., 2021), where Roth et al. (2018); Tancogne-Dejean et al. (2021) investigated the shear damage mechanism using *smiley* sample under micrometer resolution. In order to observe damage nucleation at higher magnification, based on the propagation based imaging (also called in-line holography), scanning fluorescence laminography offers the 3D imaging with pixel size ranged from 50 nm to 500 nm according to various focus-specimen distances (Helfen et al., 2009; Xu et al., 2012b).

The aim of the chapter is to study the ductile damage mechanism under proportional shear loading. In this chapter, a geometry designed for shear loading is applied under 3D X-ray synchrotron laminography. One fractured sample and one damaged sample were imaged in 3D using *in situ* micro-laminography and *ex situ* nano-laminography respectively. Strain field on middle-thickness plane was obtained from 2D image correlation of the projected 3D data and the shear damage evolution was quantified as surface void fraction. 2D observations on two samples such as scan electron microscopy (SEM) and electron back-scatter diffraction (EBSD) were chosen to study shear damage features. Two main damage features, flat crack and particle crack, were visualized and analyzed according to their initiations and progression. Finally, the shear damage mechanism was discussed from microscale down to nanoscale.

2 Methods

2.1 Specimen geometry

A thin sheet geometry of 1 mm thick so called *smiley* geometry from Roth and Mohr (2016) designed for shear loading, where a global tensile loading generates a local shear stress state in two ligaments with dimensions of 1.2×1.5×1 mm^3 in 4.1 (b). The dimensions such as offset of, notch shape have been optimized in particular for the AA2198-T8R (Roth and Mohr, 2016). The sample was manufactured from the 2 mm thick rolled sheet and the detailed dimensions were presented in the previous chapter.

Two samples are included in this chapter: the sample α was loaded *in situ* till fracture and the second sample β was deformed and unloaded so that the ligaments contained some damage. The loading history curve in terms of nominal stress and global displacement is given in 4.1 (a) for both samples in black (fractured α) and blue (deformed β) respectively.

2.2 3D X-ray synchrotron laminography

The advanced technology 3D X-ray Synchrotron Radiation Computed Laminography (SRCL), similar as Synchrotron Radiation Computed Tomography (SRCT), aims to image the regions of interest in flat samples in particular in three dimensions (Helfen et al., 2005).

An *in situ* micro-laminographic experiment was carried out on beamline ID19 at the European Synchrotron Radiation Facility (ESRF). Sample α was loaded on the same loading frame as in (Buljac, 2017; Roth et al., 2018). The volume at the region of interest was scanned at each red point in Fig.4.1 (a) during loading till fracture. At each scan, the sample was rotated around the laminographic table axis at an angle of $\theta \approx 65°$ with respect to the stationary X-ray beam axis. The 3D image was reconstructed by using a filter-back projection algorithm (Myagotin et al., 2013). Every 3D image has a dimension of 2560×2560×2300 voxels, which is physically equivalent as 1.6×1.6×1.5 mm^3 at the voxel size of 0.65 µm. It is noted as micro resolution (µR) in this chapter shown in Fig.4.1 (b).

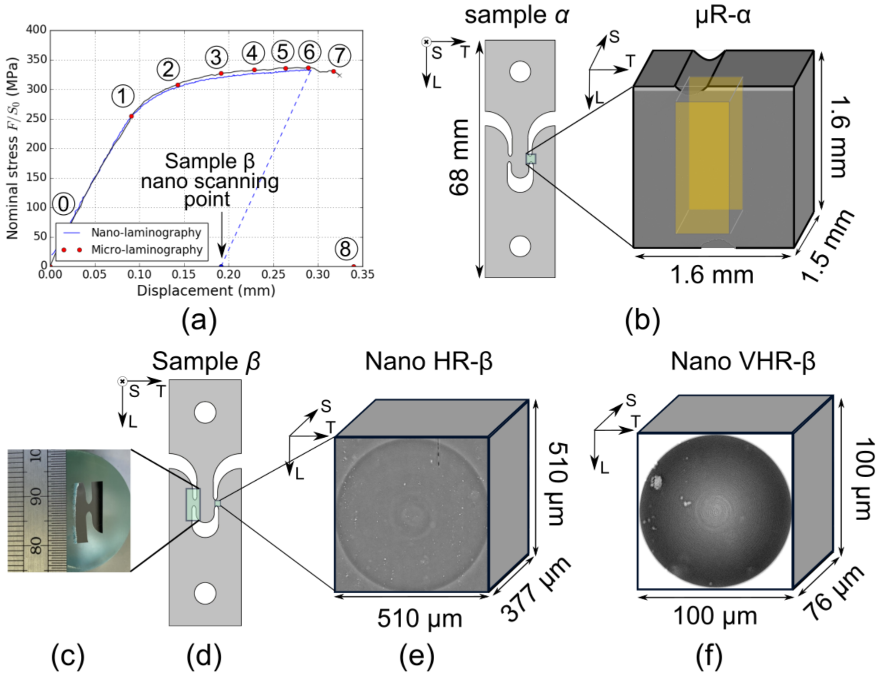

Figure 4.1: (a) Load history curve in terms of nominal stress versus displacement. (b) One ligament of the sample α was scanned at micro resolution (μR) as 1.6×1.6×1.5 mm^3 using *in situ* micro-laminography. (c) The region of one ligament was cut from (d) the deformed sample β for 2D observations. Another ligament was scanned at higher nanometer resolutions and two volumes of 2160×2160×1600 voxels were: (e) 510×510×377 μm^3 as high resolution (HR) with the voxel size of 236 nm and (f) 100×100×76 μm^3 as very high resolution (VHR) with the voxel size of 48 nm.

In order to scan higher resolution at nanoscale, another sample β was loaded till 85% failure displacement and then unloaded as seen in blue curve of the loading history in Fig.4.1 (a). One ligament of the deformed sample was cut and imaged at beamline ID16b (ESRF) using *ex situ* nano-laminography technique (Xu et al., 2012b) with voxel sizes as 236 nm and 48 nm. They are noted as high resolution (HR) and very high resolution (VHR) respectively. The final reconstructed volume has a dimension of 2160×2160×1600 voxels. Two scanned regions are equivalent as 510×510×377 μm^3 for HR in (e) and 100×100×76 μm^3 for VHR in (f).

Three features including aluminum matrix in grey, copper rich intermetallic particles in white and void in black are in the laminography. The features were segmented with a region growing algorithm from C++ based efficient python package SMIL (Faessel and Bilodeau, 2013). Damage such as void, porosity is visualized in blue and intermetallic particles in grey in the following 3D visualizations.

2.3 Projection digital image correlation (P-DIC)

Seen the low particle volume fraction in this material AA2198T8R and the highly localized strain fields, it was difficult to correlate volumes by digital volume correlation with the limited contrast in 3D data. The natural markers such as particles are not sufficient for correlation in every single slice of laminographic 3D volume data. Thus, a technique called projection DIC has been applied here as described in (Buljac et al., 2018b; Kong et al., 2022a; Morgeneyer et al., 2021; Roth et al., 2018; Tancogne-Dejean et al., 2021). The image contrast was projected along the thickness direction into one image so that the projected image has an sufficient density of natural markers for correlation. The cropped volume of 1000×1500×200 voxels were in the region of interest near the sample central plane. The contrast of white intermetallic particles contained in a 200 pixel (130 µm) thick was projected on a 2D plane along the thickness direction. The projected images at different steps could be correlated to obtain the in-plane components of displacement and strain fields. The results were only meaningful based on the plane strain assumption, i.e. that strain component along thickness direction is negligible. Compared to digital volume correlation, this technique is more robust and less time consuming. Compared to classical 2D surface image correlation, the projected technique benefits from obtaining the information inside the material bulk. Based on the commercial software $vic2D - 6$ (Correlated Solutions), the displacement field was measured with subset size and step size were set as 95 pixels (61.8 µm) and 3 pixels (2.0 µm). The strain (Hencky) field was obtained with filter size of 15.

The logarithmic strain (Hencky strain or true strain) provides the appropriate measurement especially for large simple shear strain (Onaka, 2010, 2012). Abedini et al. (2018) defined the work-conjugate equivalent strain in terms of the adopted constitutive model. The difference between the work-conjugate strain and the equivalent strain is negligible when strain is less than 0.8 (Butcher and Abedini, 2017). The equivalent strain is defined as:

$$\varepsilon_{eq} = \int \sqrt{\frac{2}{3} d\boldsymbol{\varepsilon} : d\boldsymbol{\varepsilon}} \tag{4.1}$$

However, the information in thickness direction lacks in the 2D image correlation. The third component ε_{III} is computed from plastic incompressibility assumption $\varepsilon_I + \varepsilon_{II} + \varepsilon_{III} = 1$, where ε_I, ε_{II}, ε_{III} denote the logarithmic principal strains. Hence, the 2D equivalent strain ε_{eq}^{2d} is defined as:

$$\varepsilon_{eq}^{2d} = \frac{2}{\sqrt{3}} \sqrt{\varepsilon_I^2 + \varepsilon_{II}^2 + \varepsilon_I \varepsilon_{II}} \tag{4.2}$$

2.4 2D analyses via Scan Electron Microscopes (SEM) and Electron Back-Scatter Diffraction (EBSD)

The fractography of specimen α was observed via scanning electron microscopy (SEM) in ZEISS Sigma 300 with the detector of secondary electron. The post mortem surface is observed on the LS plane down to sub-micrometer scale.

The planar features on surface of the deformed specimen β was observed in FEI Nova nanosem 450FEG. Micrographs of grain structure were obtained from electron back-scatter diffraction (EBSD) analysis with the camera (EDAX-TSL Hikari) using a step size of 0.5 micrometer and an acceleration voltage of 15 kV. A grain boundary is considered when the misorientation angle between the two grains affected is at least to 15°.

The surface was polished incrementally and thereby in a destructive way till damage features appeared. Considering to the dimension of damage features which was measured as less than 20 µm in the 3D imaging and not to remove them, 10 µm thick was removed at each polishing step. The surface was polished gradually using 7 µm down to 3 µm, 1 µm polishing paste.

3 Results

Nine volumes of *in situ* micro-laminography (µR) allow the damage evolution during shear loading to be studied till fracture of the sample α. Two volumes of *ex situ* nano-laminography exhibit damage features of the deformed sample β at high resolution (HR) and very high resolution (VHR). The damage features from another ligament of the sample β were studied in a correlative way via 2D observations by SEM and EBSD.

3.1 *In situ* results at micro resolution (µR)

The damage evolution in the selected sub-volume shown in yellow in Fig.4.1 (b) is presented in Fig.4.2 and 4.3 including (a) normal view (LT plane) and (b) side view (LS plane). The sub-volume is cropped to a size of 1000×2400×1000 voxels equivalent as 650×1560×650 μm^3.

Note that the blue area stands for the features with low gray values. Besides, two notches are included at the top/bottom borders in some steps (i.e. 0, 1, 2, 5, 6 and 7). Initially, there is hardly any obvious pre-existing porosity in this material at step 0 before loading. With loading, the nucleated damage was first captured in red circle at step 3 in the early plastic domain. Subsequently, more void nucleation appeared through the entire thickness from step 4. It continued to grow along the shear direction in L and coalesce to long flat cracks up to 100 µm in the following steps. In the meanwhile, most damage was located in the shear band region between the two notches from the normal view. At the last step 7 before fracture, the coalesced damage linked to each other in the thickness direction, which led to a macro crack path. It is noted that the damage mainly nucleated on the ligament instead of notches since the specimen geometry (e.g. offset of notches) has been optimized particularly for the AA2198-T8R (Roth and Mohr, 2016).

The corresponding 2D section of the initial damage nucleation at the plane (around 84 µm from the middle thickness plane) was addressed in Fig.4.4 (a) in support of white arrows. The flat cracks continuously grew from loading step 4 and they coalesced to a long flat crack up to 135 µm at the final step 7 before fracture. It is also concluded that

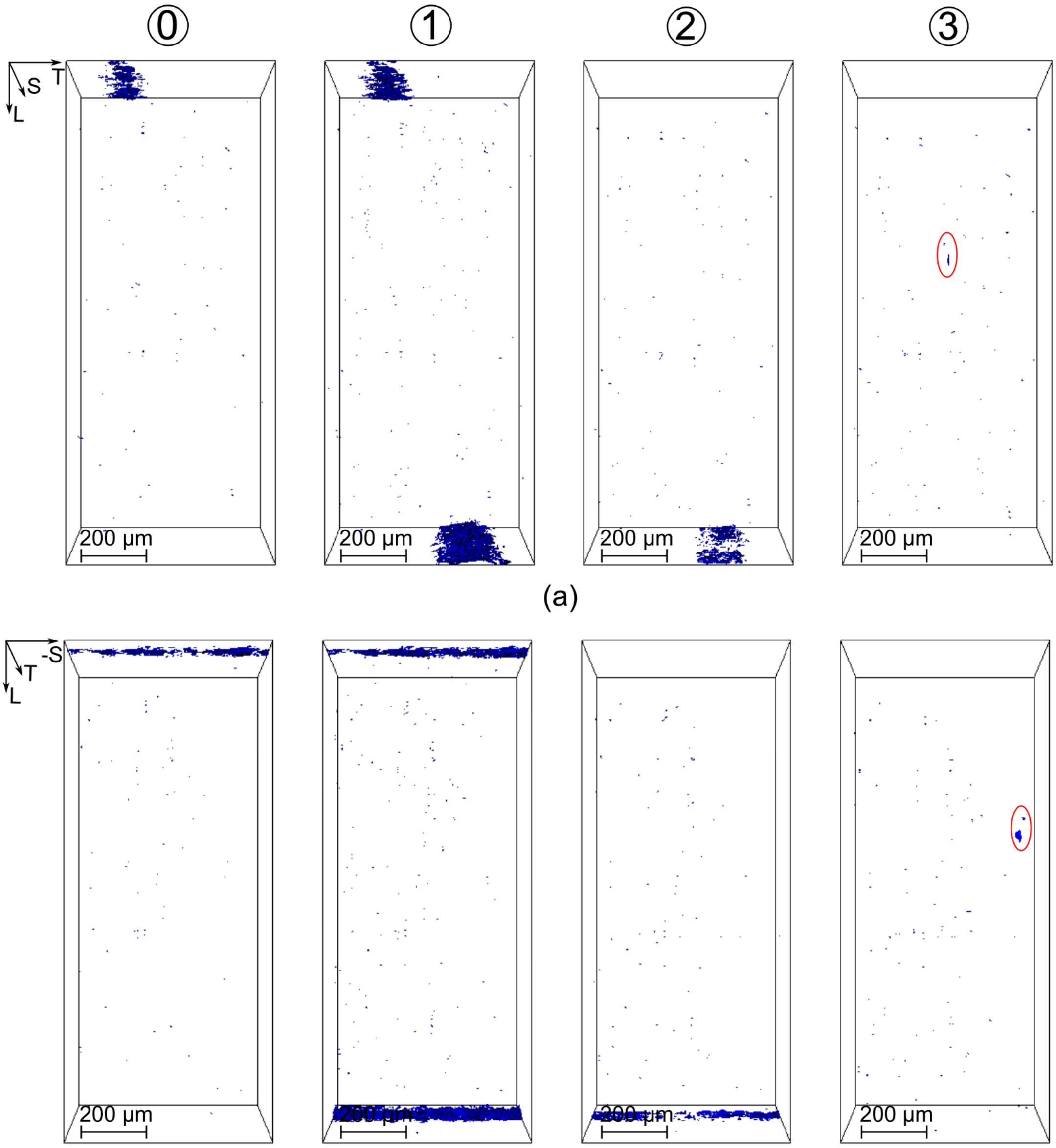

(a)

(b)

Figure 4.2: 3D views of damage in the ROI (650×1560×650 µm^3) in yellow in Fig.4.1 (b) at loading steps 0 - 3 from (a) normal view and (b) side view.

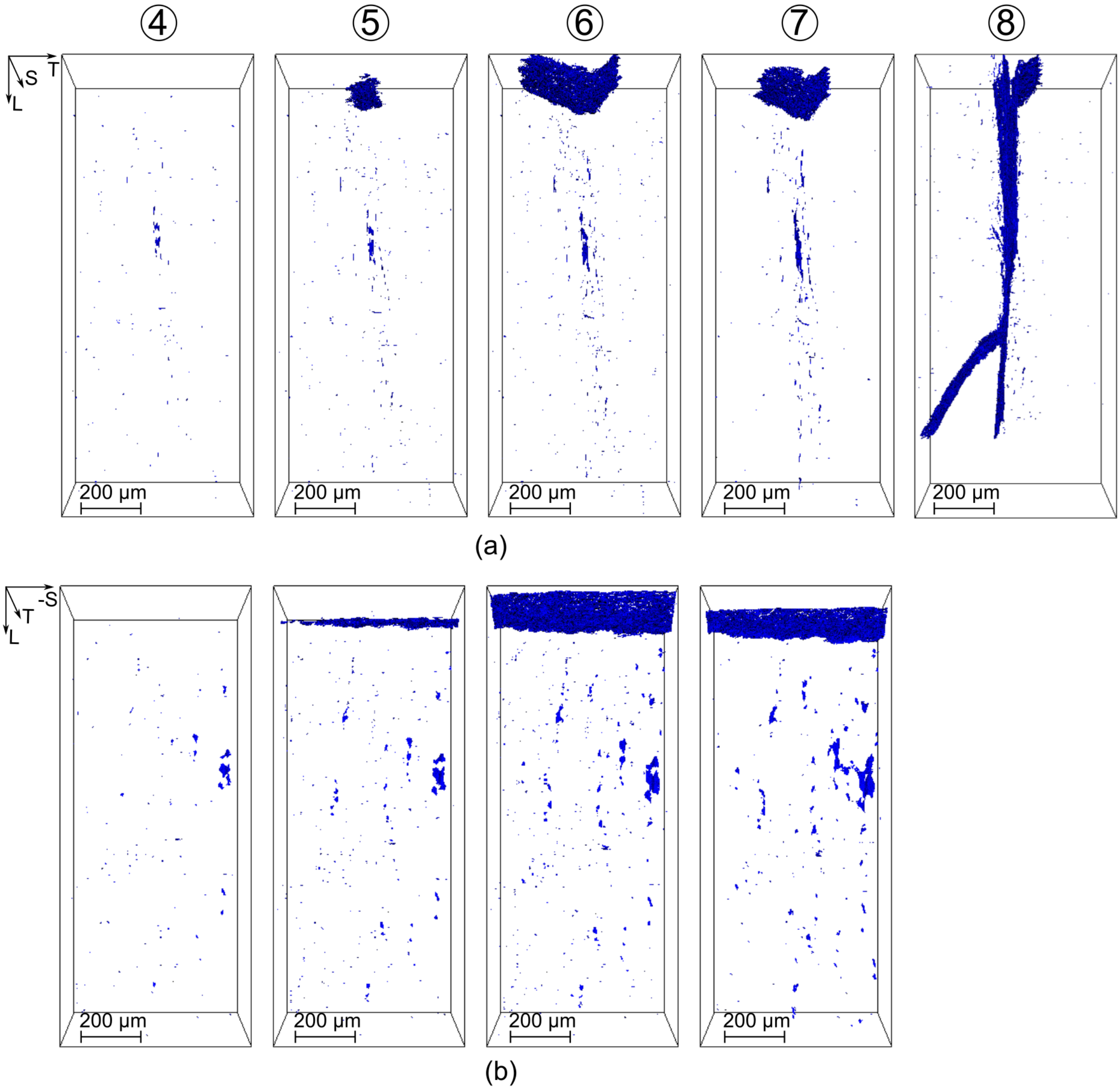

Figure 4.3: 3D views of damage in the ROI (650×1560×650 µm^3) in yellow in Fig.4.1 (b) at loading steps 4 - 7 from (a) normal view and (b) side view.

the flat crack is detrimental leading to the final crack path from the 2D section at the step 8 of fractured state. Besides, it seems this flat crack is not related to any intermetallic particles. Remarkably, this shear-induced feature has never been seen before in the same sample geometry for other alloys (FB600 steel in Roth et al. (2018), AA2024T3 in Tancogne-Dejean et al. (2021)). Due to the limited resolution (µR), feature below micrometer size cannot be clearly observed to identify the nucleation mechanism and a higher magnification (HR, VHR) observation would be indispensable to find out.

Another damage feature is the particle crack. Three particles with the length around few tens µm were found and traced in Fig.4.4 (b)(c)(d). Particles rotated under shear loading till broke into several pieces. The evolution of the particle on the plane (2 µm from the mid-plane) is shown in Fig.4.4 (b). The particle started to decohere from the matrix at step 1 and was broken at step 4. The particle crack is around 45°, which is normal the principal stress (Tancogne-Dejean et al., 2021). The particle broke into two pieces and an elongated void was generated at step 7. It is also one of the main detrimental features leading to the macro crack path. Two more particle related cracks are shown in (c) and (d). The particle on the plane (160 µm in thick away from the mid-plane) seen in (c) around 20 µm length was broken at step 2 with one crack of 56°. However, more cracks appeared locally and the angle decreased to 38°. The particle observed from the plane (around 288 µm from the mid-plane) around 15 µm with a tiny void less than 5 µm length attached on the right-top was shown in (d). The micro particle split away from the large particle resulting in a tiny gap.

3.1.1 Projection DIC

Fig.4.5 shows the strain profile along a horizontal line (T) normal to the shear band for the 200 layers (130 µm) projection DIC results. The dashed line profile is chosen and shown in the strain field. Different colors represent different loading steps from 1 to 7. The maximum equivalent strain level increased up to 0.65 at the very last step 7 before fracture. The strain profile exhibits other two peaks nearly 80 µm next to the main one, which could be explained from a crystallographic effect (cf. grain size) considering its length. Compared to the DVC results in Buljac (2017), the results from projection DIC agree well on the maximum strain level and its distribution. The 2D projected results confirmed the feasibility of projection DIC with the assumption there is negligible displacement (strain) in projection direction. Briefly, projection DIC is far less time-consuming than DVC. This technique is allowed to have access to the information inside the material bulk compared to the classical surface DIC.

3.1.2 Damage quantification as volume void fraction and surface void fraction

The segmented damage evolution in the volume of 1000×2200×1000 voxels was quantified as volume void fraction. Fig.4.6 shows the profiles of volume void fraction divided by illustrated sub-volumes of 25×2200×1000 voxels from loading step 0 to 7, where damage localized from step 4 in the shear band region of 100 µm width and the peak grew

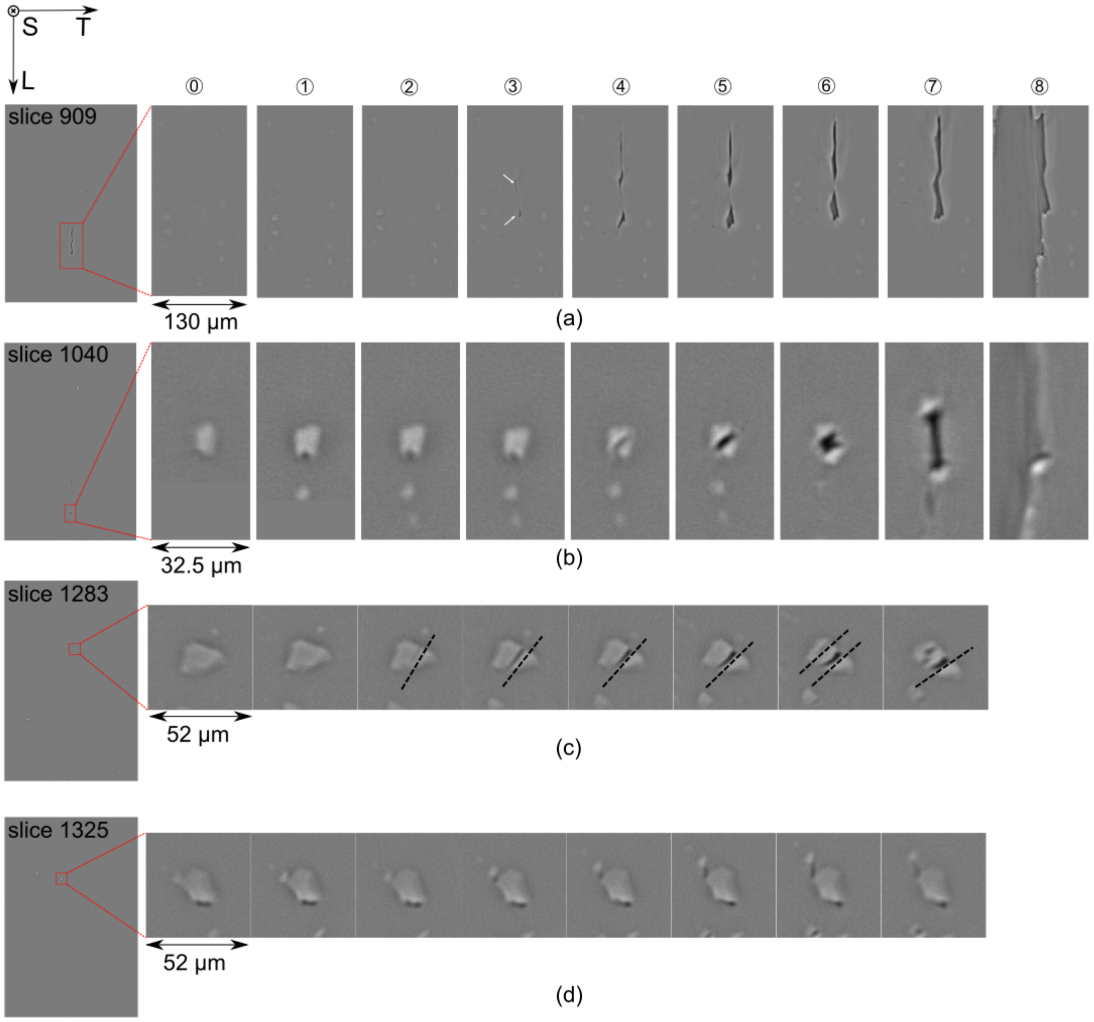

Figure 4.4: (a) Flat crack evolution on a 2D section of 200×400 texels (130×260 μm^2). Particle crack evolution on 2D sections of (b) 50×100 texels (32.5×65 μm^2), (c) 80×80 texels (52×52 μm^2) and (d) 80×80 texels (52×52 μm^2).

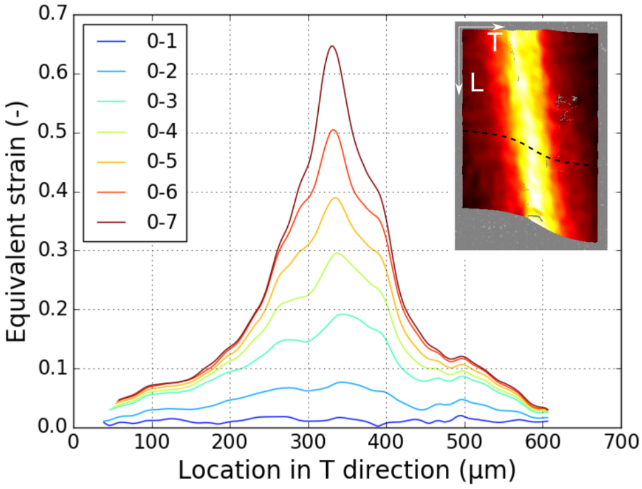

Figure 4.5: The equivalent strain profiles during shear loading from step 0 to step 7 along the horizontal line (T) from the projection DIC fields. The profile position is denoted as dashed line on the deformed strain field.

up to 0.20% at step 7 before fracture. The volume void fraction is still low because of the small width (around 10 µm) of the detrimental damage feature, flat crack. These shear cracks that contributed to the macro failure path shown in Fig.4.4 (a) covered the immense area of fracture surface. Therefore, a projected surface void fraction on the fracture surface is more accurate to quantify the shear damage.

Fig.4.7 (a) shows the raw volume data that was imaged by 3D X-ray synchrotron micro-laminography. In order to focus on the shear band region where damage distributed, a sub volume in yellow was selected as 200×1500×1000 voxels in (b). The damage features were projected along T axis (200 pixels = 130 µm) on the future fracture surface in green in (c) and the area was segmented into binary image in (d). The damage quantification is computed on the surface as surface void fraction because the detrimental flat cracks have a very low void volume fraction.

The damage evolution was quantified as surface void fraction versus equivalent strain from projection DIC profile shown in Fig.4.7 (e). Initially, the surface void fraction was less than 0.1%. It started to rise linearly with the increasing equivalent strain from step 3 till fracture up to 3%. Meanwhile, the maximum equivalent strain from T profile reached more than 0.60.

3.1.3 Fractography

Fig.4.8 exhibits the fractography of the sample α on LS plane from micrometer scale down to nano scale. A smooth trail of the flat crack around 80 µm length and 20 µm thick is found in (a). A particle of 6µm×2µm was elongated and broken into debris in (b). The sub-micro shear dimples are oriented normal to the loading direction (L as rolling

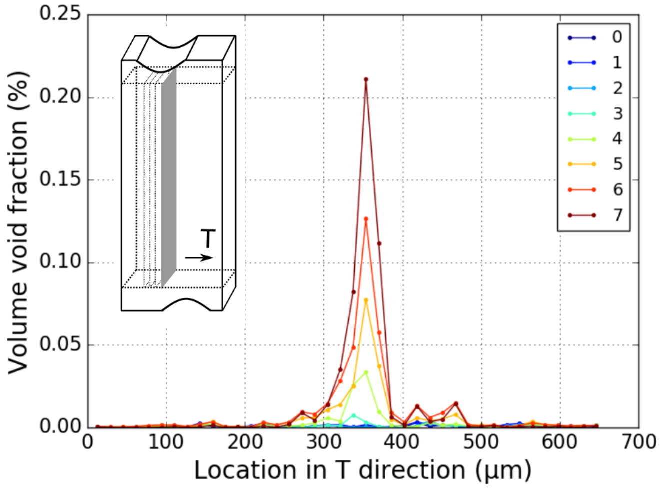

Figure 4.6: Damage quantification using volume void fraction profiles: measured by a sub-volume 25×2200×1000 voxels (equivalent 16.25×1430×650 µm^3) along T direction.

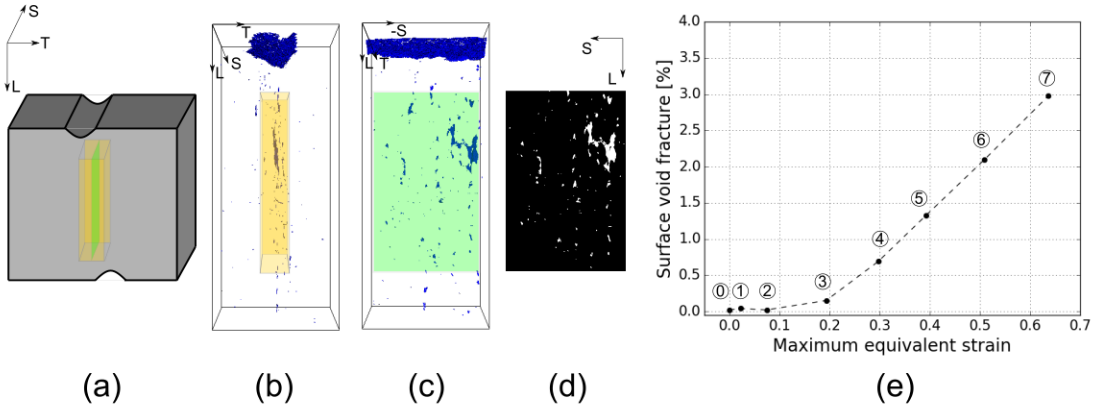

Figure 4.7: Damage quantification: (a) schematic representation of the selected ROI in yellow, (b) Most damage inside the yellow ROI was projected along T axis (130 µm) on the future fracture surface in green from the (c) side view on LS plane. (d) The projected 2D section was segmented where white stands for the damage, (e) The damage measurement as surface void fraction versus maximum equivalent strain curve at each scanning point.

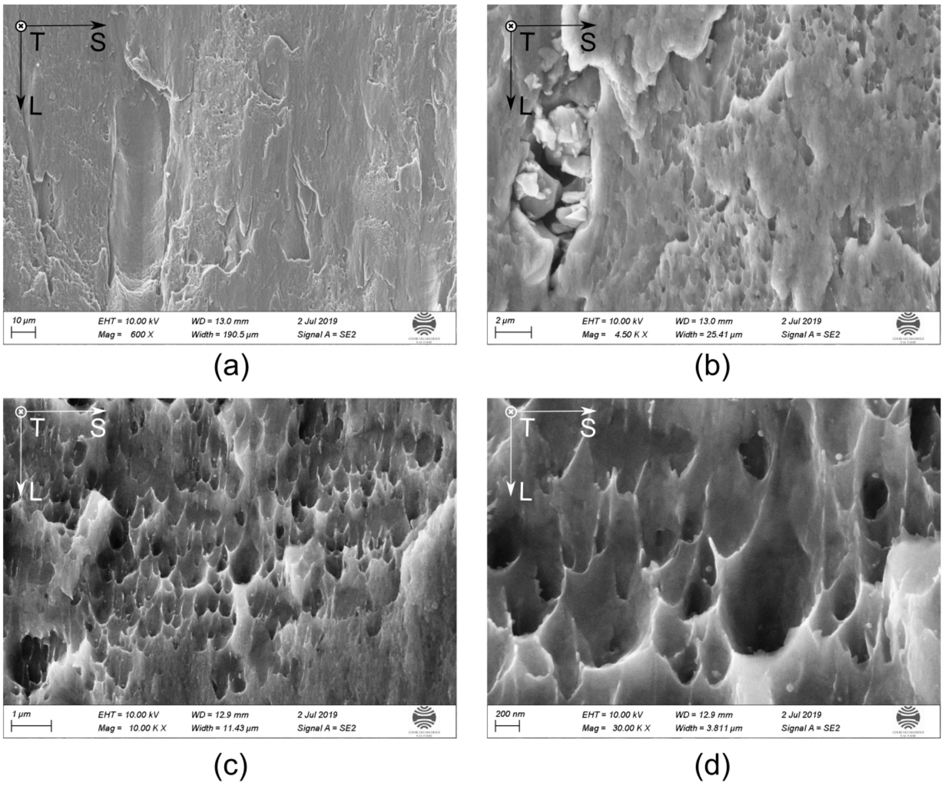

Figure 4.8: The fractography of Smiley sample α via SEM: (a) flat surface with (b) particle breaking and (c)(d) fracture dimples where dispersoids around tens nanometers are found.

direction) in (c) and (d). The disperoids down to some tens nanometer, supposedly Al_3Zr (Nayan et al., 2019), were seen in white and attached to the dimples. Their presence are probably linked to the origins of these ductile dimples.

3.2 Nano-laminography observations of shear damage in an *ex situ* sample

The microstructural features such as flat crack, particle crack including nano dispersoids were found in the micro resolution (µR) and fractography. They are likely to contribute to the final macro fracture under shear loading. However, there is no hydrostatic pressure to open the damage under shear loading. In order to study the origins of these damage features and their evolution on the nanoscale, a higher resolution scan (voxel size as 236 nm) is essential for sample β from the interrupted test. The 3D overview visualizations of the deformed sample β from high resolution (HR) nano-laminography on two 510×510×188 µm^3 volumes near the central plane are shown in Fig.4.9 (a)(b) and Fig.4.10 (a)(b), where void in blue and particles in grey. Two main damage features:

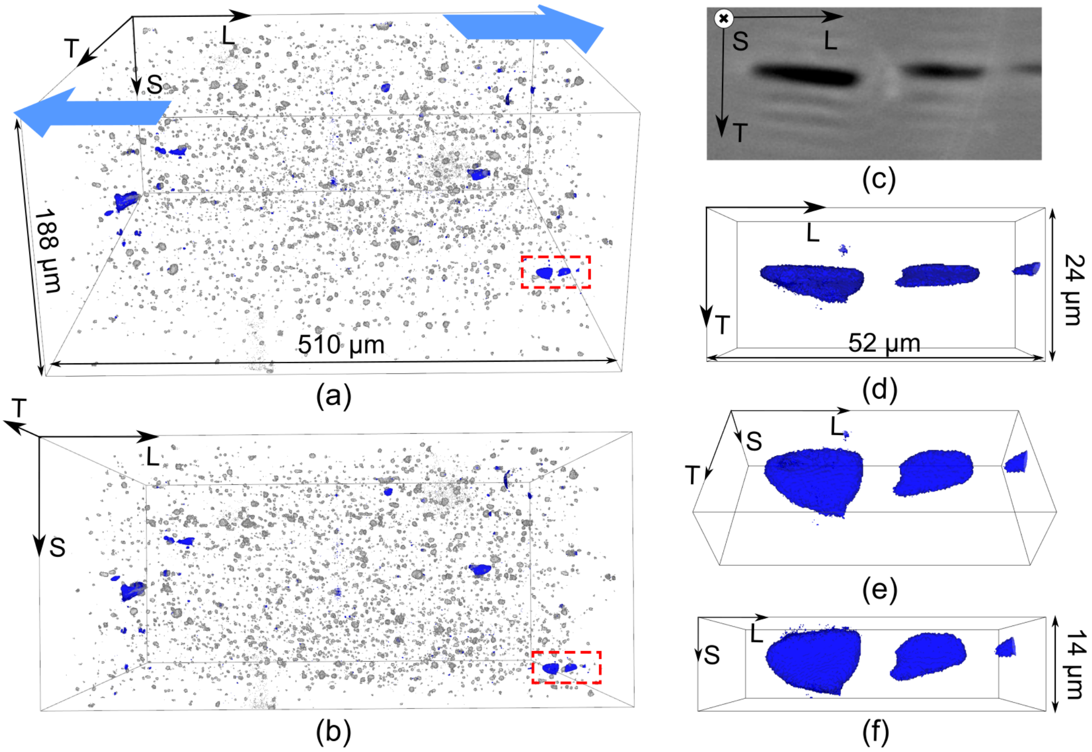

Figure 4.9: (a)(b) 3D overview visualization of the region where intermetallic particles are in grey and void in blue. (c) 2D section of a flat crack selected in red box of 52×24×14 µm^3 and its visualization from different views: (d) top view, (e) top-front view and (f) front view.

flat crack and particle crack, are both regarded as void in blue.

3.2.1 Flat crack observed at high resolution (HR)

In order to observe this detrimental damage feature, a flat crack was selected in the red box of 52×24×14 µm^3 in Fig.4.9 (a)(b). The 2D section of the crack is given in (c). The segmented crack is visualized in different 3D views to specific the damage mechanism in the deformed state. Three micro flat cracks with 15 µm length, 5 µm width and 10 µm thick were growing and coalescing to a larger flat crack up to 50 µm length. In addition, there is no particle around attached to the crack and it indicated the crack probably does not nucleate on the particle.

Another longer flat crack was chosen in Fig.4.10 (a)(b) in red frame. The sub volume of 130×47×14 µm^3 exhibits a coalesced flat crack feature at a later stage compared to the previous one. The length of damage is up to 100 µm and its width is less than 10 µm as well as 14 µm thick.

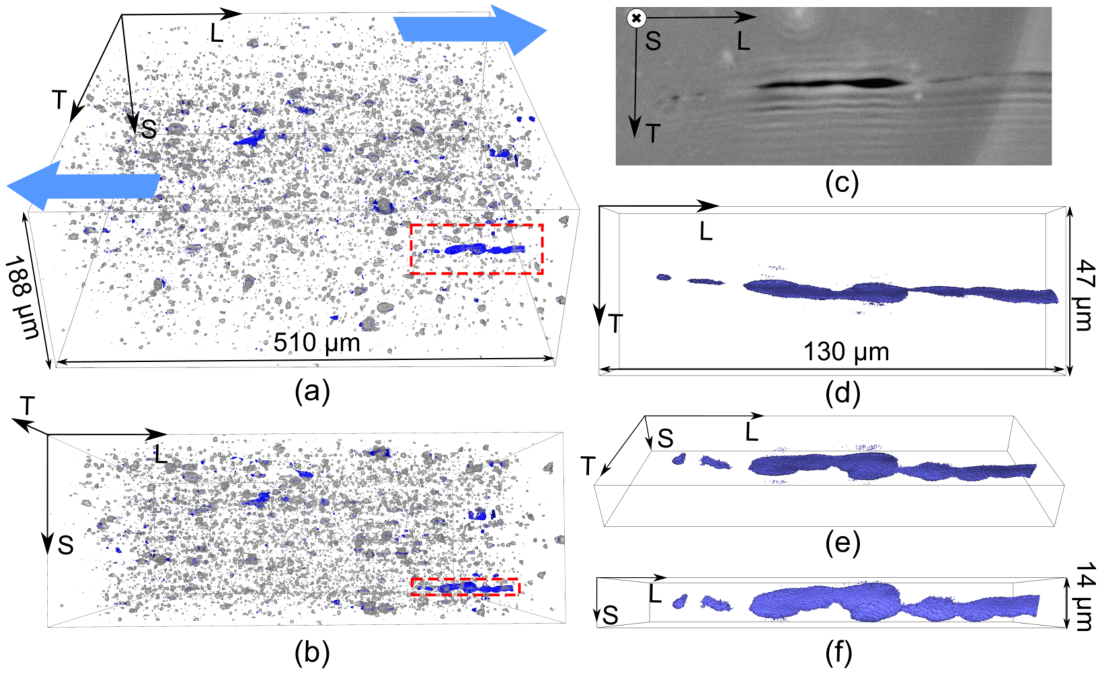

Figure 4.10: (a)(b) 3D overview visualization of the region where intermetallic particles are in grey and void in blue. (c) 2D section of another long flat crack selected in red box and its 130×47×14 µm^3 visualization from different views: (d) top view, (e) top-front view and (f) front view.

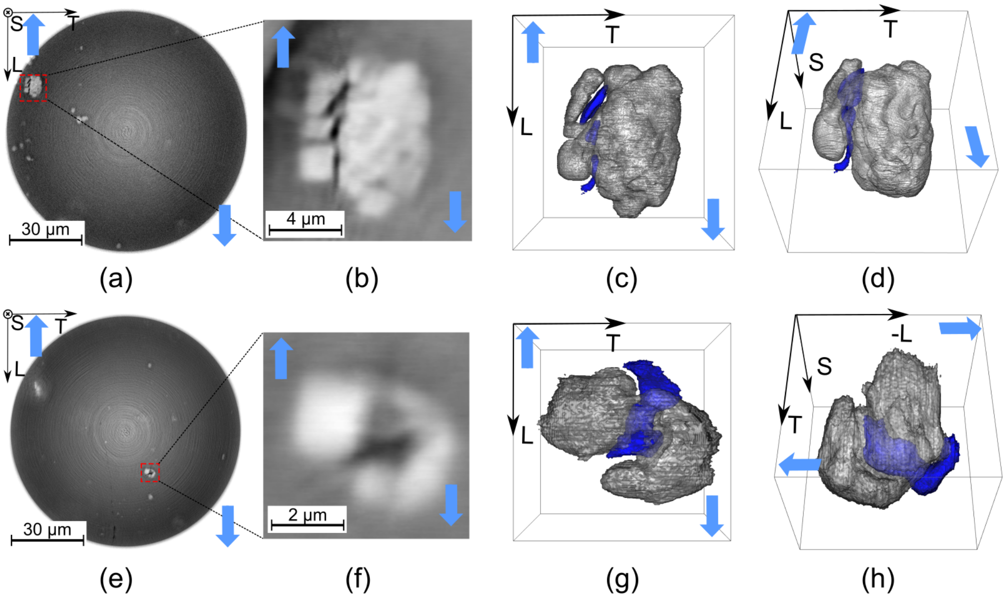

Figure 4.11: Intermetallic particle damage feature of (a) 2D section and its (b) detailed region and 12.2×11.5×9.6 µm^3 from different views: (c) top and (d) front-top views. (e) 2D section and (f) its selected and 5.8×5.8×4.0 µm^3 from different views: (g) top and (h) right-top views.

3.2.2 Particle crack observed at very high resolution (VHR)

Intermetallic particle fracture is the second damage feature during shear loading. The damaged particles' lengths ranged from several micrometers up to ten micrometers. Based on the very high resolution (VHR, voxel size down to 48 nm) nano-laminography on the deformed sample β, the particle related features including particle fracture and particle-matrix decohesion were segmented and visualized in different views. Considering the dimension of detrimental flat crack, this feature was not captured in the VHR scan.

A damaged particle in ellipse shape of 5 µm diameter was captured in the 2D slice of Fig.4.11 (a)(b) and a sub volume of 12.2×11.5×9.6 µm^3 was visualized in different top view in (c) and front-top view in (d). The particle was broken from middle under shear. Another particle with similar shape and size as 5 µm length is selected in (f) from the 2D section in (e). The particle rotation was observed under shear loading illustrated in blue. The 3D visualizations inside the sub volume as 5.8×5.8×4.0 µm^3 present the particle damage linkage to the particle-matrix decohesion in Fig.4.11 (g)(h).

Two tiny broken particles around micrometer length were exhibited in Fig.4.12 (b)(e). The rigid particles rotated and broke into debris. Fig.4.12 (c)(d) present the visualizations of the 6.4×8.2×3.4 µm^3 sub region including a particle of triangular shape of 2 µm and r. The particle fractured at the lower right corner under loading and the porosity appeared as a small part of the particle was separated. The second tiny particle was torn apart before fracture in (e). After the particle was broken, the cavities grew under local

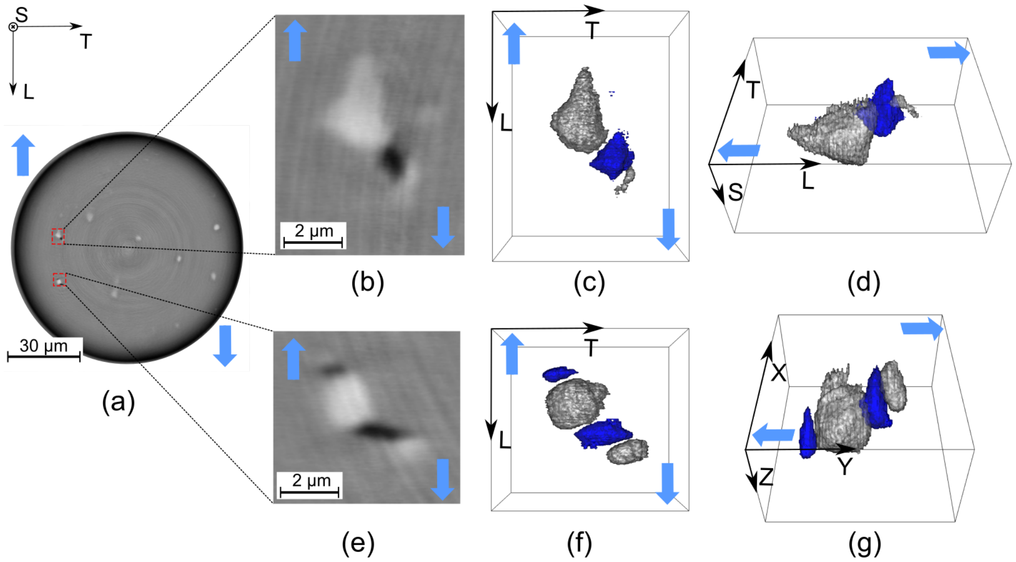

Figure 4.12: Intermetallic particle damage feature of (a) 2D section and its (b) detailed region and 6.4×8.2×3.4 μm^3 from different views: (c) top and (d) left-top views. (e) 2D section and (f) its selected and 6.2×5.8×3.4 μm^3 from different views: (g) top and (h) left-top views.

shearing. The voids and particle parts are visualized in 4.12 (f)(g). The void growth under shear was possible due to the rigid nature of the particles that kept the voids open.

3.3 Microstructural origin of flat cracks studied by SEM and EBSD

For another ligament of the deformed specimen β in 4.1 (c), the surface was polished incrementally and thereby in a destructive way till damage features appeared.

3.3.1 Origin of the flat cracks

The size of the detrimental damage features, flat cracks, ranged from several micrometer to 20 μm length and were observed in the region of interest via scanning electron microscopy (SEM). Since none of these cracks is linked to intermetallic particles, their nucleation might correspond to grain boundaries or slip bands regarding their dimensions. In order to verify these crystallographic relationship, these surfaces were assessed via destructive EBSD analyses.

Flat cracks are found and observed in Fig.4.13. These cracks were measured as around 10 μm in length and less than 3 μm in opening. Every flat crack was noted as F and its number as illustrated.

These flat cracks were found on the grain boundaries in Fig.4.14 via EBSD and they are proved to be intergranular in (b)(d)(f). In addition to these flat cracks, several

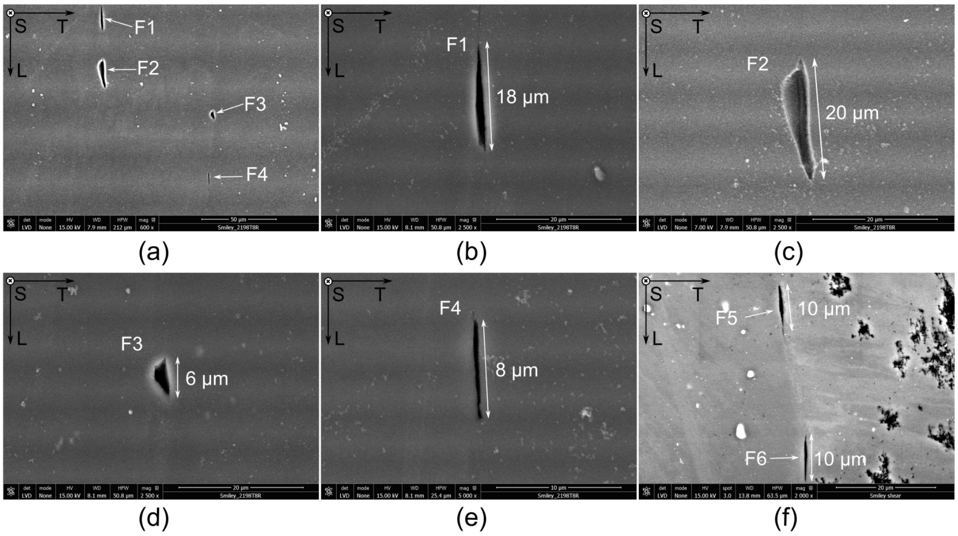

Figure 4.13: Damage feature of flat cracks via scanning electron microscopy (SEM): (a) four flat cracks noted as (b) F1 (c) F2 (d) F3 and (e) F4 on one surface and (f) two flat cracks F5, F6 on another surface where the dirt was included in the right.

slip bands in dark gray along the loading direction were also seen in the highly shear deformed region of 100 µm width. The flat cracks F1, F2 and F3, F4 were exactly situated on these slip bands, which are probably the damage initiation sites of the flat cracks. Interestingly, the orientation of slip bands changed abruptly within ‘purple’ grain seen in (b), which indicates these slip bands are possibly grain related.

Other flat cracks of similar dimension were found within grains as transgranular damage in Fig.4.15. The flat crack cluster was observed in (a) as F7 cluster and other two flat cracks F8, F9 shown in (b). The inverse pole figures indicates that these linear damage features lied both within the single grain in (d) and (f) and were thus transgranular.

The detrimental damage feature, flat cracks, are assessed both half intergranular and half transgranular statistically. It is assumed that the flat cracks could grow and coalesce to longer features up to 100 µm length as shown in 3D imaging that led to the final failure.

3.3.2 Particle crack

Other important damage features under shear are the intermetallic particle cracks. Fig.4.16 shows the cracks nucleated within the deformed particles of sizes less than 10 µm × 10 µm via SEM. Three ellipse-shaped intermetallic particles in Fig.4.16(a)(b)(d) and a stick shaped one in (c) rotated with respect to the rolling direction and had cracks inside. The crack opening orientation of four particles are similar after rotation. As the main damage feature in AA2024 (Tancogne-Dejean et al., 2021) Tancogne-Dejean et al. found the particle failures oriented normal to the principal stress orientation. The void stayed open because the second phase particles are rigid. The aluminum matrix seems

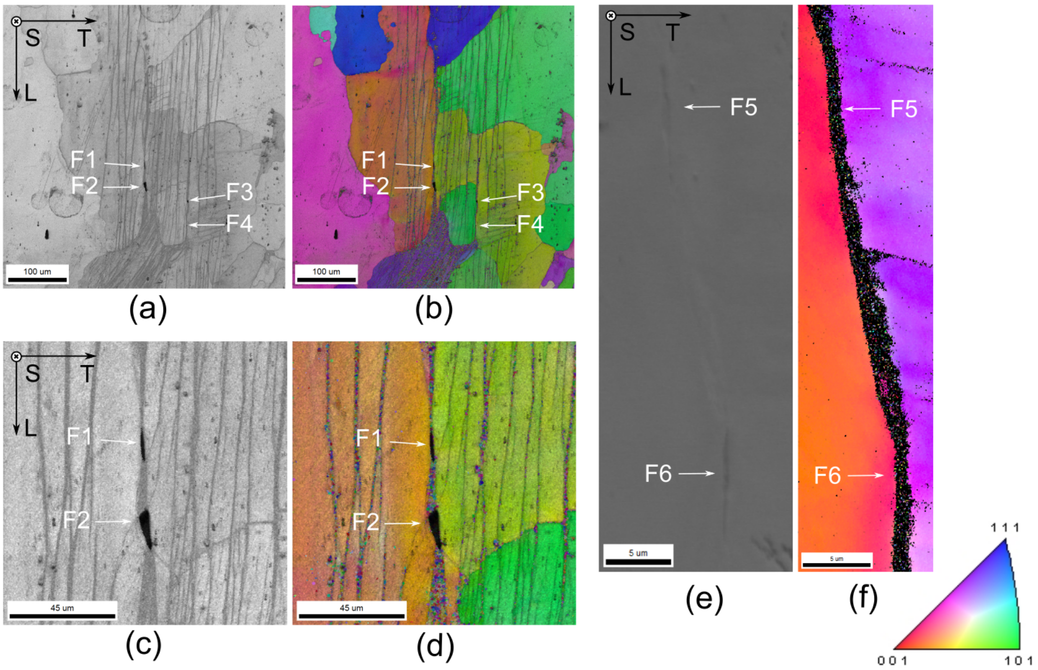

(a) (b) (c) (d) (e) (f)

Figure 4.14: The intergranular flat cracks in Fig.4.13 via EBSD analysis. Gray scale maps: image quality figures (a)(c)(e) and their related color coded maps: inverse pole figures (b)(d)(f), where (c)(d) present the zoomed region of (a)(b) respectively.

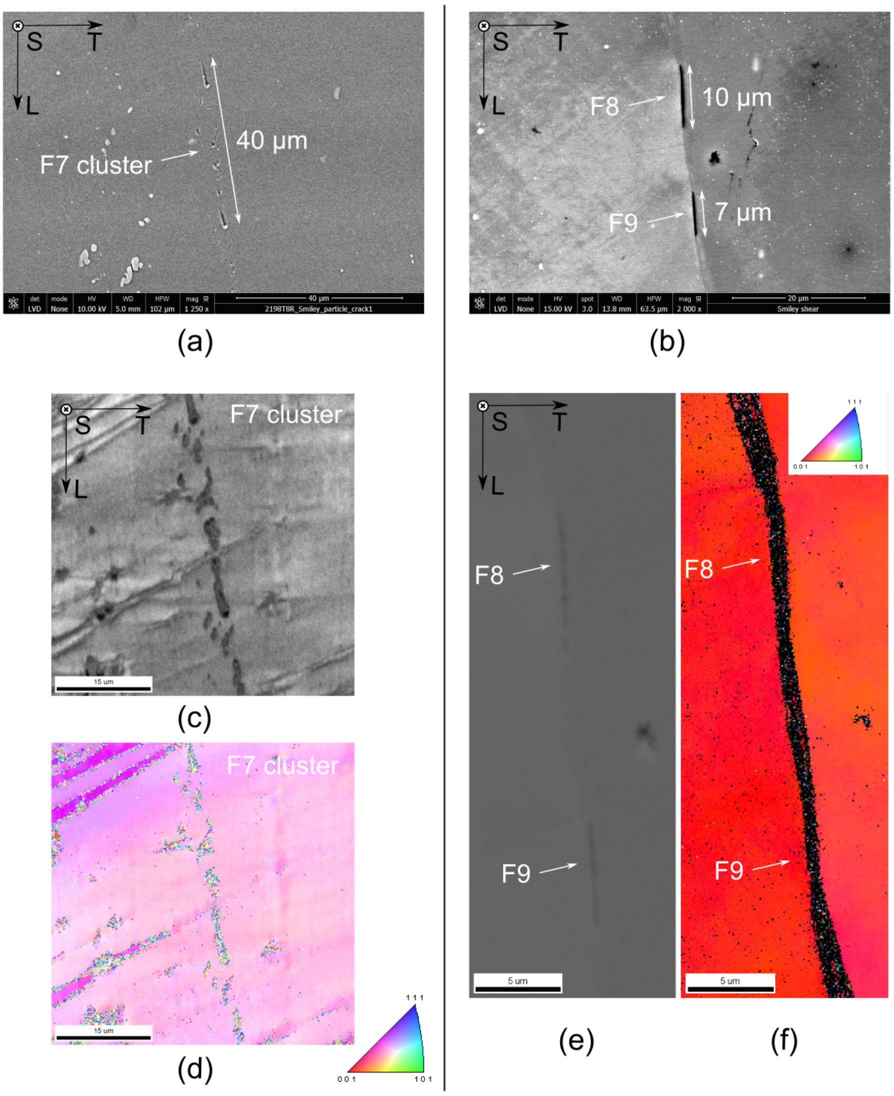

Figure 4.15: Damage feature of transgranular flat cracks via SEM: (a) a cluster of flat cracks noted as F7 cluster on surface and (b) two other flat cracks F8 and F9. These flat cracks are proved to be transgranular via EBSD analysis in (d)(f) inverse pole figures. The corresponding gray scale image quality figures in (c) and (e).

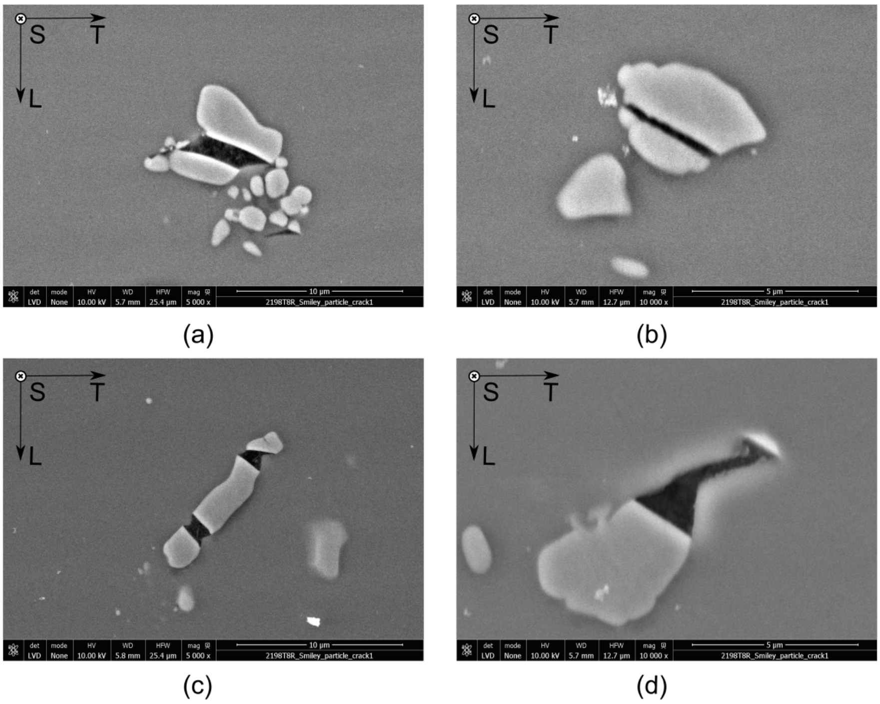

Figure 4.16: The damage feature of intermetallic particle cracks via SEM: (a)(b)(d) ellipse shaped and (c) stick shaped particles.

to flow into the voids from the both sides in Fig.4.16(d), consistent with the lox levels of stress triaxiality.

4 Discussion

4.1 Fracture mechanism under shear

Negligible amounts of pre-existing voids (less than 0.04% in Chen (2011)) are found in AA2198T8R, that elongate and close under shear as shown in AA2024T3 (Tancogne-Dejean et al., 2021). In addition, the hydrostatic pressure as driving force under shear loading is missing for void growth.

Due to a lack of pre-existing voids damage feature in this material, the nucleation of detrimental flat crack feature was studied via high resolution observations. The observed flat cracks were likely to originate from the crystallography rather than intermetallic particles. Indeed, two flat cracks were proved to be intergranular while another two flat cracks were found within the grains (transgranular) via EBSD analysis. The shear slip bands were found in the highly localized region in Fig.4.14 (c)(d) and these slip bands probably resulted in the transgranular flat cracks. The dispersoids less than 100 nm were found in the fracture surface and this could be related to the origins of transgranular flat cracks (to be checked via fatigue test in the future). A schematic figure in Fig.4.17

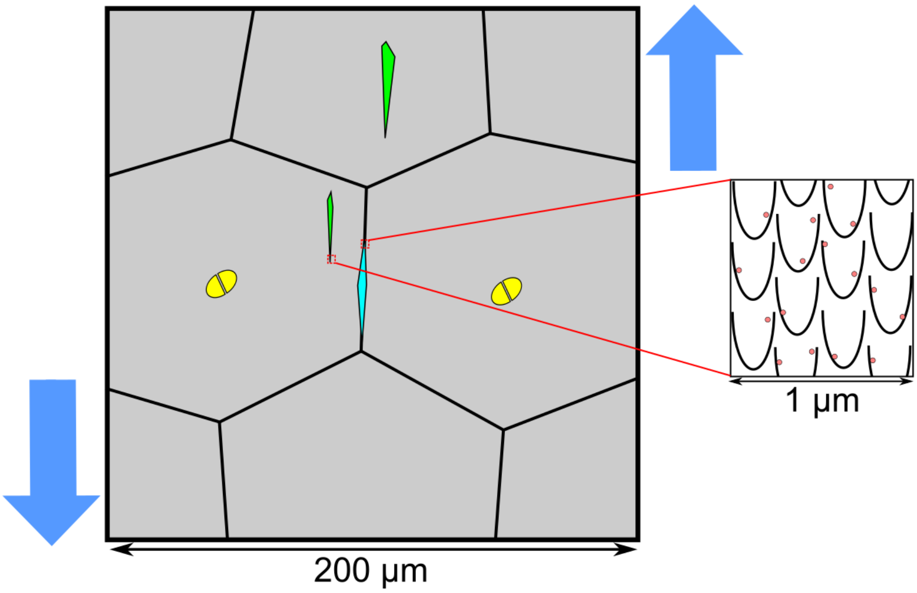

Figure 4.17: A schematic shear damage mechanism figure including flat crack features in blue and green as well as the intermetallic particle crack in yellow. The detrimental flat cracks are divided into two types: intergranular crack in blue and transgranular in green.

schematises the two main features: flat cracks (blue and green) and particle cracks (yellow). The former feature is more detrimental and could be divided into two types: intergranular crack (blue) initiated on the grain boundary and transgranular one (green) initiated on the localized shear slip bands and probably linked to the nano-dispersoids (pink) less than 200 nm, which were found on the ductile dimples.

The evolution of damage and each feature were illustrated in 4.4 from *in situ* micro-laminography. The nucleated flat cracks grew and coalesced to a longer crack, acting as a trigger for the final macro crack. Meanwhile, strong but brittle intermetallic particles were rotated, elongated and then either broken or decohered from the matrix, both resulted in voids in the material. This is one of the main damage features for AA2024T3 under shear (Tancogne-Dejean et al., 2021). Besides, due to a relatively high pre-existing porosity (0.7%) for AA2024T3, the deformation of the pre-existing voids was continuously controlled by the matrix rotation and not prone to any sudden event, even under large deformations. Roth et al. (2018) found that decohesion at the interface between the particles and matrix leads to void growth and micro crack formation under shear for FB600 steel, whose initial porosity is also negligible down to 0.05% as AA2198T8R in this study. Based on the experimental evidences, they indicated two possible final fracture scenarios: #1 - The stable-to-unstable growth of the corner cracks. #2 - Cracks propagation in an unstable manner due to shear-induced damage. From the *in situ* micro-laminography in Fig.4.4 (a), the flat cracks have formed a macro crack on the shear band at the very last step 7 before fracture. The scenario #2 seems to be more realistic for AA2198T8R.

The damage evolution was quantified as surface void fraction since the detrimental flat cracks have a very low void volume fraction. The surface void fraction grew steadily up to 3% with the increasing maximum equivalent strain reached more than 0.6.

Current models under shear-dominated loading (Roth et al., 2018; Torki and Benzerga, 2018) assume that shape changes of pre-existing voids or decohesion of rigid particle rather than void nucleation without the presence of particles. A fully coupled classical void damage at high stress triaxiality and Coulomb at the slip system scale at low stress triaxiality (shear) based ductile fracture model (Rousselier and Luo, 2014) could be applied to predict the proportional shear experiment even non-proportional load path changes. A reduced texture methodology (RTM) was used to provide computational efficiency and this approach involved a significant reduction of the number of representative crystallographic orientations. The damage nucleation along slip planes could represent the observed generation of shear cracks. This part about the numerical fracture model is given in chapter 6.

5 Conclusion

The damage nucleated under shear was studied for a AA2198T8R alloy using an in situ test and a second sample obtained by an interrupted shear test. From the 3D laminography and destructive 2D SEM/EBSD observations, two main types of damage features under shear were identified: flat cracks and intermetallic particle cracks. The former, whose direction is parallel to the loading direction (L), plays a major role in the final failure via *in situ* micro-laminography at micro resolution (μR). The length can be up to 100 μm and this feature has not been observed so far in other alloys under shear (Roth et al., 2018; Tancogne-Dejean et al., 2021). Each feature was observed down to the nanoscale via *ex situ* nano-laminography at high resolution (HR) and very high resolution (VHR) as well as the 2D SEM observation and EBSD analysis to study their link to the granular microstructure.

Conclusions are drawn in the following:

- Two main damage features, flat cracks and intermetallic particle cracks, were found in AA2198T8R under shear loading. The former is more detrimental leading to the macro failure path.

- The detrimental flat cracks do not nucleate on the particles and they are proven to be both intergranular and transgranular via EBSD analysis. The flat damage is located at the highly localized slip bands, and nano-dispersoids were found within the sub-micro dimples, which possibly could be the origin of flat crack feature.

- The intermetallic particles are rigid but brittle. They rotate under shear, then either broken or decohered from the aluminum matrix, eventually leading to voids.

- The damage evolution was quantified as surface void fraction and it steadily grew to 3% with the increasing equivalent strain up to 0.6.

Part II

Non-Proportional Load Path Changes: experiment and simulation

Chapter 5

3D *in situ* study of damage during a 'shear to tension' load path change in an aluminum alloy

A substantial reduction in ductility caused by a 'shear to tension' load path change has been found in chapter 3 for AA2198T8R. Similar to the methodology presented in the previous chapter 4 for proportional shear loading, an *in situ* X-ray laminography test is carried out to investigate the damage mechanism under this complex load path change. The strain fields are measured and compared between experimental digital image correlation (DIC) and numerical finite element (FE) calculations. The interaction between strain and damage evolution is assessed via DIC performed on projected 3D X-ray laminography data and the corresponding micro damage features are tracked and quantitatively analysed in terms of void surface fraction during loading. The damage mechanisms related to the material microstructure are detailed at the microscale. The stress states (e.g. stress triaxiality) are extensively analyzed by FE simulations using the same macroscopic model with anisotropic plasticity.

This chapter has been published in *Acta Materialia* 231 (2022) (Kong et al., 2022a).

Abstract

A load path change (LPC) from shear to tension has been studied for a recrystallized 2198 T8 aluminum alloy sheet material by 3D x-ray imaging combined with image correlation and interpreted by complementary 3D finite element (FE) simulations. A cross-shaped specimen was designed for the non-proportional loading and multiscale study. The effect of the LPC on the formability and related strain localisation, damage and failure was investigated and damage mechanisms could be clearly identified. The macroscopic tension stretch to fracture, measured by an optical extensometer during the shear to tension test, was reduced by about 20% compared to the proportional tension test. Damage, measured by *in situ* laminography imaging at µm-scale resolution, has interestingly already been found under shear, and was quantified as surface void fraction during the LPC. Strain was measured inside the material and at the mesoscale by 2D digital image correlation (DIC) on projected volume data, using the (natural) intermetallic particle contrast present in the 3D laminographic data. An accumulated equivalent strain definition, suited for the description of non-proportional loading, has been applied to the DIC data and FE simulations, indicating good agreement between both. On the microscopic scale, damage was seen to nucleate under shear load in the form of flat cracks, of similar width as the grain size, and in the form of cracks inside intermetallic particles. This damage subsequently grew and coalesced during tensile loading which in turn led to final fracture.

1 Introduction

Whilst research has focused for decades on damage and fracture at high levels of triaxial stress during proportional loading of thick components containing severe notches (Pineau et al., 2016), only more recently (Bao and Wierzbicki, 2004) deformation and failure at lower levels of stress triaxiality, i.e. below 1, have been considered. In high stress triaxiality fracture the nucleation, growth and coalescence of voids are the main damage mechanisms and stress triaxility in combination with plastic strain are identified as the driving forces of ductile damage growth (Pineau et al., 2016).

However, at low levels of stress triaxiality, complex non-monotonic relationships between strain at fracture and stress triaxiality have been found (Bao and Wierzbicki, 2004). The definition and measurement of fracture strains in these circumstances are difficult due to the highly localised final failure process (Papasidero et al., 2015). Rather phenomenological models considering strain, stress triaxiality and the Lode parameter have been used to try to fit the experimental behaviour Bao and Wierzbicki (2004). Void growth is very limited under shear as the stress triaxiality is close to zero.

Most engineering structures undergo load path changes during forming and/or during forming followed by in-service loading. At the macroscopic level even more complex and unexplained relationships between fracture strain for load path changes (LPC) were found (Brünig et al., 2021). Brünig et al. (2021) used H-shaped specimens to investigate a ‘shear to tension’ load path change for a 6082 T6 aluminum alloy. A reduction in macroscopic displacement was found when a shear pre-strain was applied before applying the tensile strain. The higher the pre-strain the higher the reduction in tensile strain. There is a lack of knowledge about the damage mechanisms under these conditions. In consequence, fracture due to load path changes is hard to predict even though it is highly application relevant.

Even the ductile damage mechanisms under monotonic low stress triaxiality loading are less clear than under high stress triaxiality loading. Gross and Ravi-Chandar (2016) investigated deformation and failure of Al 6061-T6 under shear loading via *in situ* SEM. They found that second phase particles broke, debonded or rotated. Incipient voids had a minimal influence on the deformation of this material under shear. Achouri et al. (2013) found for an HSLA steel that voids nucleated on the particle-steel interface, rotated and elongated with increasing shear strain. These surface observations are subject to surface preparation artefacts and free surface effects such as the onset of surface roughness during straining.

With recent advances in synchrotron three-dimensional (3D) imaging, damage inside the material bulk can to be studied both qualitatively and quantitatively *in situ* (Landron et al., 2012; Maire and Withers, 2014). Synchrotron laminography is suited to image regions of interest in large flat samples at micrometer resolution (Helfen et al., 2005), thereby guaranteeing that relevant mechanical conditions are present in the bulk of the material compared to surface observations. Basic failure mechanism at low triaxiality (i.e. shear) have been explored (Roth et al., 2018; Tancogne-Dejean et al., 2021) via this non-destructive 3D imaging technique. Roth et al. (2018) observed void nucleation and growth on rigid hard particles in ferrite-bainite steel under shear-dominant loading via laminography and validated shear damage phase via a 2D RVE analysis. Voids nucleated due to particle-matrix de-cohesion, subsequently elongated and aligned with the principal strain direction. Tancogne-Dejean et al. (2021) observed and followed statistically intermetallic particles and pre-existing voids under low stress triaxiality proportional shear loading for a ductile Al alloy AA2024-T3. It was found that intermetallic particles broke with cracks normal to the principal stress direction. Pre-existing voids were shown to rotate and close.

Using the 3D *in situ* images, strain inside the material can be computed via tracking if the natural image contrast, caused by the material microstructure, e.g. intermetallic particles, is sufficient. This digital volume correlation has been successfully applied to aluminum alloys (Buljac et al., 2018b; Morgeneyer et al., 2013, 2014). 2D image correlation of projected 3D data may be an alternative method when the contrast in the 3D image is low (Buljac et al., 2018b; Morgeneyer et al., 2021; Roth et al., 2018; Tancogne-Dejean et al., 2021).

Concerning the micromechanical modelling of damage mechanisms under shear loading, Fleck et al. (1989) investigated the effect of void nucleation from rigid particles and growth on macroscopic stress-strain behaviour under shear and their softening effect in a shear band. They found that accounting for particle matrix contact was important. Tvergaard (2008, 2009) simulated 2D void behaviour under simple shear and found void rotation and elongation. This process leads to final closure of voids and also to macroscopic localization. A 3D simulation for spherical voids have been carried out in (Nielsen et al., 2012). Torki and Benzerga (2018) investigated the process of void-mediated failure inside a naturally forming, i.e. stress triaxiality larger than zero, shear band and carried out numerical simulations using a continuum micromechanics framework for dilatant plasticity that captured the essential features of sub-cell deformation: a. void-induced strain localization; b. void rotation; c. void elongation. In Nahshon and Hutchinson (2008), a modification of the Gurson model was proposed to account for softening under shear supposing the presence of initial porosity. Most of these theoretical works still need experimental validation.

The material employed here is one of the third generation Al-Cu-Li alloys with higher copper over lithium ratio compared to the second generation (Buljac et al., 2018b; Warner, 2006). More precisely, the fuselage sheet alloy AA2198 in T851 temper (*i.e.* solutionized, stretched and artificially aged) is used in its recrystallized state (Buljac et al., 2016; Morgeneyer et al., 2014). The alloy had an optimized and attractive balance of tensile strength (500 MPa in rolling direction) and toughness amongst this class of third generation alloys (*e.g.* 2098T8) (Warner, 2006), and shows good properties after friction stir welding (Le-Jolu et al., 2010). Its failure mechanisms were identified as intergranular and transgranular in (Morgeneyer et al., 2014; Rousselier et al., 2017). Sub micrometre dimples were found in the slant fracture zones.

The aim of this work is to study the effect of a load path change from 'shear to tension' at low stress triaxiality on ductility, on deformation and on damage mechanisms. The experimental approach, including material, sample design and *in situ* X-ray laminography testing is introduced first. At the mesoscale, an accumulated equivalent strain is defined for load path changes and applied to both experimental digital image correlation (DIC) and numerical finite element (FE) calculations. The interaction between strain and damage evolution is assessed via DIC performed on projected 3D X-ray laminography data and the corresponding micro damage features are tracked and quantitatively analysed in terms of void surface fraction during loading. At the microscopic scale, the damage mechanisms related to the material microstructure are then analysed. The spatial distributions of the equivalent strain and stress triaxiality are extensively analysed through the loading steps by FE simulation using an anisotropic plasticity model.

2 Experimental procedure

2.1 Material

The material of interest in this study was a 2198 T851 alloy in recrystallized form, referred to as 2198T8R henceforth. Its nominal composition is given in Table 5.1.

Moderate plastic anisotropy was found in different loading directions: the rolling direction is noted as L, the long transverse direction as T, short transverse direction (thickness direction) as S and the diagonal direction (45° between L and T in the sheet plane) as D.

	Cu	Li	Zn	Mn	Mg	Zr	Si	Ag	Fe
`wt.\%`	2.9-3.5	0.8-1.1	≤ 3.5	≤ 0.5	0.25-0.8	0.04-0.18	≤ 0.08	0.1-0.5	≤ 0.01

Table 5.1: Chemical composition limits of 2198 alloy in weight percent(wt.%) (Chen, 2011)

Electron Back-Scatter Diffraction (EBSD) analysis was performed in an FEI Nova nanosem 450FEG with an EDAX-TSL Hikari EBSD camera using a step size of 0.5 micrometer and an acceleration voltage of 15 kV. Large recrystallized pancake-shaped grain structure was obtained in the LT plane shown in Fig.5.1(a). The grain size was measured by a mean linear intercept method as 82 μm in L, 80 μm in T and 20 μm in S directions. The material can be considered as homogeneous along the S direction without any grain size gradient (Chen, 2011). 2D sections of undeformed material 2198T8R from synchrotron radiation computed laminography (SRCL) (Helfen et al., 2005) image data are shown in Fig.5.1(b). The intermetallic particle (white) volume fraction is ∼0.3-0.4% while initial porosity (black) is negligible down to less than 0.03 vol.% in the aluminum matrix (grey). Moderate texture via EBSD is presented in (c) pole figure.

2.2 Mechanical testing

2.2.1 Specimen geometries

Inspired by the geometry given in (Roth and Mohr, 2016) and in order to perform the load path change tests, new specimen geometries, including a cross-shaped 'shear to tension' (ST) as well as a shear-only (SO) and a tension-only (TO) geometry were designed and are shown in Fig.5.2. The original shear sample geometry was miniaturized to be able to image the region of interest at micrometre spatial resolution by 3D synchrotron laminography imaging. A range of the dimensions of the region of interest (ROI), particularly the vertical and horizontal offsets between two hole positions, have been calculated and optimized by the finite element simulations. In the present work, all specimens were machined by the means of electrical discharge machining (EDM) from 2 mm raw sheet material of 2198T8R to 1 mm nominal thickness.

2.2.2 Mechanical *in situ* test

Experiments were performed using an *in situ* loading frame with a similar design as shown in (Morgeneyer et al., 2021). It is presented in Fig. 5.3 where pin hole loading was applied. The cross-head displacement rate was 5 μm s^{-1}, which resulted in a strain rate of the order of $10^{-4}s^{-1}$ in the gauge section. Three kinds of experiments were carried out and noted as shear-only (SO), tension-only (TO) and 'shear to tension' (ST). Mechanical *in situ* tests were carried out for the ST sample in the horizontal LT plane, where shear loading was performed in the L and tensile loading in T so that the final crack was parallel to the rolling direction. Before the laminographic experiment, several proportional pre-tests (SO,TO) without laminography scanning were performed

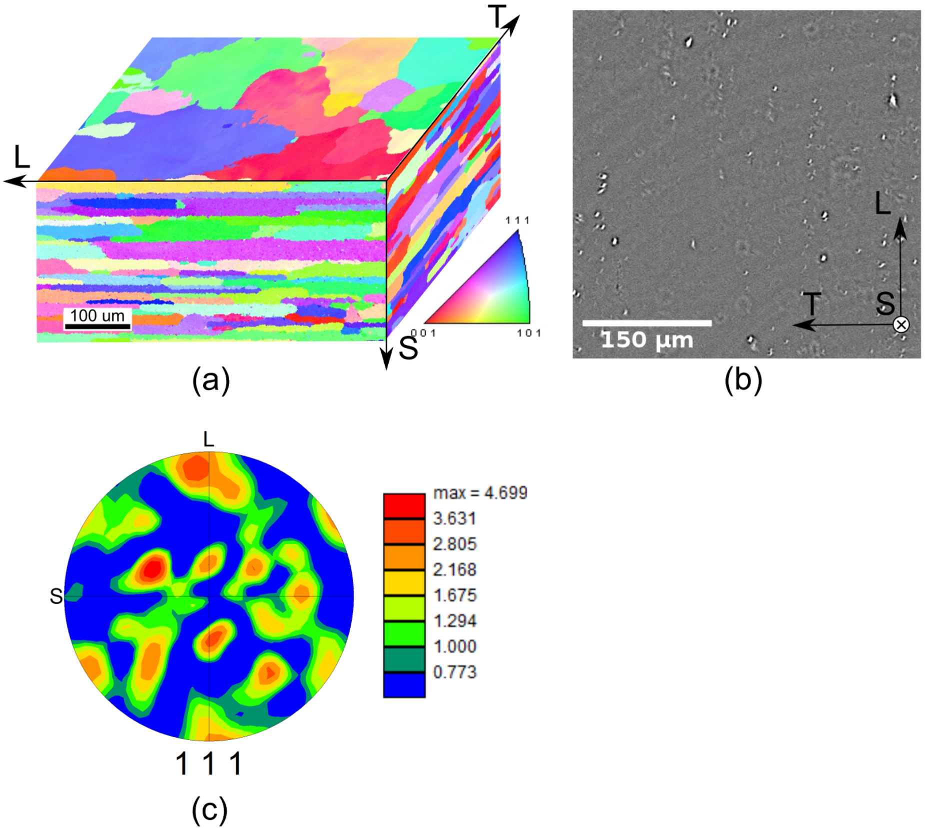

Figure 5.1: (a) Inverse pole figure indicating the 3D grain structure of 2mm 2198T8R sheet material via EBSD (the crystal orientations are given with respect to the normal of each plane), (b) 2D section of 2198T8R from high resolution 3D X-ray laminography in the L-T plane and (c) Pole figure of 2198T8R.

in the *in situ* machine. The entire database is given in chapter 3 (Kong et al., 2021).

2.2.3 Optical imaging setup for strain measurement in the region of interest (ROI)

In order to measure the deformation in the ROI of the sheet specimen with complex geometry (in particular enabling correlation of the experimental data with 3D FE simulations) and to prevent the deformation from being influenced by elastic deformation of the rig during the mechanical loading, an optical imaging setup was used to measure the surface displacements locally by DIC. To provide a suitable contrast for this, a fine random speckle pattern (average speckle size about 15 µm) was deposited on the specimen surface.

Surface images were taken with a sensor having 2048×2048 pixels (Basler acA2040 25g) in combination with different microscope optics, see Table. 5.2, providing different

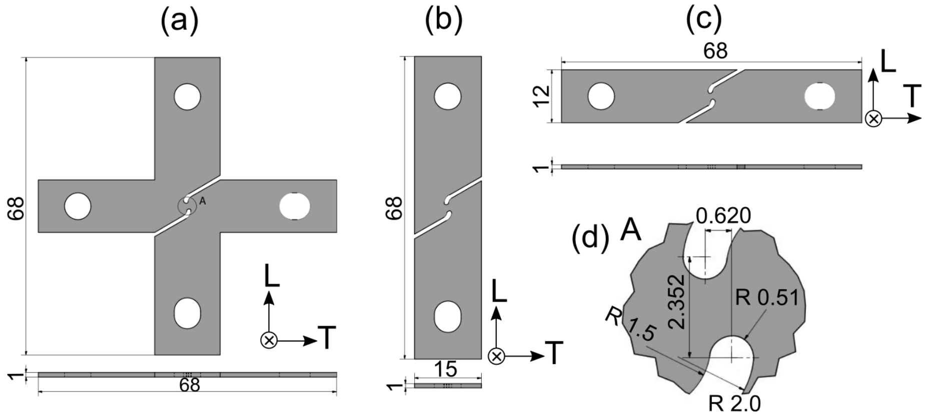

Figure 5.2: Geometries of (a) Cruciform 'shear to tension' (ST) load path change, (b) Shear-only (SO), (c) Tension-only (TO) samples and (d) the detailed geometry of the region of interest (ROI).

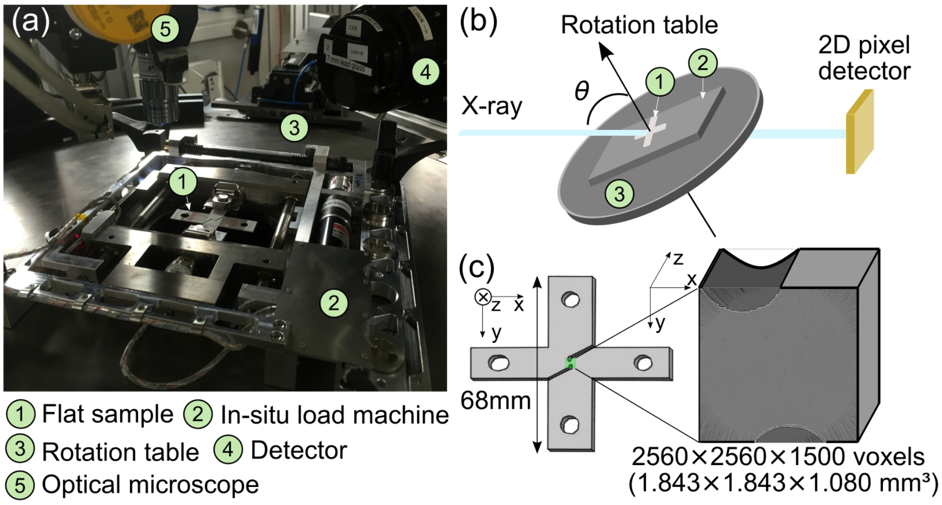

Figure 5.3: Set-up for *in situ* laminography experiments: (a) ②loading frame rig with ①a cross-shaped sample on ③laminographic table and the schemes of (b) laminographic stage and (c) 3D imaging region of interest (ROI) from the cruciform sample.

spatial resolutions and related fields of view. During the laminographic *in situ* experiment, a surface image was acquired before each laminographic scan. In contrast, the surface image set of the pre-tests conducted in laboratory of Centre des Matériaux was continuously captured at a frequency of 2 Hz.

Macro measurement Instead of utilizing the local displacement of two points as in traditional extensometer, for uniaxial tensile experiments, a 4-point-frame optical

Microscopes group	Field of view (mm^2)	pixel size (µm/px)
SILL TZM 0420/3.0-C telecentric lens	3.85×3.85	1.875
Mitutoyo VMU-V microscope + 2× objective lens	5.43×5.43	2.65

Table 5.2: Different optics and associated pixels sizes of the different experiments.

extensometer illustrated in Fig. 5.4 was introduced to measure tension in both vertical and horizontal directions as well as the shear angle in ROI and to obtain an average macro measurement in the reference frame that could be compared with numerical computation.

From the surface DIC results of the optical images taken for each loading step, the relative displacement was calculated as the difference between initial positions and deformed positions using the four selected points. A general displacement field u inside the frame was generated from bi-linear interpolations.

According to the specific geometry, the region of interest was mainly under a simple shear state, which was a composition of pure shear and rigid body rotation. The deformation gradient F_{ij} was the derivative of the deformed configuration position vector x_i with respect to the reference configuration position vector X_j (Belytschko et al., 2000). In order to remove rigid body rotation, $\mathbf{F}$ can be written by using the polar decomposition as the product of two tensors: a rotation tensor $\mathbf{R}$ and a symmetric right stretch tensor $\mathbf{U}$.

$$F_{ij} = \frac{\partial x_i}{\partial X_j} = R_{ik} \cdot U_{kj} \tag{5.1}$$

Tension stretch along x axis U_{11} and the absolute value of shear stretch U_{12} were chosen as the tensile and shear measurements respectively.

$$\mathbf{U} = \begin{bmatrix} U_{11} & U_{12} \\ U_{12} & U_{22} \end{bmatrix} \tag{5.2}$$

Accumulated equivalent strain measurement During the complex non-proportional loading path damage was accumulated. The definition of a suitable accumulated strain that can be related to the damage state was important so as to estimate strain to fracture. As other works indicated Abedini et al. (2018); Roth et al. (2018), the logarithmic strain (Hencky strain or true strain) has taken into account the influence of the strain path and is defined as:

$$\varepsilon = \frac{1}{2} \log\left(\mathbf{F}^T \cdot \mathbf{F}\right) \tag{5.3}$$

This expression provides an appropriate measure especially for large simple shear strain (Onaka, 2010, 2012).

Equivalent strain needs to be cumulative to estimate an effective strain during the load path change. The work-conjugate equivalent strain is defined in terms of the adopted constitutive model (Butcher and Abedini, 2017). However, considering the

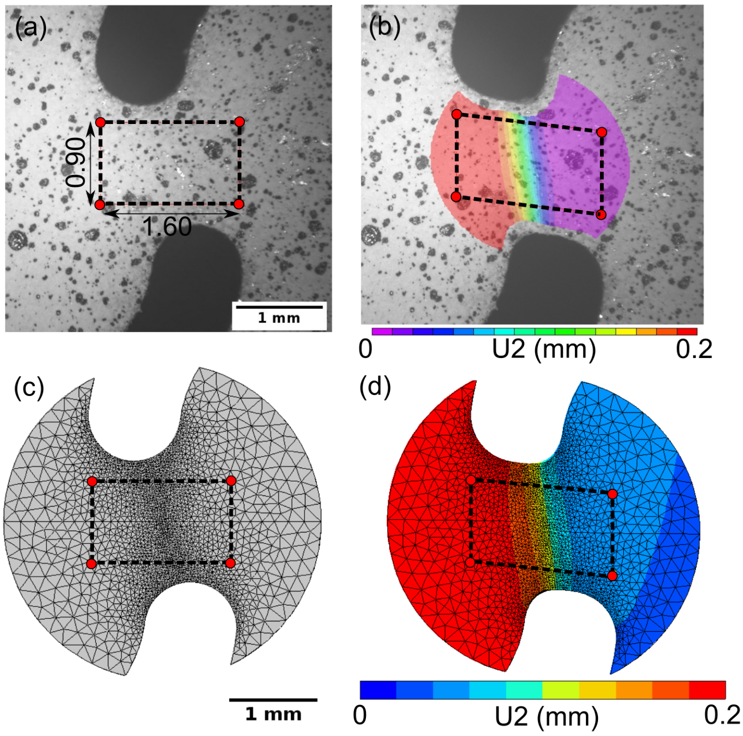

Figure 5.4: 4-point-frame visual extensometer on (a) reference and (b) deformed images for image correlation and the same 4-point-frame were chosen in (c) initial and (d) deformed steps from the finite element model to synchronize experiment and simulation.

complexity of the anisotropic model, an accumulated equivalent von Mises strain has been applied to the total strain tensor in the following as (Abedini et al., 2018) :

$$\varepsilon_{\text{cum}} = \int \sqrt{\frac{2}{3} d\varepsilon : d\varepsilon} \tag{5.4}$$

Besides, Butcher and Abedini (2017) pointed out that the difference between the equation and the work-conjugate definition for a von Mises behaviour remains negligible when strain is less than 0.8. The same strain definition was applied here for the DIC data and for the FE simulation results to have comparable fields during the non-proportional loading. The equation in Eq. 5.4 satisfies all the requirements.

Moreover, due to a lack of information in the thickness direction (S) in experimental 2D surface image correlation, the third component has been calculated from a plastic incompressibility assumption $\varepsilon_I + \varepsilon_{II} + \varepsilon_{III} = 0$. Hence, the accumulated equivalent strain increment is computed as:

$$\Delta\varepsilon_{\text{cum}}^{\text{2d}} = \sqrt{\frac{2}{3}(\Delta\varepsilon_I^2 + \Delta\varepsilon_{II}^2 + \Delta\varepsilon_{III}^2)} = \frac{2}{\sqrt{3}}\sqrt{\Delta\varepsilon_I^2 + \Delta\varepsilon_{II}^2 + \Delta\varepsilon_I \Delta\varepsilon_{II}} \tag{5.5}$$

2.2.4 Non-proportional *in situ* synchrotron laminography experiment

The *in situ* mechanical experiment, a non-proportional loading 'shear to tension' (ST) test, was carried out at the beamline ID19 (Weitkamp et al., 2010) of the European Synchrotron Radiation Facility (ESRF, Grenoble France). During the experiment, the shear loading was applied and unloaded before turning the cruciform sample by 90 degrees and loading it in tension. Tensile loading was applied until final fracture shown in Fig. 5.7. 24 scans were performed with a stationary X-ray beam with the sheet thickness direction (S) being inclined at an angle of 60° with respect to the X-ray beam axis in Fig. 5.3. An indirect detector system was employed, composed of an approx. 10 μm thick Eu-doped gadolinium gallium garnet thin-film scintillator optically coupled via microscope optics suitable for high-dose imaging (Douissard et al., 2012) and 9× effective magnification to a scientific camera (pco.edge 5.5, PCO, Kehlheim, Germany). For each scan, a series of 3600 radiographs was acquired with an exposure time of 40 ms for each projection direction at an X-ray energy of approximately 35 keV. The 3D data was reconstructed utilizing a filtered-back projection algorithm Myagotin et al. (2013) to a size of 2560×2560×1500 voxels with a physical length 0.72 µm/pixel, thus the corresponding physical volume in the material bulk was around 1843.2×1843.2×1080 μm^3 as shown in Fig. 5.3. The parameter optimization for the 3D reconstruction was performed automatically using a GPU-accelerated implementation of this algorithm (Vogelgesang et al., 2016).

Due to unforeseen instrumentation problems, the volumes of the last two steps were acquired at a lower resolution with a physical length 1.44 µm/pixel after some hours of mechanical stress relaxation.

2.2.5 3D image analysis

To segment damage, a region growing algorithm (Buljac et al., 2018b) was used. It was chosen to project the damage on one surface to obtain a surface void fraction rather than a void volume fraction, as will be discussed later. The surface on which the damage was projected was the future fracture surface (projection approximately along T direction over a length of 144 µm). The surface void fraction was computed as number of pixels that belong to the segmented projected damage divided by the number of pixels of the total area.

2.2.6 Digital image correlation analysis

We used the commercial DIC software *Vic2D-6* (Correlated Solutions) to correlate 2D surface images and 3D volumetric images taken at every load step to obtain displacement and strain fields at the selected ROI.

Surface DIC Images taken by the camera of the optical imaging setup at different loading steps have been used to correlate and generate the displacement and strain fields on the specimen surface. Subset size and step size were set as 55 pixels (146 µm) and 5 pixels (13 μm) respectively in Vic-2D for laminographic group while 55 pixels (103 μm) as subset size and 10 pixels (19 μm) as step size for the other pre-tests. All highly deformed (i.e. shear) and load path change tests were conducted with incremental correlation. Hencky strain was computed with a filter size of 15. The surface displacement fields are used here to compute the stretch via the 4-point-frame extensometer.

Projection DIC On account of the low particle volume fraction in this material, it was difficult to calculate reliable digital volume correlation data from the limited contrast in the reconstructed 3D images. Generally, single slices of laminographic 3D volume data exhibit an insufficient density of natural markers for correlation. A technique called projection DIC (p-DIC) has been applied in (Buljac et al., 2018b; Morgeneyer et al., 2021; Roth et al., 2018; Tancogne-Dejean et al., 2021) where contrast (for example using a maximum or a minimum norm), contained in several cross sections of the 3D volume data were projected along the thickness direction into one image. The contrast of white intermetallic particles contained in a 100 voxel (i.e. 72 μm) thick slice around the sample middle plane was projected on a 2D plane in Fig. 5.5. The projected 2D images for each load step could be correlated to determine the in-plane component of displacement and strain fields. Note that meaningful results were only obtained with this technique under the absence of strain field gradients (inside the projection volume of the chosen slice) along the specimen thickness direction. The onset of damage can be a problem for DIC as the hypothesis of conservation of contrast is no longer satisfied. For the present p-DIC approach this is not a major problem as the white particles (maximum grey value) are projected. In contrast, the damage is dark and does thus hardly affect the final 2D image. Only the edges of the crack, that are bright due to the phase contrast, affect the projected image, but this has not been a problem for the current correlation. Compared to digital volume correlation, this technique was more robust and saved computation time. Subset size and step size were set as 95 pixels (68.4 μm) and 10 pixels (7.2 μm) respectively in Vic-2D and incremental correlation was used. The results were exported as csv files and post processed to compute the accumulated equivalent strain via Python according to Eq. 5.5, the field of which is shown under deformed frame in Fig. 5.5 (c).

3 Computational model

The finite element method was used to estimate the stress state (e.g. access to stress triaxiality) and to obtain the accumulated equivalent strain to fracture inside the material bulk so as to compare with experimental results. All simulations were performed using the finite element software Z-set (Besson and Foerch, 1997).

3.1 Numerical finite element model

Due to the symmetry of the specimen's geometry, half of its thickness was meshed using the reduced integration quadratic tetrahedral element (c3d10R). A mixed displacement-pressure updated Lagrangian formulation was applied for the tetrahedral element to

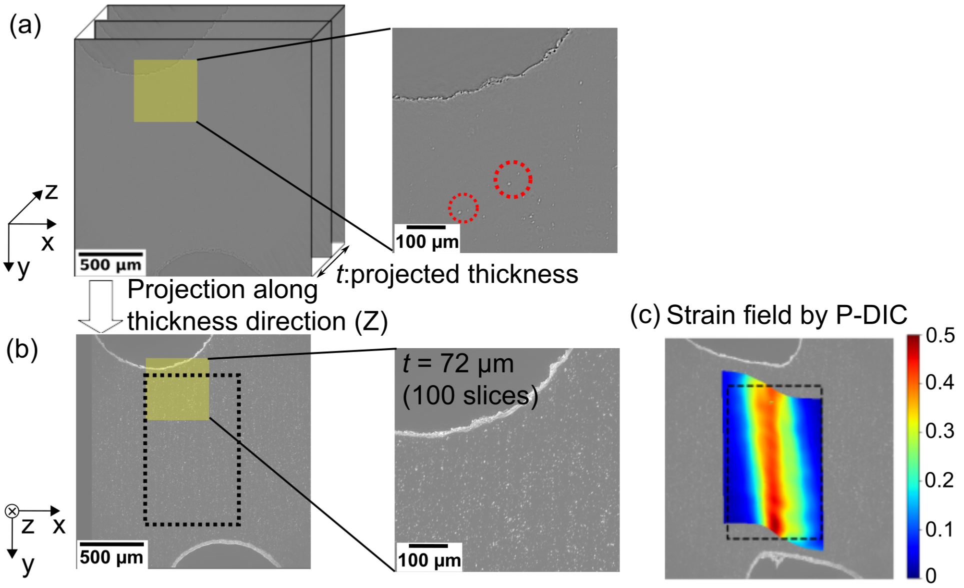

Figure 5.5: (a) Stack of 100 individual reconstructed cross sections from the 3D volume data with limited contrast have been projected to (b) an image with sufficient contrast using the maximum grey level. (c) The strain field is obtained via 2D image correlation of such projected images (of the 72 µm thick slice) before and after each loading step.

account for large plastic strain and incompressibility especially for the micro specimen series (Al Akhrass et al. (2014); Taylor (2000)). The element size varied from 30 µm to 100 µm, as illustrated in Fig.5.6. Pins were modelled as elastic steel (red part) to apply the tensile load to the specimen.

The experimentally-measured global displacement rate was set to the order of $10^{-4}\mathrm{s}^{-1}$ on the pins. In order to remove the machine compliance effect, local shear stretch U_{12} and tensile stretch U_{11}, as calculated from the deformation gradient $\mathbf{F}$ using the 4-point-frame visual extensometer, were chosen to synchronize experiment and numerical simulation.

3.2 Material behaviour

aluminum alloy 2198T8R has been modelled using a Chaboche-like (Lemaitre and Chaboche, 1990) elasto-plastic behaviour with isotropic hardening. Bron-Besson's yield criterion was applied to account for plastic anisotropy (Bron and Besson, 2004). The parameters have been calibrated with results in different loading directions and more results are discussed in chapter 3 (Kong et al., 2021).

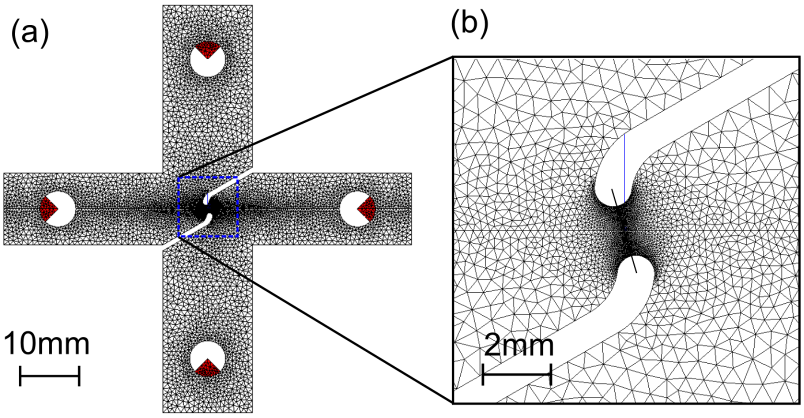

Figure 5.6: Finite element mesh of (a) cross geometry where the elements of supports are in red. (b) Region of interest (ROI) of the geometry with mesh size down to 30 µm.

4 Results

4.1 Macroscale measurement: nominal stress-stretch curves

In order to remove deformation due to sample and machine stiffness, the 4-point frame visual extensometer described in section 2 was used for a local measurement of shear stretch U_{12} and tension stretch U_{11} in the ROI. Fig. 5.7 shows the curve of the nominal stress (force F divided by the initial area of minimum cross section S_0) versus shear stretch U_{12} or tension stretch U_{11}. In Fig.5.7 (a) the result for a representative monotonic shear-only (SO) experiment is given as black dots together with the shear part of the *in situ* laminography 'shear to tension' (ST) load path change experiment as red triangles. Unloading was performed at about half the shear stretch to fracture of the SO experiment. Fig.5.7 (b) shows the result for a representative tension-only (TO) experiment as black dots together with the tension part of ST load path change result as red triangles.

The proportional loading SO experiment showed a shear stretch to fracture of $U_{12}^{f\text{SO}}$ = 0.135 within a range from 0.132 to 0.137 found by repeated testing (Kong et al., 2021), see Fig.5.7 (a). At least three tests were performed to obtain the average strain to fracture values Kong et al. (2021).A maximum nominal stress of about 325 MPa was reached. The shear part of the non-proportional load path change ST showed a very similar nominal stress-stretch curve to that of the SO experiment. Unloading of the shear to tension load path change was carried out at a shear stretch U_{12} around 0.08. The monotonic TO test shown in Fig.5.7 (b) reached nominal stresses of about 515 MPa and an average tension stretch at fracture of about 1.117 was found. The scatter in stretch to fracture from repeated testing was found in a minimum-maximum range from 1.105 to 1.130 (Kong et al., 2021). During the ST load path change test, the tension stretch U_{11} started with an initial shift of 0.025 on the tension curve as there was a slight tension stretch during shear loading. After this shear loading, a higher nominal stress at yielding was found compared to a proportional test, which was due to hardening during the shear loading without necking. The tension stretch to fracture in tension after shear was $U_{11}^{f_{ST}} = 1.104$, which was less than the average tension stretch to fracture of a tension-only test. Thus, the average tension stretch to fracture of shear followed by tensile (ST) loading ($U_{11}^{f_{ST}} = 1.098$) was 16% reduced compared to that of proportional TO loading ($U_{11}^{f_{TO}} = 1.117$). Here, if the tension stretch during shear pre-loading was not taken into account, this reduction would be even higher. A detrimental effect of the shear loading before tension on the stretch to fracture during tensile loading can clearly be identified. The origin of this detrimental effect in terms of damage micro-mechanisms is studied in the sequel.

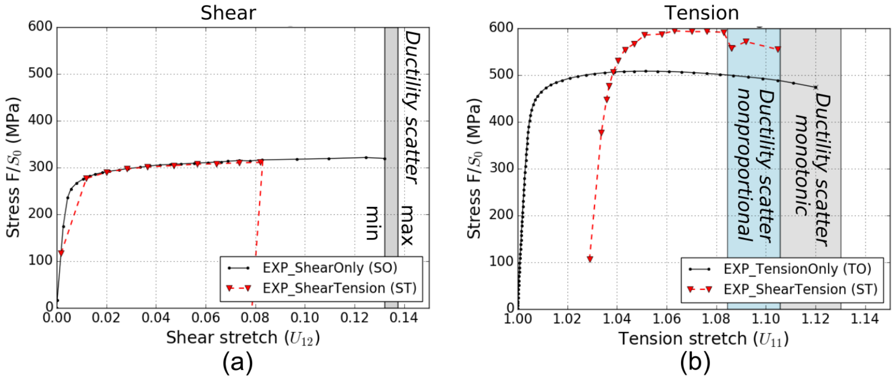

Figure 5.7: The curves of nominal stress versus (a) shear stretch U_{12} and (b) tension stretch U_{11} for two proportional loading Shear-Only (SO), Tension-Only (TO) tests as well as non-proportional loading 'shear to tension' tests. S_0 stands for the initial cross surface in region of interest (ROI).

4.2 Mesoscale analysis of strain and damage fields

This section focuses on the mesoscale analysis of strain fields, damage and stress states. The nominal stress versus stretch curve of the shear to tension load path change test is given in Fig.5.8 and the instances at which a scan was performed are shown. The simulated curve is also plotted. First, the equivalent accumulated strain fields at load increments of the 'shear to tension' test are shown for FE computations as well as for 2D projection DIC results from synchrotron laminography 3D data. The segmented damage from synchrotron laminography 3D data is shown for the 'shear to tension' LPC and compared with strain fields. Moreover, the stress state was assessed using FE where the stress triaxiality fields in the region of interest have been analysed for different loading increments. Last, the segmented damage has been quantified as surface void fraction by its projection on the future fracture surface during the non-proportional load path change.

4.2.1 Equivalent accumulated strain and damage fields

The accumulated strain fields were obtained with two different techniques: projection DIC from experimental 3D laminographic volume data and from FE simulations. In order to further assess the interaction of strain localization and damage evolution from shear to tension, the results during load path change were investigated and divided into three main periods: shear loading period in Fig. 5.8, tension elastic loading period in Fig.5.9 and tension plastic loading period in Fig.5.10. For selected load steps in Fig. 5.8, 5.9 and 5.10, the strain evolution in the highly strained middle plane region is given for the 'shear to tension' load path change. Simultaneously, the segmented damage fields were investigated in a volume (1100×1600×1000 voxels representing 792×1152×720 μm^3 shown in yellow in Fig. 5.8 (c)) of 3D laminographic data and are given in column (e) as top views, normal to the sheet plane, and in column (f) views normal to the shear plane at selected load steps indicated by the numbers in circles.

Shear loading period (steps 0-9) During shear loading, a similar shear band shape and amplitude of strain fields was found when comparing projection DIC and FEA in Fig. 5.8 (d)(g) respectively. The highly-strained shear band was situated along the line linking the two blunt notches. At the end of shear loading (step 9), the maximum equivalent accumulated strain measured by projection DIC reached up to 0.45 in shear band near the notches. Fig. 5.8 (e)(f) at the end of shear, at step 9, shows damage that nucleated and grew under shear. Such damage is commonly not expected as it is generally assumed in the literature that hydrostatic pressure is needed for damage to evolve (Pineau et al., 2016) whereas here straining occurred and localized in the region where stress triaxiality was close to zero. Damage features including large flat cracks and cracks within intermetallic particles were observed and were distributed uniformly through sample thickness during shear loading.

Tension elastic loading period (step 10-16) After unloading of the shear sequence, the sample was turned by 90 °and a tensile load was applied to the cruciform sample. The mesoscopic effect resulting from this operation are shown in Fig.5.9. The maximum strain value in the shear band only increased slightly due to the small elastic strains occurring during unloading and reloading. At the end of tension elastic domain (step 16), there was no hidden shear crack opening seen from segmented damage views in Fig.5.9 (b)(c) compared to those at the end of shear. Closed and invisible shear cracks might have been present during shear as the hydrostatic pressure was lacking to open them and make them visible in 3D imaging. This does not seem to be the case.

Tension plastic deformation sequence (step 17-24) Fig. 5.10 shows the strain and damage evolution during plastic deformation in tension up to final fracture. The shear band became wider under tensile loading and the measured equivalent accumulated strain increased up to 0.5 at the last step; number 24. With the onset of plastic deformation in tensile loading, the nucleated damage during shear loading continued to grow. Small damage features and large flat cracks could be distinguished. Subsequently the damage features coalesced into cracks that led to final failure along the shear band region in Fig. 5.10 (b)(c). During the last step before fracture (step 24), these damage features all grew very fast and coalesced into flat damage clusters. Damage evolution was mainly seen in the highly strained regions. The damage nucleated in shear loading may explain the reduction in ductility during tensile loading in Fig. 5.7(b) compared to the proportional tension-only test. The microscopic damage features evolution will be focused on in more detail in later sections below.

Fig.5.11 shows the strain profile along a horizontal line normal to the shear band for both (a) FEA and (b) projection DIC results. Here different colours represent different loading steps where FEA is shown as dashed lines and projection DIC as full lines in (c). The maximum strain level and distribution show good agreement between experiment and simulation. During shear loading, the maximum strain along the horizontal line increased from 0 to 0.4. When turned to subsequent tensile loading, maximum strain continued to increase up to 0.55 for FEA results and 0.48 for projection DIC at step 24 since the highly deformed images were not correlated by DIC for the last 2 steps. The projection DIC strain profile exhibits a second peak, which could be linked to a crystallographic effect (cf. grain size) considering its length.

4.2.2 Stress state

Thanks to FE computations, the stress state during this non-proportional load path could be evaluated. The stress triaxiality (mean stress divided by equivalent stress) distribution was analysed along two lines normal to the shear band at both the surface plane and middle plane in Fig. 5.12 (a) and (c). In Fig. 5.12 (b) and (d) the stress triaxiality profile along the shear band, i.e. in Y direction is shown. During the shear loading (blue), stress triaxiality along the shear band was near zero (between -0.1 and 0.05) for all curves, as intended. During subsequent tensile loading, the stress triaxiality increased to values from 0.4 to 0.6 at the middle plane whilst it decreased from 0.66 to 0.4 on the surface plane in Fig. 5.12 (a)(b). Thus, the middle plane was under higher stress triaxiality during the tensile loading where high strain was encountered in Fig. 5.12 (c)(d).

4.2.3 Damage quantification and analysis

Fig. 5.13 (a) shows the raw volume data of 2560×2560×1500 voxels that were imaged by 3D synchrotron laminography. In order to focus on the region of interest where damage developed, the raw volume was cut into a smaller volume with a size of 1100×1600×1000 voxels. Using a region growing algorithm (Buljac et al., 2018b), the damage (black) was segmented from aluminum matrix (grey) in Fig. 5.13 (b). It was chosen to project the damage on one surface (fracture surface) as the flat cracks are more detrimental than voids but have a very low void volume fraction. This is why the surface void fraction measurement seems to be more relevant in evaluating the damage progression. A ROI

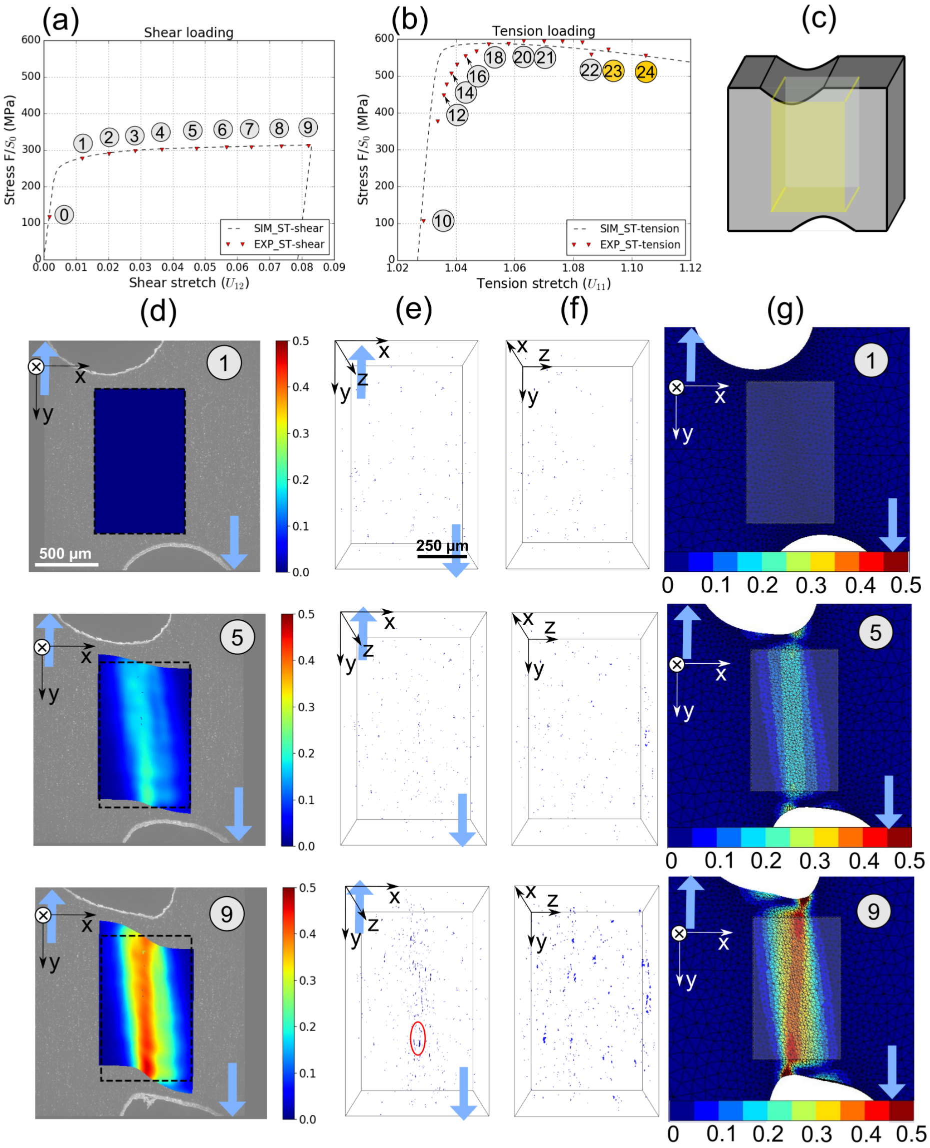

Figure 5.8: The experimental and simulated nominal stress versus stretch curves for (a) shear to (b) tension loading.(c) ROI location. Shear loading sequence: Accumulated equivalent strain fields on the middle plane in the ROI via (d) laminography data based P-DIC (72 μ*m* deep projection along *Z* axis) and (g) FEA. Segmented damage visualizations of *in situ* laminography data (c) yellow ROI (1100×1600×1000 voxels) from (e) X-Y plane and (f) Y-Z views during shear loading period from 'shear to tension' (ST) load path change.

(green) was selected where the damage along *X* axis (200 pixels = 144 μm) was projected on the future fracture Y-Z surface (yellow) as shown in Fig. 5.13 (b) and binarized as

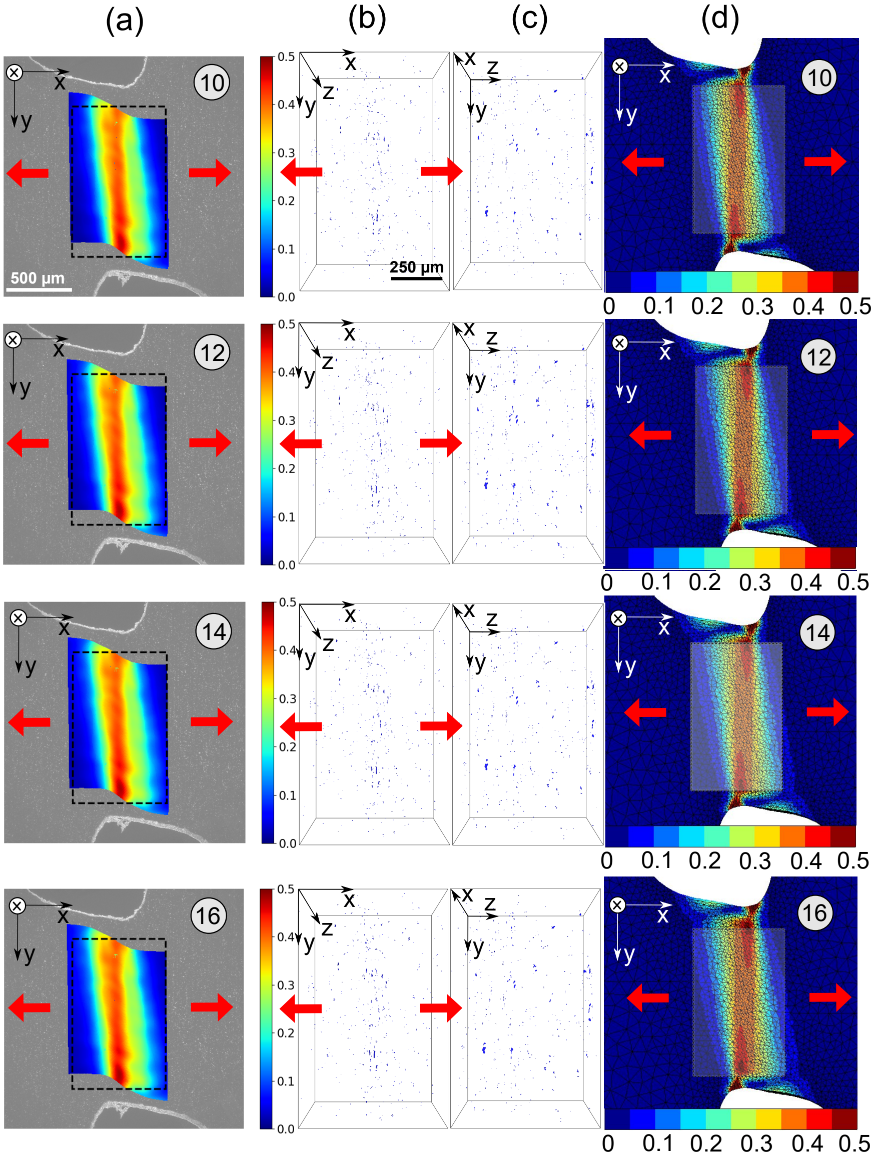

Figure 5.9: Elastic part of the tensile loading sequence: Accumulated equivalent strain fields on the middle plane via (a) laminography data based P-DIC (72 μm deep projection along Z axis) and (d) FEA. Segmented damage visualizations from *in situ* laminography data (b) X-Y plane and (c) Y-Z views during tension plastic period from 'shear to tension' (ST) load path change.

surface void fraction in Fig. 5.13 (d).

The damage evolution was quantified as surface void fraction versus equivalent accumulated strain from the P-DIC profile (last two points with dashed line are FE results) shown in Fig. 5.13 (e) during the 'shear to tension' non-proportional loading. The sur-

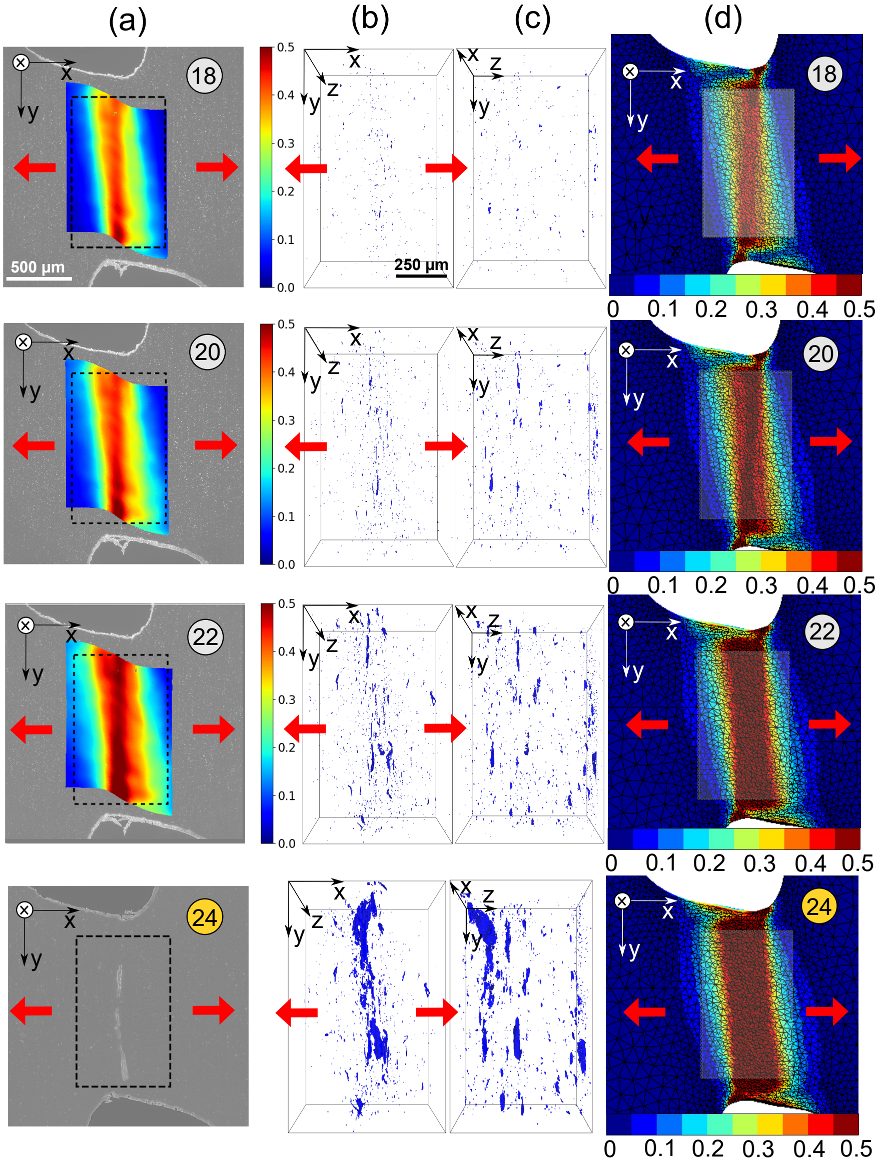

Figure 5.10: Plastic deformation part of the tensile loading sequence: Accumulated equivalent strain fields on the middle plane using (a) laminography data based P-DIC (72 µ*m* deep projection along Z axis) and (d) FEA. Segmented damage visualizations from *in situ* laminography data (b) X-Y plane and (c) Y-Z views during tension-plastic period from 'shear to tension' (ST) load path change.

face void fraction grew steadily till the end of shear where voids and flat cracks were observed. A void surface fraction of about 1 % was found at the end of shear. Then a slight decrease of void fraction was subsequently seen due to unloading followed by tensile elastic loading which closed some voids. Finally the damage surface fraction in-

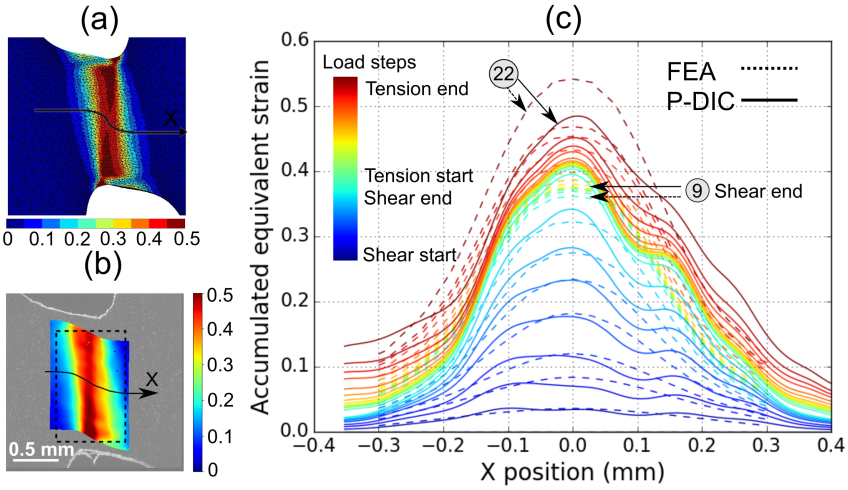

Figure 5.11: a) Indication of the horizontal profile line (X) for (a) FE and (b) for projection DIC along which the accumulated strain profiles (c) were obtained during 'shear to tension' loading by projection DIC (full line) and via FE analyses (dashed line).

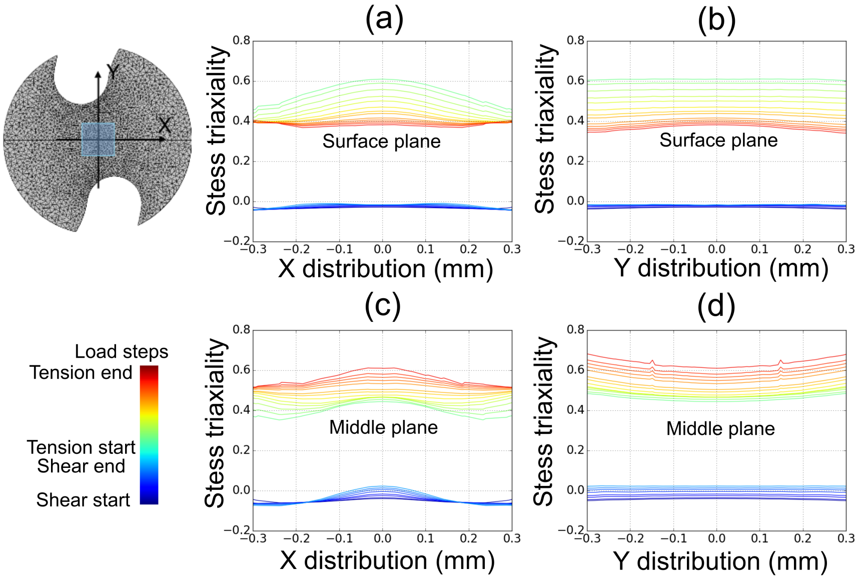

Figure 5.12: Stress triaxiality distributions along the horizontal line X axis and vertical line Y axis from shear load to tension at (a)(b) surface plane and (c)(d) middle plane from FEA calculation.

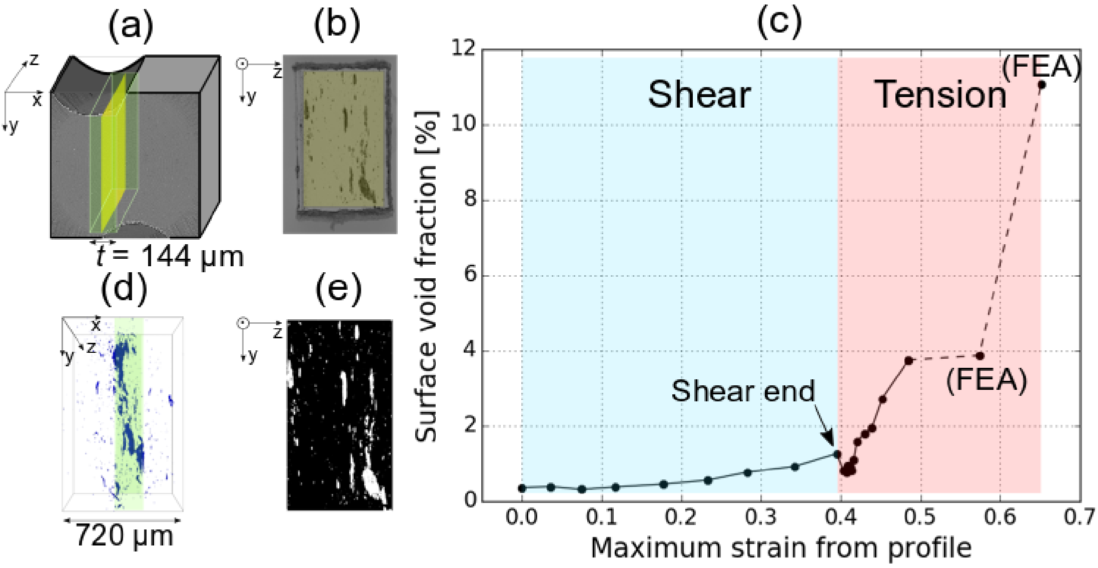

Figure 5.13: Damage quantification: (a) and (b) schematic representation of the green ROI in the scanned volume for damage surface fraction measurement, (d) Segmented damage inside green ROI from laminography volume data is projected along the X axis (144µm) on the yellow 2D plane shown (b) and in (e), (c) measured surface void fraction versus accumulated equivalent strain during the ‘shear to tension’ load path change while the strain of the last two points were from FE and their void fractions from lower resolution scans.

creased with a higher slope up to 4 % and then substantially up to 11 % during tension until reaching fracture. Please remember the damage evolution of the last two points was obtained from the scans at lower resolution and are therefore underestimated because some damage features were not able to be captured at the lower resolution.

4.3 Microscale: Damage micromechanisms

After mesoscale damage quantification during the non-proportional load path change, a deeper investigation of damage mechanisms is shown here via the high resolution 3D imaging data acquired. Two main damage features were found and focused on: flat cracks and damage linked to nucleation of voids on intermetallic particles. These features were tracked during the laminographic experiment from shear to tension loading.

4.3.1 Flat crack

One of the flat cracks is visualised in Fig. 5.14 (a) and can be followed during the loading in (d). The minimum grey value in the selected region was projected along the thickness direction Z axis to obtain a surface projected damage image of 400 pixels × 200 pixels

(288×144 μm^2) shown in in Fig.5.14 (b). The projected damage images were observed and tracked from shear to tension in Fig. 5.14 (d). Three flat cracks were first observed at step 5 and they grew slightly with shear loading. These features did not nucleate on intermetallic particles. The size in terms of length and width of these cracks resembles the typical grain size. The cracks could be intergranular or transgranular. Subsequently the cracks opened under tensile loading. They started to coalesce at step 18 and finally led to a long flat crack. The three-dimensional evolution of the flat crack is shown in Fig. 5.14 (c) where different colours represent different loading steps. It can be seen that the damage growth and coalescence is a continuous process. The crack first nucleated and then grew during shear. Under subsequent tension loading it further grew and different crack parts coalesced.

4.3.2 Intermetallic particle crack

An intermetallic particle of 30 μm × 10 μm size was tracked in Fig.5.14 (e). During shear loading, the particle rotated from $26°$ to $-25°$ with respect to the horizontal line and a fracture within the particle was formed the orientation of which was normal to the principal stress direction at end of shear (step 9) which had already been observed in (Tancogne-Dejean et al., 2021). Also a vertical crack was seen at the end of shear loading. During unloading the crack closed to some extent. They subsequently reopened and grew under tensile loading. This was particularly seen for the vertical crack.

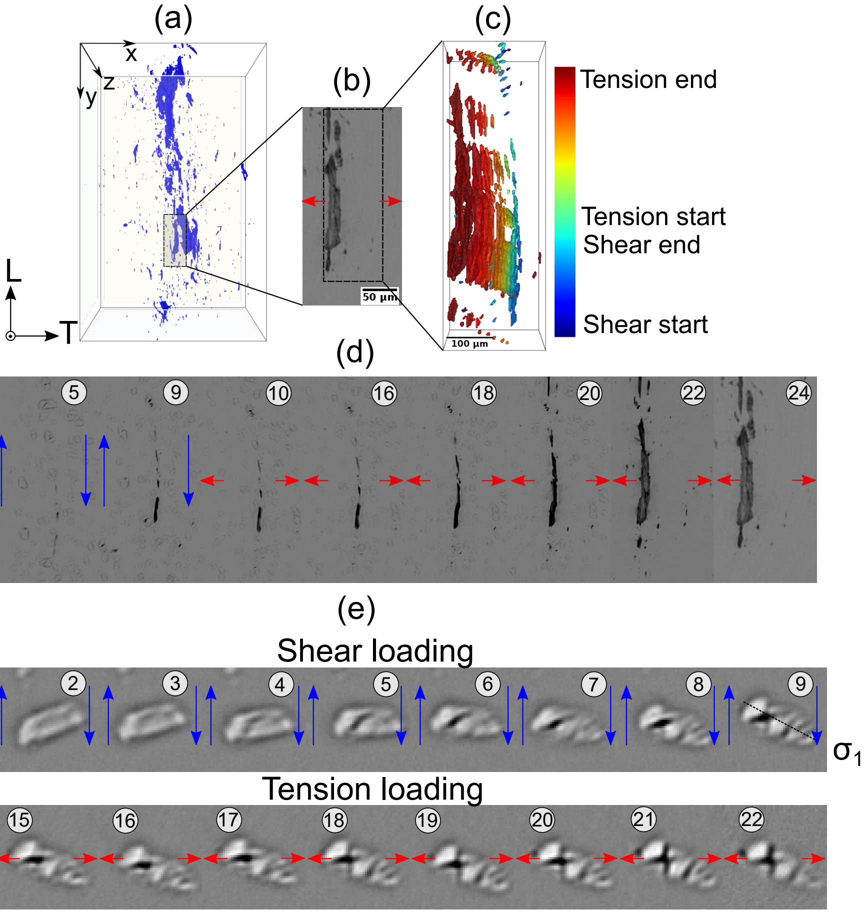

Figure 5.14: (a) Damage visualization of laminography data in the shear band region at final load step 24 before fracture where (b) one of flat cracks was tracked. (c) Local 3D damage visualization of the tracked flat crack, shown in (b), with different colours representing loading steps from shear to tension. Damage view of two typical damage features: (d) flat crack, shown in (b), evolution studied by minimum grey value projection along 100 voxels and (e) single section of the evolution of an intermetallic particle during nonproportional 'shear to tension' loading.

5 Discussion

A detrimental effect of the shear pre-loading before tension was clearly identified in the present study. The tension stretch to fracture was reduced by about 20% compared to proportional loading at the macroscale. On the one hand, the nominal tensile stress after shear pre-loading hardening increased by 20% up to 600 MPa. A higher stress level could contribute to ductility reduction. On the other hand, it was also shown that shear-dominated loading already led to damage nucleation and growth even though the stress triaxiality was close to zero. This induced damage can explain the ductility reduction.

The damage of an aluminum alloy AA2024-T3 under shear loading was investigated via synchrotron X-ray laminography in (Tancogne-Dejean et al., 2021). Particle cracking as a damage nucleation mechanism was also found in that study but no flat grain related cracks were found. The flat cracks are believed to be more detrimental for aluminum alloy 2198-T8R whilst intermetallic particles and pre-existing voids play a minor role. The flat cracks are probably linked to the material grain structure considering the crack length and width that are around several tens of micro meters. These flat cracks that nucleated under shear subsequently grew and coalesced to final cracks under tension shown in Fig.5.14(d). Similar cracks have also been found for this material in tension loading (Rousselier et al., 2017). For this material in T3 condition a crack nucleated in tension was shown to be transgranular (Buljac et al., 2018a).

Previous shear-dominated damage mechanism studies almost all focused on the void-mediated failure (i.e. void nucleation-rotation-elongation) (Roth et al., 2018; Torki and Benzerga, 2018). However, for an alloy with very limited initial porosity or pre-existing voids, the void-mediated damage mechanism is not likely to govern the failure and the origin of the detrimental flat cracks deserves further exploration. This also highlights the effect of microstructure on damage mechanisms in shear that should be investigated.

Furthermore, the damage mechanisms under load path changes are even more complex. Brünig et al. (2021) studied the remarkable effect of shear preloadings to a different extent (45%, 65% and 90%) on the ductility under tension loading. The fracture displacement of different shear preloadings was significantly reduced with that compared to proportional tensile loading. In the SEM observation of the samples that were pre-loaded in shear to 90% of the failure displacement, micro-shear-cracks were observed on fracture surfaces and are supposed to have accumulated as macro-cracks in the subsequent tensile loading. Using the advanced technique synchrotron laminography, the damage evolution could be further analysed at high resolution during load path change in terms of micro damage mechanism.

The current μm-resolution was not sufficient for a detailed study of the nucleation of flat crack features under shear loading. Synchrotron nanolaminogrpahy was successfully applied to study ductile damage for tensile loading (Hurst et al., 2021), which allows a three-dimensional insight in flat sheet specimens at voxel sizes down to 50 nm. The formation of flat cracks and intermetallic particle cracks features could be observed at a very early stage and the damage micro-mechanism under shear loading should be better studied and understood.

A similar methodology as in the present study could be applied to other load path changes: ‘tension to shear’. With 3D synchrotron laminography, the shear damage mechanism under non-proportional load path changes would be better understood up to fracture.

In this study, an anisotropic elasto-plastic material model was applied. In order to better predict damage and failure, a suitable damage model is highly necessary under different non-proportional load path changes. Current models under shear-dominant loading (Roth et al., 2018; Torki and Benzerga, 2018) assume the shape changes of pre-existing voids or decohesion of rigid particle rather than void nucleation without the presence of particles.

A fully coupled classical void damage at high stress triaxiality and Coulomb model at the slip system scale at low stress triaxiality based ductile fracture model (Rousselier and Luo, 2014) could also be applied to predict the present data of non-proportional load path changes. A reduced texture methodology (RTM) was used to provide computational efficiency and this approach involved a significant reduction of the number of representative crystallographic orientations. The damage nucleation along slip planes could represent the observed generation of shear cracks.

6 Conclusions

An *in situ* laminography multiscale experiment was carried out to study the deformation and ductile damage evolution during a non-proportional ‘shear to tension’ load path change using a cross shaped sample. Finite element calculations using an anisotropic plasticity criterion were performed to provide strain and stress state fields. Conclusions on multiple scales are drawn in the following.
On the macroscale:

- A cross shaped sample geometry for ‘shear to tension’ loading path changes was designed.
- A macro-strain metric was defined and measured optically using the DIC displacement measurements of four points during the mechanical loading, especially during non-proportional load paths. The same procedure was applied to the 3D FE simulations.
- For a load path change of type ‘shear to tension’ the tension stretch to fracture of is reduced by about 20% compared to the proportional tensile load path.

On the mesoscale:

- An accumulated equivalent strain was chosen that was suited for non-proportional load paths. It was applied to both projection DIC (performed on 3D laminography data) and to the FE simulation results, for the strain measurement in the sample mid plane.

- Similar localization shear bands have been found comparing experimental projection DIC and numerical finite element simulations in terms of shape and magnitude.
- Damage was found at the end of the shear period. The damage evolution was quantified in terms of surface void fraction as a function of the measured accumulated equivalent strain over the entire load history.

On the microscale:

- Two main types of damage features were found: intermetallic particle cracks and (most probably grain-related) flat cracks. The latter are more detrimental in this Al alloy 2198 T8R material.
- Surprisingly damage nucleation could be observed (via laminography) already at the end of shear pre-strain during which stress triaxiality was nearly zero.
- The nucleated damage grew and led to final fracture during tensile loading after the shear pre-strain.

Part III

Modeling of Ductile Damage under Load Path Changes

Chapter 6

A polycrystalline model for ductile damage under load path changes

The ductility for a ‘shear to tension’ load path change was seen reduced in previous chapters compared to a proportional tension test. Two types of damage features, grain-related flat cracks and particle-related voids, have been observed in chapter 4 under intense shear loading in an aluminum alloy 2198. The detrimental flat cracks were proved to be both transgranular and intergranular. As AA2198 contains negligible initial porosity, void evolution is limited in the absence of high stress triaxiality. The aim of this chapter is to identify a suitable model and to reproduce numerically failure in shear and tension as well as to predict the damaging effect of the shear pre-loading.

This chapter is under preparation for the potential publication.

Abstract

A ductile damage model, that fully couples classical void growth at high stress triaxiality and Coulomb model at the slip system scale for low stress triaxiality, was applied in this study for a non-proportional load path change. The Coulomb model combines the resolved normal and shear stresses for each slip plane and directions. A Reduced Texture Methodology (RTM) was used to provide computational efficiency and this approach involved a significant reduction of the number of representative crystallographic orientations. The 12-grain model using 12 crystallographic orientations was validated for non-proportional load path change experiments. The model was calibrated in plasticity against a (previous calibrated) macroscopic anisotropic plasticity model using single element calculations under proportional tension, shear and non-proportional 'shear to tension' (ST) loadings. Subsequently the damage parameters were calibrated against the proportional loading shear and tension experimental results using full 3D mesh calculations. The calibrated model succeeded in predicting the non-proportional 'shear to tension' failure. Locally, the damage indicator maxima coincided with the damage location where the damage features were observed via experimental 3D imaging.

1 Introduction

Ductile fracture of metals is known for its mechanism of void nucleation-growth-coalescence driven by high stress triaxiality (Pineau et al., 2016). Recently, more research has focused on the mechanism especially at low stress triaxiality or called shear dominated loading conditions. Many experimental works (Bao and Wierzbicki, 2004; Barsoum and Faleskog, 2007a; Brünig et al., 2021; Dunand and Mohr, 2011; Gross and Ravi-Chandar, 2016; Kong et al., 2021; Roth and Mohr, 2016; Tancogne-Dejean et al., 2021) have been performed to investigate the ductile failure under proportional and/or non-proportional shear-dominated loading paths. In the absence of high stress triaxiality, void growth is limited where no obvious increase for the main damage indicator, void volume fraction, during intense shearing. Experimentally, shear damage features have been observed in laboratory macro specimens via 2D *in situ* SEM (Achouri et al., 2013; Gross and Ravi-Chandar, 2016) and 3D X-ray synchrotron imaging (Kong et al., 2022a,b; Roth et al., 2018; Tancogne-Dejean et al., 2021). Particle related void nucleation, including intermetallic particle debris and matrix-particle debonding, were commonly seen to rotate and flatten till coalescence in ductile metals (e.g. aluminum alloys and steels). Particularly, grain-related flat cracks without attached particles were found in AA2198, which turned to be detrimental in (Buljac, 2017; Kong et al., 2022a,b). Furthermore, the damage mechanism under non-proportional load path change is even more complicated and the mechanisms cannot clearly be established by observing fracture surfaces (Brünig et al., 2021; Kong et al., 2021; Papasidero et al., 2015).

The classic Gurson model (Gurson, 1977) is not suited to predict shear failure under zero mean stress where the loss of load carrying capacity is associated to void growth and softening, and thus absent under zero stress triaxiality. Nahshon and Hutchinson (2008) modified the Gurson model so that it accommodates failure under intense shearing by letting the artificial damage parameter increase at zero stress triaxiality. The simulations using micromechanical unit cell with pre-existing cylindrical void have been performed to study shear ductile failure (Nielsen et al., 2012; Nielsen and Tvergaard, 2011; Tvergaard, 2008, 2009), and they found the void closure leading to micro-cracks that rotate in the shear field, instead of void growth to coalescence. Nielsen and Tvergaard (2011) analyzed the shear failure mechanism of primary voids and studied the effect of smaller secondary damage that exists with or nucleation in the ligaments between large primary voids that coalesce during intense shearing. Nielsen et al. (2012) performed a 3D cell-unit simulation with spherical voids where they found a good agreement between 2D results and 3D predictions when the void volume is kept constant. Despite the damage evolution is no longer linked to the void volume fraction, where closure of existing void or delayed growth were predicted in unit cell studies during shearing, the model combined the shear softening due to void distortion and inter-void linking at zero stress triaxiality. On the other hand, Madou and Leblond proposed an alternative extension (Madou and Leblond, 2012a,b, 2013; Madou et al., 2013) of the Gurson model, modelling void shape variation from spherical to ellipsoidal and void rotation. A second porosity variable g contributes to the material softening with the usual one f, f being substituted by $f{+}g$ in the plastic potential. The former can characterize the detrimental effect of voids during shear in case f is close to zero. Morin et al. (2016) applied this "ML" model to micromechanical simulations (Nielsen et al., 2012; Nielsen and Tvergaard, 2011; Tvergaard, 2008, 2009) under shear with initial voids of different shape. Morin et al. (2017) applied this model to the so called *butterfly* macro specimen under shear loading with comparison to experiments in Dunand and Mohr (2011), demonstrating that this complex model can be used in finite element calculations.

Aiming to represent an anisotropic plastic behaviour, the yield function proposed by Bron and Besson (2004), an extension from the functions given in (Barlat et al., 1991; Karafillis and Boyce, 1993), satisfactorily described yield anisotropy and Lankford coefficient simultaneously in all orientations. The macroscopic plasticity model has been applied to macro specimens at large strain under complex non-proportional load path changes (Kong et al., 2021). Cailletaud (1987, 1992) used the *physical related* hardening variables from the microscale (e.g. local slip rate) to represent complex macroscopic response. A Localization process gives the local stress in each grain and the resolved stress on each slip system based on the self-consistent homogenization scheme. Haouala et al. (2018) investigated the effect of grain size on the mechanical response based on computational homogenization of the polycrystal behaviour. Crystal plasticity finite element method (CPFEM) applied crystal plasticity directly at the Gauss point scale of polycrystalline aggregates, which has been employed on a periodic unit cell in simulating and assessing grain interactions (Gérard et al., 2009; Kanjarla et al., 2010; Roters et al., 2010). Frodal et al. (2021) applied CPFEM to different micro tensile specimens. However, a highly cost computational time is needed in this method where 300-800 hours with 24 cores are needed even with a simple damage model $\sigma_{eff}=\sigma/(1\text{-}D)$ for micro specimens, not to mention macro samples of complex geometry.

Although polycrystalline plasticity seems less *physical* than CPFEM, its computation time can be remarkably reduced. The Reduced Texture Methodology (RTM) is used to provide the computation efficiency for numerical applications (Rousselier et al., 2009, 2010; Rousselier and Leclercq, 2006; Rousselier et al., 2012), which limits the number of representative crystallographic orientations. The Rousselier porous plasticity model can be embedded into the polycrystalline framework (Méric et al., 1991) with plasticity and damage models at the slip system scale, for instance, the Coulomb ductile fracture model (Rousselier and Luo, 2014) as well as the nucleation and growth models of very small voids as second population at the slip band scale (Rousselier, 2021). 8 to 15 representative grain orientations were chosen to dramatically reduce the CPU time. Texture can be accurate if texture parameters are calibrated as well.

This chapter aims to investigate the anisotropic plasticity behaviour in an aluminum alloy 2198-T8R under non-proportional load paths. The Coulomb-Rousselier model, which combined 2.3 Coulomb slips and 2.4 classic void growth in the frame work of RTM-based polycrystalline plasticity, is presented in Section 2. Methods including material, model calibration strategy and finite element meshes are given in Section 3. Results of macroscopic stress - strain calibration and microscopic damage fields under different loading paths are presented in Section 4. The discussion of Section 5 deals with the comparison between experimental damage observation and numerical predictions as well as the effects of predictive different pre-loadings on ductility. Section 6 ends with the conclusions and perspectives.

2 Constitutive modeling

In this work, A,$\vec{A}$, $\underline{A}$, $\underline{\underline{A}}$ denote a scalar, a vector, a second order tensor and a fourth order tensor respectively. Upper-case symbols (e.g. $\underline{\Sigma}$, $\underline{E}^p$...) represent mechanical variables (e.g. $\underline{\sigma}$, $\underline{\varepsilon}$, $\underline{\beta}$, τ, γ...) at the macroscopic scale while lower-case symbols are at the microscopic scales. All the equations are written in a material embedded co-rotational frame (Rousselier et al., 2009, 2010, 2012).

A self-consistent polycrystalline model (Méric et al., 1991) was the backbone of the constitutive model. The physical based plasticity succeeded in describing the plastic anisotropy and yield surface distortion, which enabled to predict complex behaviours in complex load paths.

2.1 The self-consistent polycrystalline model

In the self-consistent method, each of N *grains* was considered as an inclusion in the homogeneous equivalent material, which represented a set of physical grains with close crystallographic orientations (or phase in the literature). The macroscopic stress $\underline{\Sigma}$ and plastic strain $\underline{E}^p$ are defined as the homogenization of every *grain* g with a volume fraction f_g in all N *grains*:

$$\underline{\Sigma} = \sum_{g=1}^{N} f_g \underline{\sigma}_g \quad \text{with} \quad \sum_{g=1}^{N} f_g = 1 \tag{6.1}$$

$$\underline{E}^p = \sum_{g=1}^{N} f_g \underline{\varepsilon}_g^p \quad \text{with} \quad \sum_{g=1}^{N} f_g = 1 \tag{6.2}$$

$$\underline{\varepsilon}_g^e \equiv \underline{E}^e = \left(\frac{1+\nu}{E}\underline{\underline{1}} - \frac{\nu}{E}\underline{1} \otimes \underline{1}\right) : \underline{\Sigma} \tag{6.3}$$

where E, ν stand for Young's modulus and Poisson's ratio in the case of isotropic elasticity.

In order to a relation between the homogenized stress at the macroscopic scale $\underline{\Sigma}$ and microscopic stress of each grain $\underline{\sigma}_g$, the scale transition rule (also called 'β rule') was applied as the localization equations (Cailletaud, 1987, 1992). It provides a general method to model the elastic-plastic transition of intergranular deformations by introducing an intermediate deviatoric strain tensor $\underline{\beta}_g$:

$$\underline{\sigma}_g = \underline{\Sigma} + C(\underline{B} - \underline{\beta}_g) \quad \text{with} \quad \underline{B} = \sum_{g=1}^{N} f_g \underline{\beta}_g \tag{6.4}$$

$$\dot{\underline{\beta}}_g = \dot{\underline{\varepsilon}}_g^p - \underline{\underline{D}} : \underline{\beta}_g \|\dot{\underline{\varepsilon}}_g^p\| \quad \text{where} \quad \|\dot{\underline{\varepsilon}}_g^p\| = \sqrt{\frac{2}{3}\dot{\underline{\varepsilon}}_g^p : \dot{\underline{\varepsilon}}_g^p} \tag{6.5}$$

Here the scalar modulus C is similar to the elastic shear modulus $\mu = E/2(1+\nu)$ according to Kröner theory (Kroner, 1961). The second invariant $\|\dot{\underline{\varepsilon}}_g^p\|$ represents the von Mises equivalent strain rate for each grain g. Sai et al. (2006) proposed the fourth order tensor $\underline{\underline{D}}$ for anisotropic materials and 10 independent components D_{ij} were needed and explained in Appendix B.1.

The RTM can make use of any polycrystalline plasticity model with a very small number of crystallographic orientations. A *grain* can be represented with a set of texture parameters including Euler angles (φ_1, Φ, φ_2) and volume fraction $frac$, where its orientation is denoted from the material frame with three successive rotations: rotation φ_1 around the axis 3 of the material reference frame, rotation Φ around the updated axis 1 and rotation φ_2 around the updated axis 3. In this study for orthotropic aluminum sheet, each texture component consists of four symmetric grain orientations as (φ_1, Φ, φ_2), (-φ_1, Φ, -φ_2), (-φ_1, -Φ, -φ_2), (φ_1, -Φ, φ_2).

It has to be remarked that the self-consistent model in present work did not consider for (i) the grain location in the aggregate, (ii) the grain size effect and (iii) the strain and stress gradients within grains (e.g. grain boundary effect was neglected).

2.2 The single crystal plasticity

This subsection presents the constitutive equations at the scale of a single crystal. The single crystal model relates the slip rate $\dot{\gamma}_s = 2\dot{\epsilon}_s$ and the resolved shear stress τ_s of each slip system ($s = 1$ to M) where the index g for each grain is omitted in the following.

The resolved shear stress τ_s at the given slip system number s is defined:

$$\tau_s = \underline{\sigma}_g : \underline{m}_s \quad \text{with} \quad \underline{m}_s = (\vec{n}_s \otimes \vec{n}_s + \vec{n}_s \otimes \vec{n}_s)/2 \tag{6.6}$$

where the orientation tensor $\underline{m}_s$ is defined with slip plane normal vector $\vec{n}_s$ and slip direction vector $\vec{l}_s$ in this plane.

For the FCC crystallographic structure in this study, octahedral slip systems $\{111\}\langle 100\rangle$ were considered with $M = 12$. A phenomenological Norton-like viscoplastic model was used for the constitutive equations of each slip system:

$$\dot{\gamma}_s = \dot{\nu}_s Sign(\tau_s - X_s) \tag{6.7}$$

$$\dot{\nu}_s = |\dot{\gamma}_s| = \max[0, (\frac{|\tau_s - X_s| - r_s}{K_s})^{n_s}] \tag{6.8}$$

$$r_s = r_s(\nu_s, \nu_t),\ \forall t \neq s \tag{6.9}$$

$$\dot{\alpha}_s = \dot{\gamma}_s - d\alpha_s \dot{\nu}_s\ ,\ X_s = c\alpha_s \tag{6.10}$$

For each slip system, an internal variable $r_s = r_s(\nu_s, \nu_t)$ is introduced for isotropic hardening, which depends on the cumulative slip ν_t of the M slip systems. The kinematic hardening parameters c and d were set as 0 in Eq.6.10 since no experimental dataset under cyclic loading was available for this material. Viscoplastic flow reached the rate-independent limit for large n_s and small K_s. For the FCC crystallographic structures, viscosity parameters K_s=K_{vp} and n_s=n_{vp} kept constant for all octahedral slip systems.

Chapter 4 presented very large strains (e.g. greater than 0.6) for shear experiments. Therefore, the dislocation structures at large strain needed to be reorganized and modeled. Luo and Rousselier (2014) had proposed a simple method to model the hardening matrix evolution with plastic strain. The isotropic hardening behaviour is controlled by three (i=1,2,3) non-linear exponential terms as following:

$$r_s = R + \sum_{i=1}^{3} Q^i \sum_{t=1}^{M} H^i_{st}[1 - \exp(-b^i \nu_t)] \tag{6.11}$$

where R is the initial critical resolved shear stress. The 12×12 symmetric hardening matrix H^i_{st} only depends on six independent components h^i_1 to h^i_6 for each hardening term. For brevity, more information about the hardening matrix H^i_{st} is given in Appendix B.2.

Texture evolution can be modeled with the RTM (Rousselier et al., 2009, 2010). Although it was not used in this work considering the higher numerical cost and parameter re-calibration, it had been tried for macro specimen in Appendix B.4.

2.3 The Coulomb fracture model at the slip system scale

In polycrystalline metals, in the absence of hydrostatic stress for particle-related void damage growth under shear loading, granular related shear flat cracks have been observed in the localization zone (Kong et al., 2022b; Luo and Rousselier, 2014). In order to model this phenomenon at the slip system scale, the total slip rate, consisting of the classical slip rate $\dot{\gamma_s}$ and an additional Coulomb slip rate $\dot{\gamma_s^C}$ activated at large strains is proposed:

$$\dot{\gamma}_s^{tot} = \dot{\gamma}_s + \dot{\gamma}_s^C \tag{6.12}$$

At the slip system scale, the only two stress components: the resolved shear stress τ_s and the normal stress stress σ_{ns} normal to the slip plane. Both affect the second slip rate activation according to Coulomb criterion with parameters c_0 in Eq.6.14 and R_0 in Eq.6.15.

$$\dot{\nu}_s^C = \dot{\gamma}_s^C Sign(\tau_s) \tag{6.13}$$

$$\dot{\nu}_s^C = \max[0, (\frac{|\tau_s| + c_0\sigma_{ns} - r_s^C}{K_0})^{n_0}] \tag{6.14}$$

$$r_s^C = R_0 + Q_0[1 - \exp(-b_0\nu_s^C)] \tag{6.15}$$

A combined damage variable d is defined to quantify damage extent with maximal Coulomb slip γ_{max}^C and porosity f:

$$d = \sqrt{(\frac{\gamma_{max}^C}{\gamma_u})^2 + (\frac{f}{f_u})^2} \tag{6.16}$$

where γ_u and f_u are ultimate values set as 3 and 0.25 respectively in this study. In related finite element computation, the broken criterion is that the Gauss point will be regarded as *broken* state if its d reaches 1. For both damage models, softening is already large at values much smaller than γ_u and f_u. At d=1, the material has almost completely lost its load-carrying capacity.

2.4 Classic void damage for particle-related porosity growth

Porous plasticity is coupled with polycrystalline plasticity (Luo and Rousselier, 2014; Rousselier and Leclercq, 2006; Rousselier and Luo, 2014) where Rousselier and Leclercq (2006) proposed an additional *grain* g=0 (G0) with a variable void volume fraction f.

G0 represents the physical voids but it is not a void in the sense of homogenization theories since the resulting stress is not zero in G0. The volume fraction of the classical *grains* (g=1 to N) is (1-f)f_g in stead of f_g. Different from Eq.6.2, once f is added, the homogenized strain rate at the macroscopic scale is written as:

$$\dot{\underline{E}}^p = (1-f)\sum_{g=1}^{N} f_g \underline{\varepsilon}_g^p + f\dot{\varepsilon}_m^p \underline{1} = \dot{\underline{E}}_{dev} + \dot{E}_m^p \underline{1} \quad \text{with} \quad \sum_{g=1}^{N} f_g + f = 1 \tag{6.17}$$

where the plastic mean strain ε_m^p=$trace(\underline{\varepsilon}^p)/3$.

The Gurson model (Gurson, 1977) as well as its extensions: the GTN model (Tvergaard and Needleman, 1984) and other derivative models (Nahshon and Hutchinson, 2008) are widely used in applications. However, they are not easy to reformulate within the polycrystalline plasticity model because of its quadratic formulation in the deviatoric stress space. The Rousselier model (Rousselier, 1981, 1987, 2001; Rousselier and Luo, 2014) was selected for the development in this study.

The viscoplastic yield condition for polycrystalline material:

$$\frac{\Sigma_{eq}}{1-f} - (\sum_{g=1}^{N} f_g \underline{\sigma}_g)_{eq} + D_1 f \sigma_1 \exp(\frac{\Sigma_m^*}{(1-f)\sigma_1}) \tag{6.18}$$

where Σ_{eq} is the von Mises equivalent stress and Σ_m is the mean (or hydrostatic) stress. D_1 and σ_1 are material parameters. As proposed in Morgeneyer et al. (2009), Σ_m is substituted with Σ_m^* to represent 3D anisotropic.

$$\Sigma_m^* = \alpha_L \Sigma_{LL} + \alpha_T \Sigma_{TT} + \alpha_N \Sigma_{NN} \quad \text{with} \quad \alpha_L + \alpha_T + \alpha_N = 1 \tag{6.19}$$

In this study, the void growth was isotropic, thus α_L=α_L=α_L=1/3 where L, T and N are principal axes of orthotropy in an orthotropic material.

The void volume fraction rate $\dot{f}$ indicates the sum of a first terms due to the mass conservation law and a second term for void nucleation:

$$\dot{f} = 3(1-f)\dot{E}_m^p + A\dot{E}_{eq}^p \tag{6.20}$$

Morgeneyer et al. (2009) assumed A can be constant between two values of E_{eq}^p and equal to zero otherwise while Chu and Needleman (1980) gave the factor A using a Gaussian function of $\dot{E}_{eq}^p$ with parameters f_N,σ_N and E_N:

$$A = \frac{f_N}{\sigma_N\sqrt{2\pi}} \exp[-(\frac{E_{eq}^p - E_N}{\sigma_N\sqrt{2}})^2] \tag{6.21}$$

In this present work, the parameters were set D_1=2, σ_1=350 MPa in Eq.6.18 and f_N=0.0034, σ_N=0.02, E_N=0.10 in Eq.6.21 as previous work in Rousselier (2021) for the same aluminum alloy.

3 Methods

3.1 Material

The target material in this study was an aluminum-copper-lithium alloy 2198 in T851 temper in its recrystallized state. As in the previous chapters, it was referred to as 2198T8R henceforth. Moderate plastic anisotropy was found in different loading directions (R: rolling direction, T: transverse direction and D: 45° from the rolling direction around the thickness direction).

As presented in chapter 3, macro and micro specimens were loaded not only in proportional loading but also non-proportional loading at room temperature. Proportional tests such as uniaxial tension (UT) tests in different loading directions and notched tensile (NT) tests in L and T, were conducted on the 2 mm thickness macro specimens. Besides, micro experiments shear-only (SO) and tension-only (TO) were carried out with the 1 mm thick micro specimens. The non-proportional tests such as 'shear to tension' (ST) and 'tension to shear' (TS) were carried out on the same series cross-shaped specimens. It means that the specimen was under first loading and unloaded before turning to the second loading. These experimental data was presented in detail and analyzed in Kong et al. (2021).

3.2 Model calibration strategy

A hybrid experimental-numerical model calibration procedure was used to identify all parameters including plasticity parameters and damage parameters. Firstly, plasticity parameters including texture parameters, slip system hardening parameters and localization parameters were calibrated with the pseudo-experimental database from the macroscopic non-damage Bron-Besson (BB) model. The parameters of BB model were calibrated with the experimental database using full meshed calculations, including uniaxial tensile tests in different orientations (L, T and D), notched tensile tests (L and T) as well as the shear test (L) in chapter. A good agreement was obtained between experiments and macroscopic BB simulations with optimized parameters. Theoretically, microscopic polycrystalline model (PC) could be calibrated in the same way but it was much more time consuming for full meshed calculations during parameter optimization. In addition, BB model was able to achieve pseudo-experiment data augmentation under more stress states even non-proportional load path changes, where exact same boundary conditions could be confirmed in simple calculations for both models. Secondly, the damage parameters were identified with fracture experiments of the micro specimens under proportional shear and tension loadings. Lastly, the optimized model was used to predict the behaviour under different non-proportional load path changes (i.e. ST and TS).

The measured Young's modulus $E = 74$ GPa and Poisson's ratio $\nu = 0.33$ were assumed as constant in the material identification. The viscosity parameters in Eq.6.8 were set as $n_s = 20$, $K_s = 25$ MPa $s^{-1/n}$. Considering that the all experimental database was at non-negative stress triaxiality, the kinematic hardening parameters c and d in

Eq.6.10 were not considered for this material and set as 0 in this study.

Step I: Plasticity parameters calibration using simple simulations with Bron-Besson model It is noted that the damage options of Coulomb damage and void growth damage were not activated since the plasticity was calibrated with the non-damage macroscopic plasticity model at this step.
Texture parameters (11): For an orthotropic texture with 3 components, Euler angles of 12 grains are represented with 3 groups (i=1,2,3) including each volume fraction $frac_i$. 4 grains in each group are symmetrically distributed as [ϕ_1^i, Φ^i, ϕ_2^i, $frac_i$], [-ϕ_1^i, Φ^i, -ϕ_2^i, $frac_i$], [-ϕ_1^i, -Φ^i, -ϕ_2^i, $frac_i$], [ϕ_1^i, -Φ^i, ϕ_2^i, $frac_i$]. In total, 11 texture variables were identified (4×3 except $frac^1$=0.25-$frac^2$-$frac^3$).
Slip system hardening parameters (22): 7 isotropic hardening parameters including R and three groups (i=1,2,3) of non-linear isotropic hardening parameters Qi, bi in Eq.6.11. Two kinematic hardening parameters (c and d) are assumed as 0 since the compression experimental data is missing. Three groups of latent hardening parameters (h_2^i to h_6^i, i = 1,2,3) were included, assuming $h_1^i = 1$.
Localization parameters (10) for the self-consistent homogenization scheme: The fourth order $\underline{\underline{D}}$ was proposed by Sai et al. (2006) for anisotropic materials. With the Voigt notation, $\underline{\underline{D}}$ has 10 independent components (D_{11}, D_{21}, D_{22}, D_{23}, D_{31}, D_{32}, D_{33}, D_{44}, D_{55}, D_{66}) for orthotropic materials. The scalar modulus C of initial elastic accommodation was fixed as 20 000 MPa (Rousselier et al., 2009).

Step II: Damage parameters calibration using 3D mesh calculations with fracture experimental data base **Damage parameters (2):** Three variables of R_0, Q_0 in Eq.6.15 and c_0 in Eq.6.14 were calibrated with the proportional experimental database (shear-only and tension-only tests) in terms of global nominal stress - stretch curves, especially on the first abrupt load drop deciding for the stretch to fracture as a sign of the damage initiation. It could be assumed that $Q_0 = -R_0$ for a complete softening. b_0 was set as 2 for a slow decrease of the critical stress, resulting in stress softening and strain localization (Rousselier, 2021; Rousselier and Luo, 2014). The viscosity parameters were set as constant such as $K_0 = 25\ s^{-1/n_0}$ and $n_0 = 20$ for the strain rate independency.

3.3 Meshes

All calculations were performed in the commercial finite element software Z-set (Besson and Foerch, 1997). During the step I for plasticity calibration, there were two types of calculations. First, the simulator performed point simulations with a given material model by controlling strain or stress components (e.g. ϵ_{11} or σ_{11}) without any element. Secondly, simple calculations including uniaxial tensile and simple shear were applied on a single hexahedral element (c3d8). During the step II for damage calibration, the cross-shaped specimen in Fig.6.1 (a) was meshed with hexahedral elements in the central region (c3d8) and triangular prism elements (c3d6). The central region mesh was Cartesian as in previous works: a Kahn specimen in Rousselier (2021). The crack was expected to propagate more or less in the mesh direction. The use of similar meshes should optimize the transferability from one geometry to another one with the same damage parameters. In order to save computation time, only the region of interest (ROI) was modeled with the polycrystalline model in red while the element set of non-ROI sample was modeled with Bron-Besson model in grey and four supporters as isotropic elastic steel with high Young's modulus ($E = 210$ GPa) in blue. In Fig.6.1, two different mesh sizes in ROI (50 μm and 100 μm) were applied and noted as coarse and fine meshes respectively, in order to investigate the mesh size effect on strain localization and crack propagation. The total element numbers were 21 776 and 70 816, where the hexaheral elements (c3d8) were 1 728 and 13 056. The latter was around eight times to the coarse mesh number.

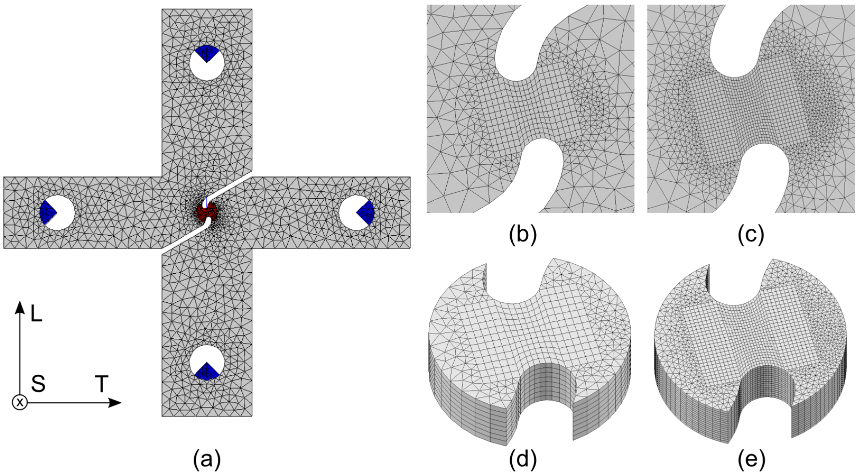

Figure 6.1: Mesh geometry: coarse mesh and fine mesh.

In order to have access to the interior results through the thickness, different cross-sections on LS plane were defined in the Fig.6.2. They are referred to as left/right-i plane according to the i layer(s) relative to the central plane (yellow) in (b). The cross-sections are rotation symmetric to the central point. For instance, left-1 and right-1 planes are rotation symmetric on LS plane.

In full meshed calculations, a Gauss point (or integration point) was considered as *broken* state when the combined damage variable d defined in Eq. 6.16 reaches 1. Once the half of Gauss points within a single element were *broken* (e.g. 4 *broken* points in a hexahedral element c3d8), the damaged element would be totally removed including all Gauss points inside.

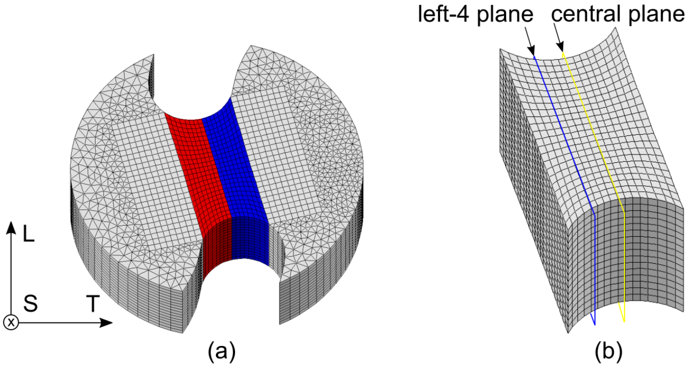

Figure 6.2: Mesh geometry: (b) a sub mesh is selected from (a) the region of interest in colors.

4 Results

4.1 Model calibration

4.1.1 Plasticity calibration

Based on the optimized parameters, Fig.6.3 presents a good agreement between simple computations from the non-damage macroscopic model (Bron-Besson, noted as BB) and the polycrystalline model (PC). Point simulations include the proportional (a)(b) uniaxial tensile (ϵ_{11} controlled) in terms of stress versus strain and lateral strain ϵ_{22} versus strain ϵ_{11}, (c) pure shear (ϵ_{12} controlled) and (d) biaxial tensile (controlling $\epsilon_{11} = \epsilon_{22}$) as well as (e) a non-proportional tensile loading after shear pre-straining ($\epsilon_{12} = 0.10$). It is noted that the hardening capacity of BB model was immediately saturated after pre-shear loading ($\epsilon_{12} = 0.10$) in (e) non-proportional loading. The calibration weight of each comparison was set differently, especially a lower weight was set in (e) non-proportional loading for comparison.

The calibrated results on single element calculations are exhibited in Fig.6.3 (f)(g) for uniaxial tensile and (h) for simple shear tests. A moderate anisotropy is shown in (f) but the Lankford ratio is smaller than 0.5. A good agreement on Lankford coefficient curves between two models is shown in Fig.6.3 (f). The curves of both models under simple shear in rolling (L) and transverse (T) directions were very close, and their yielding stress was different from the one in diagonal direction (D). In addition, a smooth wave was found from $U_2 = 0.4$ mm for PC model in Fig.6.3 (h), which came mainly from a quick hardening saturation of group one (e.g. large parameter b_1).

The optimized texture parameters are given in Tab.6.1. The dispersed EBSD pole figures in the form of stereographic projections were represented by the three colored dots in comparison to the experimental EBSD poles in Fig.6.4. Although the aim of the reduced texture was to model mechanical behaviour rather than to fit exactly the experimental texture, there was no apparent contradiction between the model and real

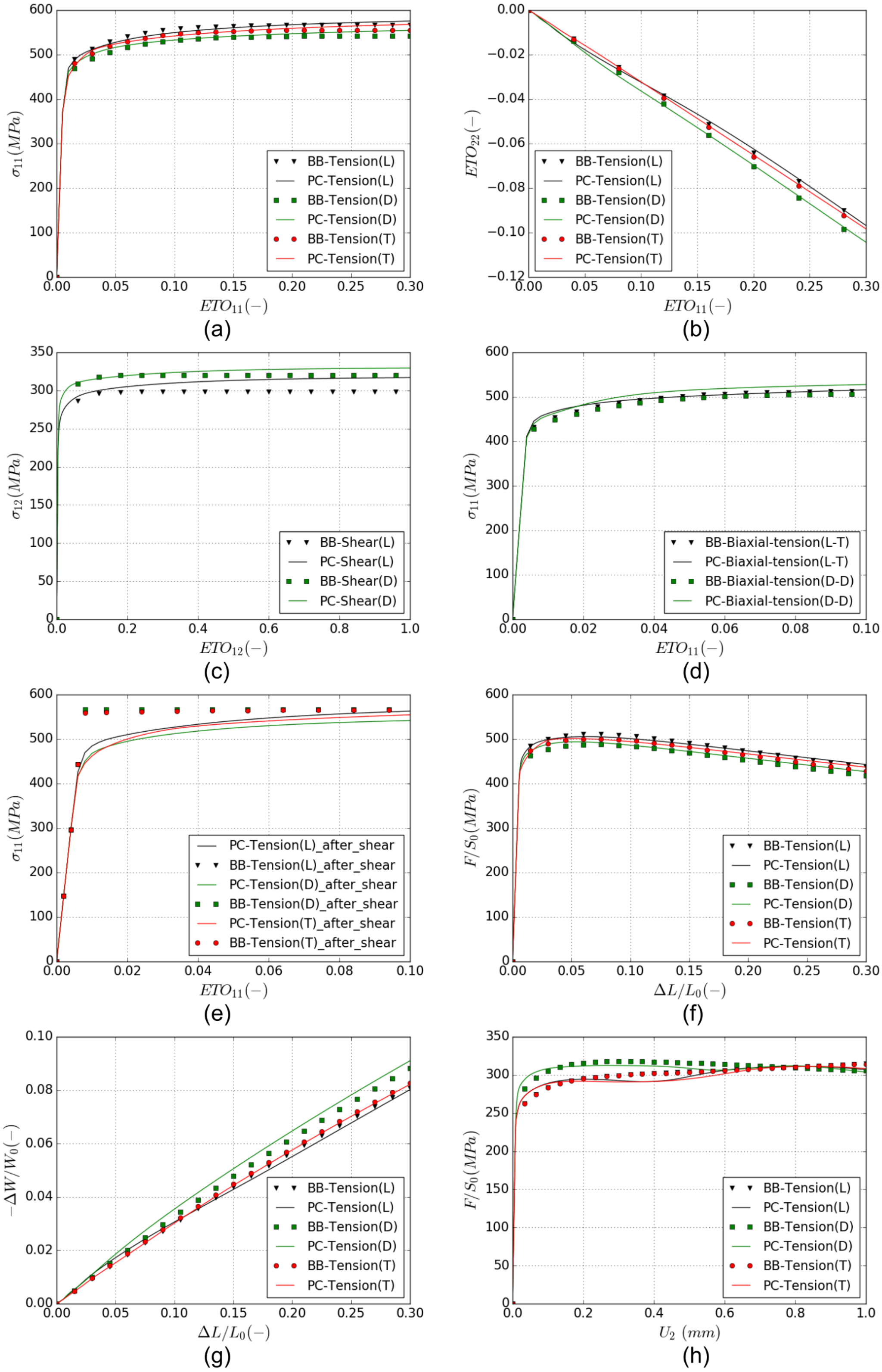

Figure 6.3: Plasticity calibration against simulations using macroscopic (no damage) Bron-Besson model: material behaviour simulations with uniaxial tensile in terms of (a) stress versus strain and (b) lateral strain versus strain, (c) pure shear, (d) bi-axial tensile, (e) shear followed by tensile loading conditions. Single element calculations on (f)(g) uniaxial tensile and (h) simple shear loading conditions.

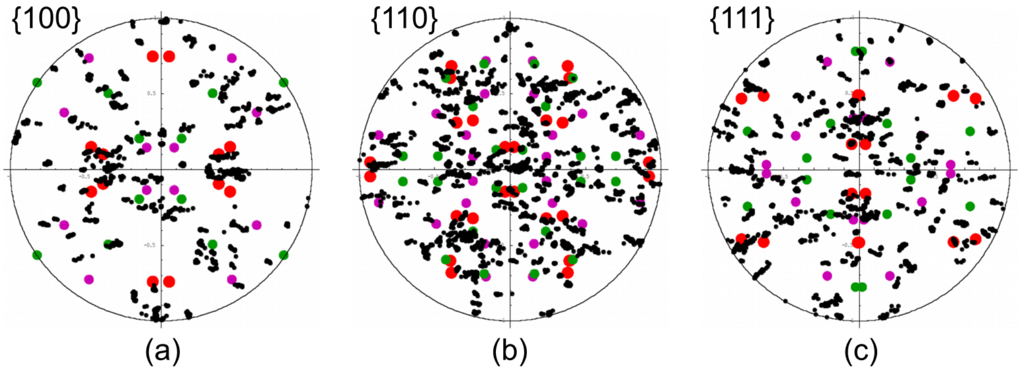

Figure 6.4: Pole figures for full-thickness specimen in black dots and the reduced texture model in colored dots in (a) {100}, (b) {110} and (c) {111} crystallographic planes.

textures. The *free of poles* zones were similar.

index i	$\phi_1^i(°)$	$\Phi^i(°)$	$\phi_2^i(°)$	$frac_i$(-)
1	17.812	51.563	-21.263	0.0930
2	56.636	18.943	-24.991	0.0790
3	-125.082	152.494	- 0.247	0.0781

Table 6.1: Optimized texture parameters including Euler angles and volume fractions for a reduced orthotropic texture with 12 grains, where three groups (i.e. i = 1, 2, 3) are represented in different colors in Fig.6.4 with four symmetric orientations each.

The other calibrated parameters are given in Tab.6.2 for slip system hardening parameters and Tab.6.3 for localization parameters. Note that the latent hardening parameter h_{14}=1.587 and h_{24}=4.381 were very large when they were calibrated with non-proportional loading. In Rousselier (2021), the larger value was h_{12}=0.197 for the same material.

4.1.2 Damage calibration

In order to calibrate damage parameters, simulations using full 3D meshes with different element size were carried out in proportional load paths including shear-only (SO) and tension-only (TO). Two meshes with different element size described above (in the figures: coarse mesh 100 µm in red and fine mesh 50 µm in blue) were used for the mesh dependency study of the polycrystalline model. Besides, the result of macroscopic BB model was included for the comparison. The calibration procedure was based on the response from coarse mesh, and the experimental ductility scatter was shown with one representative experimental database for each loading (Kong et al., 2021).

The global curves in terms of the nominal stress versus shear or tension stretch exhibited damage initiation critical points within the experimental ductility scatters in

Young's modulus E (MPa)	Poisson's ratio ν	R (MPa)	c	d
74 000	0.3	181.371	0	0

index	Q^i	b^i	h_2^i	h_3^i	h_4^i	h_5^i	h_6^i
1	35.642	21.461	4.777e-3	1.525e-3	1.587	1.132e-1	3.831e-2
2	10.062	2.287	6.142e-2	1.149e-2	4.381	1.060e-5	2.293e-5
3	14.228	1.000	1.122e-1	2.694e-2	3.139e-1	2.704e-2	1.466e-1

Table 6.2: Optimized parameters for slip system hardening.

D_{11}	D_{12}^*	D_{13}^*	D_{21}	D_{22}	D_{23}
1.311e3	1.050e3	1.088e3	7.759e2	1.027e3	5.885e2
D_{31}	D_{32}	D_{33}	D_{44}	D_{55}	D_{66}
2.367e1	3.405e1	4.345e2	2.480e2	1.398e1	8.218e3

Table 6.3: Optimized localization parameters for the self-consistent homogenization scheme, where D_{12}^* and D_{13}^* are not identified but calculated from Eq.B.2 for the comparison with previous work.

grey in Fig.6.5 for (a)(b) SO and (c)(d) TO. Two damage variables were optimized as $R_0{=}{-}Q_0{=}283$ MPa, $C_0{=}0.08$.

In Fig.6.5 (a)(b), numerical curves fitted well with the experimental one till damage initiation under shear loading. They started to become unstable with oscillations after the first force drop at $U_{12} = 0.135$ illustrated in (b). The load capacity derogated gradually after each force drop due to element removal. The point of the first load fall was considered as the damage initiation (DI) point to compare with the experimental failure (analyzed in Appendix A.2). In next section, the local fields would be investigated at the time of the DI point. Moreover, the predictive failure occurred slightly earlier in the fine mesh calculation. The load decrease, related to the crack growth rate, was larger with the fine mesh (Fig.6.5 (a)(b)).

Fig.6.5 (c)(d) shows a smooth load decrease under proportional tension load (TO). The sample was totally *broken* at $U_{11} = 1.115$, which was in the range of the experimental ductility scatter, for the coarse mesh group. The removed elements on the section indicated the macroscopic fracture path. The fine mesh group failed earlier around $U_{11} = 1.095$. The two failure points were illustrated as fracture points in (d). Note that the coarse mesh size corresponds to the Kahn specimen mesh size in Rousselier (2021), the load-crack mouth opening curve was also in agreement with the experimental curve.

Mesh size had a limited effect on the damage initiation under shear loading but a larger effect under tension loading.

4.2 Model prediction and validation under non-proportional load paths

The polycrystalline model with the optimized plasticity and damage parameters was used to predict the behaviours of non-proportional load paths 'shear to tension' (ST)

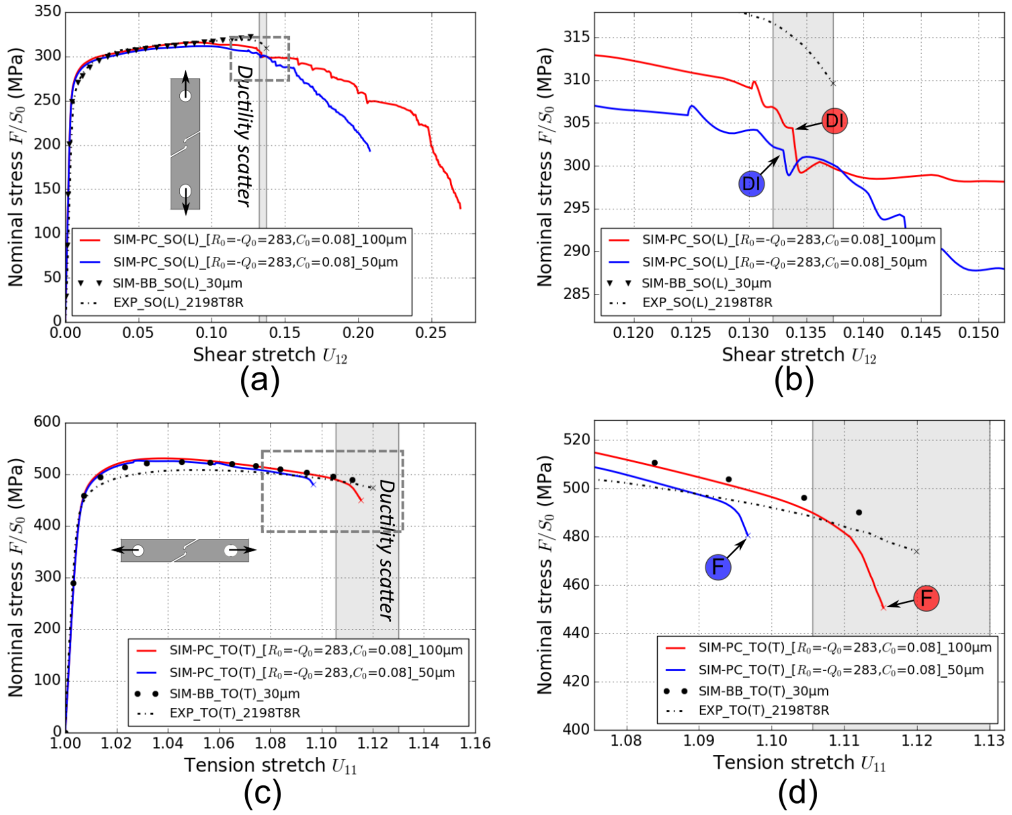

Figure 6.5: Damage parameter calibration in comparison to the experimental data: The curves in terms of nominal stress versus shear or tension stretch under proportional loading paths of (a) shear-only (SO) and (c) tension-only (TO). The detailed regions near damage initiation are zoomed in (b) for SO and (d) for TO. The experimental ductility scatters under monotonic loadings (SO and TO) are presented in grey box.

and ‘tension to shear’ (TS). It should be noticed that the non-proportional loading is not biaxial. The sample was loaded under the first loading direction and then unloaded, subsequently it was re-loaded under the second loading direction till fracture.

Fig.6.6 presents the curves in terms of nominal stress versus shear or tension stretch at (a) shear and (b) tension periods of non-proportional ‘shear to tension’ (ST) load path. Experimentally, the specimen was loaded under shear till $U_{12} = 0.081$ and then unload as illustrated in (a). Subsequently, the specimen was loaded horizontally under tensile till fracture in (b) as black dashed line. Polycrystalline simulations using meshes of two different element sizes perfectly matched the experiments during the shear pre-loading. They also had a good agreement on the experimental stress level and initial tension stretch of the subsequent tension loading, even better than the results from macroscopic non-damage model. As in Fig.6.3 (e), the BB model gave a good maximum stress (black dots) but its hardening capacity was almost saturated by the first loading in shear.

The difference between both models could be related to the non-diagonal parameters of the hardening matrices. The curves of tension loading showed a smooth force decrease due to damage softening as the proportional loading TO. However, due to the effect of shear pre-loading, there was an obvious ductility reduction and stress cross hardening compared to the proportional loading TO (Kong et al., 2021). The tension stretch from coarse mesh in red broke at $U_{11} = 1.085$ while the one from fine mesh in blue failed a bit earlier at $U_{11} = 1.065$. The ductility prediction of coarse mesh as failure stretch U_{11}^f was in the experimental scatter ranged from 1.084 to 1.106 illustrated in (b) as blue block. In summary, the polycrystalline model succeeded in predicting plasticity and ductility during the non-proportional load path 'shear to tension' (ST). Two specific steps were chosen to observe the local fields in next section: the end of shear pre-loading (SE) and tension fracture point (F).

The results of another load path change 'tension to shear' (TS) are exhibited in Fig.6.6 for (c) tension and (d) shear periods. The specimen was loaded under tension till U_{11}=1.060 and then unloaded as shown in (c). The deformed sample was subsequently loaded under shear till fracture in (d). As discussed in chapter 3, stress reduction was seen in the second shear loading due to the thickness reduction effect (cross section reduction) during pre-tension loading. The stretch to fracture of TS showed a large scatter in the blue block of Fig.6.6 (d). The average value was similar to the value of the monotonic tests SO. The ductility reduction highly depended on the pre-tension loading.

The predictive simulations showed a good agreement with the experiments and the results of macroscopic model. In TS, although there was 4% less predictive maximal nominal stress compared to the experiments at the second shear loading, the macroscopic BB model exhibited the same stress level as the polycrystalline model since the latter was calibrated in comparison to the macroscopic model instead of experiments.

The end of tension pre-loading (TE) and shear damage initiation (DI) were selected as two specific steps for the local field observation in TS. Damage initiated at $U_{12} = 0.152$ for coarse mesh and 0.105 for fine mesh. The damage initiation (DI) point of coarse mesh was in the range of the experimental scatter. After damage initiated during shear shown in (d), the nominal stress level of the coarse mesh (in red) slightly decreased or even maintained for a short distance before each severe force drop due to element removal. On the contrary, the nominal stress of the fine mesh (in blue) diminished smoothly and rapidly after the damage initiation point.

4.3 Local fields

The polycrystalline model with optimized parameters was compared to experiments in terms of global stress versus stretch curves. Mechanical fields including cumulative strain, porosity and maximal Coulomb slip were checked at damage initiation under proportional loading in Fig.6.7 for shear-only (SO) and, 6.8 for tension-only (TO). Under non-proportional loadings, the fields at the time of the pre-shear loading and tension fracture point are shown in Fig.6.9 and 6.10 respectively for 'shear to tension' (ST). The fields of the other load path changes 'tension to shear' (TS) at the time of the pre-tension loading and shear damage initiation are shown in Fig.6.11 and 6.12.

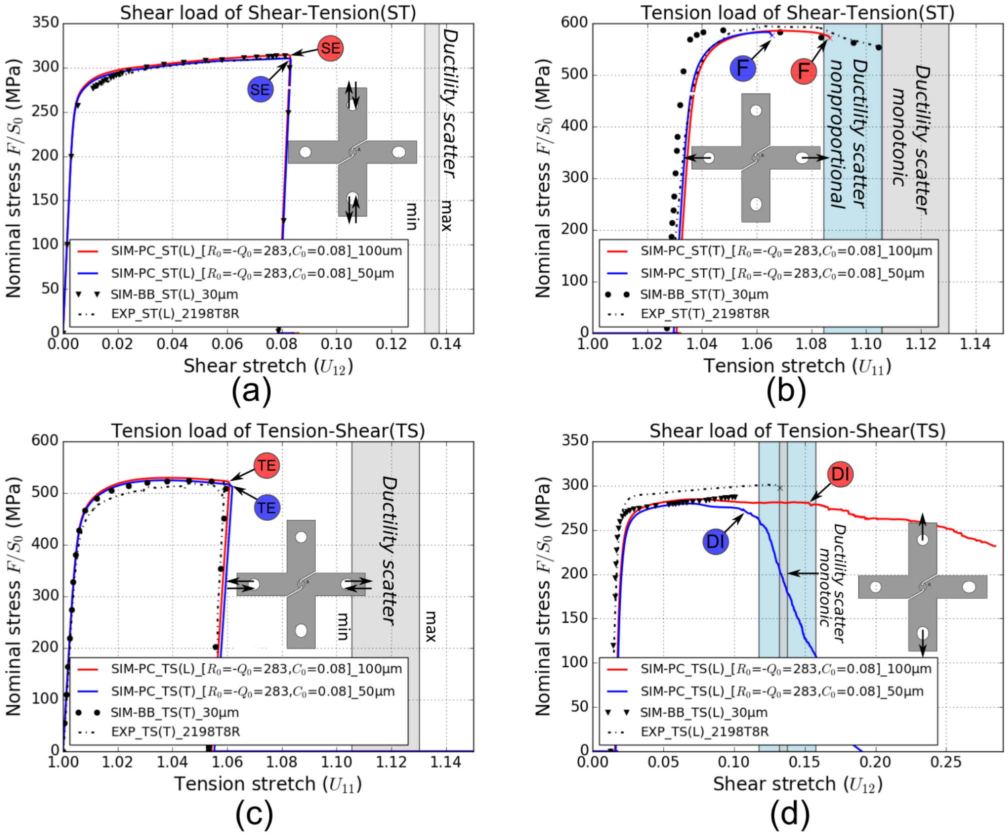

Figure 6.6: Predictions of the calibrated polycrystalline model under non-proportional load path changes: (a) shear and (b) tension loading periods in 'shear to tension' (ST) as well as (c) tension and (d) shear loading periods in 'tension to shear' (TS). The experimental ductility scatters are shown in grey box for monotonic loadings (SO and TO) and blue box for non-proportional loadings (ST and TS).

Furthermore, a combined damage variable d, defined as ultimate broken criterion in Eq.6.16, consists of porosity and Coulomb slip. Its fields under different loading paths are shown in Fig.B.1 for SO, Fig.B.2 for TO, Fig.B.3 for ST with coarse mesh, Fig.B.4 for ST with fine mesh, Fig.B.5 for TS with coarse mesh, Fig.B.6 for TS with fine mesh.

The damage location of ST was observed via 3D *in situ* X-ray laminography in the previous chapter 5. Physical damage features such as flat cracks in both intergranular and transgranular as well as intermetallic particle cracks were found. The predictive combined damage field during load path change was compared with the experimental 3D observations at the region of interest in the Discussion section.

4.3.1 Cumulative strain, porosity and maximal Coulomb slip fields

Shear-only (SO): Fig.6.7 presents the three fields (a)(b) cumulative strain, (c)(d) porosity and maximal Coulomb slip on the middle thickness plane at damage initiation (DI) points for the two meshes under proportional SO loading. A similar band was generated in the highly deformed region in both strain and porosity fields. The cumulative strain level reached up to 0.93 for the coarse mesh and 1.00 for fine mesh in the middle thick plane respectively shown in Fig.6.7 (a)(b). The element of maximal strain value was locally under highly shear state and symmetrically both elements were located at 100 µm from the notches, where the maximum porosity was also located as shown in Fig.6.7 (c)(d). Although the porosity had a relatively low level around 2 % for both calculations when damage initiated, considering that the initial porosity f_0 was set as 0.01%, the porosity significantly increased under shear loading since the region was not perfectly under simple shear state but with tensile components as discussed in the previous chapter 5. Lastly, only several activated Coulomb slips were seen at the map of damage initiation point. There were two Gauss points with ultimate Coulomb slip values ($\gamma_u = 3$) next to the elements with maximum strain and porosity. Other fully activated Coulomb slips were found on the notch edges. The activated slips were not situated on the shear band but 100 µm away from the central line.

The calculations from both coarse and fine meshes exhibited similar field distribution at the ROI. Moreover, fine mesh calculation obviously showed smoother fields and higher maximal values compared to the coarse mesh.

Tension-only (TO): Fig.6.8 exhibits the local fields of middle thickness plane at the fracture point under proportional TO loading. It was emphasized that the two fracture points were different in Fig.6.5 (d) where the sample with fine mesh *broke* earlier at U_{11}^{f} = 1.095.

Like notched tensile specimen, strain and porosity localized in the middle thickness plane on notches. The cumulative strain reached to 0.69 and 0.67 for both meshes in (a) and (b). Porosity achieved a remarkable level of more than 6%, which stood for the void growth under tension-dominated stress state. As fractography observed in chapter 3, damage features under TO including intermetallic particle break and matrix-particle debonding were found in the middle thickness plane, which resulted in large dimples. On the slip system scale, Coulomb slips were also activated only on the localized region.

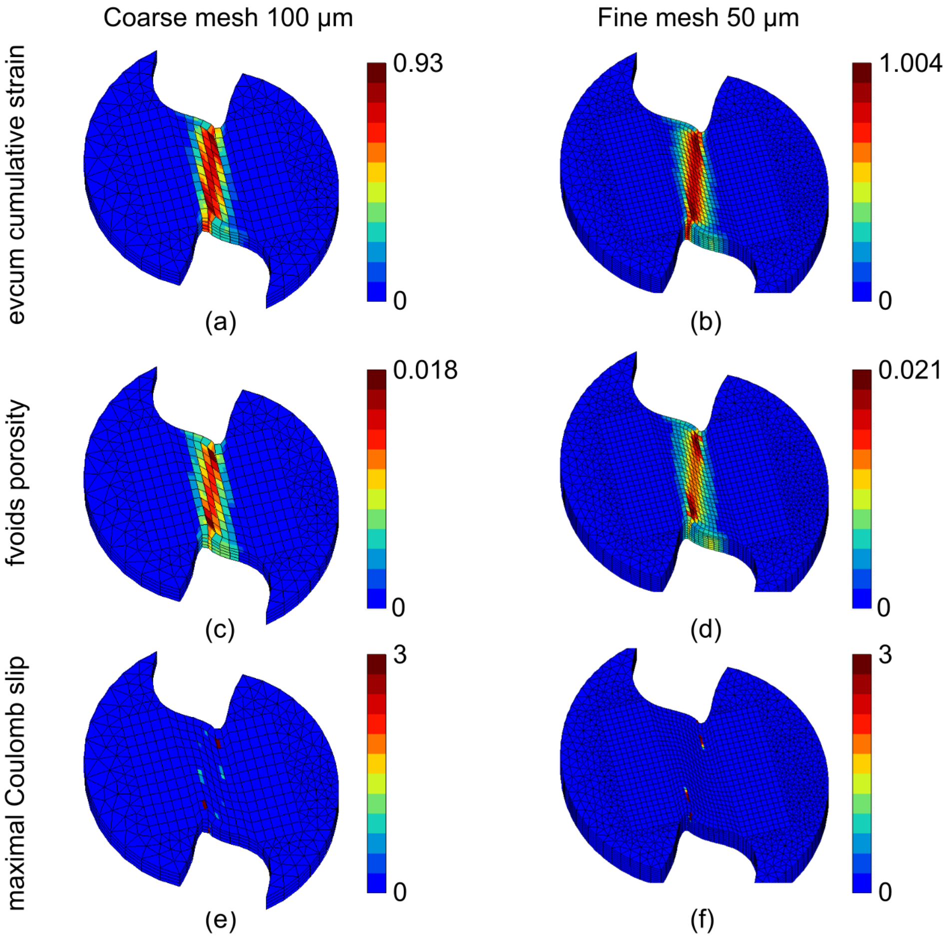

Figure 6.7: Local fields of the region of interest (ROI) on middle-thickness plane (z=0.5) at the time of damage initiation point under proportional loading shear-only (SO): (a)(b) cumulative strain, (c)(d) porosity, (e)(f) maximal Coulomb slip fields for coarse and fine meshes respectively.

Proportional TO showed a consistent localization at the middle thickness plane for three fields. Damage was likely to originate from the region and propagate along the band as experimentally observed.

'Shear to tension' (ST): For the non-proportional 'shear to tension' load path, three fields at the end of shear pre-loading (SE) are presented in Fig.6.9 and the fields at subsequent tension fracture point are exhibited in Fig.6.10. It was emphasized that tension fracture points were mesh dependent and the calculation of fine mesh failed earlier than that of coarse mesh like results under monotonic TO loading.

At the end of shear pre-loading (U_{12}=0.08), around 60% of shear stretch at damage initiation under SO $U_{12} = 0.135$, the maximal cumulative strain reached to 0.56 in Fig.6.9 (a) (0.60 for fine mesh in (b)). The shear band was generated similar to the one under proportional shear loading. The porosity level kept lower than 1% in (c)(d). The maximal strain and porosity location was 100 µm near notches. On the slip system scale, there were hardly activated Coulomb slips at the pre-shear end. The maximal Coulomb slip was only 0.075 (0.49 for fine mesh in (f)).

Fig.6.10 exhibits the evolved fields at tension fracture point after pre-shear loading. Fig.6.10 (a)(b) show the cumulative strain for two meshes. The band widened by horizontal tension loading and the highly sheared region continued to deform under tension. The maximal cumulative strain level reached to 0.74 from 0.56 (0.70 from 0.60 for fine mesh), which showed even a slight increase compared to that (0.69 for coarse mesh and 0.67 for fine mesh) under proportional TO. The similar strain level could be explained due to cumulative strain from the first shear pre-loading. The porosity fields as shown in (c)(d) presented a doubled value from 0.9% to 1.8% during the subsequent tension loading. The porosity level at failure under ST was solely one third of the one (6.1%) under proportional TO. The activated slips at shear end continued to grow during the tension. Limited elements with activated slips were seen at middle thick plane in (e) for coarse mesh while another two elements were found in (f) for fine mesh. The latter was located closer to notches.

'Tension to shear' (TS): For the other non-proportional 'tension to shear' load path, the fields are exhibited in Fig.6.11 at the end of pre-tension loading and Fig.6.12 at the shear damage initiation (DI) point.

The sample was loaded in pre-tension till $U_{11} = 1.06$, which was half of tension stretch to fraction under proportional tension-only $U_{11} = 1.115$. At the end of pre-tension loading, the cumulative strain level increased to 0.28 (0.36 for fine mesh) and the porosity grew to 0.8% (1.1% for fine mesh). Microscopically, there were no Coulomb slips activated after 6% (U_{11}=1.06) tension pre-loading. In Fig.6.5 (c)(d), global curves revealed that slip activation seemed to occur at very end of tension loading before fracture.

Fig.6.12 shows the fields when shear damage initiated under subsequent shear loading after tension pre-loading. The cumulative strain expanded to 0.97, which was very close to the value of proportional shear-only (SO). There was a near threefold increase in porosity from 0.8% to 2.4 % (from 1.1% to 2.7% for fine mesh) when applied to

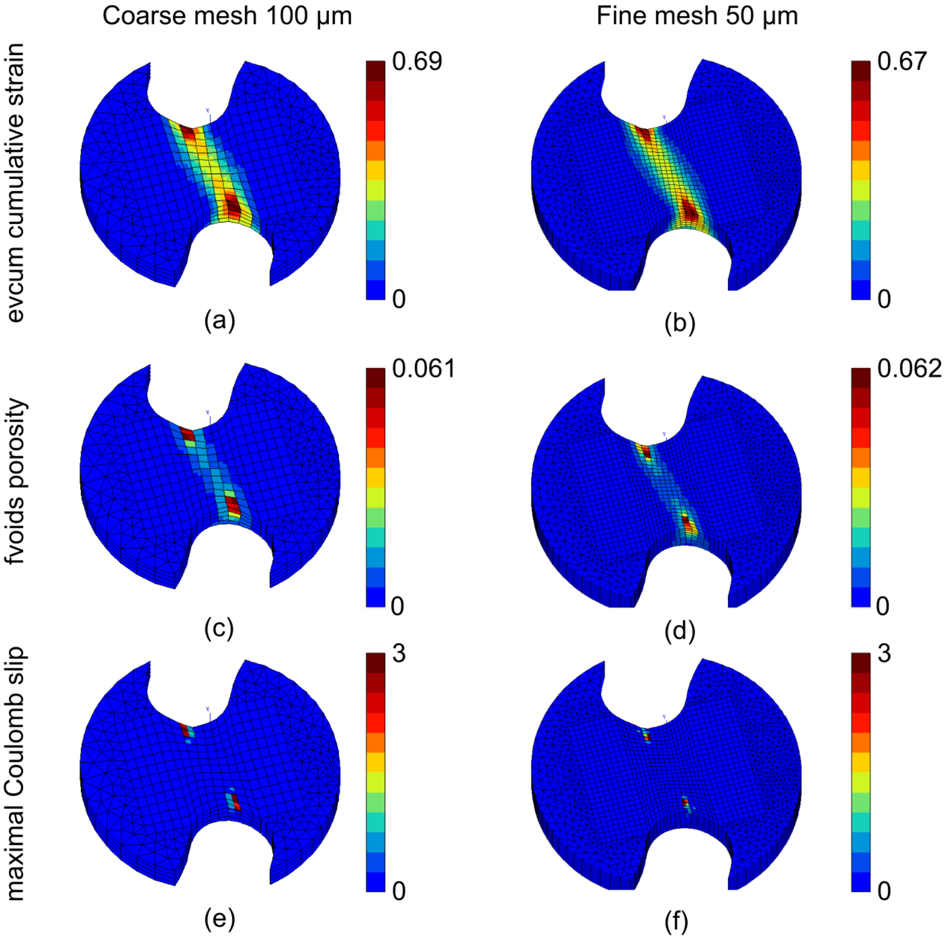

Figure 6.8: Local fields of the ROI on middle-thickness plane (z=0.5) at the time of damage initiation under proportional loading tension-only (TO): (a)(b) cumulative strain, (c)(d) porosity, (e)(f) maximal Coulomb slip fields for coarse and fine meshes respectively.

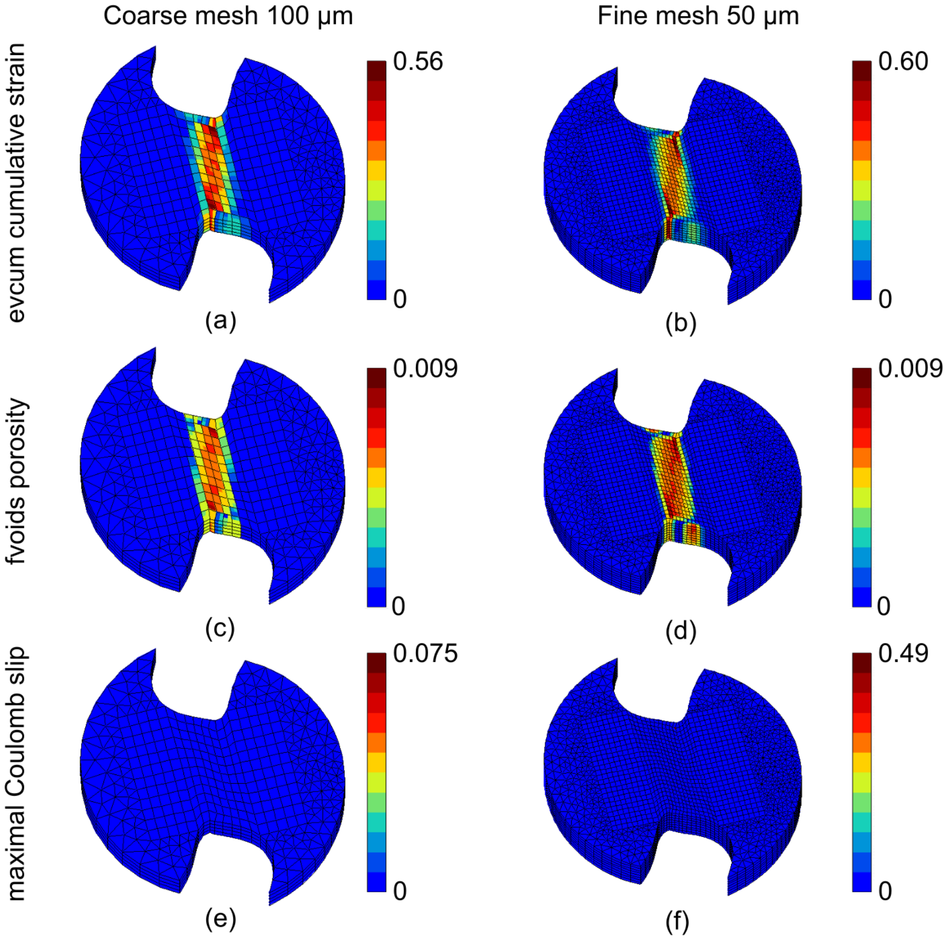

Figure 6.9: Local fields of the ROI on middle-thickness plane (z=0.5) under non-proportional loading 'shear to tension' (ST) at the end of pre-shear loading: (a)(b) cumulative strain, (c)(d) porosity, (e)(f) maximal Coulomb slip fields for coarse and fine meshes respectively.

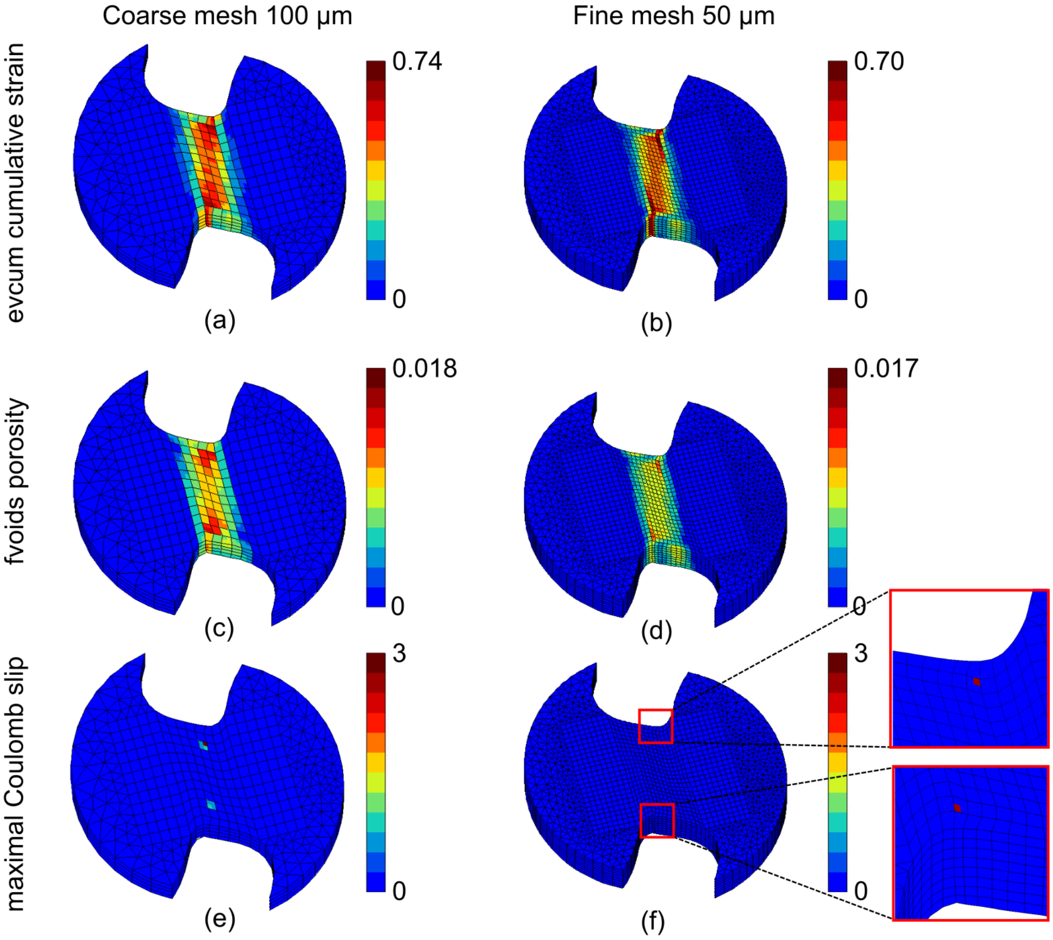

Figure 6.10: Local fields of the ROI on middle-thickness plane (z=0.5) under non-proportional loading ‘shear to tension’ (ST) at the tension fracture point: (a)(b) cumulative strain, (c)(d) porosity, (e)(f) maximal Coulomb slip fields for coarse and fine meshes respectively.

100 µm	evcum	fvoids (%)	gvCmax	50 µm	evcum	fvoids (%)	gvCmax
SO	0.93	1.8	3	SO	1.00	2.1	3
TO	0.69	6.1	3	TO	0.67	6.2	3
ST-s	0.56	0.9	0.075	ST-s	0.60	0.9	0.49
ST-t	0.74	1.8	3	ST-t	0.70	1.7	3
TS-t	0.28	0.8	0	TS-t	0.36	1.1	0
TS-s	0.97	2.4	3	TS-s	0.81	2.7	3

Table 6.4: Maximal cumulative strain evcum, porosity fvoid and Coulomb slip under different loadings including proportional SO, TO as well as non-proportional ST, TS for coarse (left) and fine (right) meshes.

shear loading. The distribution of activated Coulomb slips was similar as that under proportional SO. Several activated slips on Gauss point in (e) were at the border of strain band instead of on the band. In (f) for fine mesh, few activated slips were observed in the middle thick plane while more activated slips were found in the L-S cross section left-2 plane in (g).

In summary, the effect of tension stretch $U_{11} = 1.06$ pre-tension loading seemed to be very limited on the shear loading. The ‘tension to shear’ damage mechanism was similar to proportional SO. The pre-tension extent ($U_{11} = 1.06$) probably was not enough for bringing the damage effect and thus more simulations with different pre-tension levels would be discussed in next section.

The maximal values of cumulative strain, porosity and Coulomb slip under different loading paths above are gathered in Tab.6.4.

4.3.2 Combined damage fields

A combined damage variable, consisting of porosity on the microscale and maximal Coulomb slip at the slip system scale, was defined in Eq.6.16 to quantify the damage during various loading paths. For brevity, these combined damage fields under different load paths were in the Appendix B.3.

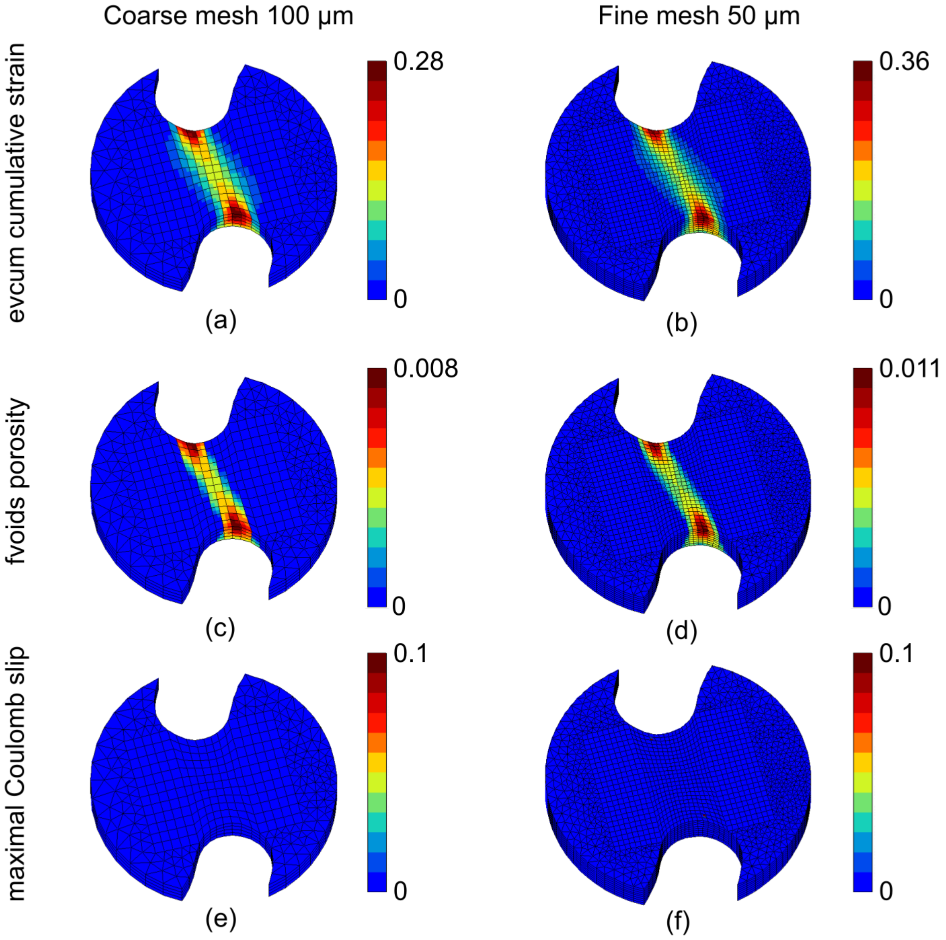

Figure 6.11: Local fields of the ROI on middle-thickness plane (z=0.5) under non-proportional loading 'tension to shear' (TS) at the end of pre-tension loading:(a)(b) cumulative strain, (c)(d) porosity, (e)(f) maximal Coulomb slip fields for coarse and fine meshes respectively.

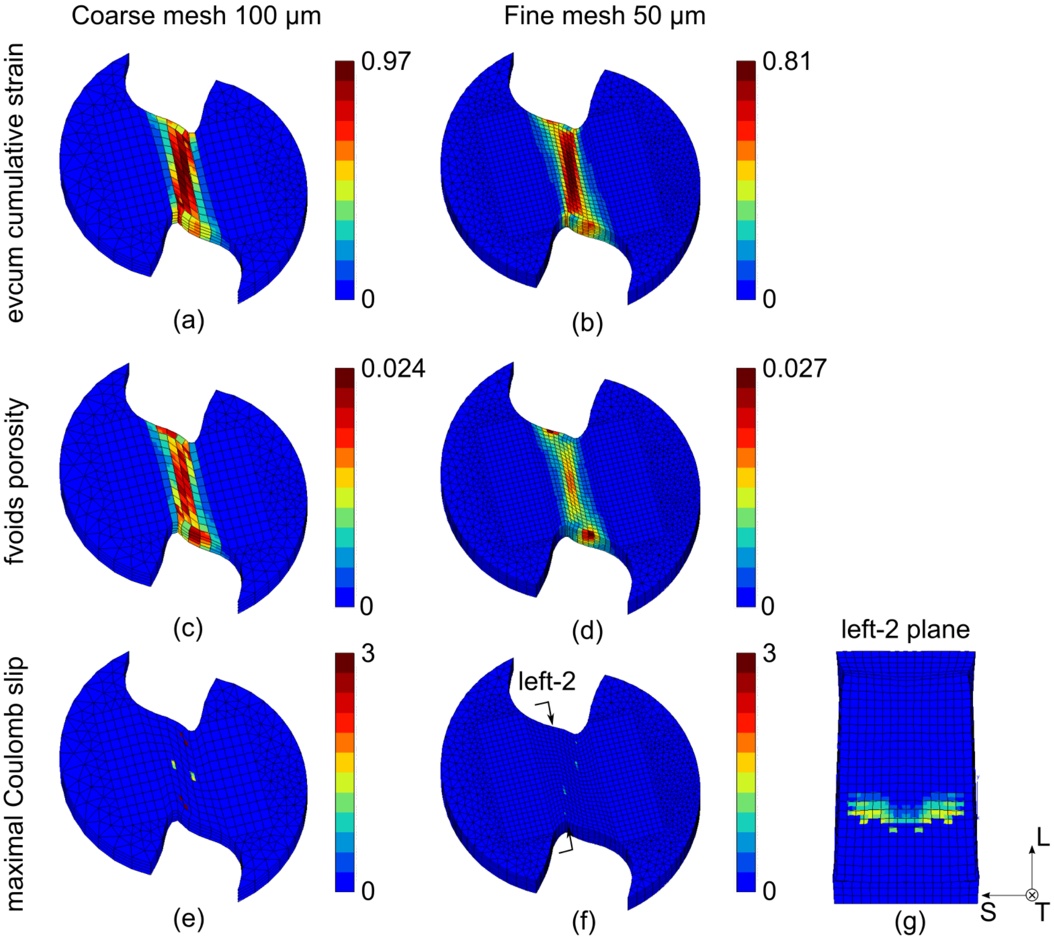

Figure 6.12: Local fields of the ROI on middle-thickness plane (z=0.5) under non-proportional loading 'tension to shear' (TS) at the shear damage initiation point:(a)(b) cumulative strain, (c)(d) porosity, (e)(f) maximal Coulomb slip fields for coarse and fine meshes respectively.

5 Discussion

In shear-failure loadings, i.e. shear-only (SO) and ‘tension to shear’ (TS), stress versus shear stretch curves were irregular after damage initiation (sudden small load drop) noted DI in Fig.6.5 (b) and Fig.6.6 (d). Load oscillations occurred after each element removal. Exceptionally, the curve of fine mesh TS was quite smooth with load slowly decreasing till failure, and the crack propagated gradually until load capacity decreased to 0. This force oscillation problem might be solved by using mesh refinement meanwhile a non-local model (Cabot and Bazant, 1987) could solve the mesh dependency problem. On the contrary, for tension-failure loadings, i.e. tension-only (TO) and ‘shear to tension’ (ST), the curve was quite smooth and damage initiates with obvious slope change. However, the simulation diverged and stopped after only less than 10 elements were *broken*. Fracture points are noted as F in Fig.6.5 (d) and Fig.6.6 (b).

Although an integral point was considered as *broken* state when combined damage variable d=1, the useful damage range was set from 0 to 0.12 in the fields above. 0.12 seems small for totally *broken* state, but the softening was already brutal. Physically, a void volume fraction equal to 0.12, is a large value in metallic alloys. In experiments from previous chapter 5, the damage quantified as surface void fraction reached around 0.1 before failure.

5.1 Experimental comparison under ST

An *in situ* laminographic experiment under non-proportional load ‘shear to tension’ (ST) was carried out at ID19 at the ESRF and described in details in the previous chapter 5. On the macro scale, the effect of pre-shear loading on ductility resulted in a 20% reduction of the tension stretch to fracture compared to the proportional tension loading. On the micro scale, two main types of damage features, intermetallic particle cracks and flat cracks, were found. Damage nucleation has already been observed at the end of shear pre-loading at nearly zero stress triaxiality. The nucleated damage grew and led to final fracture during tensile loading after shear pre-loading.

Compared to the physical observations via 3D laminography, the predictive combined damage fields of polycrystalline model under ST load path changes included the classic particle-related damage (i.e. porosity) and the transgranular flat cracks (i.e. activated Coulomb slips) on the slip system scale. The comparison of damage location between experimental observation and numerical prediction is presented in Fig.6.13. Experimentally, segmented damage in yellow sub volume ($792\times1152\times720$ μm^3) was visualized in L-T top view and L-S side view. Numerically, the damaged elements, selected from the combined damage of single Gauss point greater than 0.01, were mainly located in the shear band region. At the end of pre-shear loading, damage nucleated in the band region through the all thickness in (a) and (b). It was in good agreement with numerical simulation where damage was homogeneously distributed around 0.02 through the thickness (S) shown in (c)(d). The damage quantified as projected surface void fraction reached to 0.01 in chapter 5. The cross section was cut along the L' axis of Cartesian element, which was not parallel to the band. That was why the top-bottom symmetry of damage value was not seen in 2D section. When it turned to the subsequent tensile loading, nucleated damage at shear continued to grow and coalesced to macroscopic fractures on the band in (e) from the last scan before failure, where several flat cracks were found and distributed at the region of interest in (f). The damage indicated from polycrystalline model continued to grow as well to more than 0.10 (close to experimental quantification of surface void fraction) in the middle-thick plane shown in (g) for coarse mesh. The fields of fine mesh seemed to not be localized yet in (h) mainly due to earlier fracture point. Furthermore, the damage localization was 200 μm from the notch edge in the middle-thick plane (Z=0.5), which could be linked to the observed damage near the middle thick plane in (f). In summary, the polycrystalline model managed to indicate the location of damage initiation under shear and quantitatively damage growth under subsequent tension loading.

5.2 Prediction on effect of different pre-loading

In this study, only one type of experiment, where the sample was pre-loaded to the half of stretch to failure of proportional test, was conducted. Brünig et al. (2021) investigated the effect of 45%, 65% and 90% shear pre-loading on the followed tension loading as well as the effect of 50%, 75% and 85% tension preloading on the followed shear loading respectively. A remarkable displacement reduction was found due to pre-straining. The higher the pre-straining was, the higher the reduction in ductility. However, the mechanism behind the reduction under load path change was not clearly identified by fractography.

In order to quantitatively investigate the effect of different pre-loadings, virtual experiments with optimized polycrystalline model using 100 μm mesh have been carried out to predict the plastic behaviours and find out the origin of pre-loading effects under two non-proportional loadings ST and TS respectively.

5.2.1 'Shear to tension' (ST)

Non-proportional 'shear to tension' (ST) loadings with different shear pre-loadings ranged from U_{12}=0.03 to 0.12 (22% to 89% of shear damage initiation point U_{12}=0.135) are presented in Fig.6.13 (a) for pre-shear loading period and (b) for subsequent tension loading period. Overall it showed that the greater pre-shear loading, the smaller the tension stretch to failure. The plasticity shear hardening resulted in a higher stress level except last three simulations, whose failures occurred even before yielding probably due to large shear damage. The initial tension stretch shift, as there was a slight tension stretch during shear pre-loading, was found large with increasing pre-shear straining. If the initial tension stretch shift during pre-shear was not considered, which means all specimens were assumed to be virgin, the ductility reduction would be even higher as shown in Fig.6.13 (c). Interestingly, the short pre-shear loading simulation ($U_{12} = 0.03$ in dark blue) failed even later than the monotonic group in black. All the failure points from both original and shifted curves are shown in Fig.6.13 (d) in terms of tension stretch to failure versus pre-shear stretch, including the experimental ductility scatters from SO

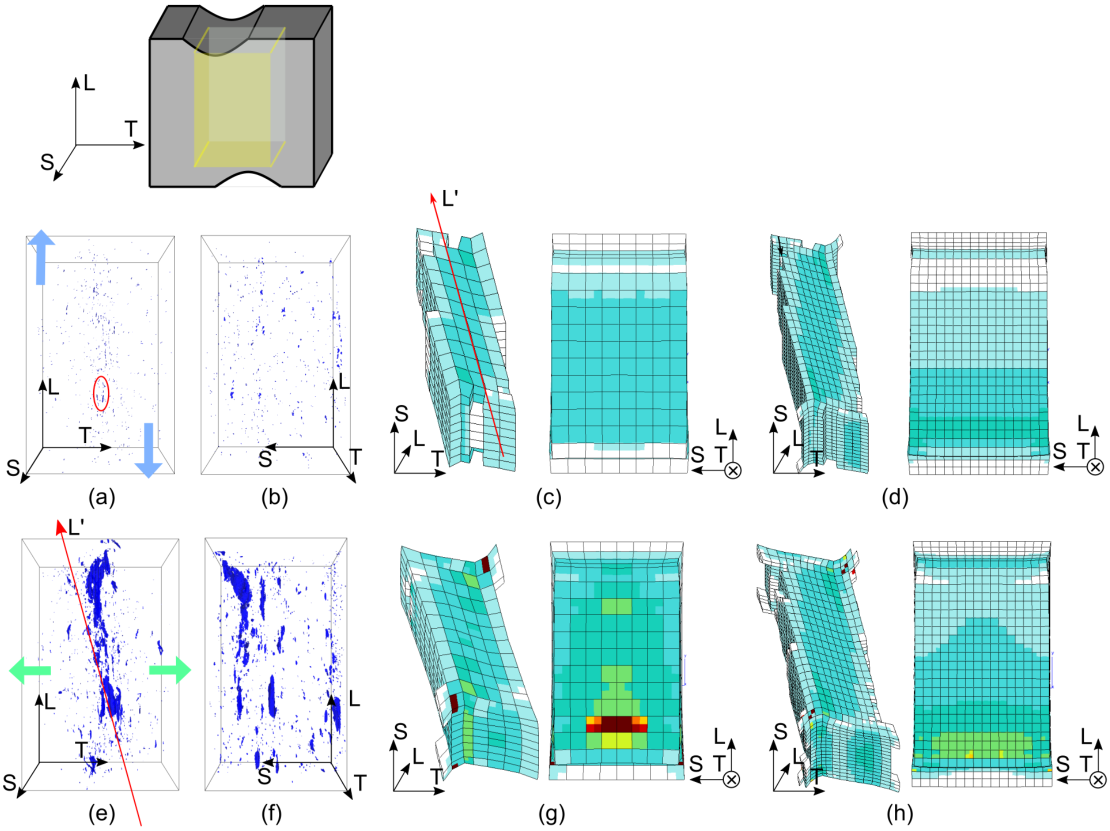

Figure 6.13: Damage visualization of yellow sub volume via 3D laminography at (a)(b) the end of pre-shear loading and (e)(f) the end of subsequent tension loading before fracture. Combined damage fields of damaged element at (c)(d) end of pre-shear loading and (g)(h) end of subsequent tension loading for coarse and fine meshes respectively.

and ST of U_{12}=0.08 as grey and blue boxes respectively. There was a linear tendency of ductility reduction with increasing pre-shear stretch except the exceedly damaged tests. Although the crystalline model was sensitive to the resolved shear stress of each slip system, three groups of U_{12}=0.07, 0.08 and 0.09 pre-loadings under similar global stress level present different tension stretch to failure. It indicated that the ductility reduction was not global stress level dependent. Experimentally it already showed that shear-dominated loading led to damage nucleation and growth even at zero stress triaxiality. The origin of ductility reduction under non-proportional loading from shear to tension is likely related to the induced shear damage, quantitatively in porosity and maximal Coulomb slips.

5.2.2 'Tension to shear' (TS)

Fig.6.15 presents the results under another non-proportional loading 'tension to shear' (TS) with different tension pre-loadings U_{11}=1.05 to 1.11 (43% to 95% of monotonic tension stretch to failure point U_{11}^{f} =1.115) at periods of (a) tension loading and (b) shear loading. With increasing the tension pre-loading, the shear stress softening was larger mainly due to thickness reduction during tension. Force dropped slowly with oscillations in the shear curves. As above, the first crucial force drop point was defined as damage initiation point. Fig.6.15 (c) presents the shifted shear curves with neglecting the tension pre-loading effect. Despite the damage initiated earlier from the large pre-loading groups (U_{11} = 1.09, 1.10 and 1.11) compared to the monotonic shear-only group, the reduction of ductility did not appear for other pre-tension groups. All shear stretch at damage initiation (DI) points from both original and shifted curves are summarized in Fig.6.15 (d), including the experimental scatters of monotonic SO and TS with U_{11}=1.05 and 1.06 as grey and blue boxes respectively. The effect of pre-tension loading on the shear stretch at DI was less clear from the predictive TS simulations with different pre-loading extent, and a large experimental scatter (the blue box in Fig.6.15) was also found in the TS experiments even with the same extent of pre-loading. As presented in the discussion of chapter 3, the strain distribution in shear band depends on the extent of pre-tension, and the latter influences the deformed extent of the ligament geometry between two notches. Brünig et al. (2021) found a strong scatter (from 0% to 47%) as well for 'tension to shear' load path changes using a H-shaped sample. In local fields of TS shown in Fig.6.11 (c)(d), only one of combined damage, porosity, was found on the notch edges at the end of pre-tension (U_{11}=1.06). The effect of low pre-tension level (U_{11}<1.10) is negligible on the damage initiation.

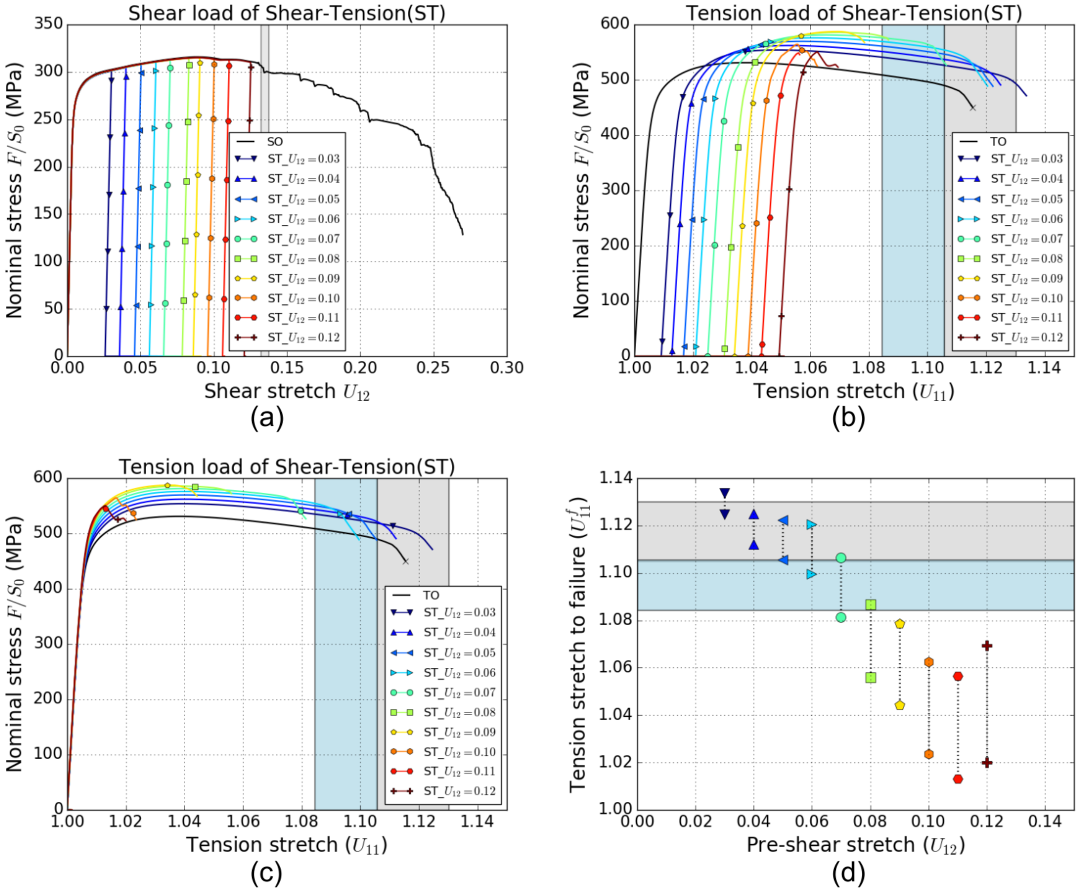

Figure 6.14: The curves in terms of nominal stress versus shear or tension stretch under non-proportional 'shear to tension' (ST) in (a) pre-shear loading and (b) subsequent tension loading. (c) The shifted curves under tension loading assumed pre-strained specimens as virgin. (d) The summary of tension stretch to failure points from original and shifted groups with regard to pre-shear stretch. The grey box represents the monotonic experimental scatter while the blue one stands for the experimental scatter of tension tests after U_1=0.08 pre-shear stretch.

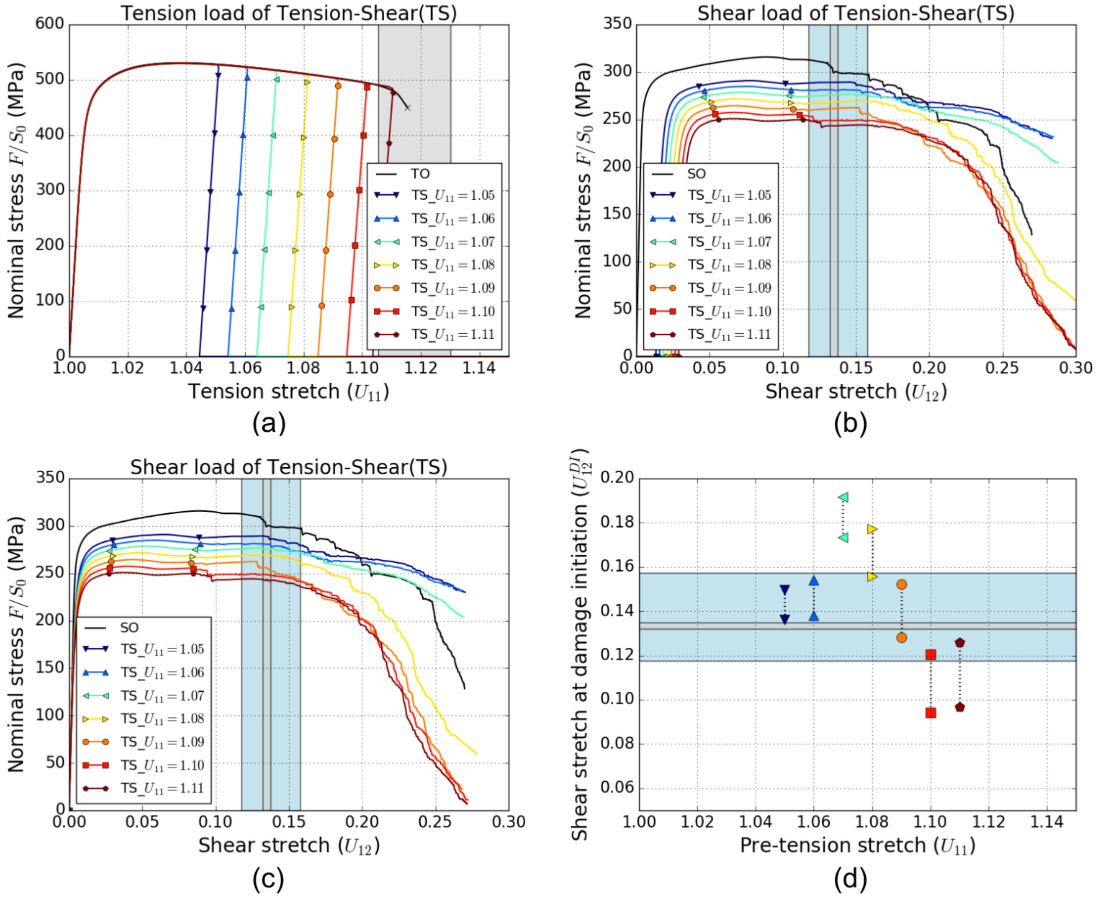

Figure 6.15: The curves in terms of nominal stress versus shear or tension stretch under non-proportional 'tension to shear' (TS) in (a) pre-tension loading and (b) subsequent shear loading. (c) The shifted curves under shear loading assumed pre-strained specimens as virgin. (d) The summary of shear stretch at damage initiation from original and shifted groups with regard to pre-tension stretch. The grey box represents the monotonic experimental scatter while the blue one stands for the experimental scatter of shear tests after U_{11}=1.05-1.06 pre-tension stretch.

6 Conclusion and perspective

The calibrated polycrystalline model was successful in predicting mechanical behaviours of full-meshed calculations in an anisotropic aluminum 2198 T8R under non-proportional loading paths. The calibration strategy includes plasticity calibration with the macroscopic elasto-plastic model with plastic anisotropy using simple simulations and then damage calibration using full-meshed calculation compared to proportional fracture experiments.

The optimized model not only agreed with experimental data in terms of macroscopic nominal stress - stretch curves, but also showed the damage location and its evolution during complex loading path changes. The physical damage was traced and observed using *in situ* laminography from shear to tension in chapter 5. The damage from shear pre-loading contributed to the ductility reduction measured by tension stretch to failure. Two types of damage features, intermetallic particle crack and flat cracks, were quantified by a combined damage variable, consisting of porosity at the classic void nucleation-growth-coalescence scale and transgranular activated Coulomb slips at the slip system scale. The combined damage was already found at the end of shear pre-loading.

In previous works, the Cartesian mesh was a reasonable choice for notched or cracked macro-specimens in tension-dominated loading. In these specimens, the experimental crack path is in the notch plane at least initially (shear lips can appear on the sheet surfaces and join to form a slant crack (Rousselier, 2021)). A 200 mm mesh for quadratic (c3d20) finite elements, equivalent to a 100 mm mesh for linear (c3d8) element, was found in good agreement with experiment. This size is confirmed in Fig.6.5 (d): the 50 mm (c3d8) mesh underestimated the ductility in tension. In the present work, the sample is a micro-specimen (the distance between the two notches is around 1.4 mm) and the crack path depends on the loading (tension TO vs. loadings with shear: SO, TS, and ST), it is not in the direction of the Cartesian mesh. In SO and TS, Figs.6.5 (a,b) and 6.6 (d), the stress-stretch curves showed a pathological effect of mesh size and numerical oscillations that are probably related to the mesh geometry.

Moreover, the polycrystalline model offered more virtual experiments under non-proportional loadings with aims to explore the effect of pre-loading on the ductility reduction. The combined damage and stress hardening/softening from pre-loading are believed to affect the stretch to failure.

In ductile fracture models that predict a softening regime at incipient final failure, softening induces localization. Although such a behaviour might be in agreement with underlying physical mechanisms, it also entails the major issue of causing ill-posedness of the boundary value problem as reported by Bažant et al. (1984) and Lorentz and Benallal (2005). From a numerical point of view, solving the governing equations, for example by finite elements, results in the absence of convergence of the results when the mesh size is decreased. Several approaches were followed to bypass or overcome this issue. In order to avoid mesh sensitivity, a non local damage theory proposed by Cabot and Bazant (1987) replaced the usual damage variable with its spatial average over a representative volume of the same size as the material characteristic length. Many other non local or regularization approaches have been proposed in the literature. The present work shows that in loadings with shear, it is necessary to use one of them to obtain a good modeling of not only incipient fracture but also crack propagation. Besides, a mesh refinement function could be also activated to probably solve load oscillation problem in shear loading simulations.

Another perspective is to consider the large rotation in the shear band region during intense shear loading. A model of texture evolution aims to take the texture rotation into account. This option has been tried in Appendix B.4, but all parameters have to be re-calibrated. Activating this option is left for future work.

Part IV

Conclusions and future work

Chapter 7

Conclusions and perspectives

The main objective of this work was to characterize the failure and associated ductile damage mechanisms in the material bulk under shear and also for complex non-proportional load paths for low stress triaxialities.

1 Conclusion

1.1 Macroscopic experiments under different load paths

- The yield strength of AA2198-T8R was about twice the one of AA2198-T3R. The ductility during uniaxial tensile and notched tensile testings was about half for AA2198-T8R compared to 2198-T3R. Interestingly, the shear-stretch to fracture measured during shear experiments was very similar for both materials.

- A cruciform sample geometry for load path changes was designed and a four-point-optical extensometer was defined to measure stretch in shear and tension for the cross-shaped sample. It aims at removing the rigid body rotations and at synchronizing the experiment with 3D finite element simulations. The non-proportional 'shear to tension' (ST) load path change led to a significant reduction of ductility (tension stretch to fracture) of 29% and 16% for AA2198-T3 and AA2198-T8 respectively. The other 'tension to shear' (TS) load path change did not reduce the shear stretch to fracture evidently. The experimental scatter in shear stretch to fracture substantially increased for both heat treatment conditions.

1.2 Ductile damage analysis

- **SEM Fractography** revealed micrometer sized dimples for the tension loading (TO and ST), while grain related flat zones and very small shear dimples linked to nano-dispersoid particles under shear loadings (SO and TS). The fracture plane of sample under 'shear to tension' (ST) was slant through the sample thickness and the crack was straight in the sample plane, indicating the pre-shear affected the failure mode as is was different from the one of the proportional tension-only (TO) sample.

- **Shear sample:** With the multiscale observations of advanced 3D laminography and 2D destructive SEM/EBSD, two main types of damage features under shear (stress triaxiality nearly zero) were identified using a so-called smiley shear sample: flat cracks and second-phase intermetallic particle cracks. The former play a major role in the final failure in the AA2198-T8R and its length can be more than 100 µm. This flat crack feature was firstly found in AA2198-T8R and not in other ductile alloys (Roth et al., 2018; Tancogne-Dejean et al., 2021). The detrimental flat cracks did not nucleate on the particles and they are proven to be both intergranular and transgranular via EBSD analysis. The flat damage is located at the highly localized slip bands, and nano-dispersoids were found within the sub-micro dimples, which possibly can be the origin of this feature. The other damage feature, damage linked to the rigid but brittle intermetallic particles, rotated under shear, then either broken or decohered from the aluminum matrix, eventually leading to voids. Shear damage evolution was observed via micro-laminography (µR). Nano-laminography on damaged specimen at high resolution (HR) allows to observe two types of shear damage features down to nanometer scale. Other nano-laminography at very high resolution (VHR), allowed to better understand particle fracture in 3D on a very localized region (100 µm×100 µm×76 µm), where flat cracks was not included.

- **'Shear to tension' load path change:** An *in situ* laminographic experiment was carried out to study the ductile damage evolution during a non-proportional load path changes in AA2198-T8R. The flat crack nucleation was found at the end of the shear pre-loading at zero stress triaxiality, which proves this shear feature is material dependent, and subsequently damage grew and led to final failure during the second tension loading after the shear pre-strain. Pre-shear has damaging effect on the ductility reduction.

- Instead of using volume void fraction as damage experimental measurement, a new surface void fraction was measured to quantify the damage in the highly deformed region for different load paths. On the other hand, an accumulated equivalent strain was defined, that is suited for non-proportional load paths. It was applied to both projection digital image correlation (performed on 3D laminography data) and finite element calculations to estimate the equivalent strain to fracture. The interaction between the evolution of damage and strain has been checked in the highly localized shear bands.

1.3 Numerical models for ductile damage

- A macroscopic model for anisotropic plasticity was fitted using experimental data of uniaxial tension and notched tensile samples in different orientations for its plastic anisotropy as well as the small shear sample. A good fit was obtained in terms of stress - strain curves.

- The model with the optimized parameters succeeded predicting the mechanical behaviour of stress - stretch curves under non-proportional complex load path changes and the predicted mechanical fields gave a good estimate of the fields measured by DIC.

- A Rousselier-Coulomb polycrystalline damage model, that combines classical void growth at high stress triaxiality and Coulomb model at the slip system scale for low stress triaxiality, is applied in this study for a non-proportional load path change. The calibration strategy, included plasticity calibration with a non-damage macroscopic model (Bron-Besson) using simple simulations and then damage calibration using full-meshed calculation compared to proportional fracture experiments, is successful.

- The optimized model not only agreed well with experimental data in terms of macroscopic nominal stress - stretch curves, but also indicated the damage location and its evolution during complex loading path changes. Compared to the physical damage traced and observed using *in situ* laminography under ST in chapter 5, the predicted damage from shear pre-loading contributed to the ductility reduction measured by tension stretch to failure. Two types of damage features, classical voids and flat cracks nucleated on slip planes, were quantified by a combined damage variable. The combined damage location was a good indicator and in agreement with the 3D experimental laminography.

2 Perspectives

Numerous perspectives of the present work arise and are given in the following:

- Similar 3D *in situ* laminographic experiments should be performed using very high resolution. The multiscale observation could be carried out with different spatial resolutions, ranging from micrometer (0.7 µm) down to nanometer (e.g., 250 nm and 50 nm).

- For the nano-laminography at very high resolution (VHR), a fast reconstruction is highly required to locate at high resolution damage features and track damage features at very high resolution. For instance, the flat crack feature can be located and observed at the nanometer scale.

- More systematic mechanical experiments under load path changes (e.g. ‘shear to tension’ (ST) and ‘tension to shear’ (TS)) with different extents of pre-loading can now be carried out to study the quantitative effect of shear or tension pre-loading on ductility and plasticity. Moreover, if possible, the experiments under complex load paths using the same cross-shaped geometry could be applied for other aluminum alloys (e.g., 2198-T3R and 2139-T3) and forming aluminum alloys (e.g., 6016).

- Apart from the shear-tension cruciform specimen, another geometry specimen has been designed for a tension to plane strain tension load path change in Fig.7.1. The horizontal loading provides the sample tension pre-loading and then the sample was loaded in vertical direction under a plane strain tension (PST) till fracture. This geometry was optimized from the geometry originally for plane strain tension by the aid of finite element calculation, so that a highly-deformed (future broken) region of 1 mm^3 is under homogeneous stress state prepared for the 3D *in situ* scanning. This work was done by an intern under my supervision. This part could be continuously conducted to investigate ductile damage mechanism under other load path change. Plane strain tension is highly application relevant as minimal ductility is found for this strain state in forming. *In situ* laminography experiments should be carried out.

- For the numerical simulation of polycrystalline model in Chapter 6, the non local models could be developed to tackle the mesh dependency problem. Besides, a mesh refinement function could be also activated to try to solve load oscillation problem in shear loading simulations. A failure criterion in shear should be more clearly identified. The model could be applied to the same material in T3 condition and even more other forming alloys, the versatility may be tested.
- For the large rotation in the shear band region during intense shear loading, the option of texture evolution in Rousselier-Coulomb model aims to take the texture rotation into account during loading. This option has been tried in Appendix B.4, the damage of Coulomb slips is located differently at the highly deformed region. However, all parameters have to be re-calibrated with activating the option in the future.

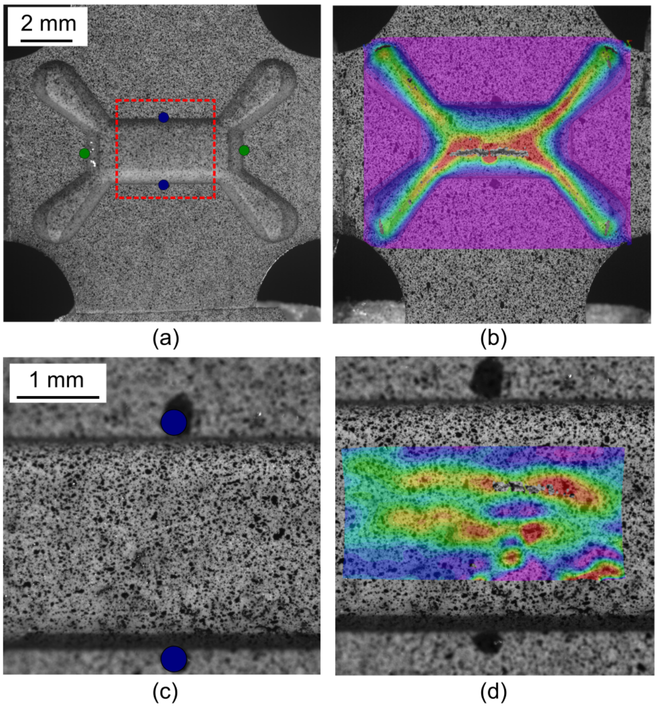

Figure 7.1: A cruciform geometry for a tension to plane strain tension (PST) load path change. Two fields of view by two detectors as 12.05×12.05 mm^2 and 3.85×3.85 mm^2 respectively in (a)(c) initial state and (b)(d) deformed state with strain field by DIC.

Appendix A

Plasticity and ductility chapter

1 Effect of out-of-plane motion on strain measurement errors for different optical set-ups

A specimen might move in the thickness direction during the loading process, which may cause an image-plane displacement gradient. If these gradients are not negligible any more, the in-plane measurement will be incorrect. This section aims to investigate the effect of out-of-plane motion in the different optic lens systems used in this thesis.

1.1 Standard lens system for measurement

According to Sutton et al. (2009), the in-plane displacement u and v are denoted as:

$$u(\Delta z) = x_s(z + \Delta z) - x_s(z) \cong (\frac{xf}{z}) \cdot S_x \cdot (-\frac{\Delta z}{z}) = x \cdot S_x \cdot (-\frac{\Delta z}{z}) \tag{A.1}$$

$$v(\Delta z) = y_s(z + \Delta z) - y_s(z) \cong (\frac{yf}{z}) \cdot S_y \cdot (-\frac{\Delta z}{z}) = y \cdot S_x \cdot (-\frac{\Delta z}{z}) \tag{A.2}$$

where f is referred to as the focal length, and (S_x, S_y) are scale factors in the coordinate directions (x, y) respectively. z defines the distance between the object and optics.

Three components of in-plane strain can be written as:

$$\varepsilon_{xx} = \frac{\partial u}{\partial x} \cong -(\frac{\Delta z}{z}) \tag{A.3}$$

$$\varepsilon_{yy} = \frac{\partial v}{\partial y} \cong -(\frac{\Delta z}{z}) \tag{A.4}$$

$$\varepsilon_{xy} = \frac{1}{2}(\frac{\partial u}{\partial y} + \frac{\partial v}{\partial x}) \cong 0 \tag{A.5}$$

It shows that an increasing out-of-plane motion Δz introduces the negative normal strain (ε_{xx} and ε_{yy}) in both directions.

1.2 Telecentric lens system for measurement

Specifically, a telecentric lens aims to reduce the effect of out-of-plane motion by arranging elements so that light passing through the entrance pupil is nearly parallel to the object axis (Sutton et al., 2009). In this case, strain measurement in Eq.A.3, A.4 and A.5 is modified by replacing the physical object distance z by an effective distance z_e. The latter is many times larger that z. Thus, the corresponding strain components are written as:

$$\varepsilon_{xx} \cong -(\frac{\Delta z}{z_e}); \quad \varepsilon_{yy} \cong -(\frac{\Delta z}{z_e}); \quad \varepsilon_{xy} \cong 0 \tag{A.6}$$

Theoretically, the effect of out-of-plane motion has been reduced with using a large effective object distance z_e.

1.3 Results of out-of-plane motion

Four different lens systems that used in the mechanical experiments in this thesis are concluded in Tab.A.1.

Detector	lens
Basler2 (acA2040-25gm)	Edmund optic MMS (obj 11)
Basler2 (acA2040-25gm)	Mitutoyo VMU-V microscope + 2× objective lens
Basler1 (PiA2400-17gm)	SILL TZM 0420/3.0-C telecentric lens
Basler2 (acA2040-25gm)	SILL TZM 0420/3.0-C telecentric lens

Table A.1: Different lens systems applied in different experiments in this thesis.

During the experiment images were captured, where the distance between optic and static specimen Δz was modified by manually changing the height of lens system as shown in Fig.A.1 (a). The *displacement* field was measured by digital image correlation and subsequently the stretches were obtained using the four-point-frame extensometer defined in this chapter.

Fig.A.1 (b)(c)(d) present the measured stretches U_{11}, U_{22}, U_{12} from different lens systems with respect to the height change Δz on a static specimen. Firstly, the systems with telecentric lens gave a stable stretch measurement. For instance in (b), U_{11} was measured less than 1.001 when height changes 0.5 mm, which was less than 1% error compared to the failure stretch $U_{11}^f = 1.13$. A similar trend was seen for ESRF systems (Basler2 + Mitutoyo lens). The system of Basler2 and Edmund optic captured the distinct images that were able to be correlated when height change even reached 1.5 mm. A linear relationship is seen similar as shown analytically. The error of in plane stretches linked to out-of-plane motion could reach 10%. For the shear stretch U_{12}, the values from all the systems were less than 0.0005 (around 0.4% compared to failure stretch U^f_{12}=0.135) and negligible as theoretically calculated in Eq.A.6.

In summary, when out-of-plane motion is within ±0.5 mm, the systems with telecentric lens and Mitutoyo lens can guarantee a trustworthy stretch measurement. It is noted that the system of basler2 detector with telecentric lens were applied to most experiments that carried out at Centres des Matériaux (CdM) while the detector Basler2 was used with Mitutoyo lens system for *in situ* laminographic experiments at beamline ID19 at the ESRF.

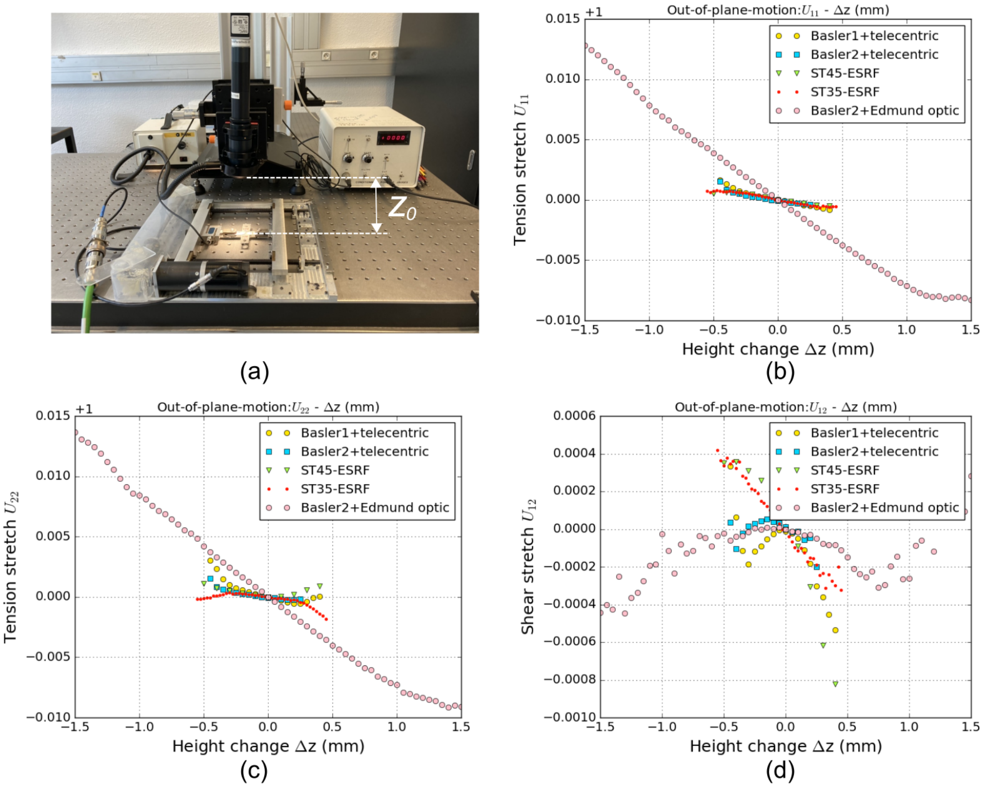

(a) (b)

(c) (d)

Figure A.1: (a) Experimental set-ups and measured normal stretch in terms of tension stretch (b) U_{11}, (c) U_{22} as well as shear stretch (d) U_{12} versus the vertical out-of-plane motion (in thickness direction Δz).

2 Machine stiffness study

The objective of this section is to find out whether the measured failure stretch is intrinsic to the material or somehow related to the elastic compliance of the machine. Moreover, a failure criterion is needed for numerical simulations as failure tends to be stable in simulations and unstable in experiments.

According to Petit et al. (2018), the total displacement u_t is equal to the sum of machine displacement u_m and sample displacement u_s. The latter can be decomposed into elastic displacement u_s^e and plastic displacement u_s^p of sample as illustrated in Fig.A.2. The displacements are decomposed as:

$$u_t = u_m + u_s = u_m + u_s^e + u_s^p = \frac{P}{K_m} + \frac{P}{K_s} + u_s^p \tag{A.7}$$

where P stands for the global applied load, K_m, K_s represent the stiffness of machine and sample respectively. It is assumed that machine only has purely elastic displacement, so that machine stiffness K_m is always constant during loading. K_s can evolve if a crack progresses.

During elastic domain, the plastic displacement of sample $u_s^p = 0$. The equation of A.7 is written as:

$$\frac{P}{K_t} = \frac{P}{K_m} + \frac{P}{K_s} \tag{A.8}$$

where K_t can be obtained from the experiment and K_s from local measurement or numerical simulation. Thus, the constant value of machine stiffness K_t can be solved.

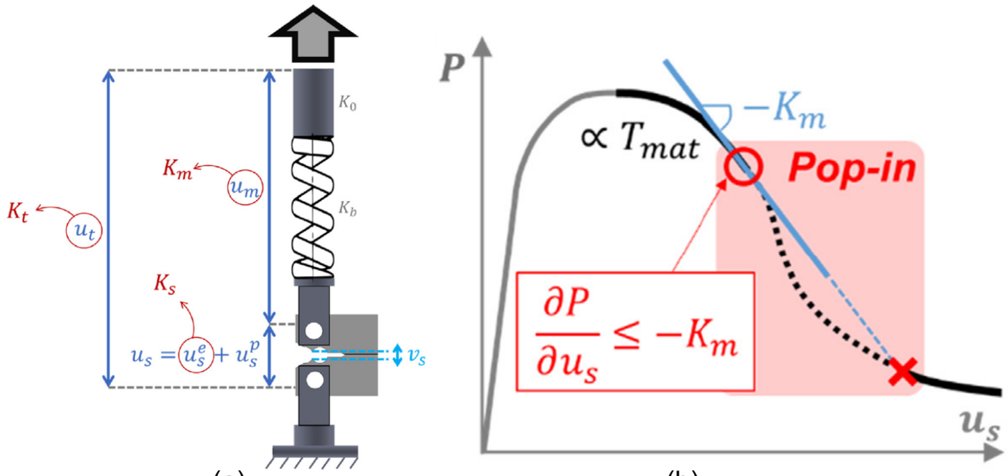

(a) (b)

Figure A.2: (a) Displacement and stiffness of the system contributors and (b) the curve of applied load P versus sample displacement u_s, where a failure criterion is used to show the pop-in instability initiation, after (Petit et al., 2018).

Under total displacement control (Δu_t=0), an instability corresponds to a sudden load drop. This resulted in a release of the elastic energy from the system and a opposite increase of sample displacement u_s. Fig.A.2 (b) presents the criterion $\Delta P/\Delta U_s \leq -K_m$ for instability initiation (Petit et al., 2018). The crack becomes stable again when the slope of experimental curve is greater than the negative value of machine stiffness -K_m.

Based on the Eq.A.8, the sample displacement u_s can be separated from the total displacement u_t by removing the effect of machine stiffness. Fig.A.3 exhibits the curves in terms of nominal stress versus sample global displacement u_s for (a) shear-only (SO) and (c) tension-only (TO) loadings.

Here two loading machines are selected for comparison: a stiff *Instron*-4204 machine with hydraulic grips and a small machine for *in situ* laminography, called *Lamix* machine. Fig.A.2 (b)(d) present the curves of the slope of $\Delta P/\Delta u_s$ versus global sample displacement u_s. Experimentally, the sudden load drops (instability) from the stiffer *Instron* machine occurred later than that from *lamix* machine, which is consistent with the higher machine stiffness K_m. In this way, the point of instability initiation can be chosen to represent a failure point for numerical simulations (full line). However, for the shear simulation in Fig.A.2 (a)(b), there is an intersection between the curve and the straight slope so called damage initiation (DI) or instability point. It indicates the simulated curve would be stable again after the instability point. More related work will be necessary to look into this issue in the aspect of numerical simulations.

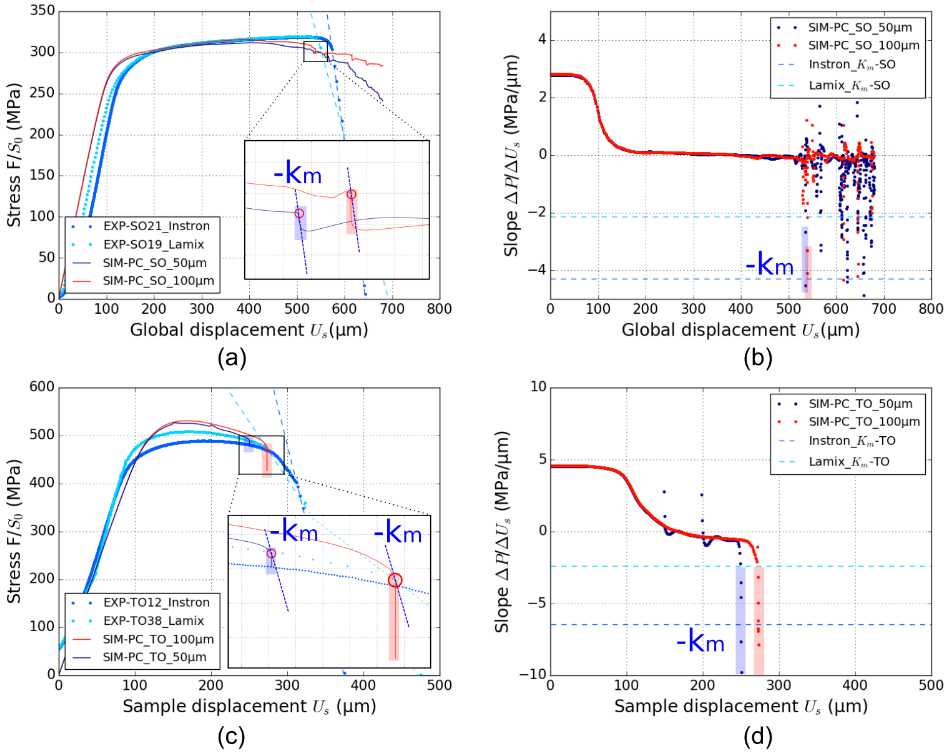

(a) (b)

(c) (d)

Figure A.3: The curves in terms of nominal stress F/S_0 versus sample displacement u_s under (a) shear-only (SO) and (c) tension-only (TO). The corresponding curves of slope $\Delta P/\Delta U_s$ versus sample displacement u_s under (b) SO and (d) TO.

3 Mesh convergence

Mesh convergence study was conducted on shear-only (SO), tension-only (TO) and 'shear to tension' (ST) simulations with element size varying from 10 µm to 200 µm. The curves force versus stretch are exhibited in Fig.A.4 (a)(b)(c)(d). The force error stands for the difference between the actual force and the reference force F_{10} from the fine mesh 10 µm on the chosen points ($U_{12} = 0.08$,$U_{11} = 1.11$). The force error versus element length is shown in Fig.A.4 (e). It is concluded that simulations have been converged with the element size down to 50 µm since the error is less than 0.2%.

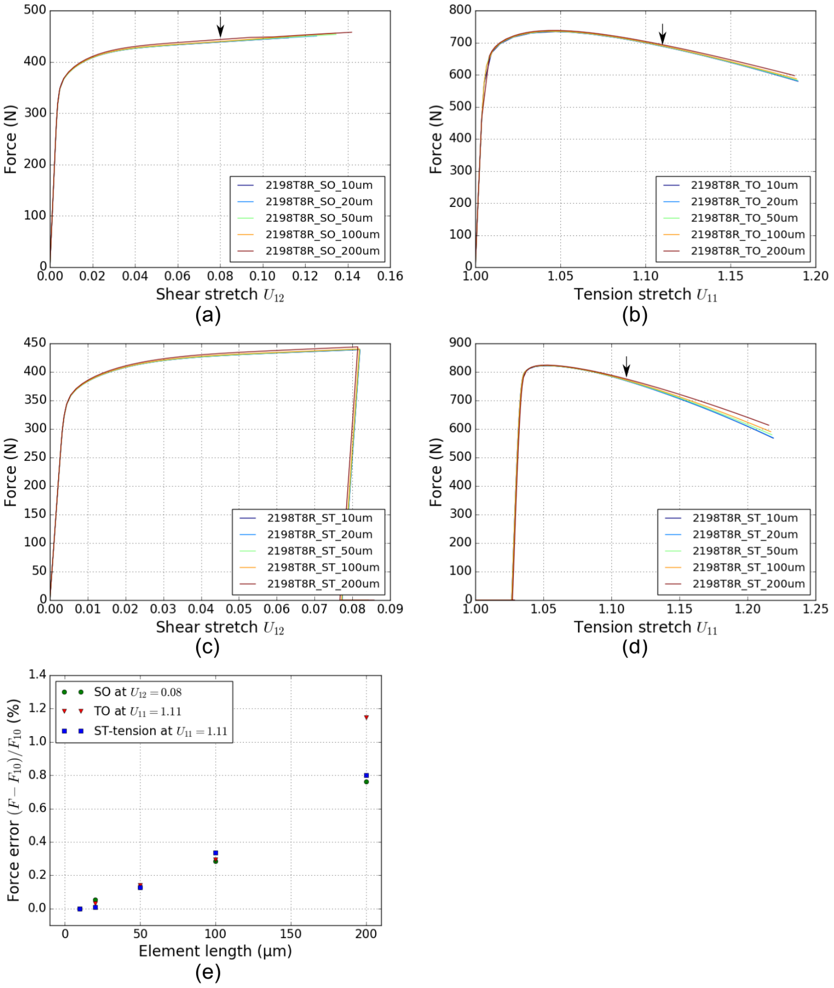

Figure A.4: The force versus stretch curves from the simulations of different mesh size from 10 µm to 200 µm under (a) shear-only (SO), (b) tension-only (TO) as well as (c) shear period and (d) tension period of non-proportional 'shear to tension' (ST).(e) Mesh convergence in terms of the curve force error versus element length size.

4 Fractography of 2198T8R

The fractography of four loading conditions TO, ST, SO and TS at various magnifications are exhibited in Fig.A.5, Fig.A.6, Fig.A.7 and Fig.A.8 via SEM. The features are similar as described for 2198T3R in Fig.3.1.4.

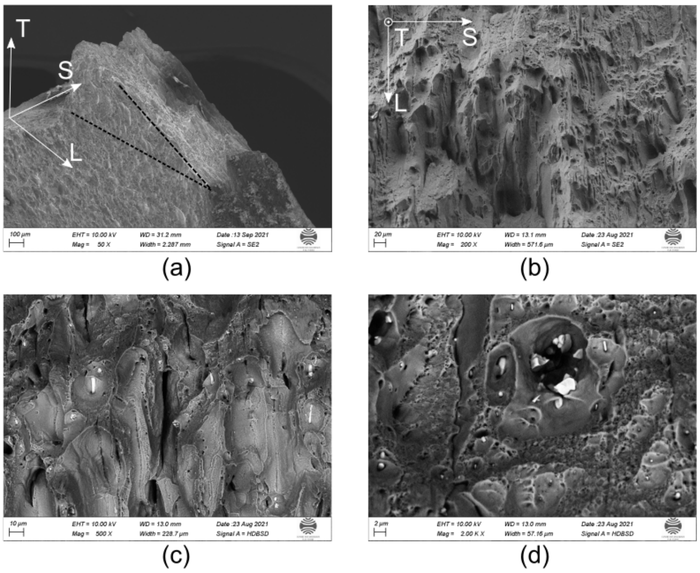

Figure A.5: Fractography via scanning electron microscopy (SEM) of 2198T8R under tension-only (TO): (a)(b) Macroscopic rouge fracture surface with (c) large dimple that initiated to the intermetallic particles and (d) medium dimples with broken particles.

5 Specimen geometries

The geometries of micro specimen series are attached in Fig.A.9 for shear-only (SO), Fig.A.10 for tension-only (TO) and Fig.A.11 for cruciform shear-tension (ST).

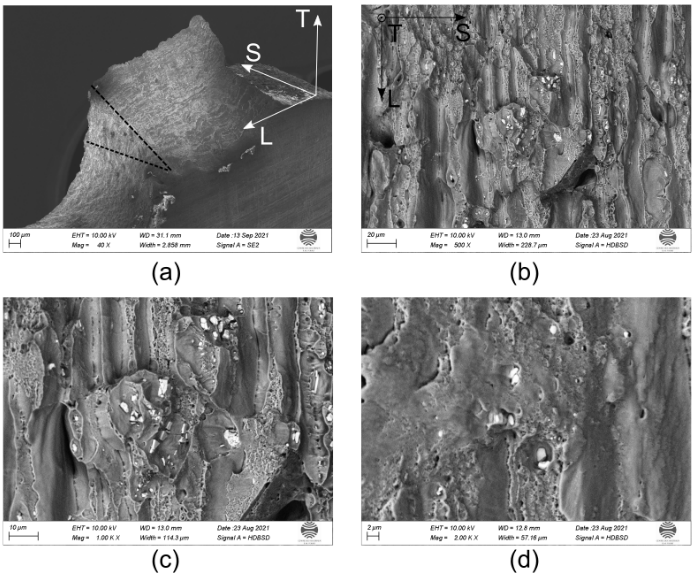

Figure A.6: Fractography via scanning electron microscopy (SEM) of 2198T8R under ‘shear to tension’ (ST): (a) Macroscopic slant fracture path in the T-S plane and relative smooth fracture surface, microscopic features like (b) large dimple that initiated to the (c) intermetallic particles and grain-shaped steps with medium dimples that initiated on the grain boundaries and (d) sub-micro dimples with the broken intermetallic particles.

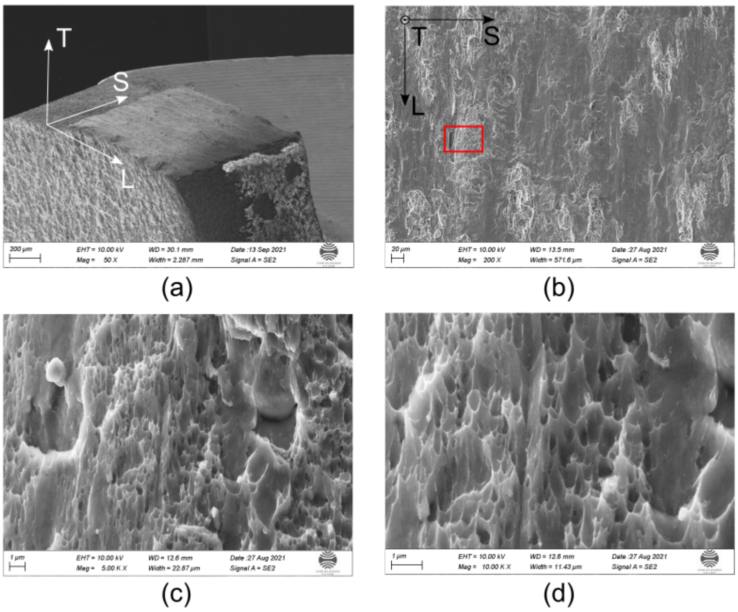

Figure A.7: Fractography via scanning electron microscopy (SEM) of 2198T8R under shear-only (SO): (a) Macroscopic smooth fracture surface, (b)(c) flat fracture surface and (d) Elongated ductile dimple cluster that initiated on the dispersoids.

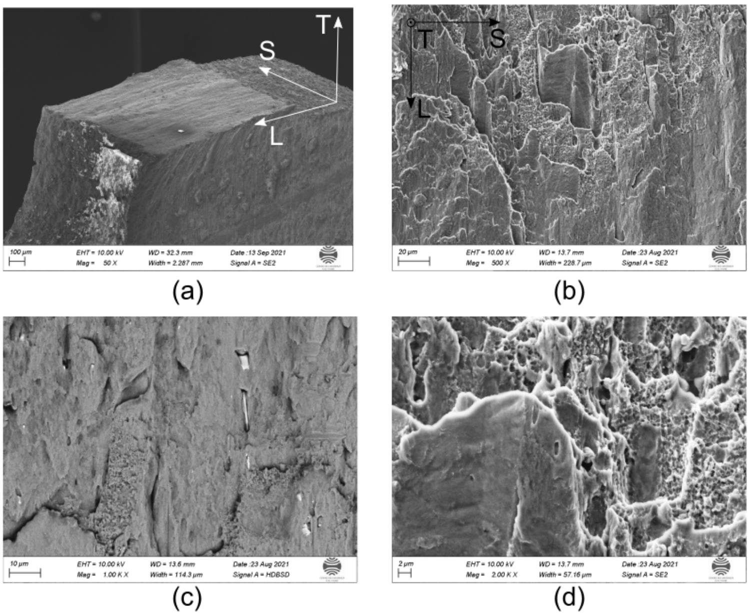

Figure A.8: Fractography via scanning electron microscopy (SEM) of 2198T8R under ‘tension to shear’ (TS): (a) Macroscopic smooth fracture surface, (b) shear fracture feature, (c) elongated intermetallic particles and (d) flat-like fracture feature with void sheeting features of sub-micro dimple cluster.

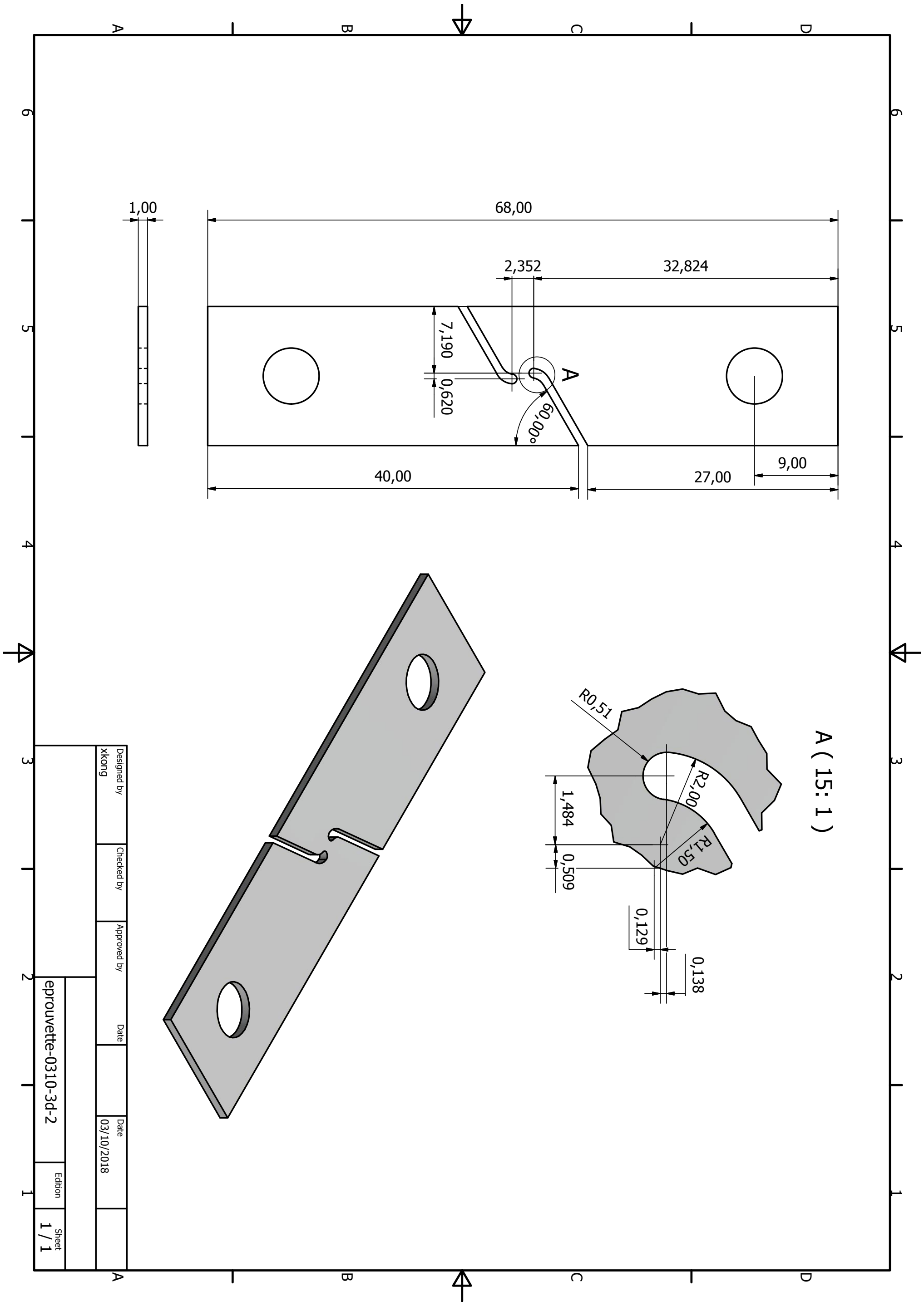

Figure A.9: Shear-only (SO) geometry.

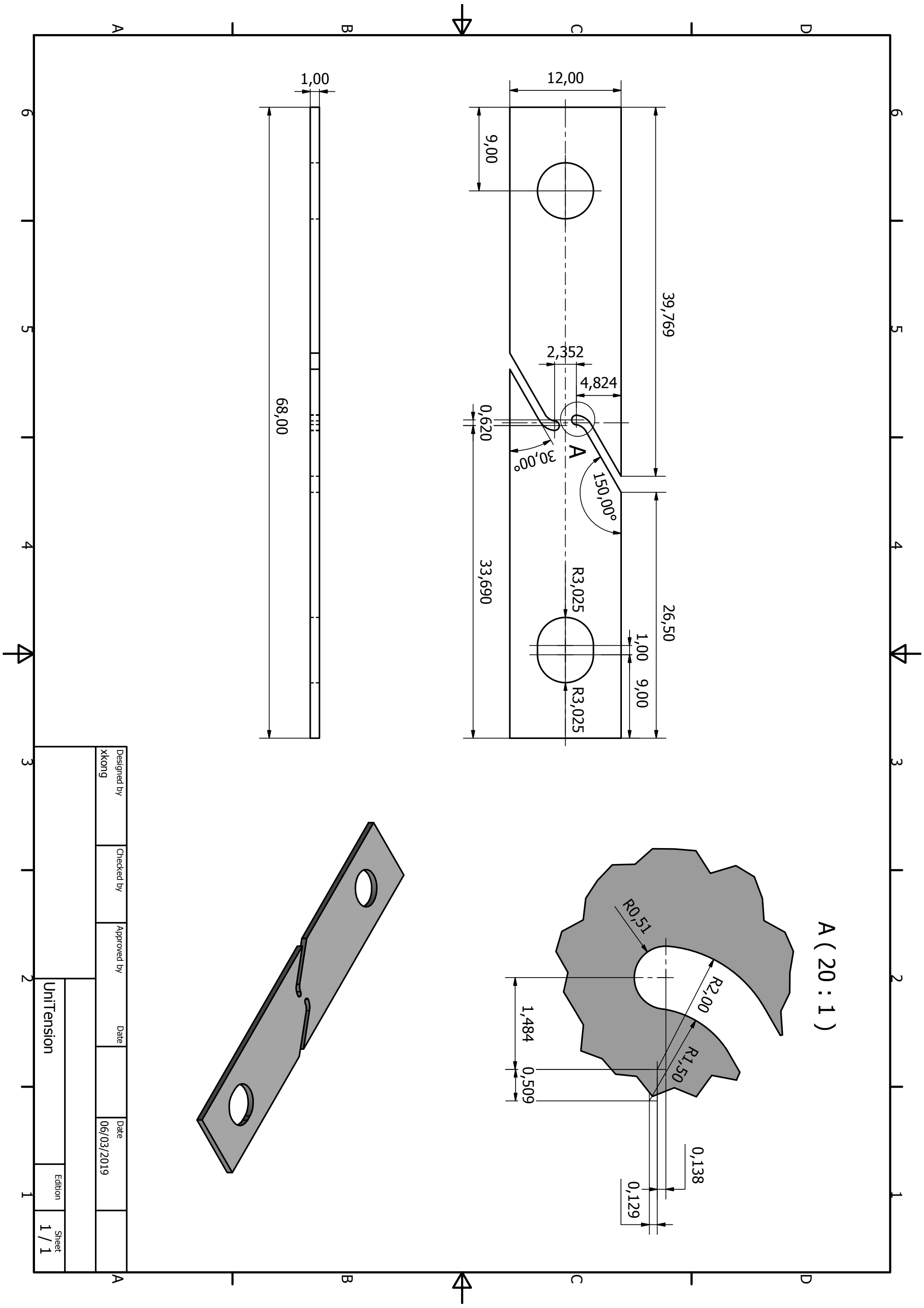

Figure A.10: Tension-only (TO) geometry.

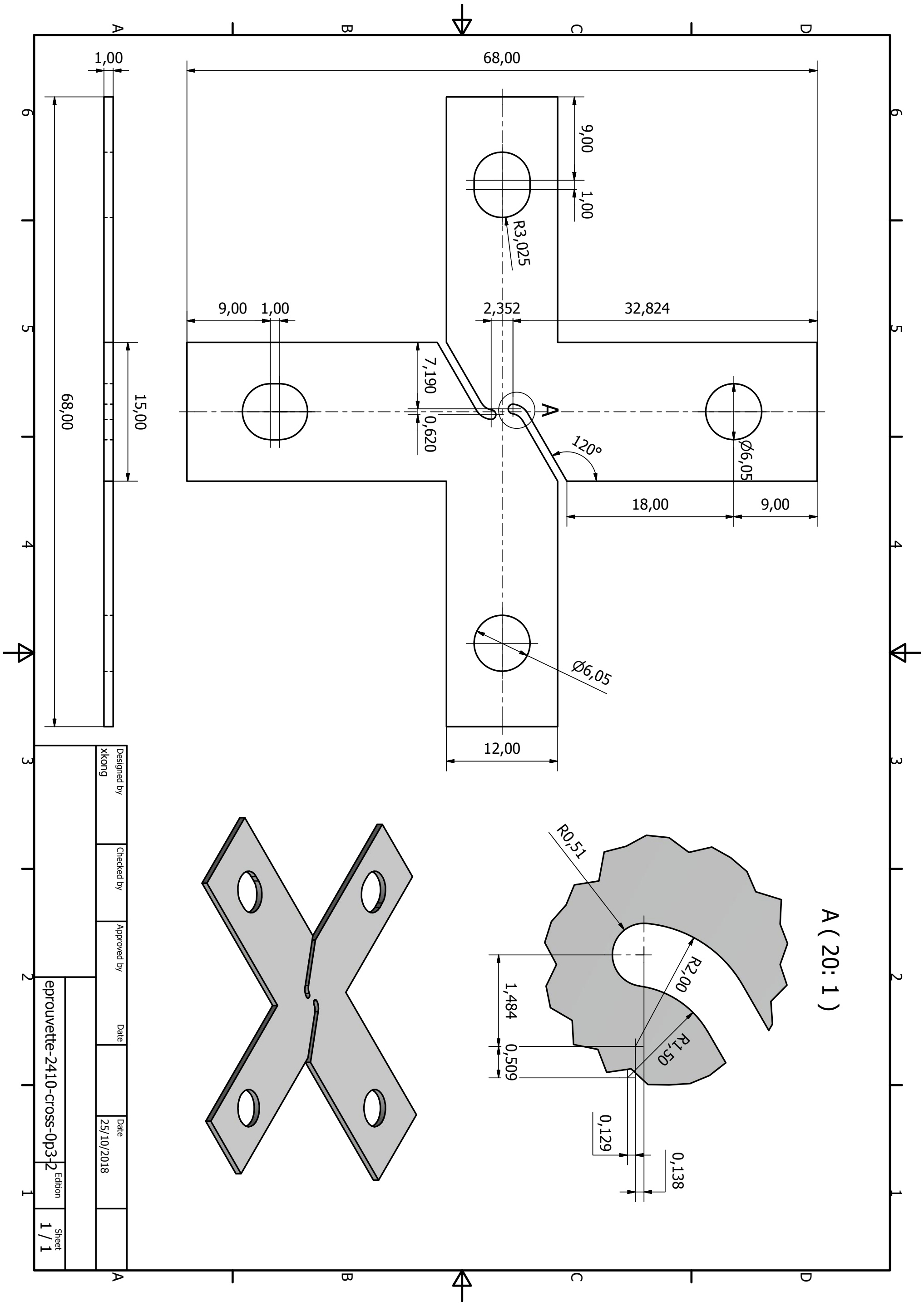

Figure A.11: The cruciform geometry for shear-tension.

Appendix B

Polycrystalline model

1 The fourth order tensor $\underline{\underline{D}}$

With Voigt notations, the form of the fourth order tensor $\underline{\underline{D}}$ for orthotropic materials is:

$$\underline{\underline{D}} = \begin{pmatrix} D_{11} & D_{12} & D_{13} & 0 & 0 & 0 \\ D_{21} & D_{22} & D_{23} & 0 & 0 & 0 \\ D_{31} & D_{32} & D_{33} & 0 & 0 & 0 \\ 0 & 0 & 0 & D_{44} & 0 & 0 \\ 0 & 0 & 0 & 0 & D_{55} & 0 \\ 0 & 0 & 0 & 0 & 0 & D_{66} \end{pmatrix} \tag{B.1}$$

The tensor $\underline{\underline{D}}$ has the symmetries in D_{ijkl}=D_{jikl}=D_{jilk}=D_{ijlk}, but it has not the strong symmetry in D_{ijkl}=D_{klij}. As $\underline{\underline{D}}$ is a linear relation between two deviatoric tensors, 7 independent components are needed from the relation:

$$D_{11} + D_{21} + D_{31} = D_{12} + D_{22} + D_{32} = D_{13} + D_{23} + D_{33} \tag{B.2}$$

In total, there are 10 independent coefficients (including three D_{44},D_{55} and D_{66}). Since D_{12} and D_{13} are not considered as variables in the optimization but calculated from Eq.B.2, the parameters in $\underline{\underline{D}}$ are optimized as followed:

$$\underline{\underline{D}} = \begin{pmatrix} 1311 & 1050^* & 1088^* & 0 & 0 & 0 \\ 775.9 & 1027 & 588.5 & 0 & 0 & 0 \\ 23.67 & 34.05 & 434.5 & 0 & 0 & 0 \\ 0 & 0 & 0 & 248.0 & 0 & 0 \\ 0 & 0 & 0 & 0 & 13.98 & 0 \\ 0 & 0 & 0 & 0 & 0 & 8218 \end{pmatrix} \tag{B.3}$$

2 The hardening matrix H^i_{st}

The 12×12 symmetric hardening matrix H^i_{st} can be denoted with different 3×3 matrices in Eq.B.5 and Eq.B.6:

$$H_{st} = \begin{bmatrix} H & H_{12} & H_{13} & H_{14} \\ H_{12}^T & H & H_{23} & H_{24} \\ H_{13}^T & H_{23}^T & H & H_{34} \\ H_{14}^T & H_{24}^T & H_{34}^T & H \end{bmatrix} \tag{B.4}$$

$$H = \begin{bmatrix} h_1 & h_2 & h_2 \\ h_2 & h_1 & h_2 \\ h_2 & h_2 & h_1 \end{bmatrix}, H_{12} = \begin{bmatrix} h_4 & h_5 & h_5 \\ h_5 & h_3 & h_6 \\ h_5 & h_6 & h_3 \end{bmatrix}, H_{13} = \begin{bmatrix} h_5 & h_6 & h_3 \\ h_4 & h_5 & h_5 \\ h_5 & h_3 & h_6 \end{bmatrix} \tag{B.5}$$

$$H_{14} = \begin{bmatrix} h_5 & h_3 & h_6 \\ h_5 & h_6 & h_3 \\ h_4 & h_5 & h_5 \end{bmatrix}, H_{23} = H_{24}^T = H_{34} = \begin{bmatrix} h_6 & h_5 & h_3 \\ h_3 & h_5 & h_6 \\ h_5 & h_4 & h_5 \end{bmatrix} \tag{B.6}$$

Each 12×12 symmetric hardening matrix H_{st}^i in Eq.B.4 only depends on six parameters h_1 to h_6 where h_1=1 for the diagonal terms according to Méric et al. (1991).

3 Combined damage fields

A combined damage variable, consisting of porosity on the microscale and maximal Coulomb slip at the slip system scale, was defined in Eq.6.16 to quantify the damage during various loading paths. The local fields at damage initiation point (DI) are shown in Fig.B.1 for proportional shear-only (SO). Fig.B.2 presents the combined damage fields at failure point under tension-only (TO). The fields of non-proportional loading path 'shear to tension' (ST) are exhibited in Fig.B.3 for coarse mesh and Fig.B.4 for fine mesh. Fig.B.5 and Fig.B.6 present the fields of the other non-proportion loading path 'tension to shear' (TS) for different meshes respectively.

shear-only (SO): The combined damage fields at shear damage initiation point are shown in Fig.B.1 for (a) coarse mesh and (b) fine mesh. A 180° rotationally symmetric band was located at the highly deformed region and the damage level of the whole band was more than 5%. There were several localized elements with high value due to activated Coulomb slips, although the maximum damage of legend was set as only 0.12. The band indicated the fracture path under SO as experiments in chapter 3.

Considering that the damage initiation points were very close for both meshes and the field of fine mesh was smoother, five cross sections on LS plane of fine mesh calculations were chosen from central plane to left-4 plane in (c) for displaying the damage distribution through the thickness direction (S). The combined damage were localized in the region 100 μm away from notches at left-4 plane. On LS planes, the damage was distributed homogeneously through the thickness from surfaces (Z=0, Z=1) to middle thick plane (Z=0.5).

Tension only (TO): Fig.B.2 shows combined damage fields at fracture point for (a)

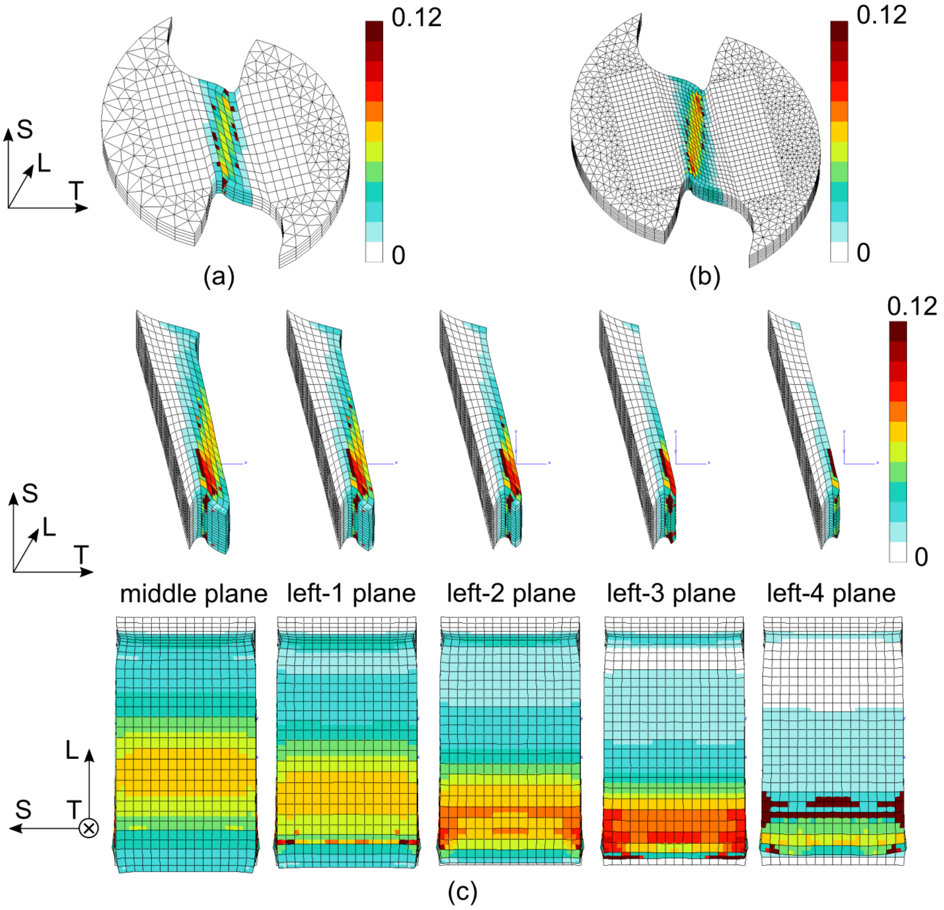

Figure B.1: Local combined damage fields of the ROI on middle-thickness plane (z=0.5) at damage initiation (DI) point under proportional loading shear-only (SO) for (a) coarse mesh and (b) fine mesh. (c) The combined damage maps at different cross sections through thickness (LS plane) for fine mesh.

coarse mesh and (b) fine mesh. Like porosity and Coulomb fields, the combined damage was localized on notches at middle thickness plane. The damage band linked the symmetric localization on notches and thus indicated the fracture path.

Different cross sections in LS plane at fracture point are presented in Fig.B.2 (c). The damage on LS planes exhibited a cross shape symmetric to the half thickness (Z=0.5). The damage was mainly localized on notches of left-2 and left-3 planes.

The damage evolution in left-2 plane is exhibited in Fig.B.2 (d). Time step ratio is defined as the proportion of current tension stretch to the failure tension stretch. The combined damage started to localize on notch at 90% time step and continued to grow. The region simultaneously expanded to 250 μm in L and 300 μm in S with increasing tension loading.

'Shear to tension' (ST): Fig.B.3 presents the combined damage fields under 'shear to tension' (ST) for coarse mesh at (a) shear pre-loading end (SE) point and (b) subsequent tension fracture point. There were little combined damage (mainly porosity) around 0.01-0.02 at the end of pre-shear loading on the ligament between two notches. The damage subsequently increased when it turned to tension loading. Two elements in middle thickness plane escalated more than 0.12, which was due to the activated Coulomb slips shown in Fig.6.10 (e).

Two cross sections attached to the localized element were chosen to exhibit the evolution from shear to tension in (c) central plane and (d) left-1 plane. On the central plane, the damage was homogeneous as 2% at the shear end. Damage started to localize on the middle-thickness from 90% tension fracture point, where the ratio is defined as the current tension stretch to the tension stretch to failure, and damage was highly localized at the four elements on central plane at the tension fracture point. On left-1 plane in (d), the damage grew to 2% homogeneously at the end of shear pre-loading. It continued to increase on a linear region near notches along S through the whole thickness and eventually reached to 7%. Most combined damage of the whole region, partly contributed from the porosity, continued to grow under the subsequent tension loading. It represented physical phenomena such as void growth under tension.

Fig.B.4 presents the combined damage fields under 'shear to tension' (ST) for fine mesh at (a) shear pre-loading end (SE) point and (b) subsequent tension fracture point. There were 2% combined damage on the band similar as the one of coarse mesh. However, it should be noticed that the fracture point of fine mesh was earlier than that of coarse mesh shown in Fig.6.6 (b). Thus, it explained that the combined damage of fine mesh at tension fracture point in (b) seemed less than that of coarse mesh in Fig.B.3 (b).

Different LS cross sections were chosen to exhibit the damage fields through the thickness at tension fracture point in Fig.B.4 (c). Damage was moderately homogeneous less than 4% from the view of central plane, left-1 plane and left-2 plane. A rectangular region in left-3 plane presented Coulomb damage around 150 μm in L, which was similar as the left-1 plane of coarse mesh in Fig.B.3 (d). In addition, there were damage localization at left-4 and left-5 planes. The region was 50 μm from notches and closed to the surface plane (Z=0, Z=1) instead of the middle-thick plane (Z=0.5).They were

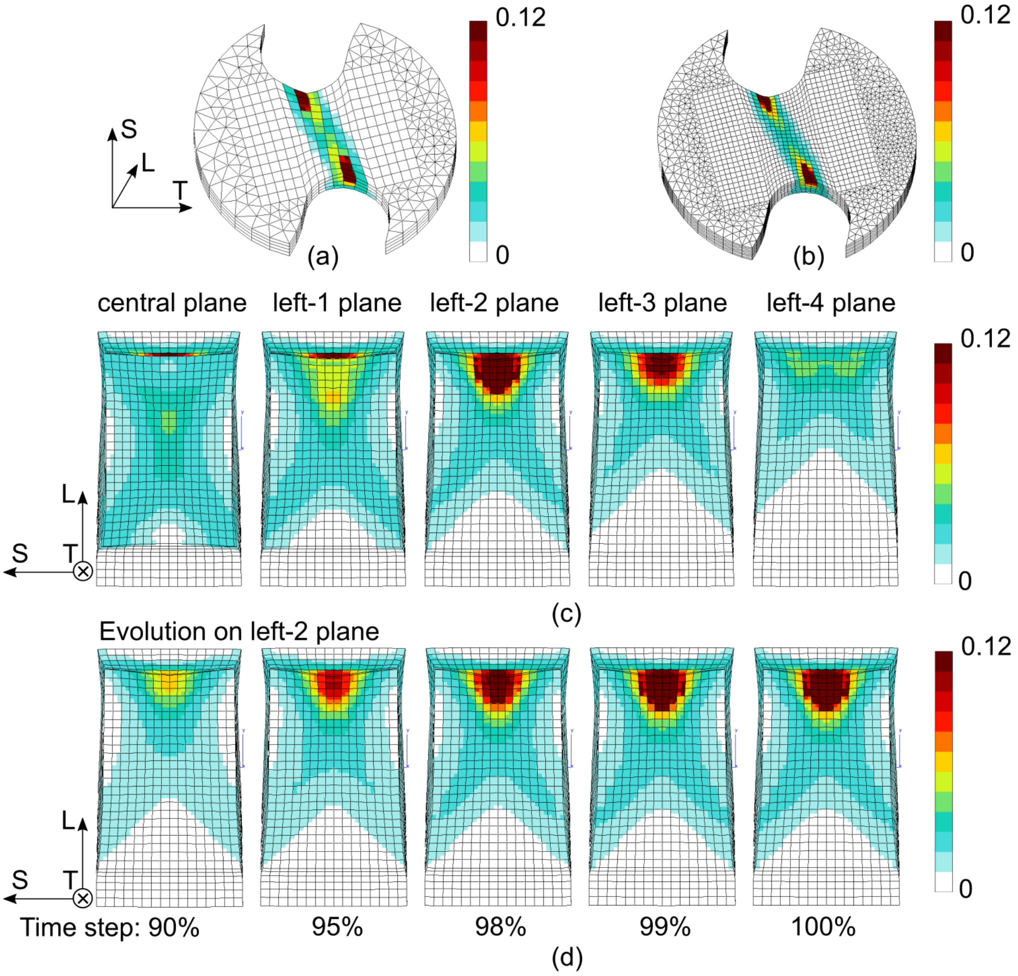

Figure B.2: Local combined damage fields at fracture point in middle-thickness plane (z=0.5) under proportional loading tension-only (TO) for (a) coarse mesh and (b) fine mesh. (c) The combined damage maps at different cross sections through thickness (L-S) for fine mesh. (d) The damage evolution on left-2 plane, where time step ratio is defined as the proportion of current tension stretch to the tension stretch to failure.

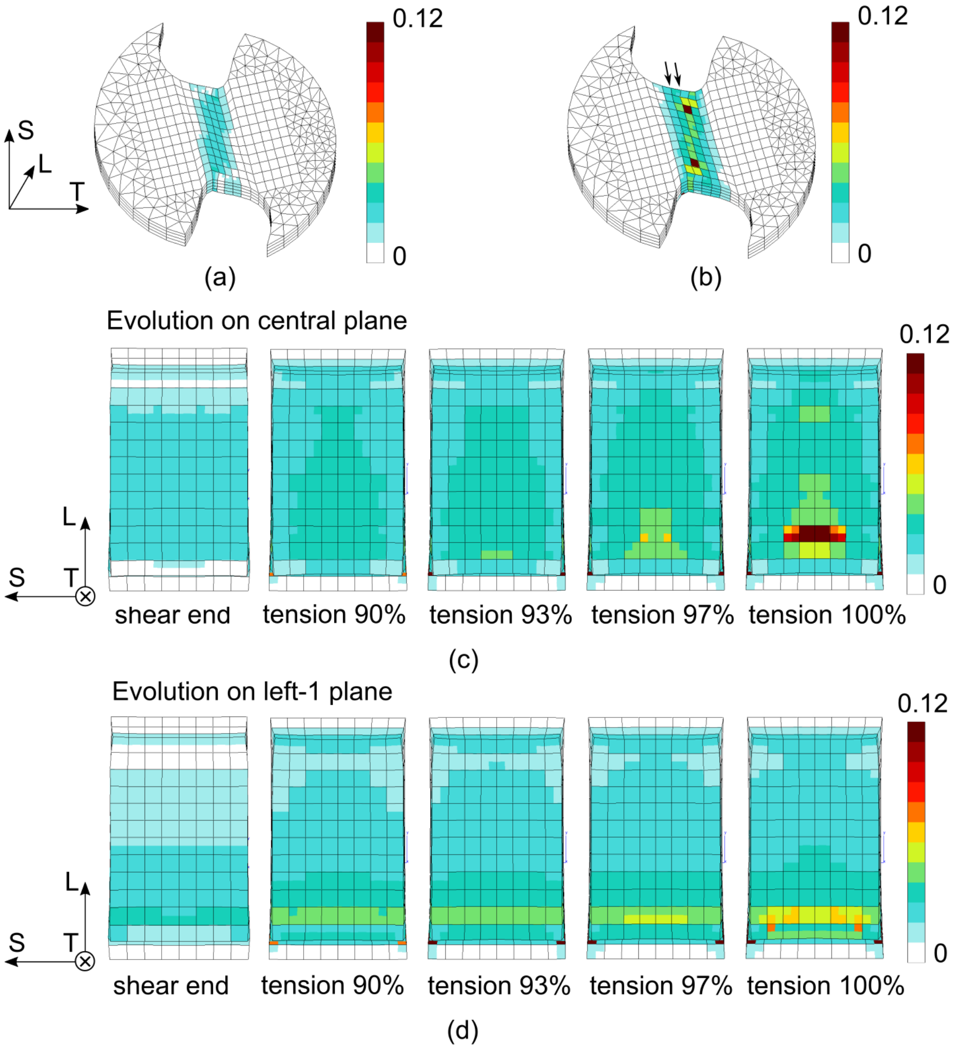

Figure B.3: Local combined damage fields of coarse mesh in middle-thickness plane (z=0.5) under non-proportional loading ‘shear to tension’ (ST) at (a) shear pre-loading end (SE) point and (b) the subsequent tension fracture point. The combined damage evolution on (c) central plane and (d) left-1 plane from shear to tension loading path changes, where the tension ratio is defined as the proportion of current tension stretch to tension stretch to failure.

rather due to the activated Coulomb slips.

The damage evolution on left-3 plane is shown in Fig.B.4 (d). The left-3 plane of fine mesh represented the plane 150 µm away from the central plane, which was near left-1 plane of coarse mesh (100 µm from the central plane). The damage evolution was very similar to left-1 plane of coarse mesh in Fig.B.3 (d).

'Tension to shear' (TS): Fig.B.5 presents the combined damage fields under 'tension to shear' (TS) for coarse mesh at (a) tension pre-loading end (TE) point and (b) subsequent shear damage initiation point. At the end of tension pre-loading, the combined damage generates a band of 2%, which was similar as in Fig.6.11(a) the cumulative strain and (c) porosity fields while no Coulomb slip was activated in this stage. The combined damage all came from the porosity part on notches. When it turned to shear loading, the damage on notches continued to grow and the whole band widened to higher level 10% shown in (b). Unlike the proportional shear-only (SO) loading, the band was parallel to the orientation of Cartesian elements. Several Coulomb slips were activated under shear and they contributed to the combined damage on the band border.

Two cross sections in LS plane were chosen to exhibit damage evolution on (c) central plane and (d) left-1 plane. On central plane, a cross-shaped damage occurred at the end of pre-tension loading and then the whole plane was under damage from surfaces (Z=0, Z=1) to middle-thickness plane (Z=0.5) till the global shear damage initiation (DI) point. Damage was homogeneous on the central plane during the shear loading. Fig.B.5 (d) shows the damage evolution on left-1 plane. The combined damage was localized on two columns of elements during the subsequent shear loading. One column is near middle ligament and the other is 100 µm from the highly deformed notch. The in-plane damage distribution of left-1 plane of coarse mesh (100 µm from the central plane) was very similar to the one on left-4 plane of fine mesh (200 µm from the central plane) under SO loading in Fig.B.1 (c). It partly resulted from the deformed geometry (e.g. offset of notches) due to the pre-tension loading as discussed in chapter.3. However, unlike the proportional loading, the damage of the pre-tension loading on notches also continued to increase from 2% to 7%.

Fig.B.6 presents the combined damage fields under 'tension to shear' (TS) for fine mesh at (a) tension pre-loading end (TE) point and (b) subsequent shear damage initiation point. The global fields were smoother than that of coarse mesh in Fig.B.5 (a)(b). It should be recalled that the shear damage initiation of fine mesh (U_{12}=0.105) was much earlier than that of coarse mesh (U_{12}=0.152). It explained the combined damage on middle-thick plane (Z=0.5) seems less than the field of coarse mesh at damage initiation point.

Moreover, the same L-S cross sections were chosen as in coarse mesh to exhibit the damage evolution from tension to shear load path changes. On central plane in (c), the cross-shaped damage around 2% from tension pre-loading continued to grow till 6%. The damage expanded from the middle-thick plane to the surfaces. On left-2 plane (100 µm from the central plane, equivalent to left-1 plane of coarse mesh) in (d), damage localization appeared through the thickness when subsequent shear stretch reaches to 93%

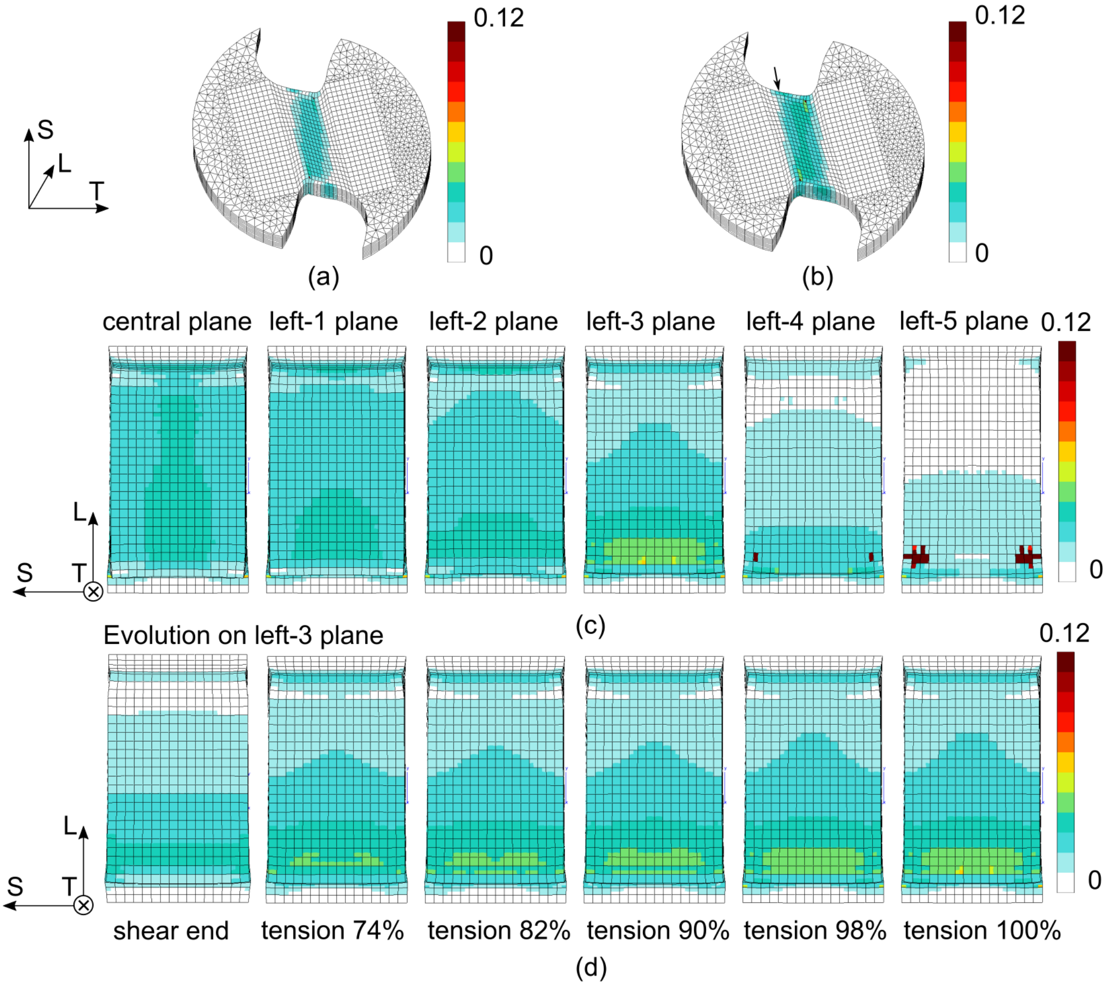

Figure B.4: The combined damage fields of fine mesh in middle-thickness plane (z=0.5) under non-proportional loading 'shear to tension' (ST) at (a) shear pre-loading end (SE) point and (b) the subsequent tension fracture point. (c) The combined damage fields of the different cross sections through thickness (L-S) at subsequent tension failure point. (d) The damage evolution on left-3 plane from shear to tension loading path changes. The tension ratio is defined as the proportion of current tension stretch to tension stretch to failure.

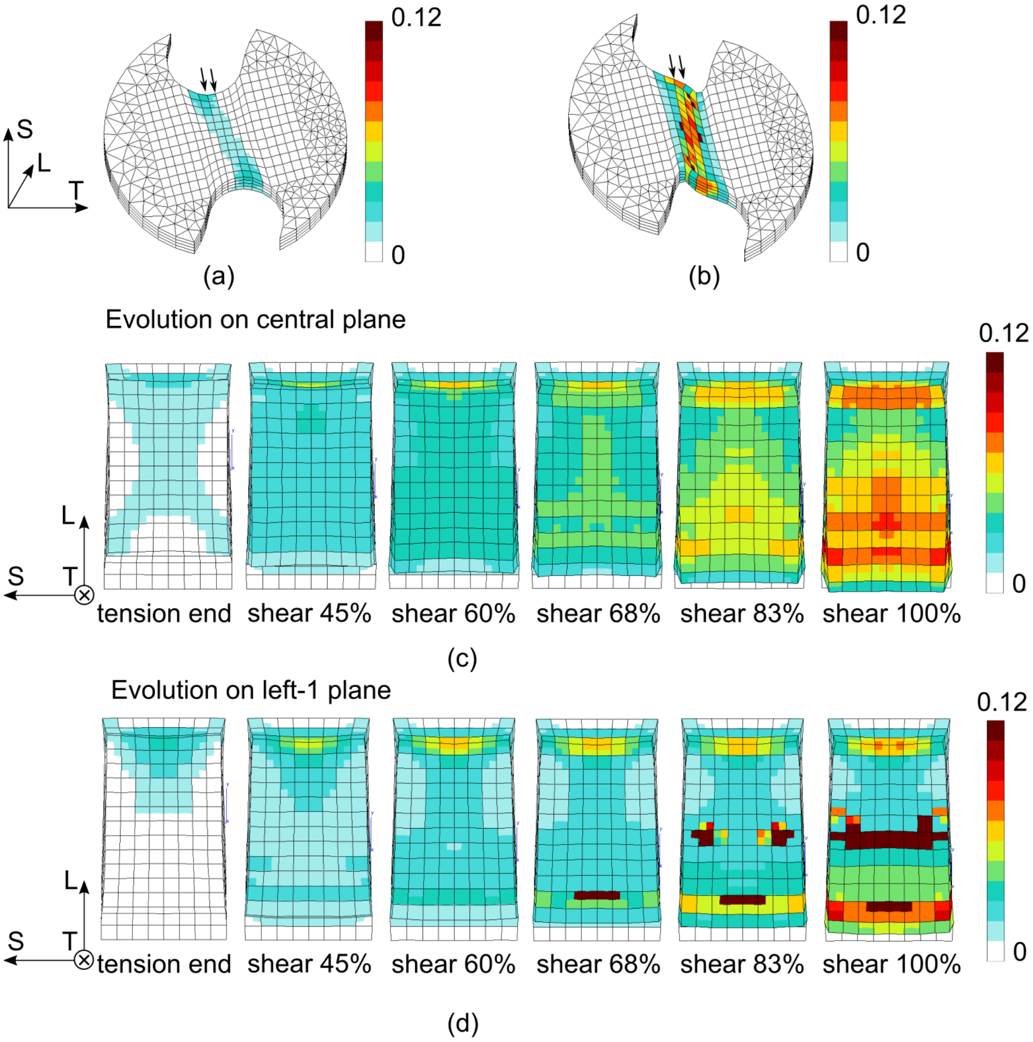

Figure B.5: Local combined damage fields in middle-thickness plane (z=0.5) under non-proportional loading ‘tension to shear’ (TS) for coarse mesh at (a) the end of pre-tension loading (TE) point and (b) shear damage initiation (DI) point. The combined damage evolution on (c) central plane and (d) left-1 plane from tension to shear loading path changes. The shear ratio is defined as the proportion of current shear stretch to the shear stretch at damage initiation point.

of that at damage initiation point. The localization was originated from the activated Coulomb slips shown in Fig.6.12 (g). The in-plane position of localization was slightly different from the position of coarse mesh, which probably was in consequence of mesh dependence. In addition, damage on notches from pre-tension loading increased more than 10%.

4 Texture evolution

During intense shear loading, there is very large deformation (i.e. cumulative strain reaches nearly 1) at the localization band. The underlying mechanism such as crystallographic texture evolution can be taken into account in this condition, see for example in Rousselier et al. (2009).

Texture evolution is modeled by actualizing the lattice orientation ($\vec{n}_s$,$\vec{l}_s$). In the material co-rotational frame, the rotation rate vanishes:

$$\underline{W}^c = 0 \tag{B.7}$$

Classically to model texture evolution, an assumption is taken that all grains have the same total rotation rate as Taylor-like hypothesis:

$$\underline{\omega}_g = \underline{\omega}_g^e + \underline{\omega}_g^p \equiv \underline{W}^c = 0, \ \forall g = 1, N. \tag{B.8}$$

The plastic rotation rate of each grain is:

$$\underline{\omega}_g^p = \sum_{s=1}^{M} \underline{q}_{sg} \dot{\gamma}_{sg} \tag{B.9}$$

where $\underline{q}_{sg}$ stands for the rotation tensor of each slip system s within the grain g:

$$\underline{q}_{sg} = (\vec{l}_{sg} \otimes \vec{n}_{sg} - \vec{n}_{sg} \otimes \vec{l}_{sg})/2 \tag{B.10}$$

The lattice rotation tensor $\underline{R}_g$ of each grain in the co-rotational frame can be obtained from:

$$\dot{\underline{R}}_g \underline{R}_g^T = \underline{\omega}_g^e = -\underline{\omega}_g^p = -\sum_{s=1}^{M} \underline{q}_{sg} \dot{\gamma}_{sg} \tag{B.11}$$

The slip systems of the actualized texture are defined by:

$$\vec{n}_{gs} = \underline{R}_g \vec{n}_{gs}(0), \vec{l}_{gs} = \underline{R}_g \vec{l}_{gs}(0) \tag{B.12}$$

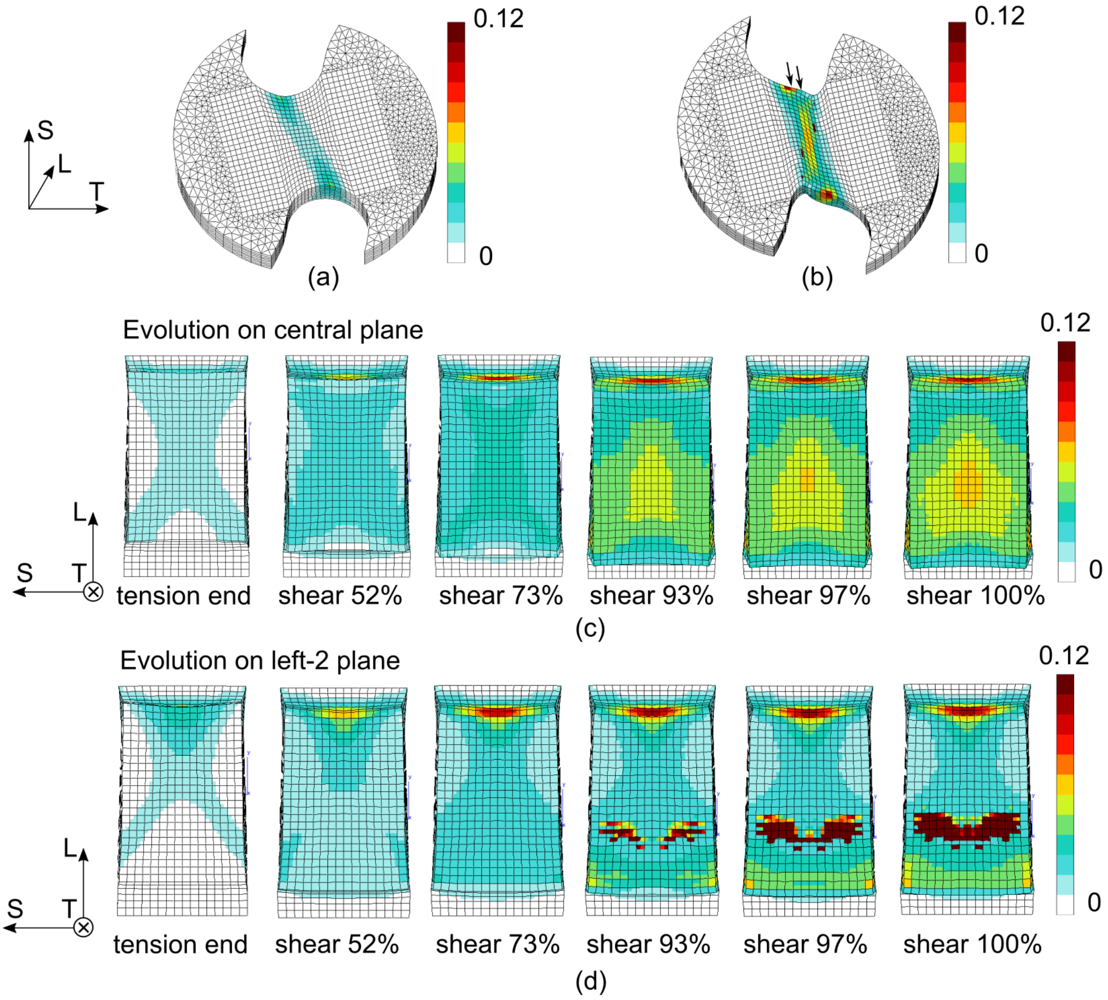

Figure B.6: Local combined damage fields in middle-thickness plane (z=0.5) under non-proportional loading 'tension to shear' (TS) for fine mesh at (a) the end of pre-tension loading (TE) point and (b) shear damage initiation (DI) point. The combined damage evolution on (c) central plane and (d) left-2 plane from tension to shear loading path changes. The shear ratio is defined as the proportion of current shear stretch to the shear stretch at damage initiation point.

It is assumed that $\underline{\omega}_g^e$ is constant during every small time increment Δt, thus Eq.B.11 can be integrated the following:

$$\underline{R}_g(t + \Delta t) = \exp(\underline{A}).\underline{R}_g(t) \tag{B.13}$$

where $\underline{A} = \underline{\omega}_g^e \Delta t$.
According to Cayley-Hamilton's theorem in Eq.B.14 for the particular form of $\underline{A}$, the development of $exp(\underline{A})$ is limited to the three terms $\underline{A}^0 = \underline{1}$, $\underline{A}^1$ and $\underline{A}^2$:

$$\underline{A}^3 = -w^2 \underline{A},\ w^2 = A_{12}^2 + A_{23}^2 + A_{31}^2 \tag{B.14}$$

$$\exp(\underline{A}) = \underline{1} + (1 - \frac{w^2}{6} + ...)\underline{A} + (\frac{1}{2} - \frac{w^2}{24} + ...)\underline{A}^2 \tag{B.15}$$

Eq.B.15 is applied in the numerical integration, with a sufficiently large number of terms. The close-form equation is the following:

$$\exp(\underline{A}) = \underline{1} + \frac{\sin w}{w}\underline{A} + \frac{1 - \cos w}{w^2}\underline{A}^2 \tag{B.16}$$

Once texture evolution option is activated in the model, all the parameters need to be optimized again for the calibration strategy. Limited to time for the re-calibration work with texture evolution, a trial calculation with current optimized parameters was launched in order to verify the effect of texture evolution. It is highly reminded that all parameters were calibrated without texture evolution, which means the new trial calculation does NOT fit with experiment in terms of nominal stress versus stretch.

Fig.B.7 presents the Maximal Coulomb slips field at damage initiation point. Unlike the field without texture evolution in Fig.6.7 (e) or (f), the Coulomb slips were activated mainly on the localization band instead of band borders. It indicates the region where the granular related flat cracks were found. This difference demonstrates the apparent effect of texture evolution on the highly deformed region under intense shear loading.

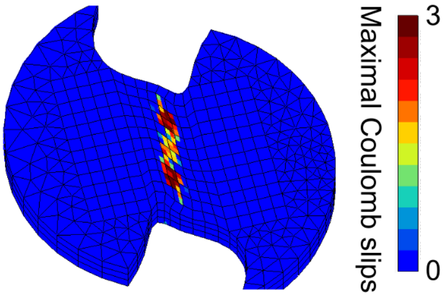

Figure B.7: Maximal Coulomb slip field under proportional shear-only (SO) with using texture evolution.

The re-calibration procedure is necessarily performed with activating option of texture evolution in the next step. The methodology in this chapter could be applied again with optimized parameters with texture evolution.

Bibliography

Abedini, A., Butcher, C., and Worswick, M. (2018). Experimental fracture characterisation of an anisotropic magnesium alloy sheet in proportional and non-proportional loading conditions. *International Journal of Solids and Structures*, 144-145:1–19.

Abedini, A., Butcher, C., and Worswick, M. J. (2017). Fracture characterization of rolled sheet alloys in shear loading: Studies of specimen geometry, anisotropy, and rate sensitivity. *Experimental Mechanics*, 57(1):75–88.

Achouri, M., Germain, G., Dal Santo, P., and Saidane, D. (2013). Experimental characterization and numerical modeling of micromechanical damage under different stress states. *Materials & Design*, 50:207–222.

Al Akhrass, D., Bruchon, J., Drapier, S., and Fayolle, S. (2014). Integrating a logarithmic-strain based hyperelastic formulation into a three-field mixed finite element formulation to deal with incompressibility in finite-strain elastoplasticity. *Finite Elements in Analysis and Design*, 86:61–70.

Anderson, T. L. (2005). *Fracture Mechanics: Fundamentals and Applications, Third Edition.* CRC press.

Asserin–Lebert, A., Besson, J., and Gourgues, A. (2005). Fracture of 6056 aluminum sheet materials: effect of specimen thickness and hardening behavior on strain localization and toughness. *Materials Science and Engineering: A*, 395(1):186–194.

Bai, Y., Teng, X., and Wierzbicki, T. (2009). On the Application of Stress Triaxiality Formula for Plane Strain Fracture Testing. *Journal of Engineering Materials and Technology*, 131(2). 021002.

Bai, Y. and Wierzbicki, T. (2008). A new model of metal plasticity and fracture with pressure and lode dependence. *International Journal of Plasticity*, 24(6):1071–1096.

Bai, Y. and Wierzbicki, T. (2009). Application of extended mohr–coulomb criterion to ductile fracture. *International Journal of Fracture*, 161(1):1.

Bao, Y. and Wierzbicki, T. (2004). On fracture locus in the equivalent strain and stress triaxiality space. *International Journal of Mechanical Sciences*, 46(1):81–98.

Barlat, F., Lege, D. J., and Brem, J. C. (1991). A six-component yield function for anisotropic materials. *International Journal of Plasticity*, 7(7):693–712.

Barsoum, I. and Faleskog, J. (2007a). Rupture mechanisms in combined tension and shear—experiments. *International Journal of Solids and Structures*, 44(6):1768–1786. Physics and Mechanics of Advanced Materials.

Barsoum, I. and Faleskog, J. (2007b). Rupture mechanisms in combined tension and shear—micromechanics. *International Journal of Solids and Structures*, 44(17):5481–5498.

Bažant, Z. P., Belytschko, T. B., and Chang, T. (1984). Continuum theory for strain‐softening. *Journal of Engineering Mechanics*, 110(12):1666–1692.

Belytschko, T., Liu, W., and Moran, B. (2000). *Nonlinear Finite Elements for Continua and Structures*. John Wiley & Sons, Ltd.

Benzerga, A., Besson, J., and Pineau, A. (2004). Anisotropic ductile fracture: Part i: experiments. *Acta Materialia*, 52(15):4623–4638.

Benzerga, A. A. and Besson, J. (2001). Plastic potentials for anisotropic porous solids. *European Journal of Mechanics - A/Solids*, 20(3):397–434.

Benzerga, A. A. and Leblond, J.-B. (2010). Ductile fracture by void growth to coalescence. In Aref, H. and van der Giessen, E., editors, *Advances in Applied Mechanics*, volume 44 of *Advances in Applied Mechanics*, pages 169–305. Elsevier.

Besson, J. (2010). Continuum models of ductile fracture: A review. *International Journal of Damage Mechanics*, 19(1):3–52.

Besson, J. and Foerch, R. (1997). Large scale object-oriented finite element code design. *Computer Methods in Applied Mechanics and Engineering*, 142(1):165 – 187.

Bron, F. and Besson, J. (2004). A yield function for anisotropic materials application to aluminum alloys. *International Journal of Plasticity*, 20(4):937–963.

Bron, F., Besson, J., and Pineau, A. (2004). Ductile rupture in thin sheets of two grades of 2024 aluminum alloy. *Materials Science and Engineering: A*, 380(1):356–364.

Brünig, M., Zistl, M., and Gerke, S. (2021). Numerical analysis of experiments on damage and fracture behavior of differently preloaded aluminum alloy specimens. *Metals*, 11(3).

Buljac, A. (2017). *Understanding, observation and quantification of ductile failure mechanisms via 3D imaging*. Theses, Université Paris Saclay (COmUE).

Buljac, A., Helfen, L., Hild, F., and Morgeneyer, T. F. (2018a). Effect of void arrangement on ductile damage mechanisms in nodular graphite cast iron: In situ 3D measurements. *Engineering Fracture Mechanics*, 192:242–261.

Buljac, A., Hild, F., Helfen, L., and Morgeneyer, T. F. (2018b). On deformation and damage micromechanisms in strong work hardening 2198 t3 aluminium alloy. *Acta Materialia*, 149:29 – 45.

Buljac, A., Shakoor, M., Neggers, J., Bernacki, M., Bouchard, P.-O., Helfen, L., Morgeneyer, T. F., and Hild, F. (2017). Numerical validation framework for micromechanical simulations based on synchrotron 3d imaging. *Computational Mechanics*, 59(3):419–441.

Buljac, A., Taillandier-Thomas, T., Morgeneyer, T. F., Helfen, L., Roux, S., and Hild, F. (2016). Slant strained band development during flat to slant crack transition in aa 2198 t8 sheet: in situ 3d measurements. *International Journal of Fracture*, 200(1):49–62.

Butcher, C. and Abedini, A. (2017). Shear confusion: Identification of the appropriate equivalent strain in simple shear using the logarithmic strain measure. *International Journal of Mechanical Sciences*, 134:273 – 283.

Børvik, T., Hopperstad, O., Berstad, T., and Langseth, M. (2001). A computational model of viscoplasticity and ductile damage for impact and penetration. *European Journal of Mechanics - A/Solids*, 20(5):685–712.

Cabot, G. P. and Bazant, Z. P. (1987). Nonlocal damage theory. *Journal of Engineering Mechanics*, 113(10):1512–1533.

Cailletaud, G. (1987). *Une approche micromecanique phenomenologique du comportement inelastique des metaux*. PhD thesis, Paris univeristy Paris 6.

Cailletaud, G. (1992). A micromechanical approach to inelastic behaviour of metals. *International Journal of Plasticity*, 8:55–73.

Chen, J. (2011). *Ductile tearing of AA2198 aluminium-lithium sheets for aeronautic application*. Theses, École Nationale Supérieure des Mines de Paris.

Chen, J., Madi, Y., Morgeneyer, T. F., and Besson, J. (2011). Plastic flow and ductile rupture of a 2198 al–cu–li aluminum alloy. *Computational Materials Science*, 50(4):1365–1371. Proceedings of the 19th International Workshop on Computational Mechanics of Materials.

Chu, C. C. and Needleman, A. (1980). Void Nucleation Effects in Biaxially Stretched Sheets. *Journal of Engineering Materials and Technology*, 102(3):249–256.

Cormack, A. M. (1963). Representation of a function by its line integrals, with some radiological applications. *Journal of Applied Physics*, 34(9):2722–2727.

Cox, T. B. and Low, J. R. (1974). An investigation of the plastic fracture of aisi 4340 and 18 nickel-200 grade maraging steels. *Metallurgical and Materials Transactions B*, 5(6):1457–1470.

Czerwinski, F. (2021). Current trends in automotive lightweighting strategies and materials. *Materials*, 14(21).

Deschamps, A., Decreus, B., De Geuser, F., Dorin, T., and Weyland, M. (2013). The influence of precipitation on plastic deformation of al–cu–li alloys. *Acta Materialia*, 61(11):4010–4021.

Dorin, T., Vahid, A., and Lamb, J. (2018). Chapter 11 - aluminium lithium alloys. In Lumley, R. N., editor, *Fundamentals of Aluminium Metallurgy*, Woodhead Publishing Series in Metals and Surface Engineering, pages 387–438. Woodhead Publishing.

Douissard, P.-A., Cecilia, A., Rochet, X., Chapel, X., Martin, T., van de Kamp, T., Helfen, L., Baumbach, T., Luquot, L., Xiao, X., Meinhardt, J., and Rack, A. (2012). A versatile indirect detector design for hard X-ray microimaging. *Journal of Instrumentation*, 7.

Dunand, M. and Mohr, D. (2011). Optimized butterfly specimen for the fracture testing of sheet materials under combined normal and shear loading. *Engineering Fracture Mechanics*, 78(17):2919–2934.

Ehrström, J.-C. and Warner, T. (2000). Metallurgical design of alloys for aerospace structures. In *Aluminium Alloys - Their Physical and Mechanical Properties*, volume 331 of *Materials Science Forum*, pages 5–16. Trans Tech Publications Ltd.

Faessel, M. and Bilodeau, M. (2013). SMIL: Simple Morphological Image Library. In *Séminaire Performance et Généricité, LRDE*, Villejuif, France.

Faleskog, J., Gao, X., and Shih, C. F. (1998). Cell model for nonlinear fracture analysis – i. micromechanics calibration. *International Journal of Fracture*, 89(4):355–373.

FLAMINGo (2021). Aluminium in cars unlocking the light-weighting potential. Technical report, European aluminum association.

Fleck, N., Hutchinson, J., and Tvergaard, V. (1989). Softening by void nucleation and growth in tension and shear. *Journal of the Mechanics and Physics of Solids*, 37(4):515–540.

Frodal, B. H., Thomesen, S., Børvik, T., and Hopperstad, O. S. (2021). On the coupling of damage and single crystal plasticity for ductile polycrystalline materials. *International Journal of Plasticity*, 142:102996.

Gao, X., Faleskog, J., and Shih, C. F. (1998). Cell model for nonlinear fracture analysis – ii. fracture- process calibration and verification. *International Journal of Fracture*, 89(4):375–398.

Gerke, S., Zistl, M., Bhardwaj, A., and Brünig, M. (2019). Experiments with the x0-specimen on the effect of non-proportional loading paths on damage and fracture mechanisms in aluminum alloys. *International Journal of Solids and Structures*, 163:157–169.

Giummarra, C., Rioja, R., Bray, G., Magnusen, P., and Moran, J. (2008). Al-li alloys: Development of corrosion resistant, high toughness aluminium-lithium aerospace alloys. In *Proc. ICAA11 conference, Aachen, Germany*, volume 1, pages 176–188.

Gologanu, M., Leblond, J.-B., and Devaux, J. (1993). Approximate models for ductile metals containing non-spherical voids—case of axisymmetric prolate ellipsoidal cavities. *Journal of the Mechanics and Physics of Solids*, 41(11):1723–1754.

Gologanu, M., Leblond, J.-B., and Devaux, J. (1994). Approximate Models for Ductile Metals Containing Nonspherical Voids—Case of Axisymmetric Oblate Ellipsoidal Cavities. *Journal of Engineering Materials and Technology*, 116(3):290–297.

Gologanu, M., Leblond, J.-B., Perrin, G., and Devaux, J. (1997). *Recent Extensions of Gurson's Model for Porous Ductile Metals*, pages 61–130. Springer Vienna, Vienna.

Gorji, M. B., Furmanski, J., and Mohr, D. (2021). From macro- to micro-experiments: Specimen-size independent identification of plasticity and fracture properties. *International Journal of Mechanical Sciences*, 199:106389.

Granum, H., Morin, D., Børvik, T., and Hopperstad, O. S. (2021). Calibration of the modified mohr-coulomb fracture model by use of localization analyses for three tempers of an aa6016 aluminium alloy. *International Journal of Mechanical Sciences*, 192:106122.

Gross, A. J. and Ravi-Chandar, K. (2016). On the deformation and failure of Al 6061-T6 at low triaxiality evaluated through in situ microscopy. *International Journal of Fracture*, 200:185–208.

Gurson, A. L. (1977). Continuum Theory of Ductile Rupture by Void Nucleation and Growth: Part I—Yield Criteria and Flow Rules for Porous Ductile Media. *Journal of Engineering Materials and Technology*, 99(1):2–15.

Gérard, C., Bacroix, B., Bornert, M., Cailletaud, G., Crépin, J., and Leclercq, S. (2009). Hardening description for fcc materials under complex loading paths. *Computational Materials Science*, 45(3):751–755. Proceedings of the 17th International Workshop on Computational Mechanics of Materials.

Haltom, S., Kyriakides, S., and Ravi-Chandar, K. (2013). Ductile failure under combined shear and tension. *International Journal of Solids and Structures*, 50(10):1507–1522.

Haouala, S., Segurado, J., and LLorca, J. (2018). An analysis of the influence of grain size on the strength of fcc polycrystals by means of computational homogenization. *Acta Materialia*, 148:72–85.

Helfen, L., Baumbach, T., Cloetens, P., and Baruchel, J. (2009). Phase-contrast and holographic computed laminography. *Applied Physics Letters*, 94(10):104103.

Helfen, L., Baumbach, T., Mikulík, P., Kiel, D., Pernot, P., Cloetens, P., and Baruchel, J. (2005). High-resolution three-dimensional imaging of flat objects by synchrotron-radiation computed laminography. *Applied Physics Letters*, 86(7):071915.

Helfen, L., Morgeneyer, T. F., Xu, F., Mavrogordato, M. N., Sinclair, I., Schillinger, B., and Baumbach, T. (2012). Synchrotron and neutron laminography for three-dimensional imaging of devices and flat material specimens. *International Journal of Materials Research*, 103(2):170–173.

Hill, R. (1950). *The mathematical theory of plasticity.* Oxford university press.

Huang, Y. (1991). Accurate Dilatation Rates for Spherical Voids in Triaxial Stress Fields. *Journal of Applied Mechanics*, 58(4):1084–1086.

Hurst, M., Helfen, L., Suhonen, H., Morgeneyer, T. F., Buljac, A., Suuronen, J.-P., Hänschke, D., and Baumbach, T. (2021). Hierarchical 4d imaging by x-ray phase-contrast nano-laminography. *submitted.*

IPCC (2021). Climate change 2021: The physical science basis. Technical report, the Sixth Assessment Report of the Intergovernmental Panel on Climate Change.

Johnson, G. R. and Cook, W. H. (1985). Fracture characteristics of three metals subjected to various strains, strain rates, temperatures and pressures. *Engineering Fracture Mechanics*, 21(1):31–48.

Kachanov, L. (1958). Time of the rupture process under creep conditions. *Otdelenie Teckhnicheskikh Nauk*, 8(1):26–31.

Kanjarla, A. K., Van Houtte, P., and Delannay, L. (2010). Assessment of plastic heterogeneity in grain interaction models using crystal plasticity finite element method. *International Journal of Plasticity*, 26(8):1220–1233. Special Issue In Honor of Lallit Anand.

Karafillis, A. and Boyce, M. (1993). A general anisotropic yield criterion using bounds and a transformation weighting tensor. *Journal of the Mechanics and Physics of Solids*, 41(12):1859–1886.

Kong, X., Chen, J. Q., Madi, Y., Missoum-Benziane, D., Besson, J., and Morgeneyer, T. F. (2021). Plasticity and ductility of an anisotropic recrystallized AA2198 Al-Cu-Li alloy in T3 and T8 conditions during proportional and non-proportional loading paths: simulations and experiments. working paper or preprint.

Kong, X., Helfen, L., Hurst, M., Hänschke, D., Missoum-Benziane, D., Besson, J., Baumbach, T., and Morgeneyer, T. F. (2022a). 3d in situ study of damage during a ‘shear to tension’ load path change in an aluminium alloy. *Acta Materialia*, page 117842.

Kong, X., Missoum-Benziane, D., Gaslain, F., Helfen, L., Hurst, M., Baumbach, T., Suhonen, H., and Morgeneyer, T. F. (2022b). Multiscale observation of ductile damage on an aluminium alloy 2198 under shear. *Under preparation.*

Koplik, J. and Needleman, A. (1988). Void growth and coalescence in porous plastic solids. *International Journal of Solids and Structures*, 24(8):835–853.

Krajcinovic, D. (1985). Continuous Damage Mechanics Revisited: Basic Concepts and Definitions. *Journal of Applied Mechanics*, 52(4):829–834.

Kroner, E. (1961). Zur plastischen verformung des vielkristalls. *Acta Metallurgica*, 9(2):155–161.

Landron, C., Maire, E., Adrien, J., Suhonen, H., Cloetens, P., and Bouaziz, O. (2012). Non-destructive 3-d reconstruction of the martensitic phase in a dual-phase steel using synchrotron holotomography. *Scripta Materialia*, 66(12):1077–1080. Viewpoint Set no. 50: Twinning Induced PlasticitySteels.

Le-Jolu, T., Morgeneyer, T. F., and Gourgues-Lorenzon, A. F. (2010). Effect of joint line remnant on fatigue lifetime of friction stir welded al–cu–li alloy. *Science and Technology of Welding and Joining*, 15(8):694–698.

Lemaitre, J. (1985). A Continuous Damage Mechanics Model for Ductile Fracture. *Journal of Engineering Materials and Technology*, 107(1):83–89.

Lemaitre, J. (1996). *A Course on Damage Mechanics*. Springer, Berlin, Heidelberg.

Lemaitre, J. and Chaboche, J.-L. (1990). *Mechanics of Solid Materials*. Cambridge University Press.

Lemaitre, J. and Desmorat, R. (2005). *Engineering Damage Mechanics: Ductile, creep, fatigue and brittle failures*. Springer, Berlin, Heidelberg.

Lorentz, E. and Benallal, A. (2005). Gradient constitutive relations: numerical aspects and application to gradient damage. *Computer Methods in Applied Mechanics and Engineering*, 194(50):5191–5220.

Luo, M. and Rousselier, G. (2014). Modeling of large strain multi-axial deformation of anisotropic metal sheets with strength-differential effect using a reduced texture methodology. *International Journal of Plasticity*, 53:66–89.

Madi, Y., Shinohara, Y., and Besson, J. (2020). Effect of prestrain on ductility and toughness in a high-strength line pipe steel. *International Journal of Fracture*, 224(1):15–29.

Madou, K. and Leblond, J.-B. (2012a). A gurson-type criterion for porous ductile solids containing arbitrary ellipsoidal voids—i: Limit-analysis of some representative cell. *Journal of the Mechanics and Physics of Solids*, 60(5):1020–1036.

Madou, K. and Leblond, J.-B. (2012b). A gurson-type criterion for porous ductile solids containing arbitrary ellipsoidal voids—ii: Determination of yield criterion parameters. *Journal of the Mechanics and Physics of Solids*, 60(5):1037–1058.

Madou, K. and Leblond, J.-B. (2013). Numerical studies of porous ductile materials containing arbitrary ellipsoidal voids – i: Yield surfaces of representative cells. *European Journal of Mechanics - A/Solids*, 42:480–489.

Madou, K., Leblond, J.-B., and Morin, L. (2013). Numerical studies of porous ductile materials containing arbitrary ellipsoidal voids – ii: Evolution of the length and orientation of the void axes. *European Journal of Mechanics - A/Solids*, 42:490–507.

Mae, H., Teng, X., Bai, Y., and Wierzbicki, T. (2007). Calibration of ductile fracture properties of a cast aluminum alloy. *Materials Science and Engineering: A*, 459(1):156–166.

Mae, H., Teng, X., Bai, Y., and Wierzbicki, T. (2008). Comparison of ductile fracture properties of aluminum castings: Sand mold vs. metal mold. *International Journal of Solids and Structures*, 45(5):1430–1444.

Maire, E. and Withers, P. J. (2014). Quantitative x-ray tomography. *International Materials Reviews*, 59(1):1–43.

Marino, B., Mudry, F., and Pineau, A. (1985). Experimental study of cavity growth in ductile rupture. *Engineering Fracture Mechanics*, 22(6):989–996.

McClintock, F. A. (1968). A criterion for ductile fracture by the growth of holes. *Journal of Applied Mechanics*, 35(2):363–371.

Mohr, D. and Doyoyo, M. (2004). Experimental Investigation on the Plasticity of Hexagonal Aluminum Honeycomb Under Multiaxial Loading . *Journal of Applied Mechanics*, 71(3):375–385.

Mohr, D. and Henn, S. (2007). Calibration of stress-triaxiality dependent crack formation criteria: A new hybrid experimental–numerical method. *Experimental Mechanics*, 47(6):805–820.

Mohr, D. and Marcadet, S. J. (2015). Micromechanically-motivated phenomenological hosford–coulomb model for predicting ductile fracture initiation at low stress triaxialities. *International Journal of Solids and Structures*, 67-68:40–55.

Monchiet, V., Cazacu, O., Charkaluk, E., and Kondo, D. (2008). Macroscopic yield criteria for plastic anisotropic materials containing spheroidal voids. *International Journal of Plasticity*, 24(7):1158–1189.

Monchiet, V., Gruescu, C., Charkaluk, E., and Kondo, D. (2006). Approximate yield criteria for anisotropic metals with prolate or oblate voids. *Comptes Rendus Mécanique*, 334(7):431–439.

Morgeneyer, T. and Besson, J. (2011). Flat to slant ductile fracture transition: Tomography examination and simulations using shear-controlled void nucleation. *Scripta Materialia*, 65(11):1002–1005.

Morgeneyer, T., Besson, J., Proudhon, H., Starink, M., and Sinclair, I. (2009). Experimental and numerical analysis of toughness anisotropy in aa2139 al-alloy sheet. *Acta Materialia*, 57(13):3902 – 3915.

Morgeneyer, T., Starink, M., and Sinclair, I. (2008). Evolution of voids during ductile crack propagation in an aluminium alloy sheet toughness test studied by synchrotron radiation computed tomography. *Acta Materialia*, 56(8):1671–1679.

Morgeneyer, T. F., Helfen, L., Mubarak, H., and Hild, F. (2013). 3D Digital Volume Correlation of Synchrotron Radiation Laminography images of ductile crack initiation: An initial feasibility study. *Experimental Mechanics*, 53:543–556.

Morgeneyer, T. F., Khadyko, M., Buljac, A., Helfen, L., Hild, F., Benallal, Ahmed Børvik, T., and Hopperstad, O. S. (2021). On crystallographic aspects of heterogeneous plastic flow during ductile tearing: 3D measurements and crystal plasticity simulations for AA7075-T651. *International Journal of Plasticity*, 144:103028.

Morgeneyer, T. F., Taillandier-Thomas, T., Helfen, L., Baumbach, T., Sinclair, I., Roux, S., and Hild, F. (2014). In situ 3d observation of early strain localization during failure of thin al alloy (2198) sheet. *Acta Materialia*, 69:78 – 91.

Morin, L., Leblond, J.-B., Mohr, D., and Kondo, D. (2017). Prediction of shear-dominated ductile fracture in a butterfly specimen using a model of plastic porous solids including void shape effects. *European Journal of Mechanics - A/Solids*, 61:433–442.

Morin, L., Leblond, J.-B., and Tvergaard, V. (2016). Application of a model of plastic porous materials including void shape effects to the prediction of ductile failure under shear-dominated loadings. *Journal of the Mechanics and Physics of Solids*, 94:148–166.

Myagotin, A., Voropaev, A., Helfen, L., Hanschke, D., and Baumbach, T. (2013). Efficient volume reconstruction for parallel-beam computed laminography by filtered backprojection on multi-core clusters. *IEEE transactions on image processing*, 22(12):5348–5361.

Méric, L., Poubanne, P., and Cailletaud, G. (1991). Single Crystal Modeling for Structural Calculations: Part 1—Model Presentation. *Journal of Engineering Materials and Technology*, 113(1):162–170.

Nahshon, K. and Hutchinson, J. (2008). Modification of the gurson model for shear failure. *European Journal of Mechanics - A/Solids*, 27(1):1 – 17.

Nayan, N., Murty, S. V. S. N., Sarkar, R., Mukhopadhyay, A. K., Ahlawat, S., Sarkar, S. K., Prasad, M. J. N. V., and Samajdar, I. (2019). The anisotropy of serrated flow behavior of al-cu-li (aa2198) alloy. *Metallurgical and Materials Transactions A*, 50:5066 – 5078.

Nielsen, K. L., Dahl, J., and Tvergaard, V. (2012). Collapse and coalescence of spherical voids subject to intense shearing: studied in full 3d. *International Journal of Fracture*, 177(2):97–108.

Nielsen, K. L. and Tvergaard, V. (2011). Failure by void coalescence in metallic materials containing primary and secondary voids subject to intense shearing. *International Journal of Solids and Structures*, 48(9):1255–1267.

Onaka, S. (2010). Equivalent strain in simple shear deformation described by using the hencky strain. *Philosophical Magazine Letters*, 90(9):633–639.

Onaka, S. (2012). Comment on “a comparison of the von mises and hencky equivalent strains for use in simple shear experiments”. *Philosophical Magazine*, 92(18):2264–2271.

Papasidero, J., Doquet, V., and Lepeer, S. (2014). Multiscale investigation of ductile fracture mechanisms and strain localization under shear loading in 2024-T351 aluminum alloy and 36NiCrMo16 steel. *Materials Science and Engineering: A*.

Papasidero, J., Doquet, V., and Mohr, D. (2013). Determination of the effect of stress state on the onset of ductile fracture through tension-torsion experiments. *Experimental Mechanics*, 54(2):137–151.

Papasidero, J., Doquet, V., and Mohr, D. (2015). Ductile fracture of aluminum 2024-t351 under proportional and non-proportional multi-axial loading: Bao–wierzbicki results revisited. *International Journal of Solids and Structures*, 69-70:459–474.

Pardoen, T. and Hutchinson, J. (2000). An extended model for void growth and coalescence. *Journal of the Mechanics and Physics of Solids*, 48(12):2467–2512.

Park, N., Stoughton, T. B., and Yoon, J. W. (2020). A new approach for fracture prediction considering general anisotropy of metal sheets. *International Journal of Plasticity*, 124:199–225.

Peirs, J., Verleysen, P., and Degrieck, J. (2012). Novel technique for static and dynamic shear testing of ti6al4v sheet. *Experimental Mechanics*, 52(7):729–741.

Petit, T., Besson, J., Ritter, C., Colas, K., Helfen, L., and Morgeneyer, T. F. (2019). Effect of hardening on toughness captured by stress-based damage nucleation in 6061 aluminum alloy. *Acta Materialia*, 180:349–365.

Petit, T., Ritter, C., Besson, J., and Morgeneyer, T. F. (2018). Impact of machine stiffness on “pop-in” crack propagation instabilities. *Engineering Fracture Mechanics*, 202:405–422.

Pineau, A., Benzerga, A., and Pardoen, T. (2016). Failure of metals i: Brittle and ductile fracture. *Acta Materialia*, 107:424–483.

Polmear, I. (2005). 3 - wrought aluminium alloys. In Polmear, I., editor, *Light Alloys (Fourth Edition)*, pages 97–204. Butterworth-Heinemann, Oxford, fourth edition edition.

Rice, J. and Tracey, D. (1969). On the ductile enlargement of voids in triaxial stress fields. *Journal of the Mechanics and Physics of Solids*, 17(3):201–217.

Roters, F., Eisenlohr, P., Hantcherli, L., Tjahjanto, D., Bieler, T., and Raabe, D. (2010). Overview of constitutive laws, kinematics, homogenization and multiscale methods in crystal plasticity finite-element modeling: Theory, experiments, applications. *Acta Materialia*, 58(4):1152–1211.

Roth, C. C. and Mohr, D. (2016). Ductile fracture experiments with locally proportional loading histories. *International Journal of Plasticity*, 79:328–354.

Roth, C. C. and Mohr, D. (2018). Determining the strain to fracture for simple shear for a wide range of sheet metals. *International Journal of Mechanical Sciences*, 149:224 – 240.

Roth, C. C., Morgeneyer, T. F., Cheng, Y., Helfen, L., and Mohr, D. (2018). Ductile damage mechanism under shear-dominated loading: In-situ tomography experiments on dual phase steel and localization analysis. *International Journal of Plasticity*, 109:169 – 192.

Rousselier, G. (1981). Finite deformation constitutive relations including ductile fracture damage. In *TRHEE-DIMENSIONAL CONSTITUTIVE RELATIONS AND DUCTILE FRACTURE*. North-Holland Publishing Company.

Rousselier, G. (1987). Ductile fracture models and their potential in local approach of fracture. *Nuclear Engineering and Design*, 105(1):97–111.

Rousselier, G. (2001). Section 6.6 - the rousselier model for porous metal plasticity and ductile fracture. In LEMAITRE, J., editor, *Handbook of Materials Behavior Models*, pages 436–445. Academic Press, Burlington.

Rousselier, G. (2021). Porous plasticity revisited: Macroscopic and multiscale modeling. *International Journal of Plasticity*, 136:102881.

Rousselier, G., Barlat, F., and Yoon, J. (2009). A novel approach for anisotropic hardening modeling. part i: Theory and its application to finite element analysis of deep drawing. *International Journal of Plasticity*, 25(12):2383–2409.

Rousselier, G., Barlat, F., and Yoon, J. (2010). A novel approach for anisotropic hardening modeling. part ii: Anisotropic hardening in proportional and non-proportional loadings, application to initially isotropic material. *International Journal of Plasticity*, 26(7):1029–1049.

Rousselier, G. and Leclercq, S. (2006). A simplified “polycrystalline” model for viscoplastic and damage finite element analyses. *International Journal of Plasticity*, 22(4):685–712.

Rousselier, G. and Luo, M. (2014). A fully coupled void damage and mohr–coulomb based ductile fracture model in the framework of a reduced texture methodology. *International Journal of Plasticity*, 55:1–24.

Rousselier, G., Luo, M., and Mohr, D. (2012). Macroscopic plasticity modeling of anisotropic aluminum extrusions using a reduced texture methodology. *International Journal of Plasticity*, 30-31:144–165.

Rousselier, G., Morgeneyer, T. F., Ren, S., Mazière, M., and Forest, S. (2017). Interaction of the portevin–le chatelier phenomenon with ductile fracture of a thin aluminum ct specimen: experiments and simulations. *International Journal of Fracture*, 206(1):95–122.

Sai, K., Cailletaud, G., and Forest, S. (2006). Micro-mechanical modeling of the inelastic behavior of directionally solidified materials. *Mechanics of Materials*, 38(3):203–217.

Shima, S. and Oyane, M. (1976). Plasticity theory for porous metals. *International Journal of Mechanical Sciences*, 18(6):285–291.

Siruguet, K. and Leblond, J.-B. (2004). Effect of void locking by inclusions upon the plastic behavior of porous ductile solids—i: theoretical modeling and numerical study of void growth. *International Journal of Plasticity*, 20(2):225–254.

Stock, S. R. (2008). Recent advances in x-ray microtomography applied to materials. *International Materials Reviews*, 53(3):129–181.

Sutton, M. A., Orteu, J.-J., and Schreier, H. W. (2009). *Image Correlation for Shape, Motion and Deformation Measurements: Basic Concepts,Theory and Applications*. Springer US, Boston, MA.

Tancogne-Dejean, T., Roth, C. C., Morgeneyer, T. F., Helfen, L., and Mohr, D. (2021). Ductile damage of aa2024-t3 under shear loading: Mechanism analysis through in-situ laminography. *Acta Materialia*, 205:116556.

Tarigopula, V., Hopperstad, O., Langseth, M., and Clausen, A. (2009). An evaluation of a combined isotropic-kinematic hardening model for representation of complex strain-path changes in dual-phase steel. *European Journal of Mechanics - A/Solids*, 28(4):792–805.

Tarigopula, V., Hopperstad, O. S., Langseth, M., Clausen, A. H., Hild, F., Lademo, O.-G., and Eriksson, M. (2008). A study of large plastic deformations in dual phase steel using digital image correlation and fe analysis. *Experimental Mechanics*, 48(2):181–196.

Taylor, R. (2000). A mixed-enhanced formulation for tetrahedral finite elements. *International Journal for numerical methods in engineering*, 47:205–227.

Tekkaya, A., Bouchard, P.-O., Bruschi, S., and Tasan, C. (2020). Damage in metal forming. *CIRP Annals*, 69(2):600–623.

Torki, M. E. and Benzerga, A. A. (2018). A mechanism of failure in shear bands. *Extreme Mechanics Letters*, 23:67–71.

Tvergaard, V. (2008). Shear deformation of voids with contact modelled by internal pressure. *International Journal of Mechanical Sciences*, 50(10):1459–1465.

Tvergaard, V. (2009). Behaviour of voids in a shear field. *International Journal of Fracture*, 158(1):41–49.

Tvergaard, V. and Needleman, A. (1984). Analysis of the cup-cone fracture in a round tensile bar. *Acta Metallurgica*, 32(1):157–169.

UNEP (2021). Emissions gap report 2021: The heat is on - a world of climate promises not yet delivered. Technical report, United Nation Environment Programme (2021).

Villanova, J., Daudin, R., Lhuissier, P., Jauffrès, D., Lou, S., Martin, C. L., Labouré, S., Tucoulou, R., Martínez-Criado, G., and Salvo, L. (2017). Fast in situ 3d nanoimaging: a new tool for dynamic characterization in materials science. *Materials Today*, 20(7):354–359.

Vogelgesang, M., Farago, T., Morgeneyer, T. F., Helfen, L., dos Santos Rolo, T., Myagotin, A., and Baumbach, T. (2016). Real-time image content based beamline control for smart 4d x-ray imaging. *Journal of Synchrotron Radiation*, 23:1254–1263.

Wanhill, R. (1994). Flight simulation fatigue crack growth testing of aluminium alloys: Specific issues and guidelines. *International Journal of Fatigue*, 16(2):99–110.

Warner, T. (2006). Recently-developed aluminium solutions for aerospace applications. In *Aluminium Alloys 2006 - ICAA10*, volume 519 of *Materials Science Forum*, pages 1271–1278. Trans Tech Publications Ltd.

Weitkamp, T., Tafforeau, P., Boller, E., Cloetens, P., Valade, J.-P., Bernard, P., Peyrin, F., Ludwig, W., Helfen, L., and Baruchel, J. (2010). Parallel-beam imaging at the ESRF beamline ID19: current status and plans for the future. In Garrett, R., Gentle, I., Nugent, K., and Wilkins, S., editors, *AIP Conference Proceedings*, volume 1234, pages 83–86.

Wilkins, S. W., Gureyev, T. E., Gao, D., Pogany, A., and Stevenson, A. W. (1996). Phase-contrast imaging using polychromatic hard x-rays. *Nature*, 384(6607):335–338.

Xavier, M. D., de Lima, N. B., Plaut, R. L., and Schön, C. G. (2015). Strain path dependence of the flc0 formability parameter in an interstitial free steel. *The International Journal of Advanced Manufacturing Technology*, 80(5):1077–1085.

Xu, F., Helfen, L., Baumbach, T., and Suhonen, H. (2012a). Comparison of image quality in computed laminography and tomography. *Opt. Express*, 20(2):794–806.

Xu, F., Helfen, L., Suhonen, H., Elgrabli, D., Bayat, S., Reischig, P., Baumbach, T., and Cloetens, P. (2012b). Correlative nanoscale 3d imaging of structure and composition in extended objects. *PLoS ONE*, 7(11):e50124.

Zhang, Z., Thaulow, C., and Jødegård (2000). A complete gurson model approach for ductile fracture. *Engineering Fracture Mechanics*, 67(2):155–168.

Zhang, Z. L. and Niemi, E. (1994). A new failure criterion for the gurson-tvergaard dilational constitutive model. *International Journal of Fracture*, 70(4):321–334.

RÉSUMÉ

Dans la recherche de matériaux plus légers et de composants à parois minces optimisés pour le transport, la connaissance des mécanismes d'endommagement ductiles caractéristiques des tôles est essentielle. Les interactions entre la déformation et l'endommagement ne sont pas encore bien comprises dans des conditions de chargement dominées par le cisaillement (faible contrainte triaxialité), sans parler de l'importance de l'application dans le cas de changements complexes de la trajectoire de chargement.

Grâce à la laminographie synchrotron 3D, l'évolution de l'endommagement d'une éprouvette de cisaillement en tôle plate en alliage Al-Cu-Li 2198 T8 recristallisé a été étudiée avec une résolution allant du micro au nanomètre. Deux caractéristiques principales de dommages, les fissures plates granulaires et les fissures de particules intermétalliques, ont été trouvées et suivies. L'origine de ces fissures plates nuisibles a été étudiée par EBSD corrélative. Les fissures se sont avérées être à la fois intergranulaires et transgranulaires. Afin d'étudier l'effet de la charge de pré-cisaillement et le mécanisme d'endommagement, une expérience laminographique *in situ* a été réalisée au cours d'un changement de trajectoire de charge de 'cisaillement à tension' (ST). La ductilité de l'essai ST était significativement réduite par rapport à l'essai proportionnel. Au microscope, les dommages 3D se sont formés sous cisaillement et ont ensuite continué à croître et à coalescer jusqu'à la rupture pendant la charge de traction, expliquant ainsi la réduction de la ductilité. Pour mieux interpréter les résultats expérimentaux, une modélisation par éléments finis (FE) a été réalisée en utilisant un modèle de plasticité anisotrope. Le modèle a réussi à prédire le comportement plastique sous des charges non proportionnelles, non seulement ST mais aussi 'tension à cisaillement' (TS), ainsi qu'à prévoir les champs de déformation équivalents accumulés mesurés par corrélation d'image numérique 2D (DIC) sur des données de volume projeté. Un modèle d'endommagement polycristallin de Rousselier-Coulomb, qui associe pleinement la croissance classique des vides pour la triaxialité des contraintes élevées et le modèle de Coulomb à l'échelle du système de glissement pour la triaxialité des contraintes faibles, a été appliqué pour modéliser l'évolution de l'endommagement sous les changements de trajectoire de charge et a réussi à prédire la réduction de la ductilité sous des charges non proportionnelles.

MOTS CLÉS

Endommagement, tomo(lamino)graphie, aluminum, transport, simulations, changement de trajet de chargement

ABSTRACT

In the pursuit of lighter materials and optimized thin-walled components for transportation, knowledge about the characteristic ductile damage mechanisms in metal sheets is key. Strain-damage interactions are still not well understood under shear dominant (low stress triaxiality) loading conditions, not to mention highly application-relevant under complex load path changes.

With 3D synchrotron laminography, the damage evolution in a flat sheet shear specimen made of recrystallized Al-Cu-Li alloy 2198 T8 was studied from micro down to nanometer resolution. Two main damage features, granular flat cracks and intermetallic particle cracks, were found and followed. The origin of these detrimental flat cracks was investigated by correlative EBSD. The cracks turned out to be both intergranular and transgranular. In order to study the effect of pre-shear loading and the damage mechanism, an *in situ* laminographic experiment was carried out during a 'shear to tension' (ST) load path change. The ductility of the ST test was significantly reduced compared to the proportional one. Microscopically, 3D damage, nucleated under shear and subsequently continued to grow and coalesce till fracture during tensile loading thereby explaining the ductility reduction. To interpret further the experimental results finite element (FE) modelling was carried out using a model for anisotropic plasticity. The model succeeded in predicting the plastic behaviour under non-proportional loadings, not only ST but also 'tension to shear' (TS), as well as in foreseeing the accumulated equivalent strain fields measured by 2D digital image correlation (DIC) on projected volume data. A Rousselier-Coulomb polycrystalline damage model, that fully couples classical void growth for high stress triaxiality and Coulomb model at the slip system scale for low stress triaxiality, was applied to model damage evolution under load path changes and succeeded in predicting ductility reduction under non-proportional loadings.

KEYWORDS

Damage, tomo(lamino)graphy, aluminum, transport, simulations, load path change.